Simulation of polydisperse bubbly flows: An investigation on physical and numerical aspects

Mohsen Shiea
* * * * * *

Supervisors
Marco Vanni, Supervisor
Antonio Buffo, Co-supervisor
Daniele Marchisio, Co-supervisor

Politecnico di Torino
March 06, 2020

I hereby declare that, the contents and organisation of this dissertation constitute my own original work and does not compromise in any way the rights of third parties, including those relating to the security of personal data.

. . . .

Mohsen Shiea

Turin, March 06, 2020

Abstract

This thesis aims at the Eulerian-Eulerian computational fluid dynamics (CFD) simulation of gas-liquid bubbly flows coupled with the Population Balance Modelling (PBM) with the main focus on investigating some physical and numerical aspects.

The Eulerian-Eulerian framework is currently the most viable approach for the CFD simulation of large-scale disperse gas-liquid flows. Differently from more complex methods, the Eulerian-Eulerian approach does not resolve explicitly the interfaces between the bubbles and the liquid phase. Instead, the physical phenomena occurring at the interface, i.e. mass, momentum and heat exchanges between the phases, are taken into account by means of some closure relations. Restricting the discussion to hydrodynamic simulations, the closure relations to describe the momentum exchange between the phases are interfacial forces, e.g. drag, turbulent dispersion, lift and wall lubrication. The predictions of Eulerian-Eulerian CFD simulations of bubbly flows depend strongly upon the choice of formulations employed for modelling these forces, among which the lift and wall lubrication forces have been the subject of ongoing investigations to overcome the lack of accurate modelling or clear physical explanation. This thesis makes use of a set of experimental data provided by the Helmholtz-Zentrum Dresden-Rossendorf to assess the performance of some available closure relations. The experimental data belongs to the measurements conducted in TOPFLOW facility for a large-scale developing turbulent bubbly flow. Two sets of models are selected, differing in the relations for the lift and wall lubrication forces. Additionally, the lift coefficient of each set is replaced with a constant value optimized to achieve the best agreement with the experiments. The results verify the need for employing negative lift coefficients in the case of large bubbles (> 5 mm). In addition, it is shown that the geometric approach to consider the wall effect results in a slightly better agreement than a standard relation, which assumes the asymmetric drainage around bubbles near the wall. Eventually, optimizing the lift coefficient highlights the importance of investigating spatially developing flows to draw general conclusions on the applicability of closure relations.

The second part of the thesis deals with coupling the PBM and CFD in order to predict the evolution of the bubble size distribution. In this regard, a literature

review is presented on the methods for the solution of the PBE with a particular attention to quadrature-based moment methods, since they are perfectly compatible with the Eulerian framework. Among these methods, the quadrature method of moments is chosen as the solution method for the CFD-PBM simulation of the TOPFLOW facility. The main challenge observed in conducting the simulations is the realizability issue, arising when high-order discretization schemes are used. Therefore, a new finite-volume scheme based on 2nd-order total variation diminishing (TVD) schemes is proposed for the solution of moment transport equations by quadrature-based moment methods. The proposed scheme is capable of preserving important properties of the transported moments, such as realizability and boundedness. The idea behind the scheme is to limit the flux of all the moments at each face of the computational cell with the same limiter value, hence being called the equal-limiter scheme. It is compared with other realizable schemes developed for the moment transport equations in several one- and two-dimensional examples. The corresponding results show the advantages of the equal-limiter scheme in improving the accuracy of the numerical prediction, avoiding under- and over-shoots in the solution and keeping the moments realizable at the same time. Eventually, the equal-limiter scheme is employed to conduct the CFD-PBM simulations of the TOPFLOW facility with two different choices for the equal limiter. The first choice is more conservative, by which the minimum of the flux limiters of all the transported moments is selected. In this case, the TVD criteria for all the transported moments are respected, however, the scheme can reduce to the 1st-order upwind scheme when the smoothness of the profiles of the moments are considerably different. The second choice for the equal limiter is the average of the flux limiters of all the transported moments, which improves the order of accuracy of the solution at the expense of not fulfilling the TVD criteria for some of the transported moments. Nevertheless, the simulation results show negligible under- and over-shoots due to this violation of TVD criteria. Finally, satisfactory predictions are obtained for the radial and axial profiles of the Sauter mean diameter in the TOPFLOW facility by conducting the CFD-PBM simulations, in which the equal-limiter scheme with the choice of the average limiter is employed. In addition, the reasons behind the observed discrepancies between the predictions and experimental measurements are discussed. The thesis concludes by summarizing the results and suggesting some future works.

Acknowledgements

Contents

Bibliography 165

Chapter 1

Introduction

Bubbly gas-liquid flows have been growing in importance across the research community, due to their widespread applications in diverse industries. These flows can be categorized as disperse multiphase systems, formed by separate gas bubbles being dispersed in a liquid phase. This type of multiphase flow can be found in different configurations, notably bubble columns [1–3], (usually vertical) pipes [4–10] and stirred tanks. Some well-known industrial applications of the mentioned configurations are multiphase chemical and biochemical reactors (e.g. Fischer-Tropsch process), boiling-water nuclear reactors, heat-exchangers, fermenters and wastewater aerated tanks. The importance of these applications has been promoting numerous researches to investigate bubbly flows by conducting experiments and Computational Fluid Dynamics (CFD) simulations.

Confining the discussion to the CFD simulation of bubbly flows, the Eulerian-Eulerian approach is the most common computational method, particularly in the context of industrial-scale simulations [11–15]. The notable feature of this approach is the assumption of interpenetrating continua, which avoids the need to track the interface between the liquid (continuous) phase and the gas (disperse) phase. Instead, the relevant phenomena occurring at the interface are taken into account via closure relations included in the average balance equations [16]. Those representing the interphase momentum transfer are called interfacial forces and play a crucial role in determining the hydrodynamic behavior of the two-phase flow. The common interfacial forces relevant to turbulent bubbly pipe flows are drag, lift, turbulent dispersion and wall lubrication [8, 17, 18]. However, the models for the description of the interfacial forces were mostly developed through theoretical and/or experimental analysis performed under certain controlled conditions, and therefore lack generality [19]. Among the mentioned forces, the lift and wall lubrication forces have been provoking ongoing debate over their physical explanation and corresponding suggested models [19–21]. For instance, the expression in Eq. (2.16) proposed by Tomiyama et al. [22] has been commonly employed to estimate the lift coefficient in various gas-liquid systems. This correlation was developed by tracking

the trajectories of single bubbles in a laminar shear flow of the glycerol-water solution. However, acceptable predictions have been obtained by using this correlation in the simulation of systems operating under conditions far from those set in the experiments by Tomiyama, e.g. air-water and steam-water systems [23]. Nevertheless, Ziegenhein in collaboration with Tomiyama has recently measured the lift coefficient in low Morton number conditions, as air-water two-phase systems, and has found smaller lift coefficients in comparison to Tomiyama's correlation [24]. The authors selected the major axis of the bubbles as the most reasonable choice for the characteristic length of the bubbles to describe the lift force dependency on the bubble size. However, they also acknowledged the dependency of the bubble major axis on the flow properties, hence the dependency of the lift force formulation on the flow properties. In another work, Sugrue [21] has recently developed an expression that considers the effects of the turbulence and bubbles' crowding, which are not present in the expression proposed by Tomiyama and co-workers. However, the maximum lift coefficients estimated by these two models differ an order of magnitude.

The correlations for the estimation of the wall lubrication force are even more controversial because of the ambiguity in the physical interpretation of the wall effect. Some of the proposed expressions [25–27] are derived from the work of Antal et al. [28], who associated the wall effect with the unbalanced drainage of the liquid around the bubbles located near the wall. These models result in a force of large magnitude near the wall that essentially pushes the gas phase completely out of the near-wall-region. On the contrary, some experimental investigations report that the bubbles might move close to the wall in the turbulent boundary layer [29–31]. Another approach applies a damping function on the lift coefficient near the wall [32]. However, it leads to a flat profile of the gas volume fraction close to the wall instead of a profile with a peak near the wall, which is observed experimentally. Recently, Lubchenko et al. [19] developed a new wall lubrication model based on the geometric analysis of bubbles close to the wall. Their model has the advantage of not yielding to zero gas volume fraction in the close vicinity of the wall.

In addition to the dependency on closure relations, Eulerian-Eulerian methods in their original formulation require the specification of the mean size of disperse phase elements. Setting this number fixed and constant, it is simply impossible to account for the polydispersity and effect of particulate processes. However, the characteristic properties of bubbles (e.g. size) change in space and time due to numerous processes, such as coalescence and break-up. As a result, bubbly flows often feature distributions of bubbles with different properties, a situation identified as polydispersity. A comprehensive CFD simulation of such flows must take into account polydispersity and therefore must include the description of the above-mentioned processes. In this regard, several researches attempted to include the description of these processes by means of a transport equation written in terms

of the bubble number density [33–37]. Although this method allows the bubble size to change in time and spatial position, no local dispersion is allowed about the mean bubble size. In other words, the bubbles located at a given spatial position are assumed to have the same size. This limitation was overcome by incorporating Population Balance Modelling (PBM) into the CFD simulations, which was realized in 00s. In this approach, the evolution of the population of bubbles in space and time is predicted through the solution of a Population Balance Equation (PBE) integrated into a CFD code. The PBE is an integro-differential equation written in terms of a number density function (NDF) that represents, at every point of the physical space, the number of bubbles with a particular state. The states of bubbles belong to the so-called phase space, i.e. the space of the properties constituted by the properties of interest (e.g. bubble size, velocity, chemical composition, temperature).

Several methods are available to solve the PBE, among which the Class or Sectional Method (CM) [37–46] and Quadrature-Based Moment Methods (QBMMs) [47–56] have been widely adopted for coupled CFD-PBM simulations of gas-liquid systems. However, the latter is much less expensive than the former from the computational point of view[47, 54]. This advantage takes on an added importance in industrial-scale simulations. In fact, QBMMs solve only a finite number of transport equations written in terms of a few integral properties of the NDF (i.e. the moments), instead of solving directly for the NDF itself [57]. However, these methods approximate the NDF (which is needed to close moment transport equations) with a summation of so-called kernel density functions, each one centered on a quadrature abscissa. The abscissas and weights of the quadrature are, in turn, calculated by using the transported set of moments.

Despite being one of the viable approaches adopted for coupled CFD-PBE simulations [54, 58–60], QBMMs pose a major practical issue called "realizability" or "consistency" of the moments, i.e. the calculated set of moments should be consistent during the simulation, meaning that there should exist a physically meaningful NDF corresponding to them. Therefore, it is important to employ suitable numerical methods designed for preventing the realizability issue as a source of simulation instability. In this regard, a main cause of the realizability issue is the scheme used for the discretization of the convective term of moment transport equations [59, 61–63], relevant to simulations of spatially inhomogeneous systems. This issue can be avoided by employing the 1$^\text{st}$-order upwind method [64]. On the contrary, employing standard high-order schemes can easily cause realizability issue, which hinders obtaining (usually desired) solutions of high-order accuracy. In the quest of achieving accurate solutions for QBMMs, novel techniques have been developed [59, 62, 63], among which the one formulated by Vikas and co-workers [62] is viable to be employed in simulations with three-dimensional unstructured grids. With this technique, called as the realizable quasi-high-order scheme, the non-realizability is overcome by the separate interpolation of abscissas (using 1$^\text{st}$-order scheme)

and weights (using high-order scheme), provided that a criterion on the simulation time-step is fulfilled. However, no analysis has been presented concerning the monotonicity-preserving property of this scheme. This property is important to avoid non-physical oscillations in the predicted solution [65]. The importance of this property is realized by considering the extensive literature on developing monotonicity-preserving methods. One notable example is the TVD (total variation diminishing) high-resolution schemes [65], which are commonly incorporated in CFD codes for the discretization of the convective term to achieve bounded solutions (i.e. no over- and under-shoots in the solution). Likewise, the boundedness in the solution of QBMMs deserves attention, since the low-order moments are often related to some physical properties of the disperse population, which are essentially bounded, such as the total mass and the total volume fraction of the bubbles [66].

The current thesis is mainly aimed at the CFD-PBM simulation of bubbly flows. In this context, two objectives are defined: 1) investigation of the interfacial forces relevant to bubbly flows, in particular the lift and wall lubrication forces, and selection of proper models to describe them; 2) development of numerical methods to perform reliable CFD simulations coupled with the PBM. Considering the objectives, the thesis is arranged in the following order: Chapter 2 describes the common methods employed for the CFD simulation of multiphase gas-liquid systems, with special attention to the Eulerian-Eulerian framework and interfacial forces. Then, a review on the PBM for the description of polydisperse systems is presented in Chapter 3, where the coupling between the PBM and CFD is also addressed. Chapter 4 discusses the results of the CFD simulations conducted for a bubbly pipe flow called the TOPFLOW facility, for which experimental data is available. Eventually, this chapter summarizes several findings about the correlations employed for the lift and wall lubrication forces. Moving to the second objective, Chapter 5 introduces a novel scheme for the solution of QBMMs named as the equal-limiter scheme, which addresses not only the realizability issue but also the accuracy and boundedness of the solution. Then, Chapter 6 discusses the advantages and shortcomings of the equal-limiter scheme by performing the two-way coupled CFD-PBM simulation of the TOPFLOW facility, and proposes a modification of the original scheme to improve its order of accuracy. The chapter ends by reporting and discussing the predictions obtained by the CFD-PBM simulations of the TOPFLOW facility.

This thesis is mainly on the basis of the material reported in the following published or submitted articles:

- M. Shiea, A. Buffo, E. Baglietto, D. Lucas, M. Vanni, D. L. Marchisio, "Evaluation of Hydrodynamic Closures for Bubbly Regime CFD Simulations in Developing Pipe Flow". In: *Chemical Engineering & Technology* 42 (2019), pp. 1618–1626.

- M. Shiea, A. Buffo, M. Vanni, D. L. Marchisio, "A novel finite-volume TVD scheme to overcome non-realizability problem in quadrature-based moment methods", accepted for publication in *Journal of Computational Physics*.

- M. Shiea, A. Buffo, M. Vanni, D. L. Marchisio, "Numerical Methods for the Solution of Population Balance Equations Coupled with Computational Fluid Dynamics", submitted to *Annual Review of Chemical and Biomolecular Engineering*.

The above indicated publications along with the other material included in this thesis are the output of several tasks carried out entirely by the PhD candidate. These tasks include mainly the literature review of the relevant subjects, analysis of the two-fluid CFD solver of OpenFOAM, addition of the required models to the original two-fluid solver, implementation of the PBM (based on the QBMM) into the solver code, development of the new discretization scheme for the solution of the QBMM, implementation of the new scheme in the CFD-PBM solver, processing/visualization of the simulation predictions, and discussion of the results.

Chapter 2

CFD Modelling of Gas-Liquid Flows

This chapter presents three main CFD approaches for the prediction of the hydrodynamic behaviour of gas-liquid systems, i.e. fully-resolved interface, Eulerian-Lagrangian and Eulerian-Eulerian. They differ chiefly in the resolved scale of the modelling. The highest resolution is offered by the fully-resolved interface as the relevant phenomena are modelled down to the micro-scale of bubble interfaces. In contrast, the Eulerian-Eulerian approach avoids the explicit modelling of the interface on the assumption of interpenetrating continua and therefore relies on macro-scale relations to describe the average interactions between the phases. Yet it is possible to take a middle approach, i.e. Eulerian-Lagrangian, that tracks the evolution of each individual bubble without resolving the bubble's interface explicitly. However, closure relations are required to describe the local instantaneous interactions between each bubble and the surrounding continuous phase. Among these methods, the Eulerian-Eulerian approach is of our interest and discussed in more detail, since it is currently the only tractable approach for the simulation of large industrial-scale simulations.

2.1 Fully-Resolved Interface

An accurate description of some important phenomena encountered in gas-liquid flows, e.g. coalescence and break-up, relies on the proper characterization of interfaces between the gas bubbles and liquid phase. This characterization requires the small-scale structures inside both phases to be fully resolved. The fully-resolved approach deals with the solution of the Navier-Stokes equations, considering the presence of interfaces between the liquid and bubbles. The governing equations are usually written for the whole flow domain, known as the one-fluid formulation [67]. Let the phases be incompressible, then the one-fluid formulation includes the

following equations [68]:

$$\partial_t(\rho\mathbf{u}) + \partial_\mathbf{x} \cdot (\rho\mathbf{u}\mathbf{u}) = -\partial_\mathbf{x}p + \rho\mathbf{g} + \partial_\mathbf{x} \cdot [\mu(\nabla\mathbf{u} + \nabla\mathbf{u}^\mathrm{T})] + \int \sigma\kappa'\mathbf{n}'\boldsymbol{\delta}(\mathbf{x} - \mathbf{x}')\,\mathrm{d}s' \tag{2.1}$$

$$\nabla \cdot \mathbf{u} = 0 \tag{2.2}$$

$$\frac{D\rho}{Dt} = 0 \tag{2.3}$$

$$\frac{D\mu}{Dt} = 0 \tag{2.4}$$

where ρ, μ, $\mathbf{u}$ and p are, respectively, the density, viscosity, velocity and pressure of the fluid at the spatial position $\mathbf{x}$ and time t. In addition, $(\nabla\mathbf{u} + \nabla\mathbf{u}^\mathrm{T})/2$ is the symmetric, deviatoric strain-rate tensor. Last, $\mathbf{g}$ denotes the acceleration due to body forces. It is evident that in this formulation, the flow fields and the material properties change abruptly across the interface. The surface integral on the right-hand side of Eq. (2.1) is over the interface and defines the effect of the surface tension (σ) on the hydrodynamic behaviour of the fluid. κ' is the curvature of the interface, $\mathbf{n}'$ the unit vector normal to the interface at the spatial point $\mathbf{x}'$, and $\mathrm{d}s'$ an infinitesimal area of the interface. $\boldsymbol{\delta}$ is the multiplication of two or three (depending on the dimensions of the problem) one-dimensional Dirac delta functions (δ). The numerical methods for the solution of Eqs. (2.1) to (2.4) are based on those developed for single-phase flows, and are able to handle the spatially rapid changes in the flow fields and material properties. These numerical methods rely on the knowledge about the location and shape of the interface. For this purpose, a technique is needed to describe and then follow the time evolution of the interface numerically. Some notable techniques can be listed as follows: the volume of fluid (VOF) [69, 70], the front tracking method [68, 71] and the level-set method [72–74]. The reader can refer to the work of Gopala and co-workers [75] for the comparative overview of these methods.

The main advantage of the fully-resolved approach over the other CFD models is that no empirical or semi-empirical relation is essentially needed to describe the bubble-bubble and bubble-liquid interactions. Therefore, this approach ensures a high-level of accuracy of the simulation predictions. Nevertheless, the fully-resolved approach is tractable only for the simulation of small-scale systems comprising a limited number of bubbles, otherwise it becomes computationally too expensive.

2.2 Eulerian-Lagrangian Approach

In this approach, the evolution of bubbles is tracked in a Lagrangian reference frame (thinking of them as point particles, see Figure 2.1), while the liquid phase is described by the relevant Eulerian fields.
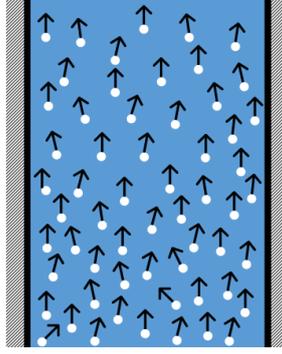
Figure 2.1: Schematic representation of bubbles in the Lagrangian reference frame.

The dynamics of a generic bubble q can be described by the following set of ordinary differential equations:

$$\frac{\mathrm{d}}{\mathrm{d}t}(x_i^{(q)}) = u_i^{(q)} \tag{2.5}$$

$$\frac{\mathrm{d}}{\mathrm{d}t}(u_i^{(q)}) = A_i^{(q)} + C_{u,i}^{(q)} \tag{2.6}$$

where $x_i^{(q)}$ and $u_i^{(q)}$ are the components of the spatial position and velocity of the bubble q. In addition, $A_i^{(q)}$ denotes the continuous acceleration of the bubble q due to the external forces, e.g. gravity, drag and lift. Last, $C_i^{(q)}$ describes the discontinuous changes in the velocity due to the bubble collisions. It is noteworthy that governing equations similar to Eq. (2.6) can be written for other properties of the bubbles such as size, concentration and temperature.

It is evident that the evolution of the bubbles depends on the state of the liquid phase surrounding them. This dependency appears in the closure relations for the $A_i^{(q)}$ and $C_i^{(q)}$. The hydrodynamics of the liquid phase are governed by the Navier-Stokes equations modified to consider the volume occupied by the gas phase and the momentum exchange between the phases:

$$\partial_t(\alpha_l \rho_l) + \partial_{\mathbf{x}} \cdot (\alpha_l \rho_l \mathbf{U}_l) = 0 \tag{2.7}$$

$$\partial_t(\alpha_l \rho_l \mathbf{U}_l) + \partial_{\mathbf{x}} \cdot (\alpha_l \rho_l \mathbf{U}_l \mathbf{U}_l) = -\alpha_l\,\partial_{\mathbf{x}}p + \alpha_l\rho_l\mathbf{g} + \partial_{\mathbf{x}} \cdot [\alpha_l\mu_l(\nabla\mathbf{U}_l + \nabla\mathbf{U}_l^{\mathrm{T}})] + \mathbf{M}_l \tag{2.8}$$

where α_l, ρ_l, μ_l, $\mathbf{U}_l$ and p are the volume fraction, density, viscosity, velocity and pressure of the liquid phase respectively. $\mathbf{g}$ is the acceleration due to the gravity. In addition, $\mathbf{M}_l$ denotes the momentum exchange between the liquid and bubbles. The above governing equations can be solved using the DNS (direct numerical simulation) or LES (large-eddy simulation) approach. However, the computational effort can be decreased by averaging the equations over time, volume or an ensemble

of infinite realizations, and then solving the resulting equation for the mean fields. In Section 2.3, the averaged equations are explained in the context of the Eulerian-Eulerian framework.

The Eulerian-Lagrangian (E-L) approach does not resolve directly the bubble interface and therefore is less expensive than the fully-resolved approach. However, it requires closure relations to describe the phenomena occurring at the interface, e.g. momentum exchange between the bubbles and the liquid phase. Some advantage of the E-L approach, particularly in comparison to the Eulerian-Eulerian approach (explained in Section 2.3), are as follows. No additional tool is required to handle the polydispersity of the population of bubbles. For instance, the drag force for a given bubble can be calculated based on its size. Moreover, the evolution of the bubble size (if necessary) can be determined by adding the relevant governing equation. Another advantage is that the E-L approach can be used for the simulation of bubble populations with a wide range of Stokes number [76]. The reason is that the E-L approach allows bubbles (with the same or different properties) located at a given position to move with different velocities. As a result, this approach can be used to simulate systems that feature non-equilibrium velocity distributions. Finally, the E-L approach can directly describe the bubble-bubble interactions, e.g. coalescence and break-up of bubbles [77].

Despite the above-mentioned advantages, the application of the E-L approach encounters some difficulties. When the two-way coupling is required, the volume of bubbles and the interaction between the bubbles and the surrounding liquid must be projected onto the Eulerian grid, which is a challenging task [78]. Furthermore, tracking all bubbles in large-scale systems is not practically feasible due to the too high computational cost. In such cases, a statistical representation is adopted, in which the large population of real bubbles are replaced by a smaller ensemble of computational bubbles [77]. However, the statistical errors due to the limited number of computational bubbles may give rise to convergence issues [79–81].

2.3   Eulerian-Eulerian Approach

The Eulerian-Eulerian (E-E) framework assumes the liquid and gas phases as two interpenetrating continua that are present simultaneously in the entire domain but with a statistical expectation, which translates into the corresponding phase volume fraction, see Figure 2.2. This assumption allows us to write the continuum mass, momentum and energy balance equations of both phases over the entire domain despite the discontinuities existing at the interfaces between the phases. Then, the local instantaneous balance equations of each phase is averaged over time, volume or an ensemble of infinite realizations to obtain the averaged equations, known as the two-fluid model (TFM) [16, 82, 83]. The averaging process helps to avoid resolving interfaces between the bubbles and liquid phase as it smooths

out discontinuities at interfaces. Instead, the relevant phenomena occurring at interfaces are described averagely through macro-scale relations. It is evident that the accuracy of solutions predicted by the E-E approach relies highly on these macro-scale relations.
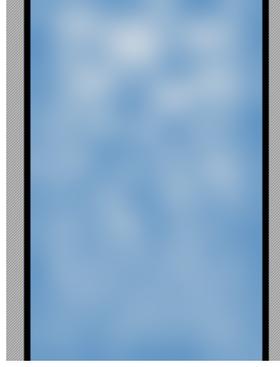
Figure 2.2: Averaged representation of two-phase flow in the Eulerian-Eulerian framework.

The averaged mass and momentum balance equations for a generic phase i (either the disperse or the continuous phases) are the following (in the absence of the mass transfer):

$$\partial_t(\alpha_i \rho_i) + \partial_{\mathbf{x}} \cdot (\alpha_i \rho_i \mathbf{U}_i) = 0 \tag{2.9}$$

$$\partial_t(\alpha_i \rho_i \mathbf{U}_i) + \partial_{\mathbf{x}} \cdot (\alpha_i \rho_i \mathbf{U}_i \mathbf{U}_i) = -\alpha_i \, \partial_{\mathbf{x}} p + \alpha_i \rho_i \mathbf{g} + \partial_{\mathbf{x}} \cdot [\alpha_i(\boldsymbol{\tau}_i + \boldsymbol{\tau}_i'')] + \mathbf{M}_i \tag{2.10}$$

where α_i, ρ_i and $\mathbf{U}_i$ are the volume fraction, density and velocity of the phase i respectively. $\boldsymbol{\tau}_i$ denotes the viscous stress tensor estimated by:

$$\boldsymbol{\tau}_i = \mu_i(\nabla \mathbf{U}_i + \nabla \mathbf{U}_i^{\mathrm{T}}) - \frac{2}{3}\mu_i(\nabla \cdot \mathbf{U}_i)\mathbf{I} \tag{2.11}$$

where μ_i is the molecular viscosity of the phase i and $\mathbf{I}$ the unit tensor with elements equal to the Kronecker delta (δ_{ij}). The second term on the right-hand side of Eq. (2.11) is negligible for the liquid phase on the assumption of incompressibility. The unclosed term $\boldsymbol{\tau}_i''$ appears in the averaged momentum balance equation due to the fluctuations of the local instantaneous phase velocity around its mean value, $\mathbf{U}_i$. The fluctuations arise because, first, the existing phase at a given position changes and second, turbulent conditions may exist in the phase i. This term is generally closed by extending single-phase RANS (Reynolds-averaged Navier–Stokes equations) to multiphase flows [54]. Therefore, Eqs. (2.9) and (2.10) are solved for the Reynolds-averaged fields and $\boldsymbol{\tau}_i''$ is modelled the same as $\boldsymbol{\tau}_i$ but using the turbulent viscosity instead of the molecular one. Last, $\mathbf{M}_i$ describes the

momentum exchange between the phases and is modelled through macro-scale relations called as interfacial forces. Some interfacial forces relevant to gas-liquid flows are drag, lift, turbulent dispersion, wall lubrication and virtual mass forces.

The TFM can be extended to systems comprising several phases. The extension of the TFM is known as the multifluid model (MFM), which consists of Eqs. (2.9) and (2.10) written for more than two phases [13, 84]. For instance, the gas phase can be divided into two classes of small and large bubbles and therefore the entire system is comprised of one liquid phase and two fictitious gas phases [45]. In the MFM, the term $\mathbf{M}_i$ takes into account the momentum exchange between phase i and all the other phases.

The main advantage of the E-E approach is the low computational cost in comparison to the previous approaches, however, at the expense of lower modelling resolution. Therefore, this approach is considered as the first candidate for the simulation of large-scale systems. Nevertheless, the E-E approach has its drawbacks. This approach is on the basis of the mono-kinetic assumption, i.e. the disperse entities (of identical or different properties) move with the same local velocity. This assumption is not valid for systems consisting of disperse entities of high Stokes number ($St > 1$) or with velocity distributions far from the equilibrium [76]. Furthermore, the TFM and MFM cannot provide information about the evolution of the distribution of bubble properties such as the bubbles size distribution. As a result, these methods are unable to describe phenomena such as coalescence and break-up of bubbles. Another issue is that macro-scale relations, e.g. interfacial forces, are usually valid for specific systems and a limited range of operating conditions, and therefore lack general applicability. It is worth repeating that the predictions of the E-E approach depends strongly on these relations. The following section discusses the interfacial forces in the context of gas-liquid flows.

2.3.1   Interfacial Forces

In the E-E approach, the momentum exchange between the liquid phase and bubbles is modelled by including average interfacial forces in the average momentum balance equation of both gas and liquid phases. The average interfacial forces are estimated by macro-scale (closure) relations that are written in terms of the known mean flow fields. The forces relevant to gas-liquid flows (considered in this thesis) are drag, lift, turbulent dispersion and wall lubrication. The following sections describe these interfacial forces along with some commonly employed closure relations for the simulation of bubbly pipe flows.

Drag Force

The gas bubbles moving through a liquid experience a friction-like force due to their relative velocity with respect to the liquid phase. This force acts on the gas

phase in the opposite direction of the relative velocity of the phases, defined as the gas velocity minus the liquid velocity. In the Eulerian framework, the drag force per unit volume is expressed by the following formula [13]:

$$\mathbf{F}_g^D = -\frac{3}{4d_b}C_D\rho_l\alpha_g\left|\mathbf{U}_r\right|\mathbf{U}_r \quad \text{and} \quad \mathbf{U}_r = \mathbf{U}_g - \mathbf{U}_l \tag{2.12}$$

In the above equation, C_D denotes the drag coefficient that is generally estimated using correlations. In addition, d_b is the bubble diameter and α_g the gas volume fraction. Furthermore, $\mathbf{U}_g$, $\mathbf{U}_l$ and $\mathbf{U}_r$ are the average gas, liquid and relative velocities respectively.
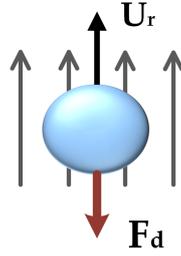
Figure 2.3: The drag force due to the relative velocity between a bubble and the liquid phase.

Among interfacial forces, the drag force has been studied extensively both theoretically and experimentally. As a result, there are reliable correlations for estimating the drag coefficient for a given system. In this thesis, the relationship proposed by [85] for slightly contaminated systems is used to calculate the drag coefficient:

$$C_D = \max\left\{\min\left[\frac{24}{Re}\left(1 + 0.15Re^{0.687}\right), \frac{72}{Re}\right], \frac{8}{3}\frac{Eo}{Eo + 4}\right\} \tag{2.13}$$

where Re is the bubble Reynolds number and Eo Eötvös number. These numbers are defined as the following:

$$Re = \frac{\rho_l\left|\mathbf{U}_r\right|d_b}{\mu_l} \quad \text{and} \quad Eo = \frac{\left|\mathbf{g}\right|(\rho_l - \rho_g)d_b^{\,2}}{\sigma} \tag{2.14}$$

ρ_g is the gas density and σ the surface tension. The Reynolds number is the ratio of the effects of inertial forces to the effects of viscous forces. The Eötvös number represents the ratio between the effects due to the buoyancy and the effects due to the surface tension. This number is used to characterize the shape of bubbles. The higher is the Eötvös number, the more distorted is the bubble shape from the spherical shape.

The first term of the correlation in Eq. (2.13) is the drag coefficient for the smallest bubbles with a low Reynolds number, which show a rigid interface. The

second term is the correction by Tomiyama and co-workers for bubbles with higher Reynolds numbers, where the interface is partially mobile. Finally, for large bubbles and high Reynolds numbers, the shape of bubbles is distorted from spherical to ellipsoidal or spherical cap and the drag coefficient is estimated based on the Eötvös number. As evident from Eq. (2.13), for large bubbles, the drag coefficient does not depend on the Reynolds number and shows an almost constant dependence on the bubble size.

Lift Force

Bubbles in a shear flow experience a force acting normal to the flow direction (Figure 2.4). The shear-induced lift force acting on the gas phase can be expressed by the following formula [86]:

$$\mathbf{F}_{\mathrm{g}}^{\mathrm{L}} = -C_{\mathrm{L}} \rho_{\mathrm{l}} \alpha_{\mathrm{g}} \mathbf{U}_{\mathrm{r}} \times (\nabla \times \mathbf{U}_{\mathrm{l}}) \tag{2.15}$$

Here, the lift coefficient is denoted by C_{L}.
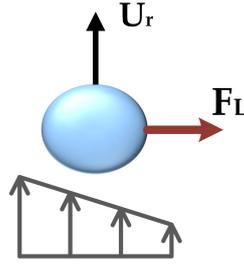
Figure 2.4: The lift force due to the shear flow of the liquid phase.

In an upward co-current flow with a monotonically decreasing velocity profile approaching the wall and $C_{\mathrm{L}} > 0$, the lift force pushes essentially the spherical bubbles towards the wall. However, experiments have shown that, for non-spherical bubbles, the force acts in the reverse direction, which is described by using a negative lift coefficient [22]. This change in the direction of the force was associated with the slanted wake created behind the non-spherical bubble. Therefore, Tomiyama and co-workers [22] proposed a correlation for the lift coefficient that depends on the Eötvös number or, in other words, the bubble size and its deformation:

$$C_{\mathrm{L}} = \begin{cases} \min[0.288 \tanh(0.121 Re), f(Eo_{\mathrm{d}})] & Eo_{\mathrm{d}} < 4 \\ f(Eo_{\mathrm{d}}) & 4 \leq Eo_{\mathrm{d}} \leq 10 \end{cases} \tag{2.16}$$

and

$$f(Eo_{\mathrm{d}}) = 0.00105 Eo_{\mathrm{d}}^3 - 0.0159 Eo_{\mathrm{d}}^2 - 0.0204 Eo_{\mathrm{d}} + 0.474 \tag{2.17}$$

In above equations, Eo_d denotes the Eötvös number calculated using the maximum horizontal dimension of the bubble (d_H) instead of the bubble size. To estimate d_H, the bubbles are assumed to have an oblate spheroidal shape with the aspect ratio given by the empirical correlation proposed by Wellek et al. [87]:

$$d_H = d_b \sqrt[3]{1 + 0.163 Eo^{0.757}} \tag{2.18}$$

Based on the experimental observations, Eq. (2.16) predicts the inversion of the lift force as the bubble shape changes to non-spherical one, i.e. as the bubble diameter increases in a system with constant properties. It should be noted that Tomiyama's correlation was obtained based on the experiments that examined the trajectory of single bubbles under laminar (Reynolds number < 50) and high Morton number conditions. However, Lucas and Tomiyama [23] showed that the critical diameter predicted by this correlation at which the lift coefficient changes its sign is also applicable to the dense turbulent flows in low Morton number systems such as air-water and steam-water flows. In addition, a recent investigation on single bubbles in an air-water low-turbulent system validates Tomiyama's correlation for such systems provided the major axis of the bubble is used to calculate Eo_d in Eq. (2.16) [88].

In contrast to the drag coefficient, a clear consensus on the lift coefficient has not been reached, mostly due to the fact that the experiments were performed in simple shear flows under a set of controlled and limited operating conditions. Moreover, the lift force predicted by Eq. (2.15) reaches, generally, its maximum at the wall due to the high liquid velocity gradient. It may prevent the gas phase from spreading towards the center of the column as the flow moves upward, giving rise to the non-physical accumulation of the gas near the wall. One remedy is to employ the wall lubrication force in the simulation, although this force is still subject to controversy and lacks general applicability [19]. Another approach is to damp the lift force to zero near the wall, as proposed by Shaver and Podowski [32]. In their model, the lift coefficient (C_L) is used for distances larger than the bubble diameter from the wall. For shorter distances, the lift coefficient is damped to zero, until the distance of half a bubble diameter from the wall, resulting in the following expression for the modified lift coefficient (C_L'):

$$C_L' = \begin{cases} 0 & y/d_b < 0.5 \\ C_L[3(\frac{2y}{d_b} - 1)^2 - 2(\frac{2y}{d_b} - 1)^3] & 0.5 \leq y/d_b \leq 1 \\ C_L & y/d_b > 1 \end{cases} \tag{2.19}$$

where y is the distance from the wall. This modification solves the problem of predicting non-physical accumulation of the gas phase near the wall. However, it predicts a flat profile for the gas volume fraction close to the wall instead of predicting a peak near the wall.

As mentioned before, Tomiyama's correlation for the lift coefficient was obtained based on the experiments under laminar conditions. Recently, Sugrue [21] presented a new correlation for the lift coefficient, which is aimed at fully turbulent flow conditions, and therefore includes not only the bubble size, but also the turbulent parameters of the flow:

$$C_{\mathrm{L}} = f(Wo)\,f(\alpha_{\mathrm{g}}) \tag{2.20}$$

with

$$f(Wo) = \min\left(0.03,\ 5.0404 - 5.0781Wo^{0.0108}\right) \tag{2.21}$$

$$f(\alpha_{\mathrm{g}}) = 1.0155 - 0.0154\exp(8.0506\alpha_{\mathrm{g}}) \tag{2.22}$$

This correlation depends on the dimensionless Wobble number, Wo, which reflects the turbulence condition of the liquid phase, as well as the bubble deformation:

$$Wo = Eo\frac{k_{\mathrm{l}}}{|\mathbf{U}_{\mathrm{r}}|^2} \tag{2.23}$$

where k_{l} is the turbulent kinetic energy of the liquid phase. It should be noted that their correlation is based on simulations that employ the wall lubrication model by Lubchenko et al. [19] (refer to Section 2.3.1), which necessitates the use of a damping function for the lift coefficient, such as the one suggested by Shaver and Podowski [32]. The model coefficients have been optimized specifically for turbulent fully developed bubbly flow conditions, and might contain compensation errors related to the prediction of the multiphase turbulence levels, due to the lack of experimental turbulence measurements in the optimization test cases. In addition, their model takes into account the group behavior of the bubbles as the number density of the bubbles (void fraction) increases. They stated that the lift coefficient should be significantly lower due to the bubble interactions when the void fraction is high (over 20%). This dependency of the lift coefficient on the void fraction is considered through the function $f(\alpha_{\mathrm{l}})$. However, this swarm effect is neglected in this thesis due to the sufficiently low local gas volume fractions in the simulated experimental conditions.

Turbulent Dispersion Force

It has been postulated that the turbulence in the continuous liquid phase has a direct effect on the migration of gas bubbles, similarly to what happens to the mass and energy transported via the turbulent dispersion. The turbulent dispersion is expected to spread gas bubbles from regions with high gas volume fraction to regions with low gas volume fraction, see Figure 2.5. Thus, virtually all the developed expressions include the gradient of the gas volume fraction. Burns et

al. (2004) proposed an expression for the turbulent dispersion force based on the Favre-averaged drag force:

$$\mathbf{F}_{\text{g}}^{\text{TD}} = -\frac{3}{4} C_{\text{D}} \frac{\alpha_{\text{g}} \rho_{\text{l}}}{d_{\text{b}}} \left| \mathbf{U}_{\text{r}} \right| \frac{\nu_{\text{l}}^{\text{turb}}}{\sigma_{\text{TD}}} \left(\frac{1}{\alpha_{\text{g}}} + \frac{1}{\alpha_{\text{l}}} \right) \nabla \alpha_{\text{g}} \tag{2.24}$$

In this expression, $\nu_{\text{l}}^{\text{turb}}$ and σ_{TD} denote the kinematic eddy viscosity of the liquid phase and the turbulent Prandtl number for the volume fraction of the disperse phase (expected to be of order unity), respectively. Furthermore, α_{l} is the liquid volume fraction. Burns et al. (2004) compared their model with other available models and stated that the studied models perform almost the same in the limit of low gas volume fraction.
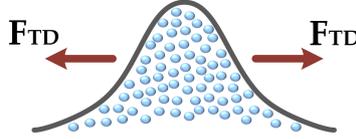
Figure 2.5: The role of turbulence in the migration of bubbles from regions with high gas fraction to regions with low gas fraction.

Wall Lubrication Force

It was observed experimentally that the bubbles located near the wall in a quiescent liquid phase tend to rise while keeping a distance from the wall. Since under these conditions, no shear is sustained in the continuous liquid phase, this behavior cannot be related to the lift force. Instead, it is suggested that the bubbles rising close to the wall experience a lateral force due to the wall presence (Figure 2.6).
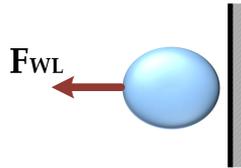
Figure 2.6: The fictitious wall lubrication force.

Antal and co-workers [28] associated this with the unbalanced drainage of the liquid phase around bubbles due to the no-slip condition on the wall for the liquid velocity. Eventually, they proposed an expression for the wall lubrication force based on a two-dimensional analysis. Later, Tomiyama and co-workers [27] reported that the Antal's expression, for bubbles far from the wall, results in a force towards the wall, which is not physically acceptable. Consequently, they modified Antal's expression and suggested a model based on the experimental observations of single

bubble trajectories in the water-glycerol solution. Subsequently, Hosokawa and co-workers [26] developed a correlation for the empirical coefficient of Tomiyama's model in order to extend the applicability of the model to a wider range of fluid properties and bubble sizes:

$$\mathbf{F}_{\mathrm{g}}^{\mathrm{WL}} = C_{\mathrm{wl}}\rho_{\mathrm{l}}\alpha_{\mathrm{g}} \left| (\mathbf{U}_{\mathrm{r}})_{||} \right|^2 \mathbf{n}_{\mathrm{w}} \tag{2.25}$$

with

$$C_{\mathrm{wl}} = C_{\mathrm{w}}\frac{d_{\mathrm{b}}}{2}\left(\frac{1}{y^2} - \frac{1}{(D-y)^2}\right) \quad \text{and} \quad C_{\mathrm{w}} = \max\left(\frac{7}{Re^{1.9}}, 0.0217Eo\right) \tag{2.26}$$

In the above expressions, $(\mathbf{U}_{\mathrm{r}})_{||}$ is the component of the relative velocity parallel to the wall, $\mathbf{n}_{\mathrm{w}}$ is the unit vector normal to the wall, D is the pipe diameter and y is the distance from the wall.

Recently, Lubchenko and co-workers [19] proposed a new approach to consider the presence of the wall. Their model imposes a parabolic void fraction profile near the wall, obtained simply using the argument that the bubbles attached to the wall have their centers located at a distance equal to the bubble radius due to their physical shape. By imposing this void fraction profile and considering an instantaneous equilibrium between the turbulent dispersion force and the wall lubrication force near the wall, it is possible to derive a model for the wall lubrication force. It should be noted that the lift force is not considered in the equilibrium, because of employing a damping model near the wall, e.g. Eq. (2.19) proposed by Shaver and Podowski [32]. Lubchenko et al. [19] stated that the approach is more general and applicable to different systems. Furthermore, it does not push the gas completely out of a certain distance from the wall, which is more consistent with the experimental observations. If the Burns model is employed to represent the turbulent dispersion, the following relationship will be obtained for the wall lubrication force:

$$\mathbf{F}_{\mathrm{g}}^{\mathrm{WL}} = \begin{cases} -\frac{3}{4}C_{\mathrm{D}}\frac{\alpha_{\mathrm{g}}\rho_{\mathrm{l}}}{d_{\mathrm{b}}}\left|\mathbf{U}_{\mathrm{r}}\right|\frac{\nu_{\mathrm{l}}^{\mathrm{turb}}}{\sigma_{\mathrm{TD}}}\left(\frac{1}{\alpha_{\mathrm{g}}} + \frac{1}{\alpha_{\mathrm{l}}}\right)\alpha_{\mathrm{g}}\frac{1}{y}\frac{d_{\mathrm{b}}-2y}{d_{\mathrm{b}}-y}\mathbf{n}_{\mathrm{w}} & y/d_{\mathrm{b}} < 0.5 \\ 0 & y/d_{\mathrm{b}} \geq 0.5 \end{cases} \tag{2.27}$$

The above wall lubrication models are compared in Figure B.1 of Appendix B, each evaluated using a meaningful set of parameters.

2.3.2 Turbulence Modelling

While the single-phase turbulence modelling has advanced considerably over last decades and has achieved a general reliability, the multiphase turbulence modelling is much less developed due to several reasons such as the lack of enough experimental data, diversity of systems, complex flow fields and different flow regimes. Nevertheless, numerous studies have been conducted to develop multiphase turbulence

models by extending existing single-phase turbulence models to multiphase systems. Concerning gas-liquid systems, the Reynolds-averaged Navier-Stokes equations (RANS) approach is commonly adopted, along with the Boussinesq approximation [11, 14, 15, 18, 89–95]. Moreover, the turbulence is normally modelled only inside the liquid phase, since the density of gas (disperse phase) is much smaller than that of liquid (continuous phase) [16]. Then, the turbulent viscosity of the liquid phase (μ_l^{turb}) is calculated by using two-equation models adapted to two-phase systems. If the $k-\varepsilon$ model is employed, the turbulent kinetic energy (k_l) and the turbulent dissipation rate (ε_l) of the liquid phase are predicted by solving the following transport equations [96]:

$$\partial_t(\alpha_l\rho_l k_l) + \partial_{\mathbf{x}} \cdot (\alpha_l\rho_l k_l \mathbf{U}_l) = \partial_{\mathbf{x}} \cdot \left[\alpha_l\left(\mu_l + \frac{\mu_l^t}{\sigma_k}\right)\partial_{\mathbf{x}}k_l\right] + \alpha_l P_k - \alpha_l\rho_l\varepsilon_l + S_k \quad (2.28)$$

$$\partial_t(\alpha_l\rho_l\varepsilon_l) + \partial_{\mathbf{x}} \cdot (\alpha_l\rho_l\varepsilon_l \mathbf{U}_l) = \partial_{\mathbf{x}} \cdot \left[\alpha_l\left(\mu_l + \frac{\mu_l^t}{\sigma_\varepsilon}\right)\partial_{\mathbf{x}}\varepsilon_l\right] + \alpha_l C_{\varepsilon 1}\frac{\varepsilon_l}{k_l}P_k - \alpha_l\rho_l C_{\varepsilon 2}\frac{\varepsilon_l^2}{k_l} + S_\varepsilon$$
$$(2.29)$$

with the turbulent viscosity calculated by the following expression:

$$\mu_l^t = C_\mu \rho_l \frac{k_l^2}{\varepsilon_l} \quad (2.30)$$

In Eqs. (2.28) and (2.29), P_k is the production of the turbulent kinetic energy and the model coefficients are generally assumed to be the same as those used in the standard single-phase $k-\varepsilon$ model proposed by Launder and Sharma [97]: $C_\mu = 0.09$, $C_{\varepsilon 1} = 1.44$, $C_{\varepsilon 2} = 1.92$, $\sigma_k = 1.0$ and $\sigma_\varepsilon = 1.3$. Last, S_k and S_ε are the source terms to consider the effect of bubbles on the turbulence in the liquid phase, i.e. the bubble-induced turbulence (BIT).

Although bubbles influence the structure of the turbulence in the liquid phase [98–101], the bubble-induced turbulence is ignored in this thesis to avoid introducing significant uncertainties due to many ambiguities surrounding the application of the available approaches for modelling it. For instance, in the context of two-equation models such as the $k-\varepsilon$ model, the most common practice is adding source terms to the transport equations of k and ε, [18, 92]. However, no consensus on the implementation of the approach is achieved yet, particularly on the choice of the time scale to estimate the added ε source, [15]. In addition, the ε source depends on an empirical coefficient that is system-dependent. Recently, a model was proposed by [88] that determines the time scale and coefficients based on the direct numerical simulations (DNS) of a bubbly channel flow. However, the DNS simulations consider only small spherical bubbles, which may limit its application to the system studied in this thesis.

2.3.3   Modelling of Polydispersity

As mentioned before, gas-liquid systems generally feature distributions of bubbles with different properties, a situation identified as polydispersity. The knowledge about the distribution of bubbles over the properties of interest is essential for a more accurate description of gas-liquid systems, particularly when property distributions are not narrow enough to support the mono-disperse assumption. Moreover, property distributions evolve in space and time due to different processes such as coalescence and break-up. In the TFM or MFM, governing equations are written in terms of average fields and properties. Thus, these models work with the average of distributions instead of distributions themselves. More importantly, these models are not capable of predicting the evolution of property distributions, which may change considerably in space and time. In this regard, the Population Balance Modelling (PBM) is a powerful tool to define property distributions and track their evolution through suitable governing equations, i.e. Population Balance Equation (PBE).

Chapter 3

Population Balance Modelling[*]

The previous chapter introduces the CFD approaches for the simulation of multiphase gas-liquid flows, placing focus on the Eulerian-Eulerian framework. However, as mentioned before, the Eulerian-Eulerian methods, e.g. two- and multi-fluid models (TFM and MFM), does not provide any information regarding the population of bubbles. For instance, the TFM and MFM require the specification of the mean bubble size and they do not account for the bubble size distribution (BSD). Moreover, the population of bubbles evolves in time due to processes such as coalescence and break-up of bubbles, which cannot be predicted by the TFM and MFM. In general, disperse gas-liquid systems often feature distributions of bubbles with different properties such as size, a situation identified as polydispersity. Therefore, a comprehensive simulation of such systems must take into account the polydispersity by tracking the evolution of bubble distributions over the properties of interest, e.g. BSD.

This chapter introduces the population balance equation (PBE) as a suitable tool for describing the evolution of the bubble population in disperse gas-liquid systems. We explain how the solution of the PBE provides a detailed level of description of the disperse gas bubbles, which is not accessible from the TFM and MFM alone, leading to a more accurate simulation of the entire gas-liquid system. In this regard, several methods for the solution of the PBE are covered, which belong to the following main categories: the class or sectional method, method of moments and quadrature-based moment methods. Eventually, this chapter discusses the incorporation of the PBE into the CFD and also some relevant numerical issues concerning the stability of simulations.

3.1   Population Balance Equation

The PBE is a continuity statement that governs the evolution of a number density function (NDF), which is postulated to exist for a population of disperse phase elements, such as gas bubbles in this thesis. The NDF defines the distribution of the disperse phase elements over the properties of interest at any time instant and physical position. These properties, called internal coordinates, characterize the disperse elements and can include velocity, size, composition, temperature, etc. The choice of the internal coordinates, denoted here by the vector $\boldsymbol{\xi}$, is system dependent. The state of a generic element q at time t can be determined by its position vector $\mathbf{x}^{(q)}$ and internal coordinates $\boldsymbol{\xi}^{(q)}$, jointly called the element state vector $(\mathbf{x}^{(q)}, \boldsymbol{\xi}^{(q)})$. The state vector of a given element specifies the location of that element in the so-called phase-space, which is a high-dimensional space consisting of the physical domain of the system $\Omega_{\mathbf{x}}$ and the domain of the internal coordinates $\Omega_{\boldsymbol{\xi}}$. Given an arbitrary point in the phase-space $(\mathbf{x}, \boldsymbol{\xi})$, the NDF $n(t, \mathbf{x}, \boldsymbol{\xi})$ is defined as the expected number density of elements in the infinitesimal volume $\mathrm{d}\mathbf{x}\,\mathrm{d}\boldsymbol{\xi}$ around that point at time t [102].

At first, let the velocity of gas bubbles be known and excluded from the internal coordinate vector. Then the PBE takes the following form [57]:

$$\partial_t n + \partial_{\mathbf{x}} \cdot (\mathbf{U}_{\mathrm{g}} n) + \partial_{\boldsymbol{\xi}} \cdot (\mathbf{G} n) = \mathcal{S}, \tag{3.1}$$

where $\mathbf{U}_{\mathrm{g}}(\boldsymbol{\xi})$ is the velocity of the gas bubbles and $\mathbf{G}(\boldsymbol{\xi})$ the rate of change of the internal coordinates due to continuous molecular processes, such as mass and heat transfer, growth and shrinkage of bubbles, chemical reactions etc. The source term $\mathcal{S}(\boldsymbol{\xi})$ describes the discontinuous changes in the internal coordinates of the bubbles due to discrete events, such as coalescence and break-up.

Eq. (3.1) is a high-dimensional transport equation that describes the evolution of the NDF not only in time and physical space but also in the domain of internal coordinates. The velocity of the bubbles in Eq. (3.1) ($\mathbf{U}_{\mathrm{g}}$) is assumed to be a known function of time, spatial position and internal coordinates ($\boldsymbol{\xi}$). In addition, the flow fields of the continuous (liquid) phase, e.g. liquid velocity ($\mathbf{U}_{\mathrm{l}}$), are generally required by the closure relations for the description of both continuous and discontinuous processes, i.e. $\mathbf{G}$ and $\mathcal{S}$. For this purpose, the velocity of both phases ($\mathbf{U}_{\mathrm{g}}$ and $\mathbf{U}_{\mathrm{l}}$) can be obtained by adopting a suitable Eulerian CFD approach, see Chapter 2.

3.1.1   Generalized Population Balance Equation

In general, the velocity of the disperse bubbles ($\mathbf{u}_{\mathrm{b}}$) can be included within the internal coordinate vector. In this case, the NDF $f(t, \mathbf{x}, \boldsymbol{\xi}, \mathbf{u}_{\mathrm{b}})$ is defined as the expected number density of bubbles in the infinitesimal volume $\mathrm{d}\mathbf{x}\,\mathrm{d}\boldsymbol{\xi}\,\mathrm{d}\mathbf{u}_{\mathrm{b}}$ around the arbitrary point $(\mathbf{x}, \boldsymbol{\xi}, \mathbf{u}_{\mathrm{b}})$ at time t. The generalization of Eq. (3.1) to include

velocity as an internal coordinate leads to the following Generalized Population Balance Equation (GPBE) [57]:

$$\partial_t f + \partial_{\mathbf{x}} \cdot (\mathbf{u}_{\mathrm{b}} f) + \partial_{\boldsymbol{\xi}} \cdot (\mathbf{G} f) + \partial_{\mathbf{u}_{\mathrm{b}}} \cdot (\mathbf{A} f) = \mathcal{S}, \tag{3.2}$$

In Eq. (3.2), $\mathbf{A}(\boldsymbol{\xi}, \mathbf{u}_{\mathrm{b}})$ is the acceleration of the bubbles due to external forces, e.g. forces exerted from the liquid phase on the bubbles. The source term $\mathcal{S}(\boldsymbol{\xi}, \mathbf{u}_{\mathrm{b}})$ is similar to that in the PBE except that it also describes the discontinuous change in the velocity of the bubbles due to discrete events.

Relationship between GPBE and PBE

It is noteworthy that Eq. (3.2) is closely related to Eq. (3.1). In fact, as highlighted in some specific applications [103–108], the GPBE can be simplified by presuming a specific form for the NDF, $f(t, \mathbf{x}, \boldsymbol{\xi}, \mathbf{u}_{\mathrm{b}}) = n(t, \mathbf{x}, \boldsymbol{\xi}) \, \delta(\mathbf{u}_{\mathrm{b}} - \langle \mathbf{u}_{\mathrm{b}} | \boldsymbol{\xi} \rangle)$, which is called the monokinetic assumption. This is equivalent to assuming that, at a given time t and location $\mathbf{x}$, the bubbles with the same internal coordinates move with the same velocity $\langle \mathbf{u}_{\mathrm{b}} | \boldsymbol{\xi} \rangle$, i.e. the mean velocity conditioned on the internal coordinates [103]:

$$\langle \mathbf{u}_{\mathrm{b}} | \boldsymbol{\xi} \rangle = \int \mathbf{u}_{\mathrm{b}} f \, \mathrm{d}\mathbf{u}_{\mathrm{b}} \, / \, n(t, \mathbf{x}, \boldsymbol{\xi}). \tag{3.3}$$

where $n(t, \mathbf{x}, \boldsymbol{\xi}) = \int f \, \mathrm{d}\mathbf{u}_{\mathrm{b}}$ is the marginal NDF. Clearly, the mean conditional velocity, $\langle \mathbf{u}_{\mathrm{b}} | \boldsymbol{\xi} \rangle$, is identical to $\mathbf{U}_{\mathrm{g}}(\boldsymbol{\xi})$. The mean conditional velocity can be calculated in different ways, by assuming for example a continuous parametric functional defined over the space of a chosen internal coordinate [57], or can be obtained by adopting the Eulerian CFD models explained in Chapter 2. It is noteworthy that Eulerian CFD models, i.e. the TFM and MFM, can be derived from the GBPE (see Figure 3.1), for which the derivation can be found elsewhere [57, 103, 104, 106, 107].

GPBE in Turbulent Flow

In turbulent flows, in which turbulence is caused by instabilities in the liquid phase, the velocity of the liquid phase $\mathbf{U}_{\mathrm{l}}(t, \mathbf{x})$ is a random vector field characterized by fluctuations that result in fluctuations of the NDF defined previously. The direct solution of the GPBE/PBE, which resolves all the relevant length and time scales, is computationally expensive and cheaper solutions are often sought. One alternative is to define a Reynolds-averaged NDF $\langle f \rangle (t, \mathbf{x}, \boldsymbol{\xi}, \mathbf{u}_{\mathrm{b}})$ over an infinitely large number of realizations of the liquid phase velocity $\mathbf{U}_{\mathrm{l}}$ [57] and derive the following equation:

$$\partial_t \langle f \rangle + \partial_{\mathbf{x}} \cdot (\mathbf{u}_{\mathrm{b}} \langle f \rangle) + \partial_{\boldsymbol{\xi}} \cdot (\langle \mathbf{G} f \rangle) + \partial_{\mathbf{u}_{\mathrm{b}}} \cdot (\langle \mathbf{A} f \rangle) = \langle \mathcal{S} \rangle, \tag{3.4}$$

leading to a Reynolds-averaged Navier-Stokes (RANS) multiphase formulation. The terms $\langle \mathbf{G} f \rangle$, $\langle \mathbf{A} f \rangle$ and $\langle \mathcal{S} \rangle$ are generally not closed because the relations describing
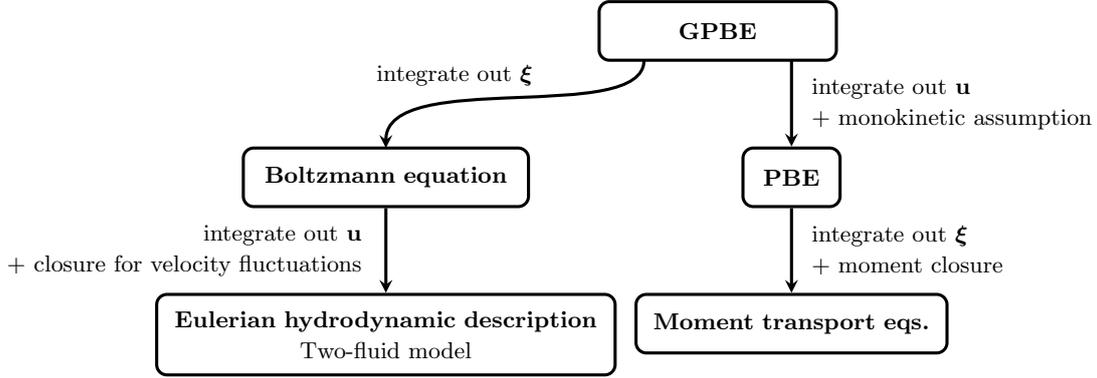
Figure 3.1: The relationship between the GPBE, PBE, moments and Eulerian CFD models

the continuous and discontinuous events can depend on the liquid phase velocity, $\mathbf{U}_l$. The above-mentioned terms are usually expressed as the summation of a mean field contribution and an additional contribution due to fluctuations, the latter of which needs a closure approximation. For example, Drew used a kinetic equation describing the evolution of particles in turbulent flows to derive an Eulerian momentum balance equation that includes a drag force due to the mean fields and an additional contribution, called turbulent dispersion force, due to turbulent fluctuations [109]. It is noteworthy that spatial filtering [110] and Large Eddy Simulation (LES) based on the self-conditioned NDF [111] can be also used to derive the GPBE of the same form of Eq. (3.4).

3.1.2 Discrete Events

The principal discrete events relevant to gas-liquid systems are the coalescence and break-up processes. For these two processes, the source term $\mathcal{S}$ in Eq. (3.1) has the following mathematical form on the assumption that the only internal coordinate is the mass (or the volume) of the bubbles (space and time dependency is omitted for brevity) [102]:

$$\mathcal{S}(\xi) = \frac{1}{2} \int_0^\xi a'(\xi - \xi', \xi)\, n(\xi - \xi')\, n(\xi)\, \mathrm{d}\xi' - n(\xi) \int_0^\infty a'(\xi, \xi')\, n(\xi')\, \mathrm{d}\xi'$$
$$+ \int_\xi^\infty b'(\xi')\, \beta'(\xi|\xi')\, n(\xi')\, \mathrm{d}\xi' - b'(\xi)\, n(\xi), \quad (3.5)$$

where $a'(\xi, \xi')$ denotes the rate of the coalescence between the bubbles whose internal coordinates are equal to ξ and ξ' (i.e. coalescence kernel) and $b'(\xi)$ the rate of break-up of bubbles whose internal coordinate is equal to ξ (i.e. break-up kernel). In addition, $\beta'(\xi|\xi')$ is the so-called daughter distribution and statistically defines

the number of daughter bubbles, whose internal coordinate is equal to ξ, born due to the break-up of a bubble with the internal coordinate of ξ'. On the right-hand side of Eq. (3.5), the first and third terms describe the birth of new bubbles due to coalescence and break-up respectively, whereas the second and fourth terms take into account the death of bubbles due to coalescence and break-up respectively.

In some cases, it is more convenient to formulate the PBE in terms of a length-based NDF, as done also in this thesis. Then, $n(t, \mathbf{x}, L) \, \mathrm{d}\mathbf{x}$ determines the expected number of bubbles with size between L and $L + \mathrm{d}L$ at spatial position $\mathbf{x}$ and time instant t. Moreover, the PBE has the same shape as expressed by Eq. (3.1), except that the source term $\mathcal{S}$ takes the following form [112]:

$$\mathcal{S}(L) = \frac{L}{2} \int_0^L \frac{a((L^3 - L'^3)^{1/3}, L')}{(L^3 - L'^3)^{2/3}} \, n((L^3 - L'^3)^{1/3}) \, n(L') \, \mathrm{d}L'$$
$$- n(L) \int_0^\infty a(L, L') \, n(L') \, \mathrm{d}L' + \int_L^\infty b(L') \, \beta(L|L') \, n(L') \, \mathrm{d}L' - b(L) \, n(L), \quad (3.6)$$

where $a(L, L')$ and $b(L)$ are the length-based coalescence and break-up kernels, respectively, and $\beta(L|L')$ the daughter size distribution. In the following, some relations for description of the coalescence and break-up of bubbles in the gas-liquid systems under turbulent conditions are introduced.

Coalescence Kernel

The coalescence of bubbles is a second-order process since it involves two bubbles – considering only binary collisions. The coalescence of two bubbles is generally modelled by splitting it into two steps: first, the bubbles should approach each other until they are separated by a thin liquid film trapped between their interfaces (collision step), and then, they should remain in contact for a sufficient time required for the liquid film to drain (film drainage step). As a results, the coalescence kernels are generally formulated as the following:

$$a(L, L') = \gamma(L, L') \, \eta(L, L') \quad (3.7)$$

where $\gamma(L, L')$ denotes the collision frequency of bubbles of size L with bubbles of size L' and $\eta(L, L')$ is the probability that the collided bubbles coalesce. The frequency of bubble collisions can be estimated by drawing an analogy with the kinetic gas theory and prescribing a relative velocity between the bubbles ($\mathbf{u}_\mathrm{r}$) [57]:

$$\gamma(L, L') = \frac{\pi}{4}(L + L')^2 \, |\mathbf{u}_\mathrm{r}| \quad (3.8)$$

The relative velocity between a pair of bubbles depends on the mechanism that brings the two bubbles together. In turbulent flows, the collision of bubbles is mainly controlled by the fluctuating turbulent velocity. When the bubble size is

comparable to the length-scale of the inertial sub-range, the following relationship can be written to estimate the collision frequency between bubbles of size L and bubbles of size L' [113, 114]:

$$\gamma(L, L') = C_\gamma (L + L')^2 \varepsilon_1^{1/3} (L^{2/3} + L'^{2/3})^{1/2} \tag{3.9}$$

The parameter C_γ can be set to 0.88 following the work by Venneker and co-workers [39], or 0.28 suggested by Prince and Blanch [115].

The probability of the coalescence, $\eta(L, L')$, is estimated by the relation suggested by Coulaloglou and Tavlarides [113]:

$$\eta(L, L') = \exp\left[-\frac{C_\eta \mu_l \rho_l \varepsilon_1}{\sigma^2}(\frac{LL'}{L + L'})^4\right] \tag{3.10}$$

The parameter C_η is set to 6.0×10^9 following the work by Laakkonen and co-workers [114]. The above relation assumes that the bubbles are deformable and they have immobile interfaces.

Break-up Kernel

The break-up of bubbles under turbulent conditions is described by determining the frequency of the collision of bubbles with the turbulent eddies and the probability of having bubbles broken due to these collisions. Moreover, it is necessary to determine statistically the size of the new bubbles that are formed after the break-up, which is generally done by defining a daughter size distribution. Following the work by Laakkonen et al. [114], the break-up frequency of a bubble with size L is estimated as written below:

$$b(L) = C_1 \varepsilon_c^{1/3} \text{erfc}\left(\sqrt{C_2 \frac{\sigma}{\rho_c \varepsilon_c^{2/3} L_p^{5/3}} + C_3 \frac{\mu_c}{\sqrt{\rho_c \rho_d} \epsilon_c^{1/3} L_p^{4/3}}}\right) \tag{3.11}$$

In the above relation, ρ_d denotes the density of the disperse phase. Furthermore, the parameters C_1, C_2 and C_3 are set to 6.0, 0.04, 0.01 as reported in their work [114]. Concerning the daughter size distribution, they proposed the following beta distribution:

$$\beta(L|L') = \left(9 + \frac{33}{2}C_4 + 9C_4^2 + \frac{3}{2}C_4^3\right)\left(\frac{L^2}{L'^3}\right)\left(\frac{L^3}{L'^3}\right)^2\left(1 - \frac{L^3}{L'^3}\right)^{C_4} \tag{3.12}$$

where the parameter C_4 is set to two in accordance to the assumption of the binary break-up [54].

3.2   Solution Methods for PBE

Many methods are available in the literature for the numerical solution of PBEs, each has been developed to address the challenges posed by the application of interest. Some notable challenges include the number of internal coordinates, considering the element velocity as an internal coordinate (i.e. solving the GPBE), and the physical and chemical phenomena involved. This section describes three principal categories of methods for the solution of PBEs. The first category is called Class or Sectional Method, which attempts to solve the PBE directly. In contrast, the second category (Method of Moments) deals with the PBE indirectly by solving for some integral properties of the NDF, i.e. moments. The last category is the quadrature-based moment methods that represents a significant breakthrough in the context of Method of Moments and therefore is addressed in a separate section. Among the ones not covered here, we should cite Monte Carlo methods [57, 102], which are currently too computationally expensive to be compatible with CFD coupling.

3.2.1   Class or Sectional Method

The class or sectional method (CM) is based on the discretization of the internal coordinate space into intervals (classes or sections), such that the PBE is transformed into a set of macroscopic balance equations in the physical domain [102]. This method has been widely applied to polydisperse systems governed by a univariate PBE. Let the space of the generic internal coordinate ξ be divided into M intervals using $M + 1$ grid points $(\xi_1, \xi_2, \dots, \xi_{M+1})$, therefore, the ith interval is defined as $I_i = [\xi_i, \xi_{i+1})$. The number density of elements in the interval I_i is given by $N_i(t, \mathbf{x}) = \int_{\xi_i}^{\xi_{i+1}} n(t, \mathbf{x}, \xi) \, \mathrm{d}\xi$, where $n(t, \mathbf{x}, \xi)$ is the NDF in Eq. (3.1). Then, the discretized formulation of Eq. (3.1) for the generic ith interval is:

$$\partial_t N_i + \partial_\mathbf{x} \cdot (\mathbf{U}_i N_i) + \int_{\xi_i}^{\xi_{i+1}} \partial_\xi (Gn) \, \mathrm{d}\xi = \int_{\xi_i}^{\xi_{i+1}} \mathcal{S} \, \mathrm{d}\xi \tag{3.13}$$

where $\mathbf{U}_i$ is the velocity by which the elements of the ith interval are transported in the physical space. The integrals in Eq. (3.13) are not closed since they generally depend on the NDF and cannot be expressed in terms of N_i [102]. A closed form of Eq. (3.13) can be achieved by assuming a functional form for the NDF. Kumar and Ramkrishna [116] proposed a general procedure in which the NDF is approximated with the following form:

$$n(t, \mathbf{x}, \xi) = \sum_{i=1}^{M} N_i \, \delta(\xi - \zeta_i). \tag{3.14}$$

The above approximation implies that all the elements belonging to the interval i are concentrated at a pivotal point ζ_i inside the interval. Another common approximation assumes a constant number density in each interval, i.e. $n(t, \mathbf{x}, \xi) =$

N_i for $\xi_i < \xi < \xi_{i+1}$ [117]. In the following, the procedure proposed by Kumar and Ramkrishna [116] is introduced without going into full detail. For the sake of simplicity, the system is assumed to be homogeneous, i.e. the variables of interest, e.g. the NDF, have no dependency on the physical space. Moreover, the contribution due to the continuous changes is neglected at this stage and will be touched upon later.

In the case of coalescence and break-up, the right-hand side of Eq. (3.13) can be written in the following closed form by assuming ξ to be a conserved property [102]:

$$
\begin{aligned}
\int_{\xi_i}^{\xi_{i+1}} \mathcal{S} \, \mathrm{d}\xi = {} & \frac{1}{2} \sum_{j=1}^{i-1} N_j \sum_{\substack{k \\ (\zeta_j + \zeta_k) \in I_i}} a(\zeta_j, \zeta_k) \, N_k \, - N_i \sum_{j=1}^{M} a(\zeta_i, \zeta_j) \, N_j \\
& + \sum_{j=i}^{M} b(\zeta_j) \, N_j \int_{\xi_i}^{\xi_{i+1}} \beta(\xi|\zeta_j) \, \mathrm{d}\xi \, - b(\xi_i) \, N_i.
\end{aligned} \tag{3.15}
$$

Kumar and Ramkrishna [116] explained in detail that the above formulation is not internally consistent, i.e. it does not generally preserve the integral properties of the NDF such as its moments. It is noteworthy that low-order moments of the NDF are associated with the conserved properties of the disperse phase. The cause of this internal inconsistency lies in the assignment of a pivotal point to the born elements, produced by the birth (first and third) terms in Eq. (3.15). For instance, let two elements belonging to the intervals I_j and I_k with pivotal points ζ_j and ζ_k coalesce to form a new element i with $\xi_i = \zeta_j + \zeta_k$. Then, the value ξ_i determines which interval the element i belongs to. However, in an arbitrarily discretized space, ξ_i may not necessarily coincide with the pivotal point of the assigned interval. The same issue may arise when an element breaks into two daughter elements, which should be assigned to two intervals. Kumar and Ramkrishna [116] proposed to assign the born elements to the nearby pivotal points, such that two integral properties of the NDF are preserved. This approach, known as the fixed-pivot approach, is quite general and is internally consistent, as far as two integral properties of the NDF are concerned [116]. It is noteworthy that the number of conserved moments can be increased by distributing the born elements to more than two pivotal points as formulated by Alopaeus et al. [118].

Despite the competitive advantages of the fixed-pivot approach over previously developed approaches [119], Kumar and Ramkrishna [116] illustrated that the fixed-pivot approach overpredicts the NDF, particularly in the case of coalescence. They stated that the over-prediction issue arises due to the fixed pivotal points and proposed a new approach based on moving pivotal points. This method involves the solution for the number density (or a property of the NDF) at moving pivotal points, the location of which is governed by a differential equation. The locations of pivotal points change in such a way as to ensure preservation of the targeted

properties. In another attempt to improve the predictions, a new technique was developed, called the cell-averaging technique, which assigns the born elements to the pivotal points on the basis of the average value of their internal coordinates [120]. Numerical tests showed that the cell-averaging technique improves the results considerably, on which more details can be found elsewhere [120].

Concerning the continuous change of the internal coordinate, the third term on the left-hand side of Eq. (3.13) can be written as follows:

$$\int_{\xi_i}^{\xi_{i+1}} \partial_\xi (Gn) \, \mathrm{d}\xi = (Gn)|_{\xi_{i+1}} - (Gn)|_{\xi_i}, \qquad (3.16)$$

and it can be interpreted as the net flux of elements to/from the interval I_i, which is equal to the difference between the fluxes at the bounds of I_i. However, the NDF at the bounds of intervals is not known and must be approximated by interpolating the values at two neighbouring pivotal points. The upwind scheme is the simplest interpolation approach. Consider a generic bound ξ_i at which the number density $n(\xi_i)$ is needed. If the rate of continuous process at the bound $G(\xi_i)$ is positive, then $n(\xi_i) = N_{i-1}$, otherwise $n(\xi_i) = N_i$. The upwind scheme is first-order and therefore it suffers from numerical diffusion [57]. Numerical diffusion can be avoided by integration over the characteristic curves [121], but this method is not suited for being incorporated in CFD codes. A more viable alternative is employing high-order schemes [122–124] which, however, do not guarantee the positivity of the N_i [121]. To overcome this issue numerous methods have been proposed [102, 121]

Last, class or sectional methods can be extended to bi- and multi-variate PBEs [125, 126]. However, these extensions are not covered here as they are currently not compatible with CFD implementations because of their exceedingly large computational cost [51, 52, 54].

3.2.2 Method of Moments

The previous section mentioned several difficulties in tracking the evolution of the NDF through the direct solution of the PBE, which mainly arise due to the discretization of the internal coordinate space. In a pioneering work, Hulburt and Katz argued that the NDF contains too much information for many engineering applications and proposed an approximate system of description that tracks the evolution of moments of the NDF instead of the NFD itself [127]. In the most general form, the moments of the NDF are defined as:

$$\begin{aligned} m_{k_1,k_2,\ldots,k_d,k_{d+1},k_{d+2},k_{d+3}}(t,\mathbf{x}) &= \langle \xi_1^{k_1} \xi_2^{k_2} \ldots \xi_d^{k_d} u_1^{k_{d+1}} u_2^{k_{d+2}} u_3^{k_{d+3}} \rangle \\ &= \int_{\Omega_{\boldsymbol{\xi}}} \int_{\Omega_{\mathbf{u}_\mathrm{b}}} \xi_1^{k_1} \xi_2^{k_2} \ldots \xi_d^{k_d} u_1^{k_{d+1}} u_2^{k_{d+2}} u_3^{k_{d+3}} \, f(t,\mathbf{x},\boldsymbol{\xi},\mathbf{u}_\mathrm{b}) \, \mathrm{d}\boldsymbol{\xi} \, \mathrm{d}\mathbf{u}_\mathrm{b}, \end{aligned}$$

$$(3.17)$$

where $\mathbf{k} = (k_1, k_2, \ldots, k_d, k_{d+1}, k_{d+2}, k_{d+3})$ is the exponent vector. Each element of $\mathbf{k}$ is the order of the moment with respect to the corresponding internal coordinate or velocity component. The moments offer two key advantages that make the method of moments (MOM) attractive. First, the moments are functions of only time and space, i.e. they are Eulerian fields, and therefore an approach based on the moments is perfectly compatible with the solution methods readily available in CFD codes. The second advantage is that the low-order moments are related to some macroscopic properties of the disperse phase, which are physically meaningful and generally measurable. It is noteworthy that, in many applications, the ultimate aim of solving the PBE is to predict these macroscopic properties of the disperse phase.

A simplified example helps to elaborate on the subject without loss of generality. Let the internal coordinates consist of the mass of the elements $\xi = M$ and the velocity. Then, the MOM involves the solution of a number of transport equations written in terms of the moments of the NDF. The moments $\langle \xi^0 u_1^0 u_2^0 u_3^0 \rangle$, $\langle \xi^1 u_1^0 u_2^0 u_3^0 \rangle$, and $\langle \xi^0 u_1^1 u_2^0 u_3^0 \rangle$, $\langle \xi^0 u_1^0 u_2^1 u_3^0 \rangle$ and $\langle \xi^0 u_1^0 u_2^0 u_3^1 \rangle$ exemplify the importance of low-order moments since, they represent respectively: the total particle number density, the average particle mass density and the three components of the total particle momentum density.

The transport equation for a generic moment, $\langle \xi^{k_1} u_1^{k_2} u_2^{k_3} u_3^{k_4} \rangle$, is derived by multiplying the GPBE, Eq. (3.2), with the function $g(\xi, \mathbf{u}_b) = \xi^{k_1} u_1^{k_2} u_2^{k_3} u_3^{k_4}$, and by integrating over the internal coordinate phase space:

$$\partial_t \left(\int_{\mathbb{R}^+} \mathrm{d}\xi \int_{\mathbb{R}^3} g f \, \mathrm{d}\mathbf{u}_b \right) + \partial_{\mathbf{x}} \cdot \left(\int_{\mathbb{R}^+} \mathrm{d}\xi \int_{\mathbb{R}^3} \mathbf{u}_b g f \, \mathrm{d}\mathbf{u}_b \right)$$
$$+ \int_{\mathbb{R}^+} \mathrm{d}\xi \int_{\mathbb{R}^3} g \, \partial_\xi (Gf) \, \mathrm{d}\mathbf{u}_b + \int_{\mathbb{R}^+} \mathrm{d}\xi \int_{\mathbb{R}^3} g \, \partial_{\mathbf{u}_b} \cdot (\mathbf{A}f) \, \mathrm{d}\mathbf{u}_b = \int_{\mathbb{R}^+} \mathrm{d}\xi \int_{\mathbb{R}^3} g \mathcal{S} \, \mathrm{d}\mathbf{u}_b \tag{3.18}$$

The first term is the derivative of the moment with respect to time, $\partial_t \langle \xi^{k_1} u_1^{k_2} u_2^{k_3} u_3^{k_4} \rangle$. The second term is the moment transport in the physical space, which appears as the spatial derivative of a higher-order moment

$$\partial_{\mathbf{x}} \cdot \left(\int_{\mathbb{R}^+} \mathrm{d}\xi \int_{\mathbb{R}^3} \mathbf{u}_b g f \, \mathrm{d}\mathbf{u}_b \right) = \partial_{x_1} \langle \xi^{k_1} u_1^{k_2+1} u_2^{k_3} u_3^{k_4} \rangle + \partial_{x_2} \langle \xi^{k_1} u_1^{k_2} u_2^{k_3+1} u_3^{k_4} \rangle$$
$$+ \partial_{x_3} \langle \xi^{k_1} u_1^{k_2} u_2^{k_3} u_3^{k_4+1} \rangle, \quad (3.19)$$

giving rise to the closure problem described in Section 3.2.2. The third term on the left-hand side of Eq. (3.18) can be simplified further by integration by part [57]:

$$\int_{\mathbb{R}^+} \mathrm{d}\xi \int_{\mathbb{R}^3} g \, \partial_\xi (Gf) \, \mathrm{d}\mathbf{u}_b = - \int_{\mathbb{R}^3} (gGf)|_{\xi=0} \, \mathrm{d}\mathbf{u}_b - \int_{\mathbb{R}^+} \mathrm{d}\xi \int_{\mathbb{R}^3} \partial_\xi (g) \, Gf \, \mathrm{d}\mathbf{u}_b. \quad (3.20)$$

The first term on the right-hand side takes into account the appearance/disappearance of the disperse phase elements at the origin, which may be nonzero depending on

the sign of G, i.e. if $g(\xi)$ is not zero and negative at the origin [57, 128]. Likewise, the integration by part simplifies the fourth term on the left-hand side of Eq. (3.18):

$$\int_{\mathbb{R}^+} d\xi \int_{\mathbb{R}^3} g\, \partial_{\mathbf{u}_b} \cdot (\mathbf{A}f)\, d\mathbf{u}_b = -\int_{\mathbb{R}^+} d\xi \int_{\mathbb{R}^3} \mathbf{A}f \cdot \partial_{\mathbf{u}_b}(g)\, d\mathbf{u}_b. \qquad (3.21)$$

Closure Problem in MOM

The moment transport equations, i.e. Eq. (3.18), are not in closed form, except in a few simple cases [57]. One reason is that a set of transport equations written for a number of moments may contain terms that depend on higher-order moments. The addition of new moment transport equations for the higher-order moments would not solve the problem because the new equations give rise to new higher-order moments. However, the higher-order moments can be readily calculated if the NDF is known. In general, the knowledge of the NDF is also needed to calculate the source term and transport terms in the space of internal coordinates and velocity, see Eq. (3.18). This is the main issue raised by the MOM, which is known as the closure problem. Several methods have been developed to close the moment transport equations, such as: interpolative closures [129], reconstruction of the NDF with an assumed functional form [130–132] and approximating the NDF using a quadrature formula [58, 112, 133]. The reader can find more details on developed closures in [57, 134]. Here, we focuses on the closures based on the quadrature formula, known as Quadrature-Based Moment Methods (QBMMs), which has more general applicability than other proposed closures.

3.2.3 Quadrature-Based Moment Methods

In QBMMs, the NDF is approximated with an N-node quadrature formula, i.e. a summation of N weighted kernel density functions, each centered on a node/abscissa of a Gaussian quadrature approximation. The most commonly employed kernel density function is the Dirac delta function. The idea originated with McGraw [133], who employed an N-node Gaussian quadrature to approximate the integrals in the moment transport equations for the solution of a univariate PBE and named the approach quadrature method of moments (QMOM). The algorithm calculates the N abscissas and N weights of the quadrature from the $2N$ transported moments. In another work, Marchisio and Fox [58] developed a similar method, named the direct quadrature method of moments (DQMOM), by which the quadrature approximation is transported in space and time such that the moments evolve according to the proper transport equations. In the following sections, both approaches are explained in detail. Moreover, the extension of the QMOM to bi- and multi-variate PBEs (i.e. the conditional quadrature method of moments, CQMOM) is also discussed. Last, an introduction is given on the extended quadrature method of moments (EQMOM), which is useful in applications that require a

continuous reconstruction of the NDF.

Quadrature Method of Moments

McGraw [133] proposed that the unclosed integrals of the moment transport equations could be approximated by employing an N-node Gaussian quadrature formula. It is equivalent to assuming the following functional form to approximate the NDF (for a univariate problem):

$$n(t, \mathbf{x}, \xi) \approx \sum_{p=1}^{N} w_p(t, \mathbf{x})\, \delta[\xi - \xi_p(t, \mathbf{x})] \tag{3.22}$$

where $w_p(t, \mathbf{x})$ and $\xi_p(t, \mathbf{x})$ are the weight and abscissa of the node p. In the above expression, δ denotes the Dirac delta function. The moment of order k of the approximated NDF can be expressed as follows:

$$m_k = \int_{\mathbb{R}^+} \xi^k n(\xi)\, \mathrm{d}\xi \approx \sum_{p=1}^{N} w_p\, \xi_p^k \tag{3.23}$$

where m_k is an alternative notation for $\langle \xi^k \rangle$. The above relationship implies that knowledge about the first $2N$ moments enables us to determine the N weights and N abscissas of the quadrature approximation in Eq. (3.22) by solving the following set of nonlinear equations:

$$m_0 = \sum_{p=1}^{N} w_p\,, \quad m_1 = \sum_{p=1}^{N} w_p\, \xi_p^1\,, \quad \ldots \quad m_{2N-1} = \sum_{p=1}^{N} w_p\, \xi_p^{2N-1}. \tag{3.24}$$

The above set of nonlinear equations are usually solved by employing well-conditioned recursive inversion algorithms such as the product-difference (PD) algorithm [135] and the Chebyshev algorithm [136]. The latter has the advantage of being applicable to distributions with zero mean value, i.e. $m_1 = 0$, in contrast to the PD algorithm [57]. It is noteworthy that the weights and abscissas obtained from the solution of Eq. (3.24) reproduce exactly the moments up to order $2N - 1$.

The QMOM employs an N-node quadrature approximation to solve the transport equations for a set of moments of a PBE. The procedure of the QMOM can be explained by writing the transport equation of a generic moment of order k derived from the PBE (Eq. (3.1)):

$$\partial_t(m_k)\, +\, \partial_{\mathbf{x}} \cdot (\mathbf{U}_{\mathrm{g},k} m_k) = \delta_{k,0}\, G(0)\, n(0)\, +\, k \int_{\mathbb{R}^+} \xi^{k-1}\, G n\, \mathrm{d}\xi\, +\, \int_{\mathbb{R}^+} \xi^k \mathcal{S}\, \mathrm{d}\xi, \tag{3.25}$$

where $\delta_{k,0}$ is the Kronecker delta and $\mathbf{U}_{\mathrm{g},k}$ denotes the transport velocity of the k-order moment defined by:

$$\mathbf{U}_{\mathrm{d},k} = \frac{1}{m_k} \int_{\mathbb{R}^+} \xi^k \mathbf{U}_{\mathrm{d}}(\xi)\, n\, \mathrm{d}\xi. \tag{3.26}$$

The first term on the right-hand side of Eq. (3.25) appears only in the transport equation of the zeroth-order moment.

This term is particularly challenging in the case of negative G, or in other words when the disperse phase elements are shrinking and disappearing. More detailed discussion on the subject can be found in [106, 137]. In the latter reference, a method is suggested to reconstruct a continuous NDF by using the maximum entropy maximization, which enables the evaluation of the NDF at the origin (i.e. $\xi = 0$). In addition, a robust and efficient quadrature-based method was developed by Yuan and co-workers [138] to reconstruct a continuous NDF, see Section 3.2.3. The second term on the right-hand side of Eq. (3.25) can be approximated using the N-node Gaussian quadrature formula:

$$k \int_{\mathbb{R}^+} \xi^{k-1} \, G(\xi) n(\xi) \, \mathrm{d}\xi \approx k \sum_{p=1}^{N} w_p \xi_p^{k-1} G(\xi_p). \tag{3.27}$$

The source term in the case of coalescence and break-up is approximated likewise (assuming that ξ is a conserved property such as mass and volume of elements) [57]:

$$\begin{aligned}
\int_{\mathbb{R}^+} \xi^k \mathcal{S} \, \mathrm{d}\xi \approx{}& \frac{1}{2} \sum_{p=1}^{N} w_p \sum_{q=1}^{N} (\xi_p + \xi_q)^k a(\xi_p, \xi_q) \, w_q - \sum_{p=1}^{N} \xi_p^k \, a(\xi_p, \xi_q) \, w_p \\
&+ \sum_{p=1}^{N} \left(\int_{\mathbb{R}^+} \xi^k \beta(\xi|\xi_p) \, \mathrm{d}\xi \right) b(\xi_p) \, w_p - \sum_{p=1}^{N} \xi_p^k \, b(\xi_p) \, w_p.
\end{aligned} \tag{3.28}$$

The weights and abscissas of the quadrature formula in Eqs. (3.27) and (3.28) are determined by inverting the first $2N$ moments. Therefore, it is necessary to track the evolution of the first $2N$ moments by solving the corresponding transport equations. At each time step, the quadrature formula is determined by means of an inversion algorithm, which uses the $2N$ transported moments available from the previous time step or the initial conditions. It is noteworthy that the inversion algorithm fails if the moments are not realizable, i.e. the moment set is not inside the moment space. To explain the moment space, one should note that any number density function $n(\xi)$ defined on a support Ω_ξ can be associated with a positive measure (μ) such that $\mathrm{d}\mu = n(\xi)\mathrm{d}\xi$. One can consider all the possible measures defined on the same support Ω_ξ, which together form a space of measures, denoted by $\mathcal{P}$. Then, each possible measure $\mu \in \mathcal{P}$ determines a possible vector of k moments (from order 0 to k): $\mathbf{m}_k = (m_0, m_1, \ldots, m_k)$. Eventually, the kth-order moment space $(\mathcal{M}_k)$ on the support Ω_ξ is defined as the space formed by all the possible $\mathbf{m}_k$, each corresponding to a $\mu \in \mathcal{P}$ or mathematically: $\mathcal{M}_k = \{\mathbf{m}_k = \int_{\Omega_\xi} (\xi^0, \xi^1, \ldots, \xi^k) \, \mathrm{d}\mu \mid \mu \in \mathcal{P}\}$. A set of moments $(m_0, m_1, \ldots, m_k)$ should belong to the moment space $\mathcal{M}_k$ to be realizable, otherwise no positive measure can be found with such a set of moments. The characterization of the moment space $\mathcal{M}_k$ for three common supports $\Omega_\xi = (-\infty, \infty)$, $\Omega_\xi = (0, \infty)$ and $\Omega_\xi = (0,1)$ is found

in [139]. For problems with semi-infinite positive supports, the positivity of the following Hankel determinants guarantees the realizability of the moment set $\mathbf{m}_k$ [140]:

$$\mathcal{H}_{2p+q} = \begin{vmatrix} m_q & \cdots & m_{p+q} \\ \vdots & \ddots & \vdots \\ m_{p+q} & \cdots & m_{2p+q} \end{vmatrix} \geq 0 \quad \text{for} \quad q = 0,1 \quad \text{and} \quad \{p|p \in \mathbb{N}_0, 2p+q \leq k\} \tag{3.29}$$

The realizability issue is mainly due to the numerical methods that deal with the discretized moment transport equations, which are not the same as the exact equations. This fact necessitates employing numerical methods that are designed to prevent the realizability issue [59, 62–64, 141].

In general, a quadrature formula with more nodes yields more accurate approximation of integrals in the moment transport equations and an approximation of higher quality for the NDF. However, a quadrature with more nodes means more moments to be tracked, hence the need for more computational resources. In addition, the recursive algorithms for the calculation of the weights and abscissas become less stable as the number of nodes increases, and convergence gets difficult for typically $N > 10$ [57]. However, Marchisio and colleagues [112, 142] showed that satisfactory predictions can be achieved by employing a quadrature approximation with $2 \leq N \leq 4$ for simple coalescence and break-up problems. Moreover, QMOM predictions have acceptably small overall error not only for the tracked moments but also for higher-order moments [112].

Concerning bi- and multi-variate PBEs, the main challenge is the determination of the weights and (multidimensional) abscissas of the quadrature from the mixed moments, since the PD and Chebyshev algorithms are applicable only to univariate quadratures. The next section focuses on the extension of the QMOM to such cases by using conditional moments.

Conditional Quadrature Method of Moments

This section deals with the application of the QBMM to the solution of bi- and multi-variate PBEs. Let the NDF be defined over the space ($\Omega_{\boldsymbol{\xi}}$) of d internal coordinates, $\boldsymbol{\xi} = (\xi_1, \xi_2, \ldots, \xi_d)$. Then, the NDF can be approximated with the following functional form:

$$n(t, \mathbf{x}, \boldsymbol{\xi}) \approx \sum_{p=1}^{N} w_p(t, \mathbf{x})\, \boldsymbol{\delta}[\boldsymbol{\xi} - \boldsymbol{\xi}_p(t, \mathbf{x})] \;, \quad \boldsymbol{\delta}[\boldsymbol{\xi} - \boldsymbol{\xi}_p(t, \mathbf{x})] = \prod_{\alpha=1}^{d} \delta[\xi_\alpha - \xi_{\alpha;p}(t, \mathbf{x})] \tag{3.30}$$

where $w_p(t, \mathbf{x})$ is the weight of the node p with abscissas $\boldsymbol{\xi}_p = (\xi_{1;p}, \xi_{2;p}, \ldots, \xi_{d;p})$ located in the joint space of the internal coordinates. The reader should bear in mind that the above quadrature is not a Gaussian quadrature. Moreover, univariate

inversion methods such as the PD and Chebyshev algorithms are not applicable to multivariate density functions. The moments of the above approximation can be expressed as follows:

$$\langle \xi_1^{k_1} \xi_2^{k_2} \ldots \xi_d^{k_d} \rangle = m_{k_1,k_2,\ldots,k_d} = \sum_{p=1}^{N} w_p \prod_{\alpha=1}^{d} \xi_{\alpha;p}^{k_\alpha}. \tag{3.31}$$

The closure problem can be overcome by determining the quadrature approximation of order N, defined by N weights and N d-dimensional abscissas/nodes. The weights and abscissas of the quadrature nodes can be found by using a set of $N(d+1)$ moments. The inversion approach is desired to retain some main properties of univariate inversion algorithms [57].

First, it should be noniterative otherwise its application to practical CFD simulations will be computationally expensive. Second, it should construct a mathematically and physically meaningful quadrature approximation – in other words, abscissas should be located in the support of the internal coordinates and weights should be non-negative. Last, the weights and abscissas obtained from the moments of an N-point density function should represent exactly the same N-point density function. Several methods have been developed to determine the high-dimensional quadrature points, such as the brute-force algorithm [143], the tensor-product algorithm [60, 144–146] and the conditional quadrature method of moments (CQMOM) [147, 148], just to cite the most popular. Only the last method is discussed here since it is generally more stable and accurate.

For the sake of brevity, the explanation focuses on bi-variate NDFs. The extension of the following procedure to more than two internal coordinates can be found in [57]. In addition, the application of the CQMOM to the kinetic equations, i.e. three velocity components as the internal coordinates, is discussed by Yuan and Fox [148]. In the CQMOM, the NDF is approximated by the following functional form:

$$n(t,\mathbf{x},\boldsymbol{\xi}) \approx \sum_{p_1=1}^{N_1} \sum_{p_2=1}^{N_2} w_{p_1}(t,\mathbf{x})\, w_{p_2,p_1}(t,\mathbf{x})\, \delta[\xi_1 - \xi_{1;p_1}(t,\mathbf{x})]\, \delta[\xi_2 - \xi_{2;p_2,p_1}(t,\mathbf{x})], \tag{3.32}$$

where w_{p_1} and $\xi_{1;p_1}$ are the weights and abscissas calculated from the pure moments with respect to the first internal coordinate (ξ_1) by using a univariate inversion algorithm. Instead, w_{p_2,p_1} and $\xi_{2;p_2,p_1}$ are the conditional weights and abscissas to be obtained by conditioning the second internal coordinate (ξ_2) on each abscissa of the first one ($\xi_{1;p_1}$). The calculation of the conditional weights and abscissas exploits the relationship between the mixed moments and the conditional NDF ($n_{2|1}$). First, the conditional NDF is defined by:

$$n_{2|1}(\xi_2|\xi_1) = \frac{n(\xi_1,\xi_2)}{n_1(\xi_1)}, \tag{3.33}$$

35

where $n_1(\xi_1) = \int_{\Omega_{\xi_2}} n(\xi_1, \xi_2) \, d\xi_2$ is the marginal NDF of ξ_1. The moments of $n_1(\xi_1)$ are the same as the pure moments of $n(\xi_1, \xi_2)$ with respect to ξ_1 and therefore can be expressed in terms of w_{p_1} and $\xi_{1;p_1}$. Then, the mixed moments can be written as follows:

$$
\begin{aligned}
m_{k_1, k_2} &= \int_{\Omega_{\xi_1}} \xi_1^{k_1} n_1(\xi_1) \, d\xi_1 \int_{\Omega_{\xi_2}} \xi_2^{k_2} n_{2|1}(\xi_2 | \xi_1) \, d\xi_2 \\
&= \sum_{p_1=1}^{N_1} w_{p_1} \xi_{1;p_1}^{k_1} \int_{\Omega_{\xi_2}} \xi_2^{k_2} n_{2|1}(\xi_2 | \xi_{1;p_1}^{k_1}) \, d\xi_2 = \sum_{p_1=1}^{N_1} w_{p_1} \xi_{1;p_1}^{k_1} \langle \xi_2^{k_2} \rangle (\xi_{1;p_1}),
\end{aligned}
\tag{3.34}
$$

where $\langle \xi_2^{k_2} \rangle (\xi_{1;p_1})$ denotes the conditional moments. Using the above relationship, the $N_1(2N_2 - 1)$ conditional moments can be obtained from the solution of the linear systems of the following form written for $k_2 = 0, ..., 2N_2 - 1$:

$$
\begin{bmatrix}
1 & \cdots & 1 \\
\xi_{1;1} & \cdots & \xi_{1;N_1} \\
\vdots & \ddots & \vdots \\
\xi_{1;1}^{N_1-1} & \cdots & \xi_{1;N_1}^{N_1-1}
\end{bmatrix}
\begin{bmatrix}
w_1 & & & \\
& w_2 & & \\
& & \ddots & \\
& & & w_{N_1}
\end{bmatrix}
\begin{bmatrix}
\langle \xi_2^{k_2} \rangle (\xi_{1;1}) \\
\langle \xi_2^{k_2} \rangle (\xi_{1;2}) \\
\vdots \\
\langle \xi_2^{k_2} \rangle (\xi_{1;N_1})
\end{bmatrix}
=
\begin{bmatrix}
m_{0,k_2} \\
m_{1,k_2} \\
\vdots \\
m_{N_1-1,k_2}
\end{bmatrix}.
\tag{3.35}
$$

The above linear system of equations, known as Vandermonde linear system, is non-singular as long as the abscissas $\xi_{1;p1}$ are distinct. The reader is referred to [149] for an efficient algorithm to solve the linear systems of the Vandermonde form. Finally, for each $\xi_{1;p1}$ a univariate inversion algorithm is applied to the corresponding set of conditional moments to find the corresponding conditional weights (w_{p_2,p_1}) and abscissas ($\xi_{2;p_2,p_1}$). Although the pure moments can be kept realizable by employing an appropriate numerical scheme, the realizability of the conditional moments is not guaranteed. In this case, the realizability issue can be overcome by applying the 1-D adaptive quadrature technique proposed by Yuan and Fox [148]. With this technique, the maximum number of conditional moments belonging to the moment space is determined and consequently, the number of nodes for the second internal coordinate (at each $\xi_{1;p1}$) is adjusted accordingly.

One should pay attention to the selected order of internal coordinates' conditioning as it changes the set of controlled moments (i.e. moments used in the reconstruction of the NDF). Nevertheless, all the moments controlled in the CQ-MOM belong to the optimal moment set; see Section 3.2.3 for the definition and importance of this set.

Direct Quadrature Method of Moments

The direct quadrature method of moments (DQMOM) was first introduced by Marchisio and Fox [58] to avoid the need for an inversion algorithm, particularly in the case of bi- and multi-variate problems. Although the inversion of moments in

bi- and multi-variate problems was later overcome by the CQMOM, the DQMOM has received considerable attention from the scientific community. Furthermore, the DQMOM can be applied to univariate problems.

In contrast to the QMOM and CQMOM, the DQMOM employs transport equations written in terms of the weights w_p and weighted abscissas $\varsigma_{\alpha;p} = w_p \xi_{\alpha;p}$. Therefore, there is no need to employ an inversion algorithm except for the initialization of the weights and abscissas according to the initial conditions of the moments. Let the NDF be defined over the space of two internal coordinates and governed by the following bi-variate PBE:

$$\partial_t n + \partial_{\mathbf{x}} \cdot (\langle \mathbf{u}_{\mathrm{b}} | \xi_1, \xi_2 \rangle n) + \partial_{\xi_1}(G_1 n) + \partial_{\xi_2}(G_2 n) = \int \mathcal{S} \, \mathrm{d}\mathbf{u}_{\mathrm{b}}. \tag{3.36}$$

The DQMOM approximates the NDF with the functional form in Eq. (3.30). Then, the following transport equations can be written for the weights and weighted abscissas [58]:

$$\begin{aligned}
\partial_t w_p + \partial_{\mathbf{x}} \cdot (\langle \mathbf{u}_{\mathrm{b}} \rangle_p w_p) &= s_p^w, \\
\partial_t(\varsigma_{1;p}) + \partial_{\mathbf{x}} \cdot (\langle \mathbf{u}_{\mathrm{b}} \rangle_p \varsigma_{1;p}) &= s_{1,p}^\varsigma, \\
\partial_t(\varsigma_{2;p}) + \partial_{\mathbf{x}} \cdot (\langle \mathbf{u}_{\mathrm{b}} \rangle_p \varsigma_{2;p}) &= s_{2,p}^\varsigma,
\end{aligned} \tag{3.37}$$

where $\langle \mathbf{u}_{\mathrm{b}} \rangle_p = \langle \mathbf{u}_{\mathrm{b}} | \xi_{1,p}, \xi_{2,p} \rangle$ denotes the velocity of the quadrature node p, and s_p^w, $s_{1,p}^\varsigma$ and $s_{1,p}^\varsigma$ are the source terms of the transport equations to be determined. The unknown source terms can be found by first replacing the NDF in Eq. (3.36) with the functional form in Eq. (3.30) specialized for a bi-variate problem and then by applying the moment transformation of a generic order $\mathbf{k} = (k_1, k_2)$ [58]:

$$\sum_{p=1}^{N}(1 - k_1 - k_2)\xi_{1,p}^{k_1}\xi_{2,p}^{k_2}s_p^w - \sum_{p=1}^{N} k_1 \xi_{1,p}^{k_1-1}\xi_{2,p}^{k_2}s_{1,p}^\varsigma + \sum_{p=1}^{N} k_2 \xi_{1,p}^{k_1}\xi_{2,p}^{k_2-1}s_{2,p}^\varsigma = \bar{h}_{k_1,k_2}, \tag{3.38}$$

where $\bar{h}_{k_1,k_2}$ takes into account the change of the moment due to the continuous and discontinuous events and therefore is problem dependent. A system of $3N$ linear equations (equal to the number of unknowns) can be formed by writing Eq. (3.38) for $3N$ moments of different order. The solution of the linear system can be expressed in the matrix form $\mathbf{s} = \mathcal{A}^{-1}\mathbf{h}$, where $\mathbf{s} = [s_1^w \ldots s_N^w \; s_{1,1}^\varsigma \ldots s_{1,N}^\varsigma \; s_{2,1}^\varsigma \ldots s_{2,N}^\varsigma]^T$ and $\mathcal{A}$ is the coefficient matrix. The matrix $\mathcal{A}$ should be non-singular and therefore requires some considerations. First, the abscissas must remain distinct in order to prevent singularity. Thus, using too many nodes is not recommended since the probability of two nodes approaching each other increases with the addition of more nodes [57]. Another important point is the choice of the moment set, which is studied by Fox in detail [150]. Fox established a methodology to choose a set of moments, called the optimal moment set, that results in a non-singular coefficient matrix $\mathcal{A}$. Eventually, Author reported the optimal moment sets for problems with

$1 \leq d \leq 3$. The concept was developed by using $N = r^d$ nodes for $r \in \mathbb{Z}_{>0}$, which treats all the internal coordinates equally. It is noteworthy that there are other choices for the moment set, which are valid but not optimal. However, one should try to use a moment set that covers the important moments, i.e. those with physical significance, and that includes enough mixed moments to avoid losing the correlation between the internal coordinates. For more details, the reader is referred to the discussion of choosing the moment set in [57].

Extended Quadrature Method of Moments

The previous QBMMs approximate the NDF with an N-point discontinuous distribution, i.e. a summation of N weighted Dirac delta functions. However, some applications require a continuous reconstructed NDF to correctly model the phenomena involved, e.g. evaporating sprays [137]. Yuan et al. [138] suggested a method, called the extended quadrature method of moments (EQMOM), which employs a parametric continuous kernel density function (KDF) instead of the Dirac delta function:

$$n(t, \mathbf{x}, \xi) \approx \sum_{p=1}^{N} w_p(t, \mathbf{x}) \, \delta_\sigma[\xi; \xi_p(t, \mathbf{x})], \tag{3.39}$$

where $\delta_\sigma(\xi; \xi_p)$ is a chosen KDF, which depends on the parameter σ. The weights and abscissas associated with the KDF are denoted by w_p and ξ_p. The determination of the parameter σ requires that one additional moment should be tracked, in comparison to the $2N$ moments tracked in the QMOM. The KDF is required to reduce smoothly to the Dirac delta function in the limit of $\sigma \to 0$, meaning that the quadrature can be reconstructed from the first $2N$ moments when $\sigma = 0$. The choice of the KDF is problem dependent, i.e. the support of the KDF should be consistent with the support of the internal coordinate. Common KDFs are Gaussian distribution with infinite support $(-\infty, \infty)$, gamma and log-normal distributions with semi-infinite positive support $[0, \infty)$ and beta distribution with finite support $[0, 1]$. Moreover, it is practically important that the selected KDF can be defined in terms of the weight function $w(\theta)$ for a known family of orthogonal polynomials. In the following, the algorithm for the calculation of the weights and abscissas of the quadrature approximation as well as the parameter σ are explained for a univariate NDF with a semi-infinite positive support. The application of the EQMOM to problems with infinite or finite supports is similar and can be found elsewhere [57, 138]. In addition, the reader is referred to [57] for the extension of the EQMOM to multivariate problems.

As mentioned previously, a suitable choice of the KDF for problems with support of $[0, \infty)$ is the gamma distribution. Then, the NDF is approximated by the

following summation of N weighted parameterized gamma distributions:

$$n(\xi) \approx \sum_{p=1}^{N} w_p \frac{\xi^{\lambda_p-1}e^{-\xi/\sigma}}{\Gamma(\lambda_p)\sigma^{\lambda_p}} \quad \text{and} \quad \lambda_p(t,\mathbf{x}) = \frac{\xi_p}{\sigma}, \tag{3.40}$$

where Γ is the gamma function. The moments of the NDF can be expressed as:

$$m_k(t,\mathbf{x}) = \sum_{p=1}^{N} w_p \frac{\Gamma(\lambda_p+k)}{\Gamma(\lambda_p)}\sigma^k = \sum_{p=1}^{N} w_p\xi_p^k + \sum_{p=1}^{N} w_pP_{k-1}(\xi_p,\sigma), \tag{3.41}$$

where $P_{k-1}(\xi_p,\sigma)$ is a homogeneous polynomial of order $k-1$ with respect to ξ_p and σ. The summation $\sum_{p=1}^{N} w_p\xi_p^k$ is indeed the kth-order moment of the quadrature in the limit $\sigma = 0$, and here is denoted by m_k^*. Eq. (3.41) can be written for the first $2N+1$ moments to calculate the weights and abscissas as well as the parameter σ of the quadrature. An important observation is that the right-hand side of Eq. (3.41) can be rewritten in terms of only m_k^* and σ. Subsequently, the two sets of moments $\mathbf{m} = (m_0, m_1, \ldots, m_{2N})$ and $\mathbf{m}^* = (m_0^*, m_1^*, \ldots, m_{2N}^*)$ can be related through the matrix form $\mathbf{m} = \mathbf{B}(\sigma)\mathbf{m}^*$. The matrix $\mathbf{B}(\sigma)$ is a lower-triangular matrix, which allows us to calculate the moment m_k^* from the moments $(m_0, m_1, \ldots, m_k)$ for a given value of σ. Eventually, the following iterative approach can be used to determine the quadrature approximation [138]:

1. Guess the parameter σ and calculate the first $2N$ moments $(m_0^*, m_1^*, \ldots, m_{2N-1}^*)$ using $\mathbf{m}^* = \mathbf{B}^{-1}(\sigma)\mathbf{m}$

2. Find the weights w_p and abscissas ξ_p from the moments $(m_0^*, m_1^*, \ldots, m_{2N-1}^*)$ by employing the adaptive quadrature algorithm,

3. Use the weights and abscissas to calculate $m_{2N}^* = \sum_{p=1}^{N} w_p\xi_p^{2N}$,

4. Calculate the scalar function $J(\sigma) = m_{2N} - m_{2N}^* - \sum_{p=1}^{N} w_pP_{2N-1}(\xi_p,\sigma)$

5. Guess a new σ until the convergence $J(\sigma) = 0$ is achieved for the smallest σ.

In the above approach, the adaptive quadrature algorithm allows us to cope with the non-realizable set of moments. Once the quadrature is determined, it can be used to close the terms appearing in the moment transport equations, i.e. Eq. (3.39). For this purpose, a general integral of the NDF is considered:

$$\int_{\Omega_\xi} g(\xi)n(\xi)\,\mathrm{d}\xi = \sum_{p=1}^{N} w_p \int_{\Omega_\xi} g(\xi)\delta_\sigma(\xi;\xi_p)\,\mathrm{d}\xi = \sum_{p=1}^{N}\sum_{q=1}^{N'} w_pw_q^{(p)}\,g(\xi_q^{(p)}), \tag{3.42}$$

where $g(\xi)$ is a generic function of the internal coordinate. In Eq. (3.42), the integral of the KDF $\delta_\sigma(\xi;\xi_p)$ is approximated by a quadrature formula, for which the weights $w_q^{(p)}$ and abscissas $\xi_q^{(p)}$ can be calculated from the recursion coefficients that are known in advance. Moreover, the number of nodes of the second quadrature (N') does not depend on N and can be increased independently to improve the accuracy.

3.2.4   Selection of the Solution Method

A key factor in selection of the solution method is the number of internal co-ordinates. For univariate problems, the CM and QMOM are regarded as the first candidates. The CM is more suitable for simulation of systems in which the NDF can be measured directly. In contrast, the QMOM provides information about some (usually measurable) integral properties of the NDF. From the computational point of view, the QMOM is less demanding than the CM. In fact, achieving a reasonable accuracy by the CM generally requires a large number of intervals/classes, which is computationally expensive, particularly when disperse phase elements span a wide region of the phase space [112]. Therefore, the QMOM is the preferred method for the CFD simulation of spatially heterogeneous systems, specifically those of large-scale [105]. Furthermore, the CM should use high-order schemes when the system under study involves continuous events, in particular if the number of intervals cannot be increased sufficiently. However, employing high-order schemes usually leads to instabilities. In contrast, QBMMs handle continuous events easily, if the growth rate is positive. In the case of negative growth rates, e.g. evaporation/dissolution, the EQMOM can be used to estimate the value of the NDF at the origin of the relevant internal coordinate. Moreover, the EQMOM should be generally used when the particulate processes of interest are highly localized in the phase space [151]. In fact, with other QBMMs, some phenomena may be ignored if there is no node/abscissa in the region where they are active. Furthermore, the addition of nodes does not necessarily improve the situation as the QMOM shows unpredictable behaviour in response to the increase in the number of nodes, when highly localized phenomena are present [151]. In such cases, the CM and EQMOM are more appropriate.

In the case of bi- and multi-variate PBEs, QBMMs are generally the preferred methods. Both the DQMOM and CQMOM were developed to overcome the difficulties of moment inversion in bi- and multi-variate problems. However, the CQMOM has some advantages over the DQMOM. First, the equivalence between the DQMOM and QMOM/CQMOM is lost in pure hyperbolic PBEs [57], in contrast to spatially homogeneous systems. Moreover, the DQMOM is not valid for purely hyperbolic PBEs in the presence of (spatial or time) discontinuity in the weights and abscissas, because the transport equations in Eq. (3.37) are derived on the assumption that the weights and abscissas are continuous functions of time and space [57]. Another point is that the DQMOM does not guarantee the conservation of the moments except for the moments of order zero and one, and needs corrective terms to respect the conservation of the moments of higher-order [57]. Last, when a continuous NDF is needed, the CQMOM can be extended to use a KDF other than the Dirac delta function, i.e. the extended conditional quadrature method of moments [57].

3.3   Implementation in CFD

As mentioned previously, the solution of the GPBE/PBE provides detailed information about the disperse phase, which can result in a more accurate solution. For instance, a more accurate estimation of the drag force can be obtained by using the instantaneous size distribution of the disperse phase elements instead of a fixed constant element size. At the same time, the solution of the GPBE/PBE requires knowledge of the flow fields. Therefore, it is necessary to adopt a suitable approach to couple the CFD and GPBE/PBE, as explained in the following section.

3.3.1   Monokinetic Models

Monokinetic models, e.g. the TFM and MFM, assume zero velocity dispersion around the mean velocity (or mean velocities) of elements located at the same spatial coordinates at a given time and characterized by the same internal coordinate. This assumption is valid for elements with small Stokes numbers (St < 1) [152]. Within this context, the simplest approach assigns one velocity, $\mathbf{U}_d(t, \mathbf{x})$, to all elements of the disperse phase, which depends only on the spatial coordinates and time and not on the internal coordinates. The common methods for obtaining the velocity of the disperse phase, required to solve the PBE, include the mixture and two-fluid models [40, 47, 49–51, 55, 105, 153–155], although the dusty gas approach [156] and the equilibrium Eulerian approach [152] can be used for sufficiently small elements [76], see Figure 3.2. At the same time, the polydispersity of the elements can be described through the solution of the PBE, Eq. (3.1), by using a suitable method, as described in the previous section.
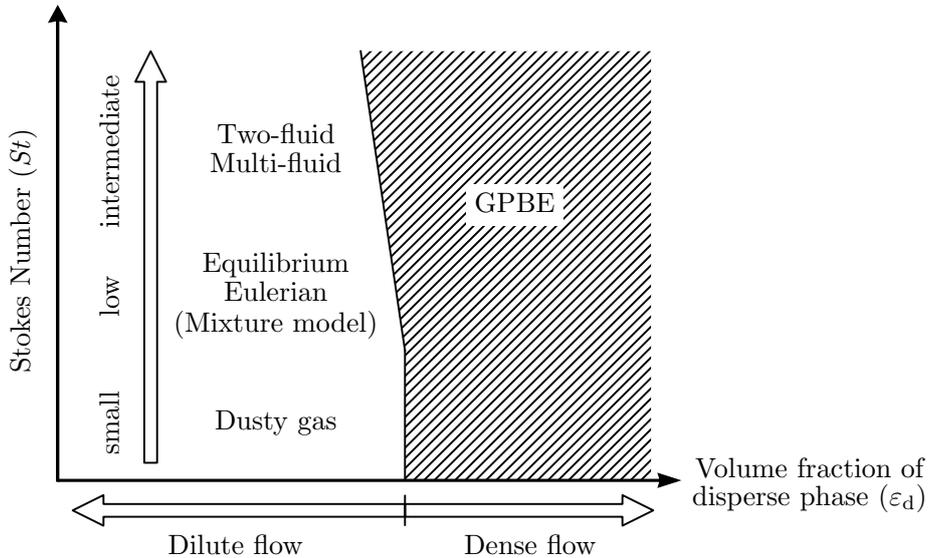

Figure 3.2: Applicability of Eulerian CFD models for the simulation of multiphase flows

When the CM is used to solve the PBE, the coupling terms are evaluated using the properties of each class of the disperse elements. In contrast, if we adopt the QMOM, the coupling terms are calculated by using either the average properties of the disperse elements, which are associated with the moments, or the quadrature nodes separately [54].

The assumption of identical element velocity can be relaxed partially by employing a multifluid approach, where the elements are grouped into several phases based on the value of an internal coordinate (usually size). This approach, called the multifluid model (MFM), is particularly useful when the system under study is highly polydisperse, see Figure 3.3. When the CM is chosen to solve the PBE [40, 42, 45, 103, 157], each class is assumed to move with its own velocity. In the case of the QMOM and DQMOM [105, 108, 158, 159], each node of the quadrature moves with a unique velocity. The velocity of each class (or node in the case of the QMOM and DQMOM) can be obtained by solving a momentum balance equation written for the corresponding class (or node), see Chapter 2.
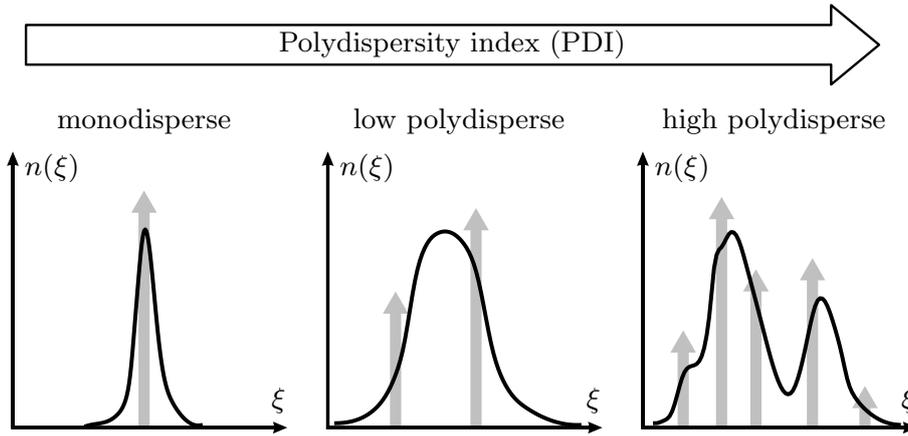
Figure 3.3: Polydispersity index indicates how wide is the distribution of disperse phase elements over the space of the internal coordinate. The gray arrows in above plots can be thought of as the nodes of the quadrature that approximates the underlying NDF (shown by the solid line) or as the number of element groups required to consider the polydispersity appropriately.

The monokinetic assumption is not valid in the case of elements with large Stokes numbers, since large elements do not adapt quickly to the surrounding fluid velocity and therefore the effect of their initial conditions lasts for a long time [152]. For instance, this assumption may lead to nonphysical predictions in dilute systems consisting of particles characterized by large Stokes numbers, where particle trajectory crossing (PTC) can occur [64, 145]. The PTC refers to a situation in dilute systems where the particles of different velocity (regardless of their properties) can cross each other without collision. A possible approach to describing such systems is adoption of a polykinetic model.

3.3.2 Polykinetic Models

It is necessary to include the element velocity as an internal coordinate, when dealing with disperse systems far from equilibrium or consisting of elements characterized by very large Stokes numbers. In such cases, the evolution of the disperse phase in space and time is entirely governed by the GPBE, Eq. (3.2), while the continuous phase is described by Eqs. (2.9) and (2.10). The interaction between the phases is taken into account through the exchange terms in the governing equations of both phases. The quadrature-based methods are preferred to solve the GPBE since the application of the CM to this equation is not tractable. In this regard, the QMOM, DQMOM and specifically CQMOM are promising tools to solve the GPBE [57, 64, 106, 145–148].

When the disperse system is very dilute, the effect of the disperse phase on the flow field of the continuous phase can be assumed negligible [57, 160]. Thus, one-way coupling suffices to describe the effect of the continuous phase on the evolution of the disperse phase elements. The flow fields of the continuous phase are predicted by the solution of the single-phase Navier-Stokes equations. At each time-step, the governing equations of the continuous phase are solved to predict the flow fields of the continuous phase, which eventually will be used to estimate the closure relations in the GPBE. It is possible to advance the GPBE with several smaller time-steps within each time-step of the CFD solver, if the time-scale of the phenomena affecting the elements is comparably smaller than the characteristic time-scale of the continuous phase [160].

However, the effect of disperse elements on flow fields of the continuous phase becomes significant as the number density of elements increases. Thus, governing equations of the continuous phase should include exchange terms due to the presence of the disperse phase elements, e.g. Eqs. (2.9) and (2.10) [161, 162]. Convergence issues may arise in the two-way coupling due to the explicit exchange terms included in the governing equations. For instance, the drag force generally depends on the relative velocity of the phases and, if handled explicitly, hinders convergence. The convergence rate can be improved by adopting the partial elimination algorithm [163]. The application of the partial elimination algorithm to CFD-QMOM simulations is explained by Passalacqua and co-workers [160, 161].

3.3.3 Numerical Issues of QBMM

Efficient numerical methods for solving the PBE must provide sufficiently accurate solutions as well as ensure the stability of the simulation. A major reason of simulation instabilities is the appearance of non-physical solutions during the simulation, i.e. the realizability issue associated with the QBMM. The realizability issue appears mostly when standard high-order schemes are employed for the independent advection of the moments [61]. These schemes aim mainly at achieving

high-order and oscillation-free solutions for transported variables. However, the moments are linked variables that belong to the moment space, therefore, a selected numerical scheme must additionally ensure that the moment space is preserved. Unfortunately, only 1st-order schemes, e.g. the upwind scheme, are guaranteed to yield realizable moment sets provided that the Courant–Friedrichs–Lewy (CFL) condition is satisfied [64]. It is noteworthy that the CFL condition generally serves as the criterion for the stability of the CFD simulations. The 1st-order schemes, albeit being very stable, generally produce diffused solutions for computationally affordable grid sizes. Therefore, if high-order solutions are required, one must employ high-order schemes that are specifically designed to overcome the realizability issue.

In a pioneer work, Vikas and coworkers proposed the quasi-high-order realizable scheme, which interpolates separately the weights and abscissas of the quadrature (instead of the moments) from the cell centers to the faces [62]. In this approach, the quadrature weights on the faces are obtained with a high-resolution (HR) total variation diminishing (TVD) scheme whereas the quadrature abscissas on the faces are obtained by using the 1st-order upwind scheme. With this technique, the realizability issue is avoided if a criterion for the time-step is fulfilled [62]. This approach can be applied for the solution of both PBEs and GPBEs. Moreover, it can be simply implemented in CFD codes, regardless of the spatial dimensionality and mesh type. Another notable approach preserves the moment space by advecting a sequence of positive variables, called ζ, which are connected to the moments [63]. The application of the original version of this approach to arbitrary unstructured grids is not straightforward. Nevertheless, Passalacqua and coworker extended the applicability of this approach to unstructured meshes [164].

In addition to the realizability issue, the boundedness of the solution is another important numerical aspect because the low-order moments are associated with some average physical properties of the elements, which are bounded in nature [66]. This aspect should be considered in the selection of the numerical solution method if a bounded solution for the moments is desired. In Chapter 5, we argue that an oscillation-free (bounded) solution for the moments is not necessarily guaranteed when the high-resolution TVD schemes are not applied directly to the moments, as in the case of the quasi-second-order realizable scheme. Eventually, we propose a technique to apply the high-resolution TVD schemes directly to the moments without encountering the realizability issue, which is based on using an identical limiter (equal-limiter) for all the transported moments.

3.3.4 QMOM for Compressible Fluids

The density of a disperse gas phase may vary in the domain due to, for example, the change in the hydrostatic pressure. The change in the gas phase density must be taken into account in the PBE, if the internal coordinates depend on it. For

instance, the bubble size (or volume) in gas-liquid flows changes as the gas density increases or decreases. In this case, the time evolution of a length- or volume-based NDF is affected by the density change. In the following, the derivation of the PBE for a length-based NDF, $n_L(t, \mathbf{x}, L)$, is provided. Here, the size of the bubble is denoted by L. For this purpose, it is convenient to start from the mass-based definitions because it does not depend on the gas density, i.e. it is a conserved quantity. Thus, we begin by defining the mass-based NDF, $n_M(t, \mathbf{x}, M)$, in such a way that $n_M \, dM$ determines the number of bubbles with mass between M and $M + dM$ located around point $\mathbf{x}$ at time t. By this definition, the following population balance equation can be written (assuming negligible interphase mass transfer):

$$\partial_t(n_M) + \partial_{\mathbf{x}} \cdot (\mathbf{U}_g n_M) = \mathcal{S}' \tag{3.43}$$

where $\mathcal{S}'(t, \mathbf{x}, M)dM$ is the rate of discrete changes in the number of bubbles with mass between M and $M + dM$ due to the coalescence and break-up phenomena. In the next step, the mass-based moment of generic order k', $m'_{k'}$, is defined as follows:

$$m'_{k'}(t, \mathbf{x}) = \int_0^\infty n_M(t, \mathbf{x}, M)M^{k'}dM \tag{3.44}$$

Using this definition, the mass-based PBE, Eq. (3.43), can be transformed to the transport equation for the mass-based moment of generic order k' as written below:

$$\partial_t m'_{k'} + \partial_{\mathbf{x}} \cdot (\mathbf{U}_g m'_{k'}) = \bar{\mathcal{S}}'_{k'} \tag{3.45}$$

where $\bar{\mathcal{S}}'_{k'}$ is only function of $\boldsymbol{x}$ and t, and denotes the following integral:

$$\bar{\mathcal{S}}'_{k'}(t, \mathbf{x}) = \int_0^\infty \mathcal{S}'(t, \mathbf{x}, M)M^{k'}dM \tag{3.46}$$

Now, the mass of each bubble is related to its size by the the following relation, $M = \frac{\pi}{6}\rho_g L^3$, on the assumption that the bubble shape is spherical. Moreover, it is trivial to show that the length-interval between L and $L + dL$ can be mapped approximately ($\sim \mathrm{O}(dL^2)$) onto the mass-interval between M and $M + dM$, where $dM = \frac{\pi}{2}\rho_g L^2 dL$. Then it follows that the number of bubbles in both intervals is the same – in other words $n_M dM = n_L dL$. This equality helps to relate the mass-based moments to the length-based ones:

$$m'_{k'} = \int_0^\infty n_M M^{k'}dM = \int_0^\infty n_L(\frac{\pi}{6}\rho_g L^3)^{k'}dL = (\frac{\pi}{6}\rho_g)^{k'}m_{3k'} = (\frac{\pi}{6}\rho_g)^{k/3}m_k$$

where k is equal to $3k'$. Then, the above relation is used to substitute the mass-based moments on the left-hand side of Eq. (3.45) with the length-based ones:

$$\begin{aligned}
\text{LHS} &= (\frac{\pi}{6})^{k/3}\left\{\partial_t\left[(\rho_g)^{k/3}m_k\right] + \partial_{\mathbf{x}} \cdot \left[\mathbf{U}_g(\rho_g)^{k/3}m_k\right]\right\} \\
&= (\frac{\pi}{6}\rho_g)^{k/3}\left[\partial_t m_k + \partial_{\mathbf{x}} \cdot (\mathbf{U}_g m_k)\right] + \frac{k}{3}(\frac{\pi}{6})^{k/3}(\rho_g)^{-1+k/3}m_k\left[\partial_t \rho_g + \mathbf{U}_g \cdot \partial_x \rho_g\right] \\
&= (\frac{\pi}{6}\rho_g)^{k/3}\left[\partial_t m_k + \partial_{\mathbf{x}} \cdot (\mathbf{U}_g m_k) + \frac{k}{3}m_k\frac{1}{\rho_g}\frac{D\rho_g}{Dt}\right],
\end{aligned} \tag{3.47}$$

where $\dfrac{D}{Dt}$ denotes the material derivative and $\dfrac{1}{\rho_g}\dfrac{D\rho_g}{Dt}$ is the volume dilatation of the gas phase calculated by the CFD solver.

The right-hand side of Eq. (3.45) defines how the moments (either mass-based or length-based) evolve under the effect of the coalescence and break-up phenomena. However, referring to Eq. (3.46), it is based on the mass-based rate of bubble birth/death, i.e. $\mathcal{S}'(t,\mathbf{x},M)$. However, the objective is to obtain moment transport equations that are fully length-based, which allows us to use directly length-based kernels for the estimation of the coalescence and break-up contributions. To achieve it, a length-based rate of birth/death of bubbles, $\mathcal{S}(t,\mathbf{x},L)$, is defined such that $\mathcal{S}(t,\mathbf{x},L)dL$ specifies the discrete change in the number of bubbles with the length between L and $L+dL$ due to the coalescence and break-up phenomena. As mentioned before, the mass-based interval between M and $M+dM$ can be mapped to the length-based one, L and $L+dL$. Thus, the changes in the number of bubbles due to the discrete processes in both intervals are the same – in other words $\mathcal{S}'dM = \mathcal{S}dL$. Now, the right-hand side of Eq. (3.45) can be transformed as follows:

$$\text{RHS} = \int_0^\infty \mathcal{S}'M^{k'}dM = \int_0^\infty \mathcal{S}(\frac{\pi}{6}\rho_g L^3)^{k/3}dL = (\frac{\pi}{6}\rho_g)^{k/3}\int_0^\infty \mathcal{S}L^k dL = (\frac{\pi}{6}\rho_g)^{k/3}\ \bar{\mathcal{S}}_k \tag{3.48}$$

Then, the length-based moment transport equation follows from Eqs. (3.47) and (3.48):

$$\partial_t m_k + \partial_{\mathbf{x}}\cdot(\mathbf{U}_g m_k) + \frac{k}{3}m_k\frac{1}{\rho_g}\frac{D\rho_g}{Dt} = \bar{\mathcal{S}}_k \tag{3.49}$$

3.4 CFD-PBM Codes

Apart from the numerous in-house codes reported in the literature, there are several commercial and open-source CFD codes that incorporate the PBE. Table 3.1 summarizes some available CFD-PBM codes along with their main features. Our choice of software for incorporating PBE into CFD is OpenFOAM, which is an open-source software written based on C++ programming language. The big advantage of OpenFOAM is the availability of the source code, which offers great flexibility for additions and modifications.

3.4.1 In-House Code Using OpenFOAM

As reported in Table 3.1, the OpenFOAM software offers the possibility of solving PBE through specific built-in solvers, e.g. *reactingEulerFoam*. However, in this thesis, we use our own implementation of the PBE in another built-in solver of OpenFOAM, which is developed for simulation of two-phase flows, called as *twoPhaseEulerFoam*. Figure 3.4 depicts the incorporation of the PBE into the

Table 3.1: Commercial and open-source CFD codes with the implementation of PBE

CFD code	Governing equations	Solution methods	Notes
OpenFOAM[a]	Eq. (3.1) Eq. (3.2)	CM QMOM[b] CQMOM[b] EQMOM[b]	– Multifluid approach is available – Possibility of solving several population balances – Realizable advection schemes are implemented
Ansys Fluent	Eq. (3.1)	CM QMOM DQMOM	– Multifluid approach is available
Ansys CFX	Eq. (3.1)	CM	– Multifluid approach is available – PBE is written in terms of mass-based NDF – Continuous events and nucleation are not available
StarCMM	Eq. (3.1)	CM	– Multifluid approach is available – Adaptive discretization

[a]open-source; [b]as part of the OpenQBMM project (https://www.openqbmm.org)

TFM. It should be noted that the implementation is mainly aimed to track the evolution of the bubble size distribution. In other words, the code solves the PBE written in terms of a univariate NDF, which defines the distribution of the bubbles over the bubble size as the internal coordinate. At the beginning of each time-step, the inversion algorithm is used to calculate the quadrature abscissas and weights from the moments of the previous time-step. Both PD and Chebyshev inversion algorithms are implemented. It should be noted that the Chebyshev algorithm is modified based on the 1-D adaptive quadrature technique proposed by Yuan et al. [148]. Then, the source terms due to the coalescence and break-up of bubbles are calculated by using the quadrature approximation. The next step is to solve the moment transport equations by inserting the disperse phase velocity (calculated by the TFM in the previous time step) and the source terms into Eq. (5.3). Finally, the two-way coupling is achieved by calculating the Sauter mean diameter from the moments of the NDF (that indeed represents the bubble size distribution), which is eventually used in the constitutive relations of the TFM.
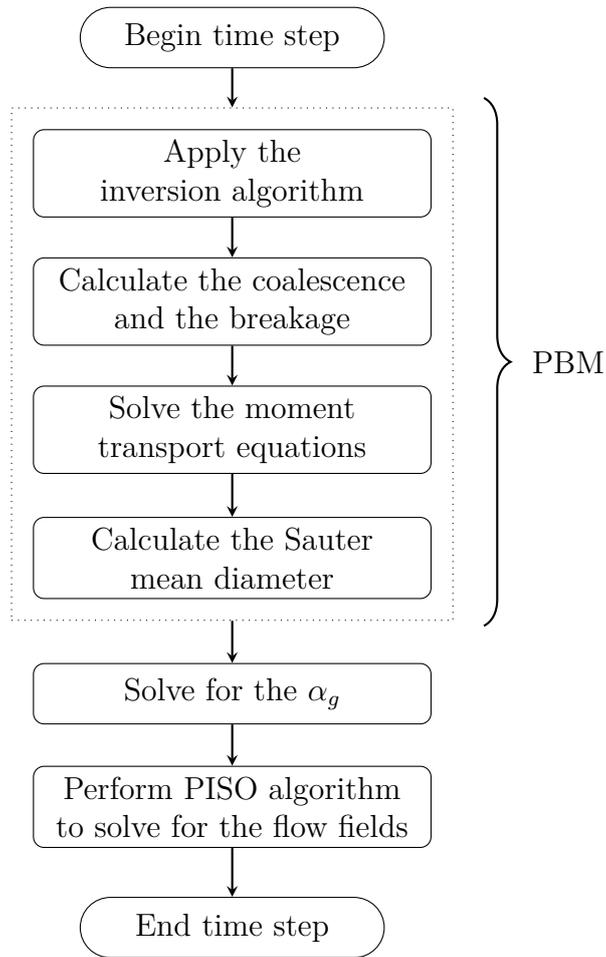
Figure 3.4: Flow diagram of the PBM implementation coupled with two-fluid solver of OpenFOAM, i.e. *twoPhaseEulerFoam*

Chapter 4

CFD Simulation of Bubbly Flows[*]

This chapter deals with the Eulerian-Eulerian CFD simulation of turbulent bubbly flows with particular attention to the interfacial forces, especially the lift and wall lubrication forces. In this regard, two set of closure relations are selected and the numerical predictions obtained by each set are compared with the experimental data of an air/water two-phase flow in an adiabatic vertical pipe [9]. It is noteworthy that these closures are employed in two prominent models recently proposed for the simulation of bubbly flows [21, 165]. To our knowledge, this is the first time that the selected closures are tested against this experimental data, characterized by a developing profile, using OpenFOAM software (v4.1). In fact, the experimental data includes the measurements of several interesting properties at different axial heights, tracking the flow development through the pipe and providing improved insight into the performance of the selected models. A sensitivity analysis on the lift coefficient is additionally performed for each test case to obtain the best agreement on the basis of the gas volume fraction predictions, which allows us to draw further conclusions on the employed closures, as well as providing insights toward future improvements.

4.1 Geometry and Operating Conditions of the Simulated Flow

The experimental setup simulated in this thesis is the TOPFLOW test facility at Helmholtz-Zentrum Dresden-Rossendorf (HZDR), shown in Figure 4.1. Moreover,

---

[*]This chapter is mainly based on the following published article:

M. Shiea, A. Buffo, E. Baglietto, D. Lucas, M. Vanni, D. L. Marchisio, "Evaluation of Hydrodynamic Closures for Bubbly Regime CFD Simulations in Developing Pipe Flow". In: *Chemical Engineering & Technology* 42 (2019), pp. 1618–1626.

the corresponding data, used here as the benchmark, is taken from the report by Beyer and co-workers [9].
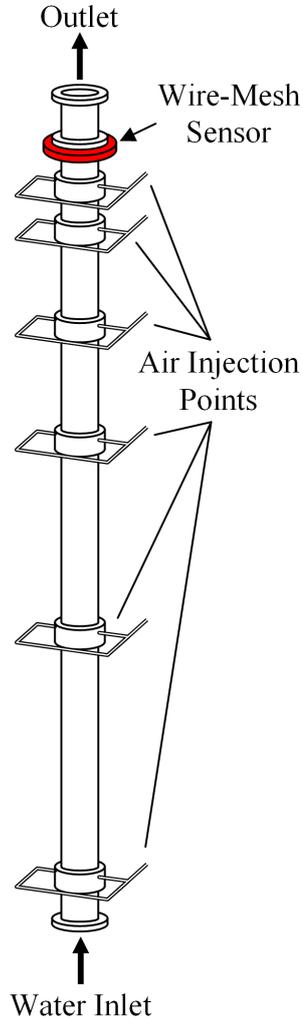

Figure 4.1: Schematic diagram of the TOPFLOW test facility

The experimental rig consists of a vertical pipe with inner diameter of 0.1953 m and height of 8 m, in which water and air bubbles flow upward concurrently. The pipe operates at constant temperature of 30°C. The radial profiles of the gas volume fraction, gas velocity and bubble size distribution were measured via a wire mesh sensor located at the top of the pipe. The gas phase, air, is injected through one of the injection rings located at the specified distances below the measuring sensor, see Table 4.1. The outlet pressure is adjusted in such a way to have the same pressure of 2.5 bars at the active injection ring. Thus, it can be thought of as fixing the position of the injection ring and moving the measuring sensor. This

technique allows us to study the development of the flow in the axial direction. Moreover, each injection ring consists of 72 orifices with the diameter of 1 mm, equally distributed around the pipe to mimic the bubble generation at the solid wall with a given rate.

The measurements were conducted by a two-level low-temperature wire-mesh sensor with a resolution of 64x64. It belongs to the intrusive measuring techniques, and is based on the difference of electrical conductivity between water (slightly conductive) and air (insulator). More details on the design of the measuring sensor is available in the reference [9]. Moreover, general information on wire-mesh sensors and their advantages and disadvantages can be found in the literature [166–169]. Here, it suffices to mention that several uncertainties exist about data obtained by wire-mesh sensors due to different sources such as the calculation of the void fraction from the conductance measurements, the effect of the (intrusive) sensor on the flow field and the physical dimension of the sensor [169]. This fact is also true for the available experimental data used in this thesis, and should be borne in mind when comparing the simulation results with the experiments.

Table 4.1: The distance of the air injection rings from the wire-mesh sensor

Distance from the sensor (m)	0.22	0.34	0.49	0.61	1.44	1.55	2.48	2.6	4.42	4.53
Height to diameter ratio	1.1	1.7	2.5	3.1	7.4	7.9	12.7	13.3	22.6	23.2

Measurements related to six different combinations of liquid and gas superficial velocities are selected for the purpose of validation. All the six operating conditions are in bubbly flow regime. The corresponding air and water inlet flow rates along with the average bubble sizes are reported in Table 4.2. The simulations are conducted separately in the first "nominally" 2-meter and 5-meter portions of the pipe, therefore, two average bubble sizes are evaluated using the corresponding experimental data as reported in Table 4.2. Here, the nominal 2-meter and 5-meter columns are long enough to compare the simulation predictions with the available experimental data up to the distance 1.55 (m) and 4.53 (m) between the air injection point and the wire-mesh sensor, respectively. The calculation of the average bubble diameter from the measured experimental data is described in Appendix C.

For the above range of bubble sizes (4.05 to 9.11 mm), the terminal velocity of bubbles in partially-contaminated water at 30°C varies between 0.236 to 0.246 m/s, obtained by making a balance between the buoyancy and drag forces and by using Tomiyama's correlation for the drag coefficient, Eq. (2.13). Thus, the bubble Reynolds number calculated by using the terminal velocity changes between 1191 to 2796 for the reported range of bubble sizes.

Table 4.2: Experimental conditions of the simulated test cases; the case number corresponds to the classification by Beyer et al. [9]

Case No.	Superficial liq. velocity (m/s)	Superficial gas velocity (m/s)	d_b^{ave} (mm) (2-meter)	d_b^{ave} (mm) (5-meter)	Re_l
008	1.017	0.0025	4.05	4.24	2.48×10^5
042	1.611	0.0096	4.25	4.36	3.93×10^5
040	0.641	0.0096	4.93	5.01	1.56×10^5
028	0.405	0.0062	5.22	5.34	9.88×10^4
063	1.017	0.0235	6.50	6.46	2.48×10^5
072	0.405	0.0368	9.11	7.65	9.88×10^4

It is noteworthy that the average bubble size of the selected test cases remains virtually constant along the length of the pipe except for the case 072, which experiences a noticeable drop at the beginning of the flow up to the height of 1.55 m, see Figure 4.2.

Last, Beyer and co-workers pointed out that the mass flow rates of the gas phase calculated from integrating the measured profiles show an increase of about 20% in comparison to the more precise values obtained from the flow controller [9]. Therefore, in a recent work by the group at HZDR, all radial profiles of the air volume fraction were divided by a factor of 1.2 in order to compensate for that increase [165]. The same correction is applied here to all the radial profiles of the air volume fraction reported in the subsequent figures.

4.2 Simulation Setup

4.2.1 Solver Details and Settings

The adopted simulation method is the Eulerian-Eulerian two-fluid model, described in Chapter 2. Moreover, although the system under study is poly-disperse by nature, the investigation of the interfacial forces (aimed by this chapter) is conducted by assuming mono-disperse condition, i.e. imposing a fixed bubble size obtained from the experimental data reported in Table 4.2, which is the most common preliminary assumption used for studying practical industrial-scale problems. Furthermore, the average bubble size does change negligibly along the axial direction for all the selected test cases, except for the test case 072, see Figure 4.2. The polydispersity and change of the average bubble size is addressed in Chapter 6 by
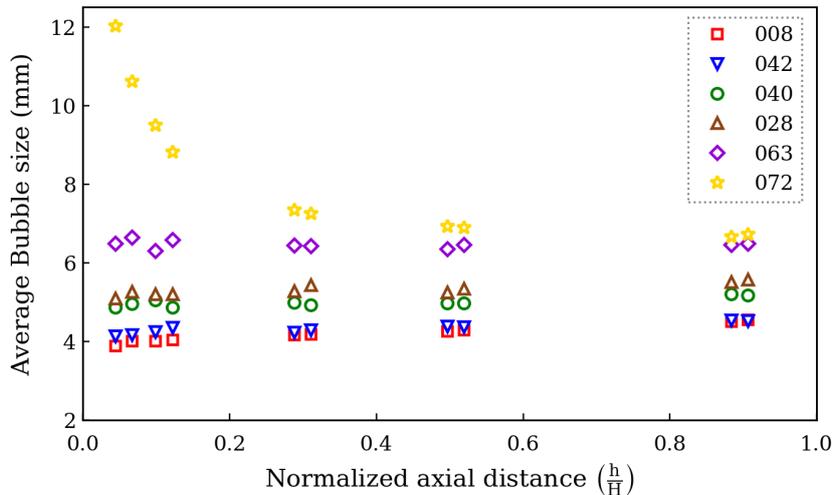
Figure 4.2: Axial change of the average bubble size for the selected test cases ($H = 5$ m)

coupling the CFD with the PBM.

The implementation of the two-fluid model in the OpenFOAM CFD software v4.1, *twoPhaseEulerFoam*, is used to solve the corresponding governing equations. This solver is written based on the PIMPLE algorithm, which is an iterative implicit method based on the PISO (pressure-implicit with splitting of operators) and SIMPLE (semi-implicit method for pressure linked equations) algorithms. The equations to be solved include the balance equation for the gas volume fraction (mass conservation) and two momentum balance equations for both gas and liquid phases. In each time step, first the balance equation for the gas volume fraction is solved using the field values of the previous time-step/PIMPLE-iteration. The solver uses an explicit method developed for the convective-only transport equations, called Multidimensional Universal Limiter for Explicit Solution (MULES), to solve the balance equation for the gas volume fraction. It serves to keep the solution of the gas volume fraction bounded. Next, the liquid volume fraction is calculated using the fact that the summation of the phase volume fractions is equal to one, $\alpha_g + \alpha_l = 1$. Then, the momentum balance equations are written using the velocities of the previous time-step/Pimple-iteration, which are subsequently used to write a Poisson equation for the pressure. The Poisson equation indeed forces the mass conservation. It is noteworthy that OpenFOAM uses the Rhie and Chow interpolation [170] to compute the pressure gradient in the direction normal to the faces, which is needed for the solution of the Poisson equation. Once the pressure is calculated, the velocities can be corrected accordingly. The iterations will be continued until a specified convergence criterion is achieved in each time-step or the maximum correction loops are performed. Those numerical schemes and settings that are different with respect to the default recommendations of the OpenFOAM

software are reported in Table 4.3.

Table 4.3: Discretization schemes and solver settings

Discretization schemes		solver settings	
Gradient Scheme	Multidirectional Cell-limited Least Squares	No. of updates to all equations in each time step (*nOuterCorrector*)	10
Divergence Scheme	LimitedLinear 1.0 for air volume fraction	No. of solving pressure equation and correcting momentum (*nCorrector*)	3
Laplacian Scheme	Linear Corrected	No. of updates to the explicit non-orthogonal correction (*nNonOrthogonalCorrector*)	3
snGrad Scheme	Corrected	No. of loops for the solution of the air volume fraction equation (*nAlphaCorr* and *nAlphaSubCycles*)	2 and 3

It is worth explaining that the limited gradient scheme is used to cope with sharp profiles that may occur in some test cases, particularly near the wall. Gradient limiters may cause the numerical diffusion, however, contour plots of some preliminary simulations showed that it happens only in the circumferential direction in this specific system. Hence the average radial profiles remain virtually unchanged. Moreover, the divergence scheme *LimitedLinear* is used for the discretization of the convective term of all the solved balance equations. It is a 2$^{\text{nd}}$-order TVD (Total Variation Diminishing) scheme. Furthermore, the non-orthogonality of the grid is compensated by adding explicit corrections to the interpolated face values required by the discretization schemes. Since the corrections are explicit (calculated based on the values of the previous iteration), the pressure equation is solved more than once in each PISO loop to update these corrections. The number of corrections is indicated as *nNonOrthogonalCorrector* in Table 4.3. Moreover, *nCorrector* reported in Table 4.3 is the number of PISO loops, which update the velocities after solving the pressure equation in each PIMPLE loop. Finally, PIMPLE loops update the velocity equations using the values of the previous timestep or PIMPLE iteration. The number of PIMPLE loops is specified as *nOuterCorrector* in Table 4.3.

Last, all the interfacial forces described in Chapter 2 are available in *twoPhaseEulerFoam* solver, except for Sugrue's correlation and Lubchenko's approach, which are implemented by modifying the original solver.

4.2.2 Mesh Design

To speed-up the model assessment, two different configurations are selected as the simulation domain, with the pipe heights of 1.806 m (137088 cells) and 5.206 m (365568 cells), corresponding to the first nominally 2-meter portion and the first nominally 5-meter portion of the experimental setup. The idea is to use the first geometry to tune the lift coefficient (when necessary), whereas the second geometry is employed to assess the agreement with experiments, without any further adjustment. The selected domains are discretized by using the multiblock structured o-grid type mesh shown in Figure 4.3.

<center>(a)   (b)   (c)</center>
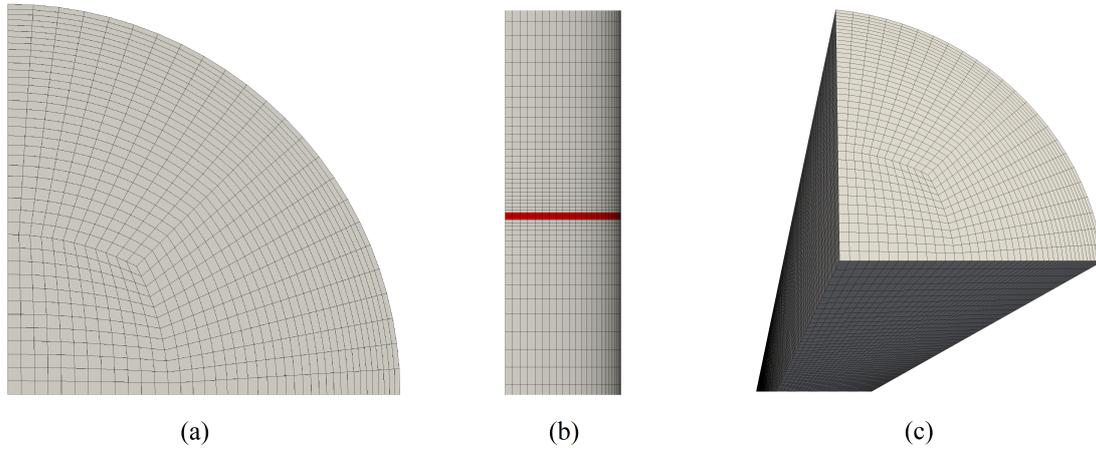
Figure 4.3: The designed mesh for the purpose of simulation. a) cross-section of the mesh; b) the injection boundary; c) three-dimensional view of the mesh.

The mesh size is selected according to a grid independence study considering several factors, i.e. achieving grid independent results, reasonable computational time, the capability of capturing the profile near the wall and avoiding the viscous sublayer close to the wall. Some details on the grid independence study can be found in Appendix D. The symmetry of the system allows us to simulate a quarter of the pipe, resulting in a significant reduction in the number of computational cells. Moreover, the injection ring is modelled as a circular shell of 6 mm height around the wall at a distance of 20 cm from the bottom of the pipe, in order to mimic the behavior of the real system.

4.2.3 Boundary Conditions

The adopted boundary conditions are similar to those normally used for single-phase flow: imposed liquid velocity is specified at the bottom of the domain, while constant gas velocity is used for the side injection boundary, a constant pressure conditions is used at the outlet and symmetry boundary conditions applied on the

symmetry planes. The imposed liquid velocity at the bottom of the pipe is defined as a fully developed turbulent radial profile. It should be noted that the liquid velocity has no-slip condition on the wall, whereas air is allowed to slip over the wall. Furthermore, the standard single-phase wall functions are used to estimate the near-wall behavior of the non-resolved velocity profile.

4.2.4   Investigated models for Interfacial Forces

This section explains the set of models selected for the simulation of the TOPFLOW test facility. Before introducing the selected models, it is enlightening to perform a study on the role of the interfacial forces on the predictions. Figure 4.4 shows the predicted results obtained from the simulation of the 2-meter configuration operating at experimental condition 028. The predictions include the radial profiles of the air volume fraction and phase velocities at two sections, one close to the injection ring (at a distance of 0.49 m) and the other far from the injection ring (at a distance of 1.55 m). The simulations are done without emphasizing on the choice of a particular relation to model each force. Moreover, the contribution of virtual mass is assumed negligible in this thesis, since the effect of this force is significant in the case of strongly accelerating flows, whereas, the pipe flow under study is stationary and the phase velocities change gradually in the axial direction.

The drag force, modelled by using Tomiyama's correlation (Eq. (2.13)) for the drag coefficient, is included in all the simulations, and is required to balance the buoyancy since it is the only force acting in the vertical direction in the system under study. As expected, the drag force alone is not able to reproduce the spread of the gas phase in the radial direction. Bubbles are injected at the wall, and a radial force is necessary to address the redistribution of bubbles. Not surprisingly, the predicted gas phase velocities are also incorrect, as the accumulation of the gas phase near the wall drives the high gas peak in the first computational cell.

The lift force is described by using a constant coefficient with the Shaver and Podowski damping factor (Eq. (2.19)). In the current system, the lift force acts radially, but its direction (outward or inward) depends mostly on the bubble size and liquid velocity. Here, for this experimental condition (028), the lift coefficient is set to 0.03, consistently with the value reported by Shaver and Podowski [32]. While in the general case the lift force can have relevant effect on the gas radial distribution, in the present case, its role is negligible due to the small value of the lift coefficient, as apparent by comparing the predictions obtained by employing only the drag force with those obtained by employing both the drag and lift forces, yellow and green lines of Figure 4.4 respectively. Nevertheless, the small effect of the lift force under this condition enables us to identify better the role of the turbulent dispersion and the wall lubrication forces, as explained in the following.

As mentioned in Chapter 2, a force is indeed required to push the gas away from the wall. The turbulent dispersion force, expressed by Burns' model (Eq. (2.24)),
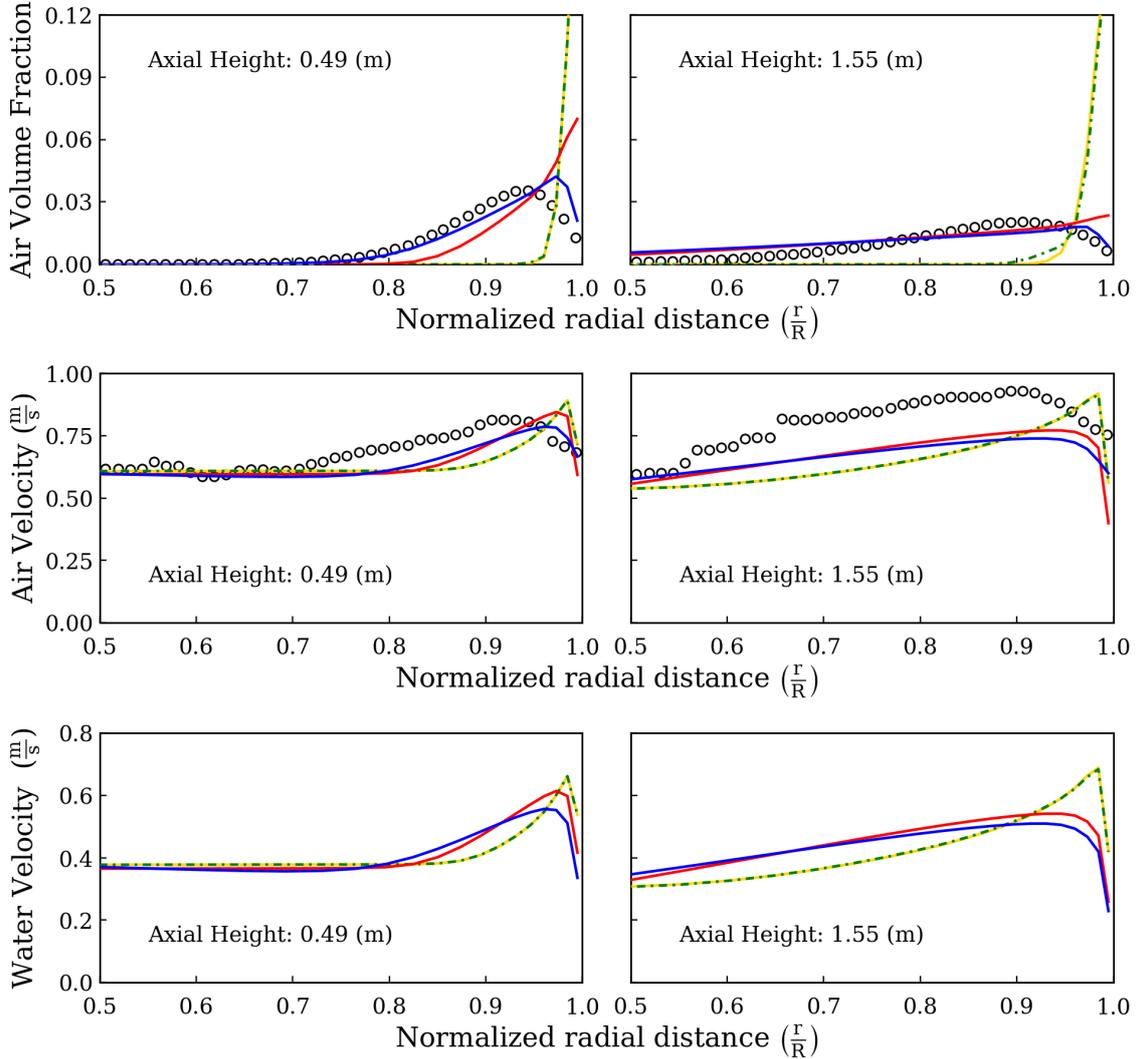
Figure 4.4: Comparison of the experimental data (hollow markers) with predictions obtained by including different combination of forces in the simulation of experimental condition 028: 1- only drag force (yellow solid line); 2- drag and lift forces (green dot-dash line); 3- drag, lift and turbulent dispersion forces (red solid line); 4- drag, lift, turbulent dispersion and wall lubrication forces (blue solid line).

works against the gradient of the void fraction distribution, and therefore helps in spreading the gas phase considerably (continuous red line in Figure 4.4). The discrepancy between the measured and predicted results at the lower sections suggests that the turbulent dispersion contribution is not sufficient to describe the spread of the gas phase in regions near the injection ring, and a further contribution to drive the gas away from the wall is required. It is noteworthy that the predicted radial profiles of the air velocity are also improved by the addition of the turbulent

dispersion force as a consequence of the improved predictions for the gas volume fraction.

However, the results obtained by the different combinations of drag, lift and turbulent dispersion forces indicate that these forces alone are not capable of describing the peak near the wall. Only adding the wall lubrication force, here by employing Lubchenko's approach (Eq. (2.27)), results in the appearance of the near-wall-peak in the radial profiles of the gas volume fraction (continuous blue line in Figure 4.4), in agreement with the experimental observation. It is, therefore, necessary to include this contribution to describe properly the radial spread of the gas phase.

After studying the effect of the interfacial forces, four set of models are considered to be investigated, as summarized in Table 4.4. In Model I, the interfacial forces are estimated using the closures relations suggested by Rzehak and Krepper [165] for the simulation of bubbly flows. Model II adopts the same closures of Model I, with the exception of the lift coefficient formulation, which is optimized for each experimental condition to produce the best possible agreement between the simulation predictions in the 2-meter column and the experimental data. Model III is inspired from the model recently proposed by Sugrue [21]. Again, in Model IV, closures reproduce those of Model III except for the optimized lift coefficient, which is varied for each experimental condition to have the simulation results in the 2-meter pipe match the experimental data.

Table 4.4: Selected set of models for the purpose of simulation

Model No.	Drag coefficient	Lift coefficient	Turbulent dispersion force	Wall lubrication force
I	Tomiyama [a]	Eq. (2.16) by Tomiyama	Burns [b]	Eq. (2.26) by Hosokawa
II	Tomiyama [a]	Constant optimized coefficient	Burns [b]	Eq. (2.26) by Hosokawa
III	Tomiyama [a]	Eq. (2.20) by Sugrue with damping factor by Shaver and Podowski [c]	Burns [b]	Eq. (2.27) by Lubchenko
IV	Tomiyama [a]	Constant optimized coefficient with damping factor by Shaver and Podowski [c]	Burns [b]	Eq. (2.27) by Lubchenko

[a] Eq. (2.13); [b] Eq. (2.24); [c] Eq. (2.19)

The value of the lift coefficients used in Models II and IV are optimized for each experimental condition by simulating the 2-meter pipe and attempting to achieve the best agreement with the measured radial profile of the air volume fraction. It should be clarified that the purpose of this optimization is not to quantify the lift coefficient since there exist several uncertainties concerning other aspects of the simulation, e.g. turbulence modelling. These uncertainties cannot be resolved unless more comprehensive experimental data including the liquid velocity and turbulence parameters is gathered. Nevertheless, the optimization results illuminate several issues such as the effect of the lift coefficient sign, the deficiency of the evaluated correlations and the importance of studying the lift coefficient under developing conditions. The optimization is done by minimizing the following error function:

$$
\text{Relative Error} = \frac{\displaystyle\sum_i \left(\frac{\displaystyle\sum_j \left| \alpha_j^{\text{sim.}} - \alpha_j^{\text{exp.}} \right| \left(R_j^2 - R_{j-1}^2 \right)}{\displaystyle\sum_j \alpha_j^{\text{exp.}} \left(R_j^2 - R_{j-1}^2 \right)} \right)\Bigg|_{\text{at } L_i} \cdot (L_i - L_{i-1})}{\displaystyle\sum_i (L_i - L_{i-1})} \tag{4.1}
$$

In the above expression, R_j and L_i denote, respectively, the radial and axial coordinates of the locations at which local experimental data is available. In addition, $\alpha_j^{\text{exp.}}$ and $\alpha_j^{\text{sim.}}$ are the experimental and predicted local air volume fraction at R_j respectively.

The same models are then tested on the 5-meter pipe and their capability to reproduce the experimental observations is assessed.

4.2.5 Turbulence Modelling

In this study, only continuous phase turbulence is considered in the simulations since the density of the disperse phase is much smaller than that of the continuous phase. The RANS approach is adopted in this thesis, along with the Boussinesq approximation. The turbulent viscosity is calculated by using the standard $k-\varepsilon$ model, scaled by the liquid phase volume fraction. A complete description of the $k-\varepsilon$ model can be found in the literature [26].

It should be noted that the bubble-induced turbulence is not included in this thesis to avoid introducing further uncertainties. Although bubbles influence the structure of the turbulence in the liquid phase [27-30], many ambiguities surround the application of the available approaches for considering the bubble-induced turbulence. For instance, in the context of two-equation models such as $k-\varepsilon$ model, the most common practice adds source terms to the transport equations of k and ε [4, 31]. However, no consensus on the implementation of this approach is achieved yet, particularly on the choice of the time scale to estimate the ε source term [32].

4.3 Results and Discussion

As explained before, the simulations are conducted in two configurations with the nominal heights of 2-meter and 5-meter corresponding to the first two meters and the first five meters of the pipe, respectively. In the following, the results obtained from the simulation of each configuration are reported in two separate parts. It should be noted that the "axial height" shown on each plot indicates the distance of the sampled section from the air injection point. Moreover, for some experimental conditions with very low gas content in the center of the pipe, the "Normalized Radial Distance" axis starts from a value higher than zero to increase the resolution of the graphs near the wall.

4.3.1 Simulation of the 2-meter Configuration

The simulations of the 2-meter pipe, which are much faster to be carried out, aim at finding an optimum lift coefficient for Models II and IV. These Models differ in the expression employed for the wall lubrication force, see Table 4.4. It is worth reiterating that Model IV uses Lubchenko's approach for modelling the wall lubrication force, which requires a damping factor being applied to the lift coefficient in regions close to the wall. Eventually, the optimum lift coefficients are employed in Models II and IV to simulate the 5-meter configuration and to analyze the corresponding predictions. In the following, two figures are reported for each experimental condition, each obtained by employing one of the two wall lubrication models used in Models II and IV. Finally, the lift coefficients to be used in Model II and IV are plotted along with those estimated by the correlations developed by Tomiyama and Sugrue, see Figure 4.17.

Experimental Condition 008

Figures 4.5 and 4.6 show the radial profile of the air volume fraction obtained by using, respectively, Hosokawa's correlation and Lubchenko's approach for the wall lubrication force under experimental condition 008. As can be seen in these figures, the lift coefficient can be varied to achieve a satisfactory agreement with the experimental data. For this experimental condition, the radial profiles of liquid and air velocity are monotonically decreasing from the column center to the wall, see Figures A.1 and 4.18. Thus, employing a positive lift coefficient yields to lift forces that push the bubbles towards the wall. At the same time, the wall lubrication force acts in the reverse direction only in the region close to the wall. As a result, a wall-peaked profile is predicted, which matches the experimental data. As can be seen in Figures 4.5 and 4.6, the location of the peak predicted by both wall lubrication models is in good agreement with the experimental data for the attempted values of the lift coefficient. Then, the spread of the gas phase in the

radial direction can match the experiments by tuning the lift coefficient. Considering all six sections in the first two meters of the pipe, the lift coefficients that reproduces best the experimental data are 0.15 and 0.19 for the cases of employing Hosokawa's correlation and Lubchenko's approach, respectively.
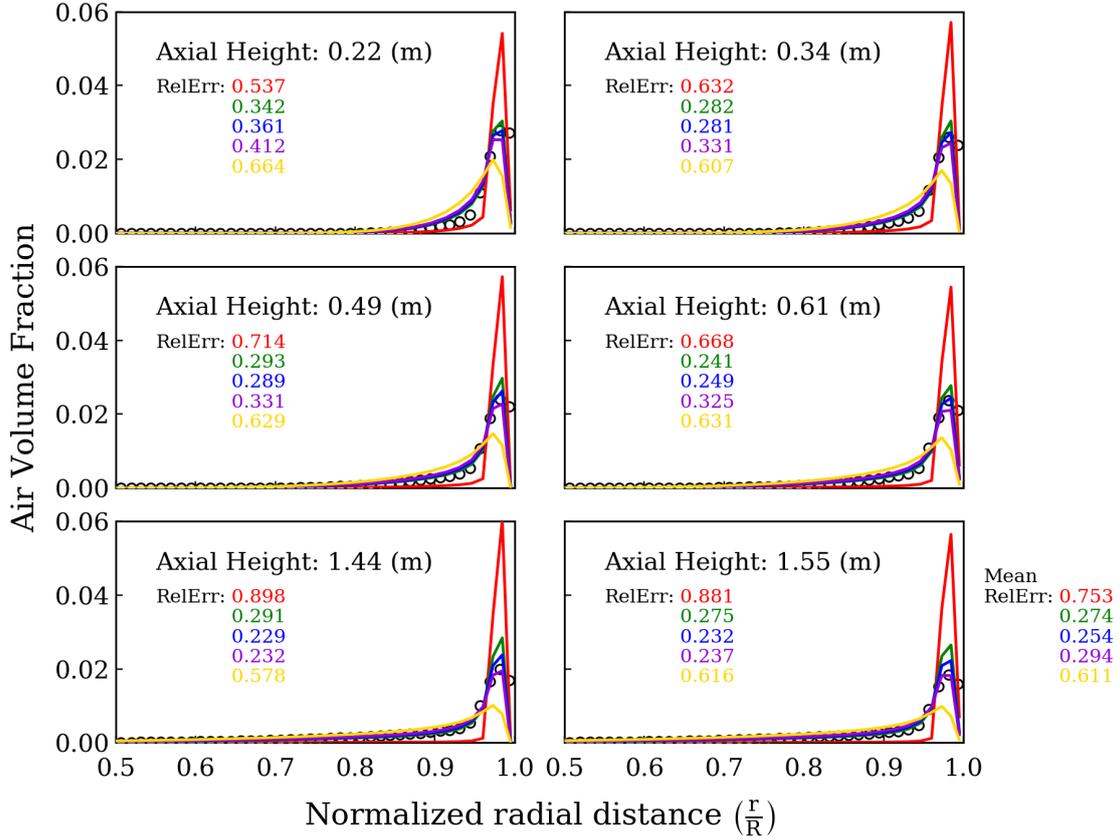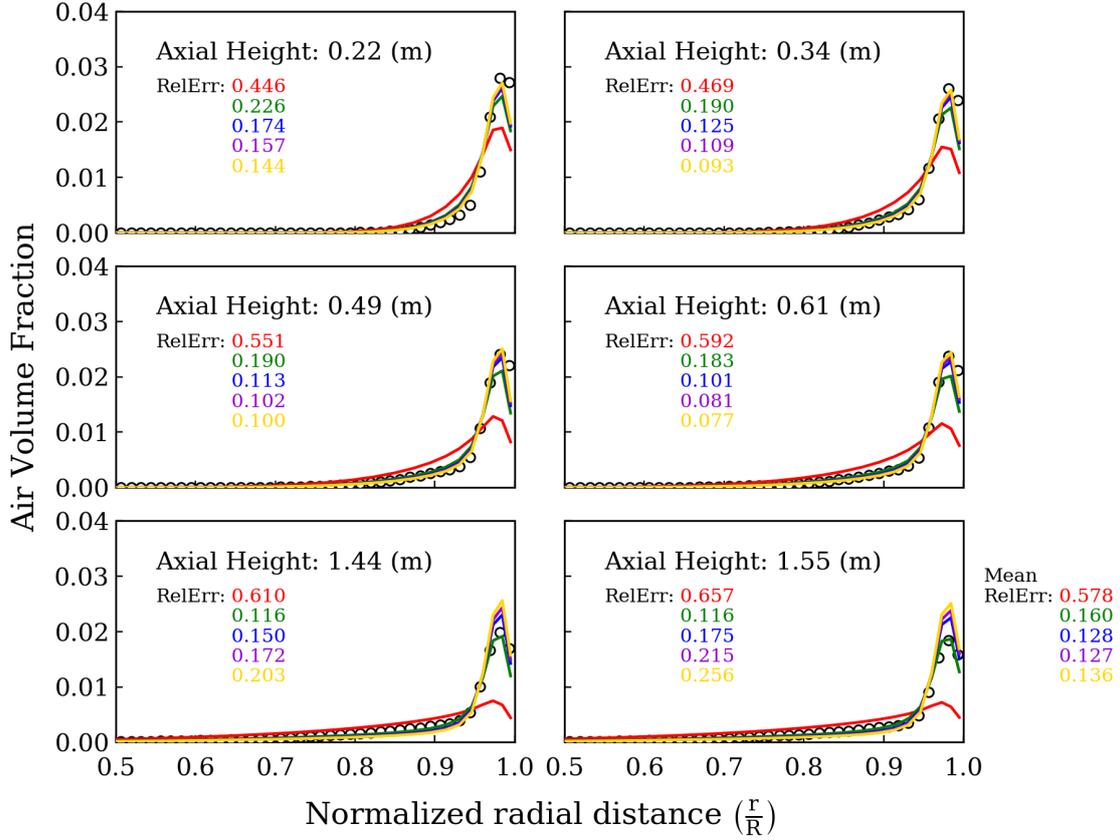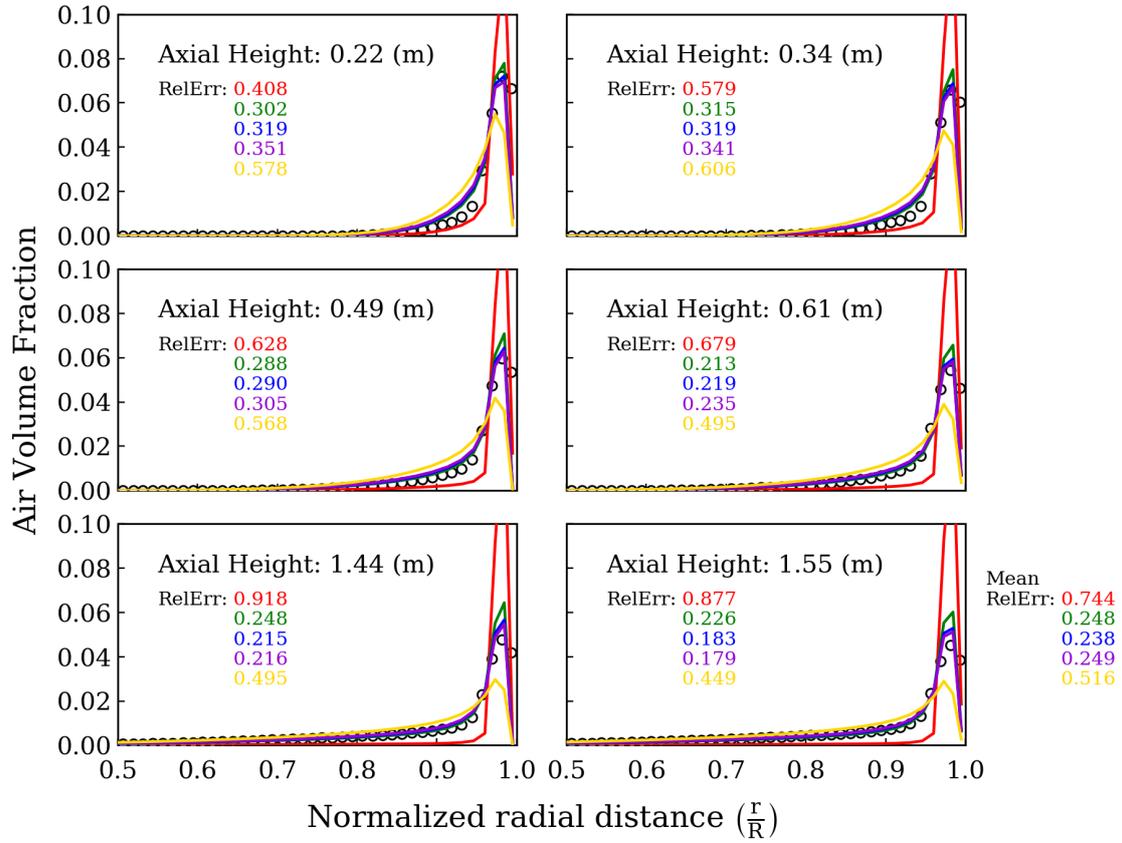

Figure 4.5: The radial profile of the air volume fraction obtained for experimental condition 008 by employing Hosokawa's correlation for the wall lubrication force and different lift coefficients: C_L by Tomiyama (red curve); $C_L = 0.16$ (green curve); $C_L = 0.15$ (blue curve); $C_L = 0.14$ (violet curve); $C_L = 0.1$ (yellow curve).
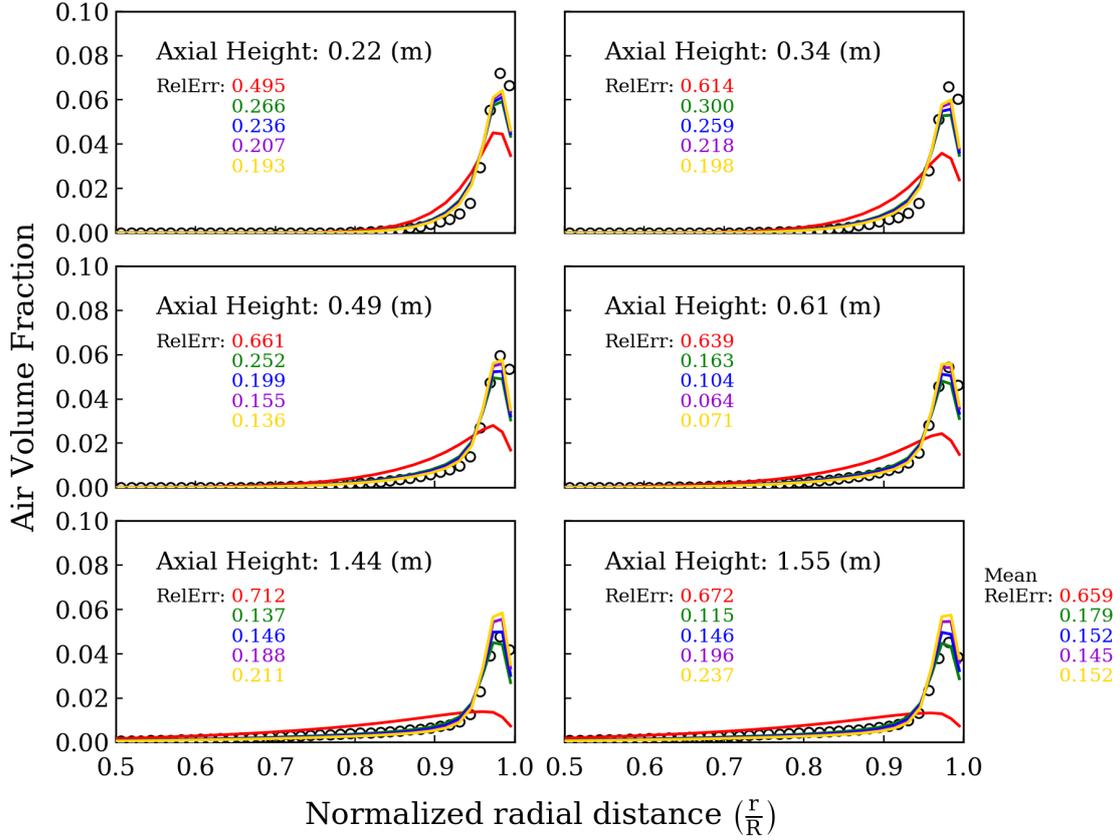
Figure 4.6: The radial profile of the air volume fraction obtained for experimental condition 008 by employing Lubchenko's approach for the wall lubrication force and different lift coefficients: C_L by Sugrue (red curve); $C_L = 0.15$ (green curve); $C_L = 0.18$ (blue curve); $C_L = 0.19$ (violet curve); $C_L = 0.2$ (yellow curve).

Experimental Condition 042

For this experimental condition, the same argument presented for experimental condition 008 can be put forward, as illustrated by Figures 4.7 and 4.8. Eventually, the optimum lift coefficients for this experimental condition are 0.14 and 0.19 for the wall lubrication models by Hosokawa and Lubchenko, respectively.

It is noteworthy that this experimental condition has also monotonically decreasing velocity profile for both the liquid and air phases (same as experimental condition 008), as shown in Figures A.3 and 4.19. Moreover, both of these experimental conditions have smaller average bubble sizes than the other investigated experimental conditions, see Table 4.2.
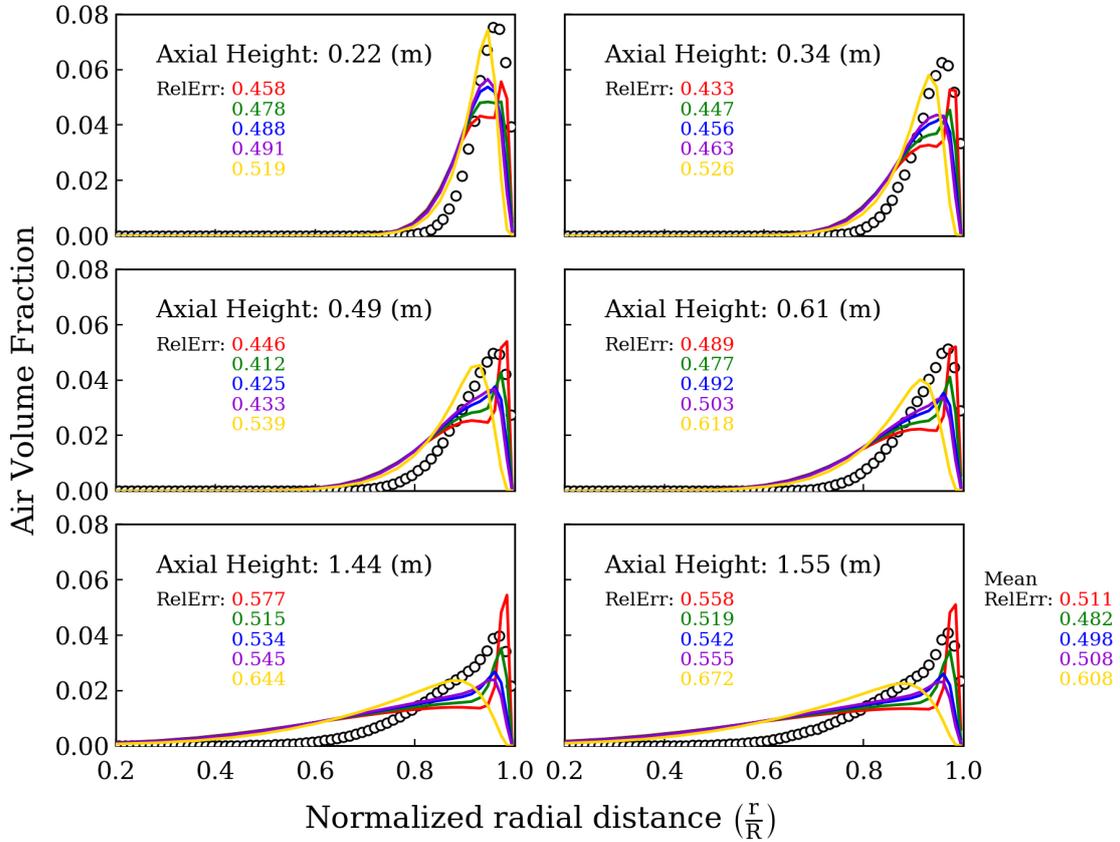
Figure 4.7: The radial profile of the air volume fraction obtained for experimental condition 042 by employing Hosokawa's correlation for the wall lubrication force and different lift coefficients: C_L by Tomiyama (red curve); $C_L = 0.15$ (green curve); $C_L = 0.14$ (blue curve); $C_L = 0.13$ (violet curve); $C_L = 0.1$ (yellow curve).

Figure 4.8: The radial profile of the air volume fraction obtained for experimental condition 042 by employing Lubchenko's approach for the wall lubrication force and different lift coefficients: C_L by Sugrue (red curve); $C_L = 0.15$ (green curve); $C_L = 0.17$ (blue curve); $C_L = 0.19$ (violet curve); $C_L = 0.2$ (yellow curve).

Experimental Condition 040

Figure 4.9 shows the effect of changing the lift coefficient on the radial profiles of the air volume fraction for experimental condition 040 in the case of employing Hosokawa's correlation to calculate the wall lubrication force. In this experimental condition, the liquid and air velocity profiles have a peak near the wall, as can be seen in Figures A.5 and 4.20. Therefore, the lift force has different sign at the different sides of the peak of the liquid velocity profile. In the case of using a positive lift coefficient, the lift force pushes bubbles against the wall at the right side of the peak of the liquid velocity profile, while it has a reverse effect at the other side of the peak. The profiles obtained by using the positive lift coefficients in Figure 4.9, particularly the red and green ones, show how the interaction of the lift and wall lubrication forces causes a peak to appear in the profile of the air volume fraction. On the contrary, a negative lift coefficient results in a lift

force that pushes the bubbles towards the peak of liquid velocity profile regardless of the bubble location. The yellow profile in Figure 4.9 shows that the lift force (calculated with the negative coefficient) and the wall lubrication force together push the bubbles from the wall at the right side of the peak of liquid velocity profile. At the left side of the peak of the liquid velocity profile, the lift force (calculated with the negative coefficient) pushes the bubbles towards the peak of the liquid velocity profile. Consequently, the peak of the air volume fraction profile coincides with the one of the liquid velocity profile, however, the location of the peak is not in agreement with the experiments. The optimum lift coefficient obtained for this experimental condition is 0.14, if the wall lubrication force is modelled by Hosokawa's correlation.

Figure 4.9: The radial profile of the air volume fraction obtained for experimental condition 040 by employing Hosokawa's correlation for the wall lubrication force and different lift coefficients: C_L by Tomiyama (red curve); $C_L = 0.14$ (green curve); $C_L = 0.1$ (blue curve); $C_L = 0.08$ (violet curve); $C_L = -0.05$ (yellow curve).

The above argument is also valid when Lubchenko's approach is employed to model the wall lubrication force, as can be seen in Figure 4.10. The predictions

obtained by employing Lubchenko's approach does not result in zero gas volume fraction close to the wall, which is an advantage over Hosokawa's model. Moreover, Lubchenko's approach tends to predict the peak of the air volume fraction profile at the radius of the average bubble diameter, which is in agreement with the measured data for this experimental condition. The optimum lift coefficient to be used with Lubchenko's approach for experimental condition 040 is -0.015.
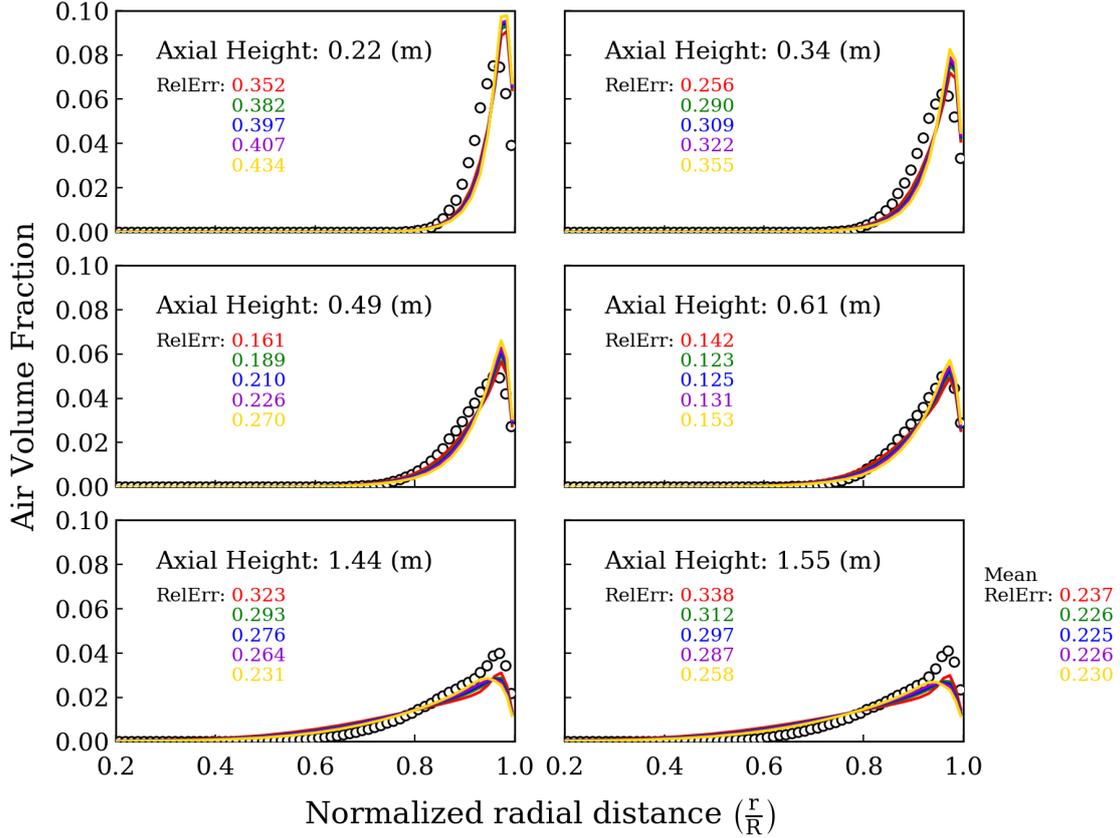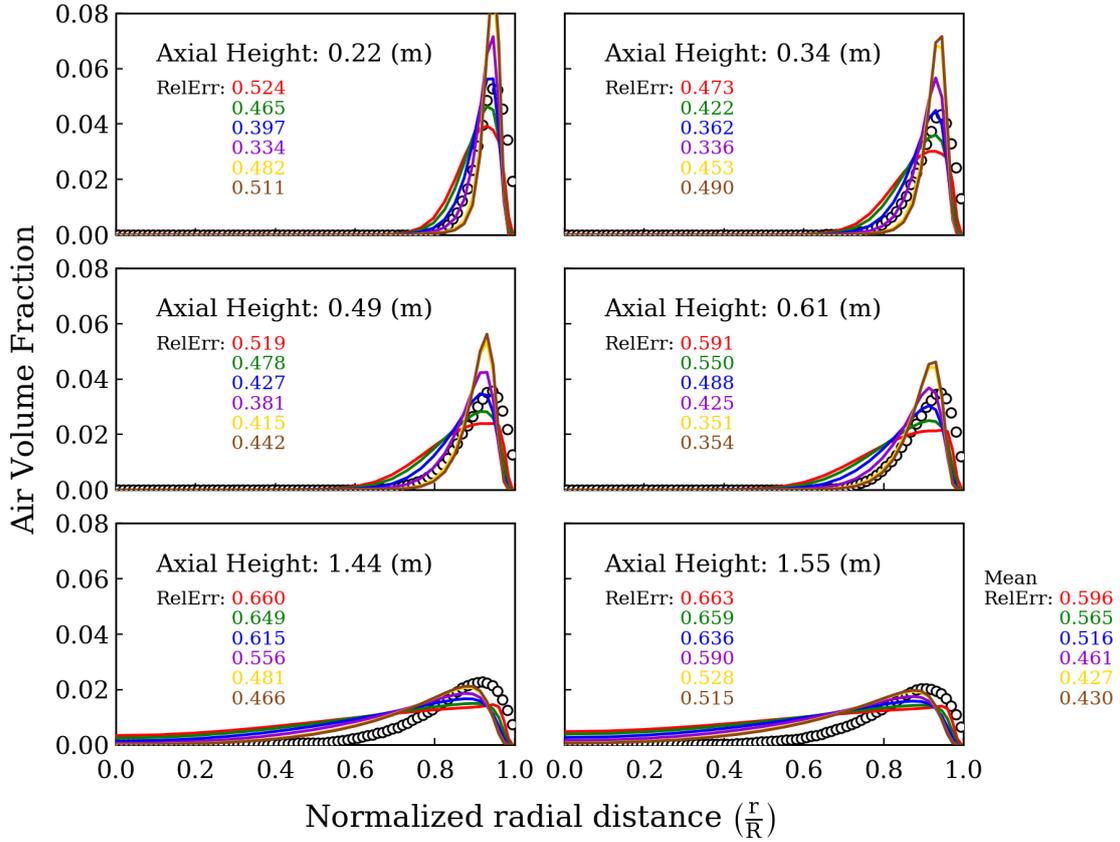

Figure 4.10: The radial profile of the air volume fraction obtained for experimental condition 040 by employing Lubchenko's approach for the wall lubrication force and different lift coefficients: C_L by Sugrue (red curve); $C_L = 0$ (green curve); $C_L = -0.015$ (blue curve); $C_L = -0.025$ (violet curve); $C_L = -0.05$ (yellow curve).

Experimental Condition 028

Likewise, in this experimental condition, the liquid velocity profile has a peak near the wall, as can be seen from Figure A.7. Therefore, the direction of the lift force depends on the position of the bubble with respect to this peak. Particularly, when a negative lift coefficient is used, the gas phase is pushed toward the peak of the liquid velocity profile from both sides of this peak. Figure 4.11 shows that the

larger is the absolute value of the negative lift coefficient, the more the gas phase is squeezed to cause a higher peak in the air volume fraction profile. Considering the wall lubrication force, the profiles in Figure 4.11 are obtained by employing Hosokawa's correlation and, as mentioned previously, they suffer from the free–of–gas zone near the wall, particularly in the case of using negative lift coefficients. The reason is that, in such cases, both the lift and wall lubrication forces push the gas phase from the wall and this situation worsens by using negative coefficients of larger absolute values. Nevertheless, in this experimental condition, the optimum lift coefficient to be used with Hosokawa's wall lubrication force is found to be -0.25, which can be considered as a very large negative value. It is noteworthy that with this lift coefficient, the free–of–gas zone near the wall is unacceptably wide.

Figure 4.11: The radial profile of the air volume fraction obtained for experimental condition 028 by employing Hosokawa's correlation for the wall force and different lift coefficients: C_L by Tomiyama (red curve); $C_L = 0.05$ (green curve); $C_L = -0.05$ (blue curve); $C_L = -0.15$ (violet curve); $C_L = -0.25$ (yellow curve); $C_L = -0.27$ (brown curve).

In the case of employing Lubchenko's approach, the air volume fraction profiles shown in Figure 4.12 reflect a similar trend as the lift coefficient changes, especially

when it has negative value. However, the change in the profiles near the wall are very small, which can be attributed to the damping factor applied to the lift force near the wall (by using the model by Shaver and Podowski).
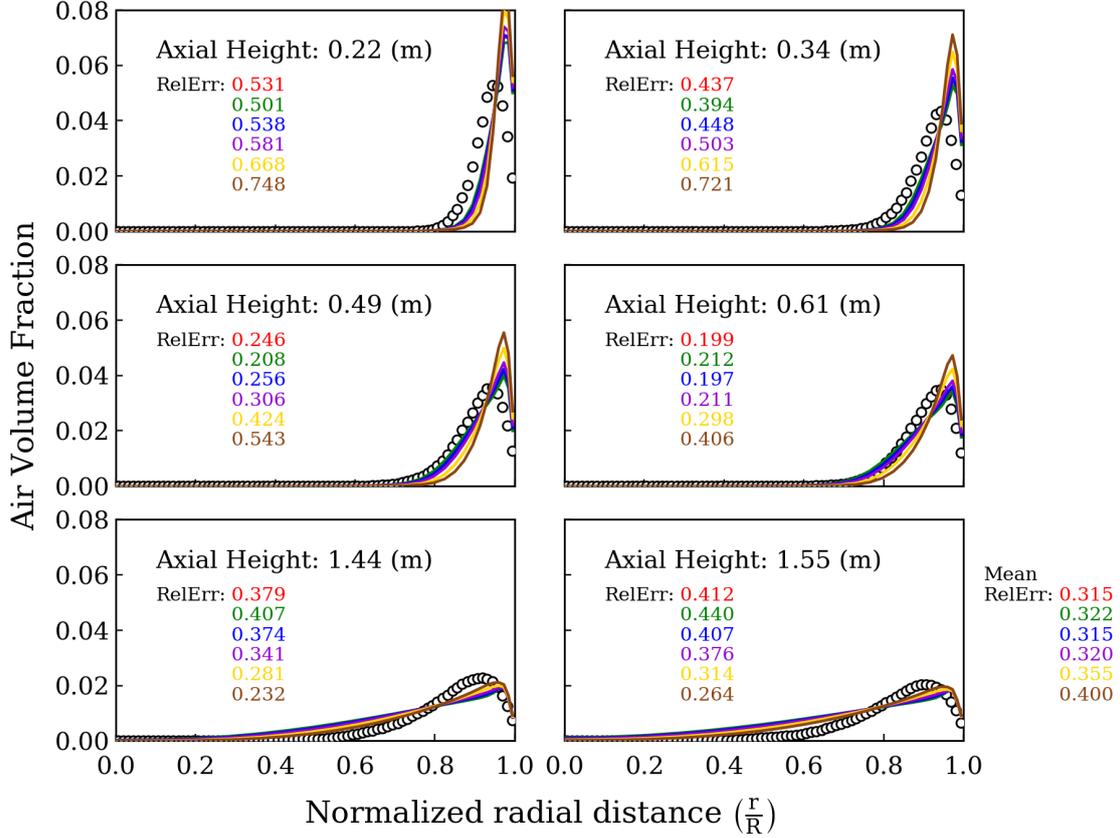

Figure 4.12: The radial profile of the air volume fraction obtained for experimental condition 028 by employing Lubchenko's approach for the wall force and different lift coefficients: C_L by Sugrue (red curve); $C_L = 0.05$ (green curve); $C_L = 0.025$ (blue curve); $C_L = 0$ (violet curve); $C_L = -0.05$ (yellow curve); $C_L = -0.1$ (brown curve).

In addition, the predictions obtained by employing several positive lift coefficients are shown Figure 4.12 and the optimized lift coefficient found to be used with Lubchenko's approach in this experimental condition is 0.025, which is indeed very small and therefore the produced lift force has negligible effect on the distribution of the gas in the radial direction. In other words, the radial distribution is mainly the outcome of the turbulent dispersion and wall lubrication forces. Another notable point is that the free–of–gas zone does not appear by employing Lubchenko's approach, which is an advantage over Hosokawa's correlation. However, Lubchenko's approach causes the peak of the air volume fraction profile to be located at a distance equal to the bubble radius from the wall, which does not match exactly the one observed in the experiments.

68

Experimental Condition 063

For this experimental condition, the predictions for air volume fraction obtained by employing Hosokawa's correlation and Lubchenko's approach are shown in Figures 4.13 and 4.14, respectively. In general, the same argument made in the case of experimental conditions 040 and 028 applies also to this experimental condition. When the wall lubrication force is modelled by Hosokawa's correlation, a negative lift coefficient produces a lift force that works in the same direction of the wall lubrication force in regions close to the wall. As a result, the peak in the air volume fraction profile is displaced too much towards the center of the column, when compared to the experimental data. Moreover, a large free–of–gas zone is created near the wall. The optimized lift coefficient is found to be 0.07, although a negative lift coefficient is expected. An explanation can be the large non-physical wall lubrication force predicted due to the larger bubble size, which eventually displaces the peak in the air volume fraction too much in the case of employing a negative lift coefficient.
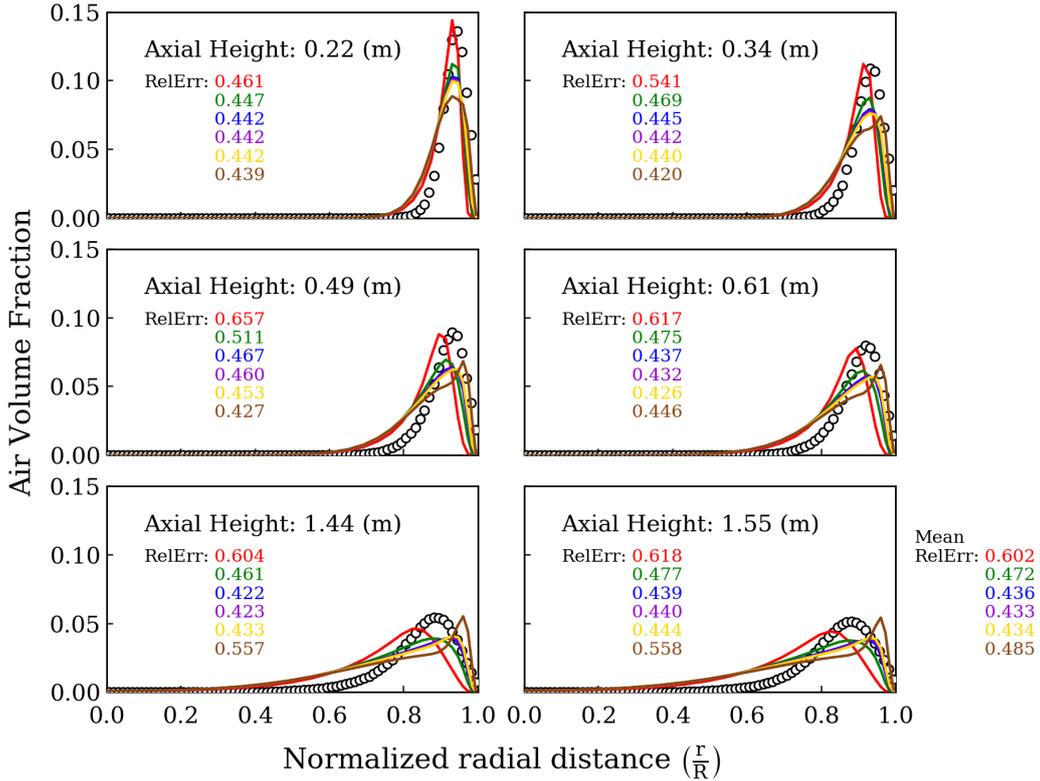
Figure 4.13: The radial profiles of the air volume fraction obtained for experimental condition 063 by employing Hosokawa's correlation for wall force and different lift coefficients: C_L by Tomiyama (red curve); $C_L = 0$ (green curve); $C_L = 0.06$ (blue curve); $C_L = 0.07$ (violet curve); $C_L = 0.08$ (yellow curve); $C_L = 0.15$ (brown curve).

69

In the case of modelling the wall lubrication force with Lubchenko's approach, the change in the lift coefficient (even sign change) does not show a significant effect on the predictions in the simulated portion of the pipe. Nevertheless, the optimized lift coefficient is found to be -0.05. Similar to the two previous experimental conditions, the free–of–gas zone does not appear in the predictions with this wall lubrication model.
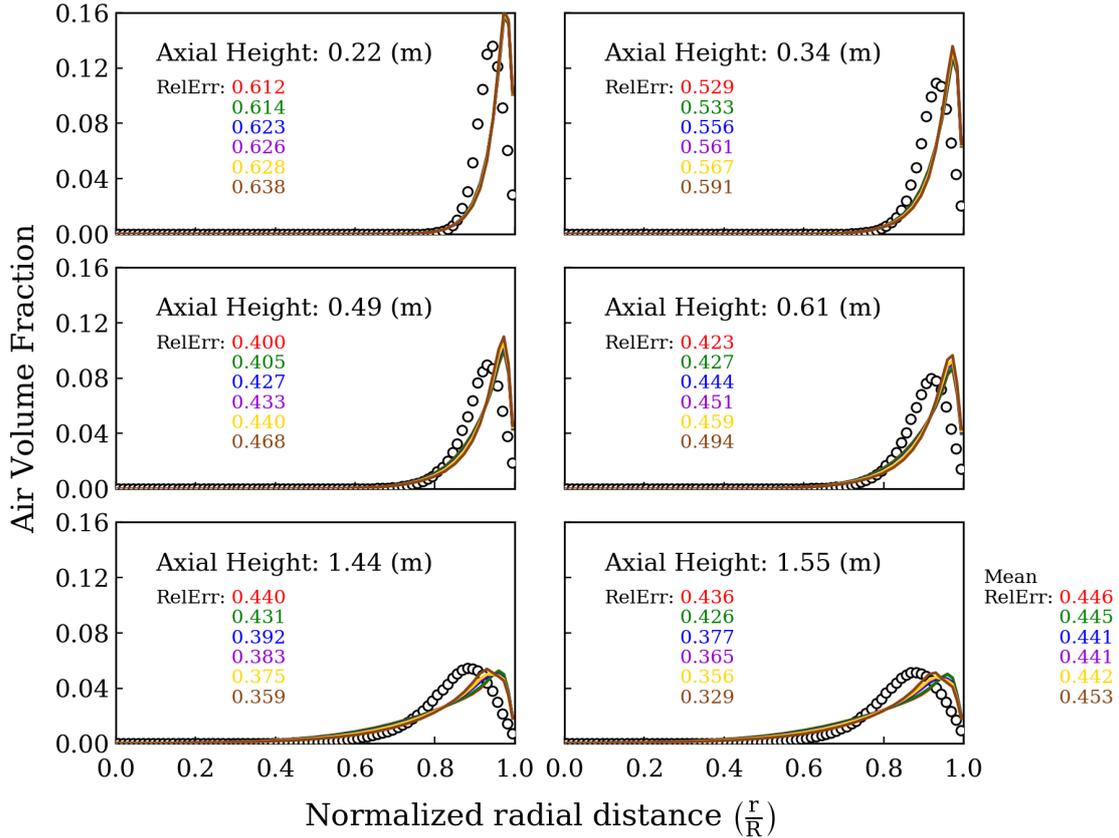

Figure 4.14: The radial profile of the air volume fraction obtained for experimental condition 063 by employing Lubchenko's approach for the wall lubrication force and different lift coefficients: C_L by Sugrue (red curve); $C_L = 0$ (green curve); $C_L = -0.04$ (blue curve); $C_L = -0.05$ (violet curve); $C_L = -0.06$ (yellow curve); $C_L = -0.1$ (brown curve).

Experimental Condition 072

This experimental condition have the largest average bubble size than the others. Moreover, the measurements show a considerable decrease in the average bubble size along the first 1.5 m length of the pipe from the injection ring, see Figure 4.2. When Hosokawa's correlation is used, negative lift coefficients reproduce the peak

observed in the measured air volume fraction profiles. The optimized one is found to be -0.1. However, similar to experimental conditions 040, 028 and 063, the profiles suffer from the fact that no gas phase exist near the wall due to the exaggerated wall lubrication force.
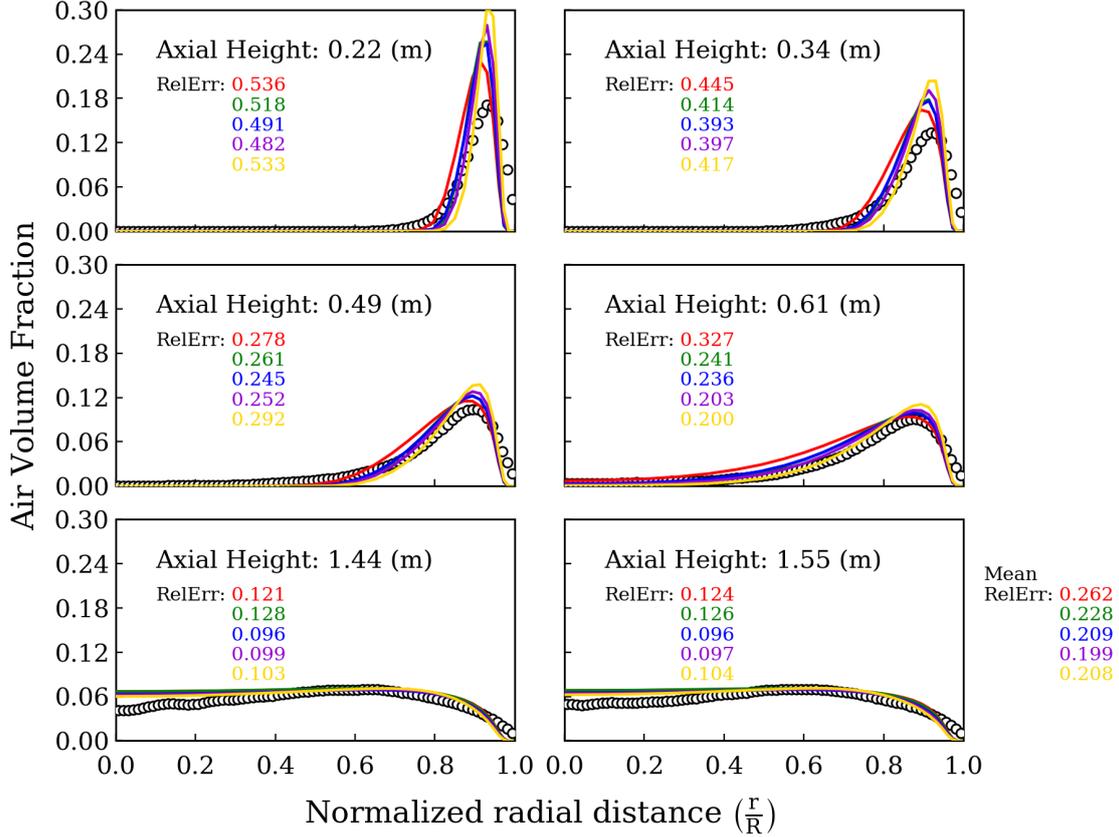

Figure 4.15: The radial profile of the air volume fraction obtained for experimental condition 072 by employing Hosokawa's correlation for the wall lubrication force and different lift coefficients: $C_L = -0.025$ (red curve); $C_L = -0.05$ (green curve), $C_L = -0.07$ (blue curve), $C_L = -0.1$ (violet curve), $C_L = -0.15$ (yellow curve).

Concerning the predictions obtained by employing Lubchenko's approach, the same argument made for experimental condition 063 applies also here. The optimized lift coefficient is found to be 0.1, which is positive and not expected, although the change in the lift coefficient does not show a considerable effect on the predicted air volume fraction profiles in the simulated portion of the column. Last, the predicted location of the peak of the air volume fraction profile does not match the experiments. However, the good point is that, in this experimental condition, Lubchenko's approach allows the gas phase to exist near the wall in contrast to Hosokawa's correlation.
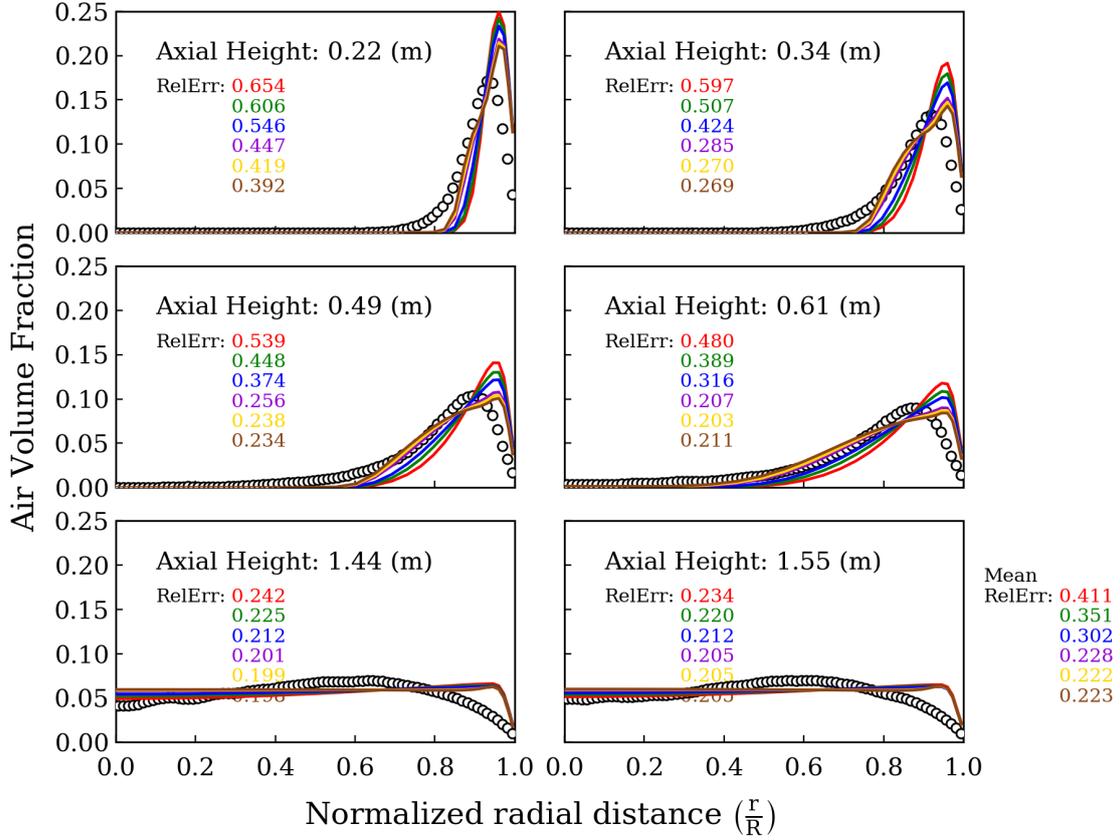
71

Figure 4.16: The radial profile of the air volume fraction obtained for experimental condition 072 by employing Lubchenko's approach for the wall lubrication force and different lift coefficients: C_L by Sugrue (red curve); $C_L = -0.05$ (green curve); $C_L = 0$ (blue curve); $C_L = 0.08$ (violet curve); $C_L = 0.1$ (yellow curve); $C_L = 0.12$ (brown curve).

Optimized Lift Coefficients

The lift coefficients predicted by Tomiyama and Sugrue correlations, employed in Models I and III respectively, together with the optimized values to be used in Models II and IV (based on the simulations of 2-meter pipe) are plotted in Figure 4.17. Concerning experimental conditions 008 and 042, which have monotonic phase velocity profiles and smaller bubbles sizes, the optimized lift coefficients to be used in models II and IV, and those estimated by Tomiyama's and Sugrue's correlations are all positive. For these experimental conditions and considering only the first two-meter of the pipe, Tomiyama's correlation overestimates the lift coefficient, whereas Sugrue's correlation underestimates it. It is worth reiterating that, for these experimental conditions, the predicted air volume fraction profiles show a clear trend as the lift coefficient is changed by employing either wall lubrication model (i.e. Hosokawa's correlation and Lubchenko's approach). This facilitates

finding an optimized lift coefficient to be used by either wall lubrication model in these experimental conditions. Moreover, the values obtained to be used in Models II and IV are close to each other, see Figure 4.17. However, this is not true for the other test cases, which have non-monotonic phase velocity profiles and larger bubble sizes, as it is hard to observe a clear trend since the optimization gives positive and negative values of the lift coefficient, see Figure 4.17. For instance, the positive optimized lift coefficient found to be used in model II for experimental condition 063 and to be used in model IV for experimental conditions 028 and (particularly) 072 are not expected. In fact, in the following section, the importance of using negative lift coefficient for these experimental conditions are illustrated by considering the results of the simulation of the 5-meter pipe.
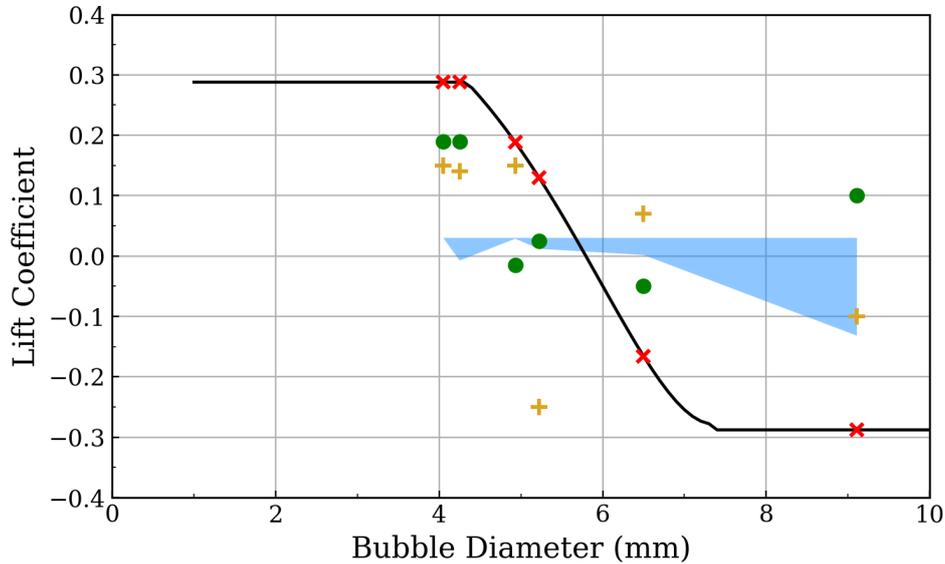
Figure 4.17: Optimized lift coefficients for the simulated experimental conditions in comparison to the estimated ones by Tomiyama's (red × markers) and Sugrue's (Blue area) correlations. Black curve depicts Tomiyama's correlation. Yellow + and green ● markers correspond to optimized lift coefficients in the case of modelling the wall lubrication force with Hosokawa's correlation and Lubchenko's approach respectively.

4.3.2 Simulation of the 5-meter Configuration

In this section, the four models in Table 4.4 are employed to simulate the 5-meter pipe operating under the six experimental conditions, and eventually they are evaluated by considering their corresponding predictions for the radial profiles of the air volume fraction and air velocity under each experimental condition. The other predictions for which no experimental data is available, i.e. the radial profiles of the liquid velocity and turbulence parameters, are reported in Appendix A. It is noteworthy that the arguments presented previously based on the results of the 2-meter pipe simulations apply also here, and the results shown in the following help in making conclusions considering a larger portion of the column.

Experimental Condition 008

For experimental condition 008, both Models I and III result in their maximal lift coefficient, 0.288 and 0.03 respectively. As it can be seen from Figure 4.18, Model I predicts a high value for the lift coefficient that prevents the gas bubbles from spreading towards the center of the pipe while the lift coefficient estimated by Model III is not large enough to push the bubbles towards the wall. Instead, Models II and IV show good agreement with the experimental radial profiles of the air volume fraction in the first two meters of the pipe, for which the lift coefficient is optimized. However, it is evident that larger discrepancy arises in the sections higher than two meters. It implies that good agreement could be achieved at high sections if a smaller value of the lift coefficient were used, however, at the expense of losing the agreement in the lower sections of the pipe. All the models predict satisfactorily the measured air velocity profile except Model I, where a non-physical accumulation of the gas near the wall results to an unexpected behavior in the velocity profile, see Figure 4.18. It can be associated with the numerical issues that emerge due to the very large gradient across a few layers of the cells near the wall.
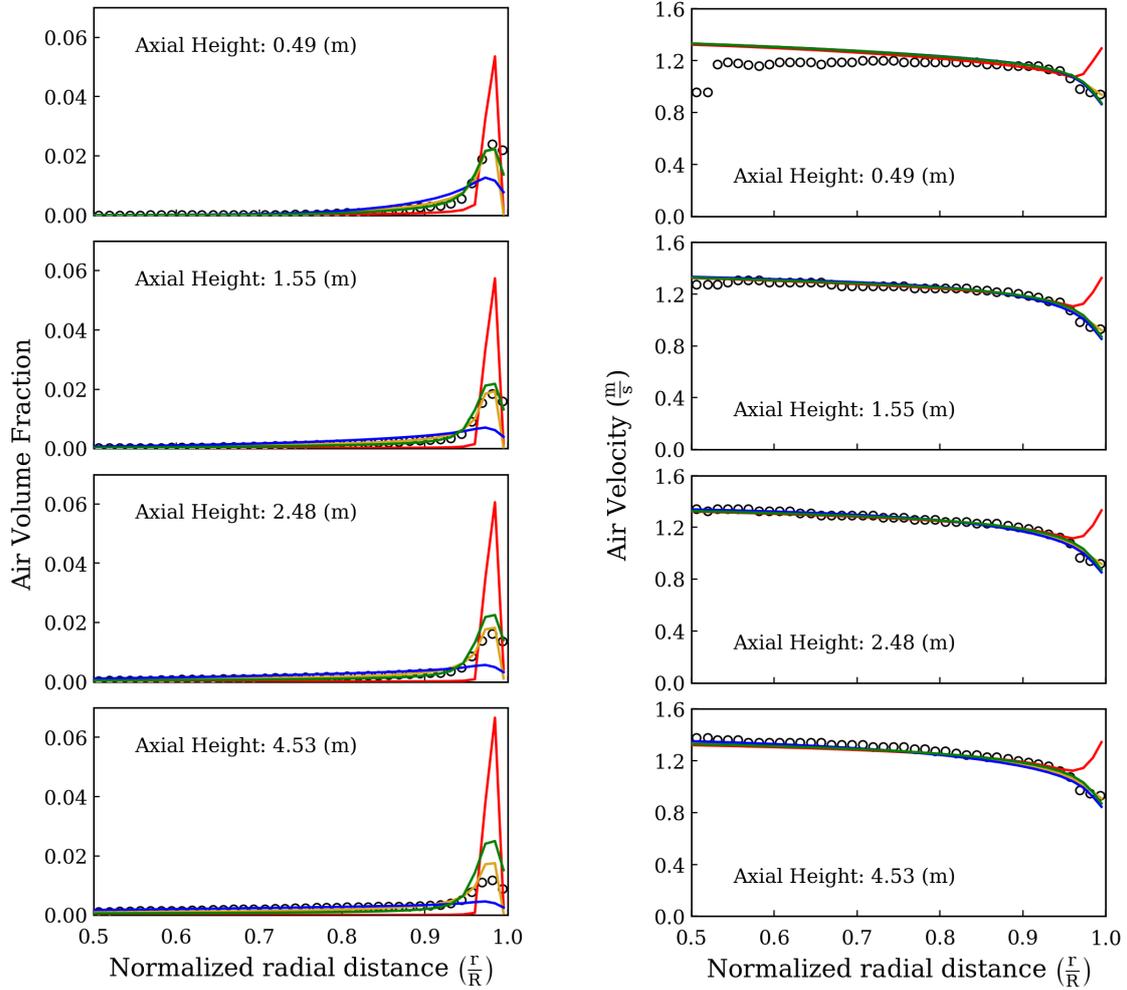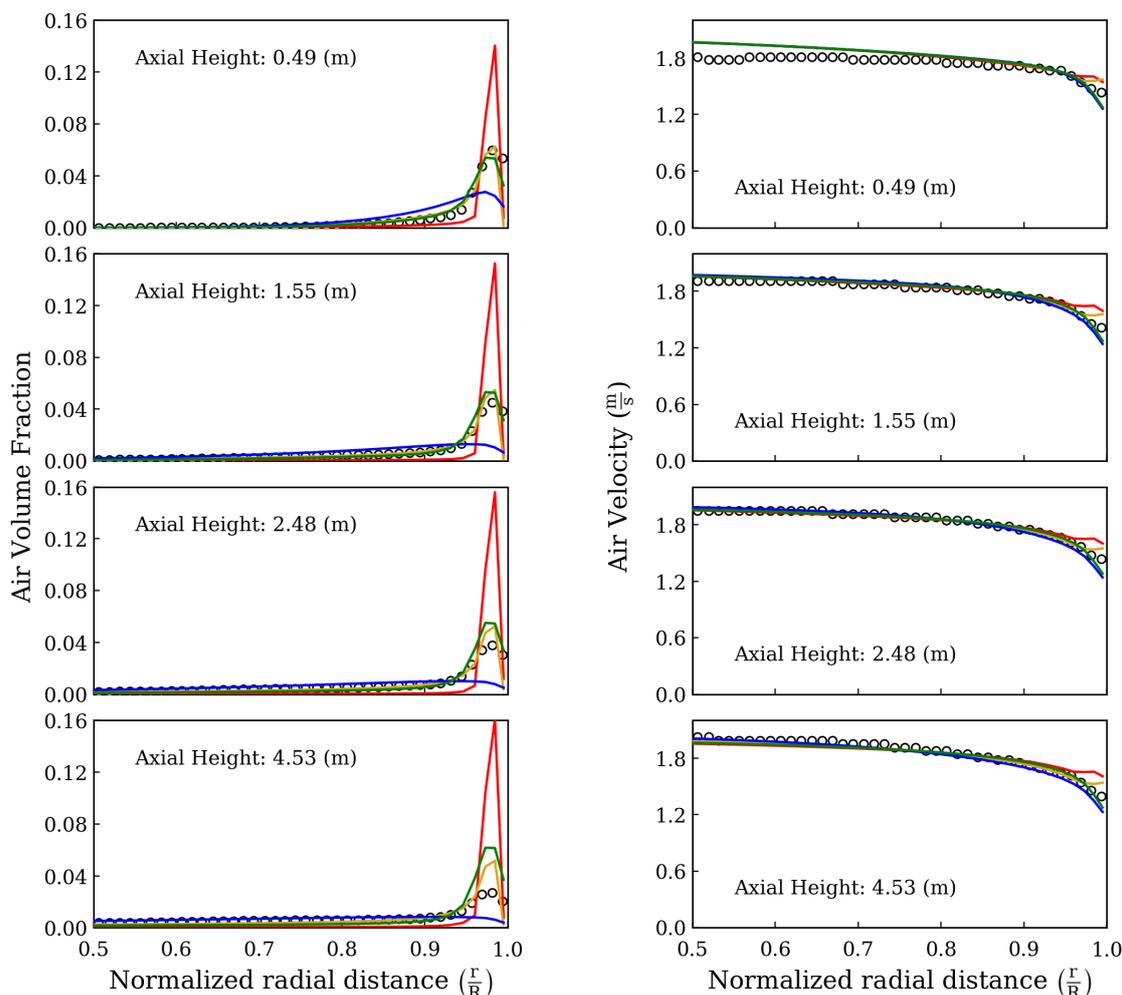
Figure 4.18: Radial profiles of the air volume fraction and velocity predicted by the tested models versus the experimental data (hollow markers) for experimental condition 008. Red curve: Model I; yellow curve: Model II ($C_L = 0.15$); blue curve: Model III; and green curve: Model IV ($C_L = 0.19$).

Experimental Condition 042

Similar findings are obtained for experimental condition 042, shown in Figure 4.19. The common features of these two experimental conditions (i.e. 008 and 042) that make them distinct from the other conditions are the monotonically decreasing velocity profile in the radial direction, lower total gas holdup and smaller average bubble diameter.
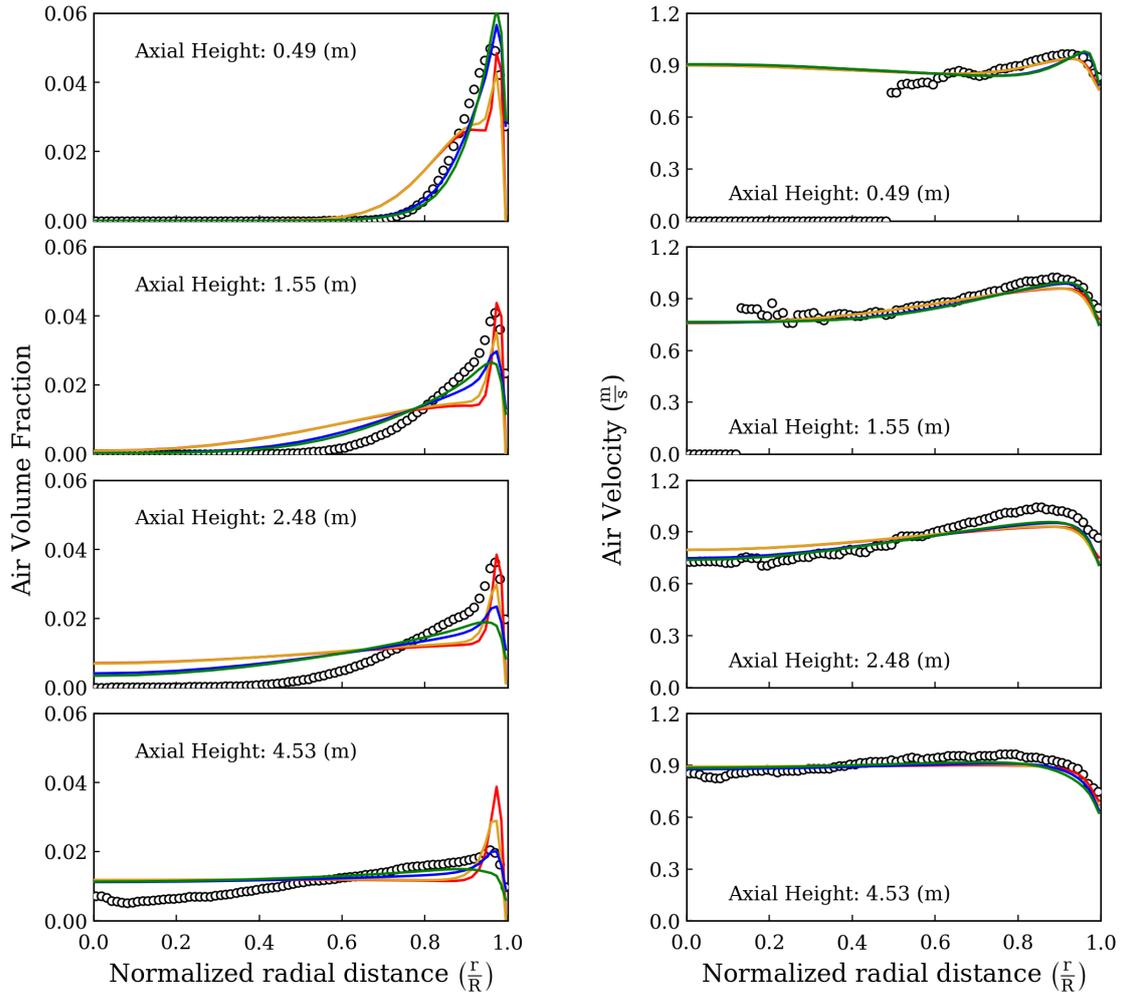
Figure 4.19: Radial profiles of the air volume fraction and velocity predicted by the tested models versus the experimental data (hollow markers) for experimental condition 042. Red curve: Model I; yellow curve: Model II ($C_L = 0.14$); blue curve: Model III; and green curve: Model IV ($C_L = 0.19$).

Experimental Condition 040

For experimental condition 040, the profiles of the air volume fraction obtained by Model III (Figure 4.20) are quite satisfactory in the entire domain. The estimated lift coefficient by this closure equals 0.03, while Model IV has the optimized lift coefficient of -0.015, obtained from simulations of the 2-meter pipe. Comparing the results obtained by Models III and IV at the lower levels reveals that they perform almost identically, thus any lift coefficient value around zero can be considered optimal in the first 2-meter portion of the pipe (see also Figure 4.10). However, employing small positive lift coefficients, e.g. Model III, results in good agreement

not only at the lower sections but also at the higher ones. It indicates that the difference between using positive and negative lift coefficients becomes more apparent in the upper sections. On the contrary, the air volume fractions predicted by Models I and II are comparatively worse than those obtained by employing Model III. This finding could be associated with the high value of the lift coefficient. Regarding the air velocity profiles, the results obtained by all the models are in good agreement with the experimental data (Figure 4.20).

Figure 4.20: Radial profiles of the air volume fraction and velocity predicted by the tested models versus the experimental data (hollow markers) for experimental condition 040. Red curve: Model I; yellow curve: Model II ($C_L = 0.15$); blue curve: Model III; and green curve: Model IV ($C_L = -0.015$).
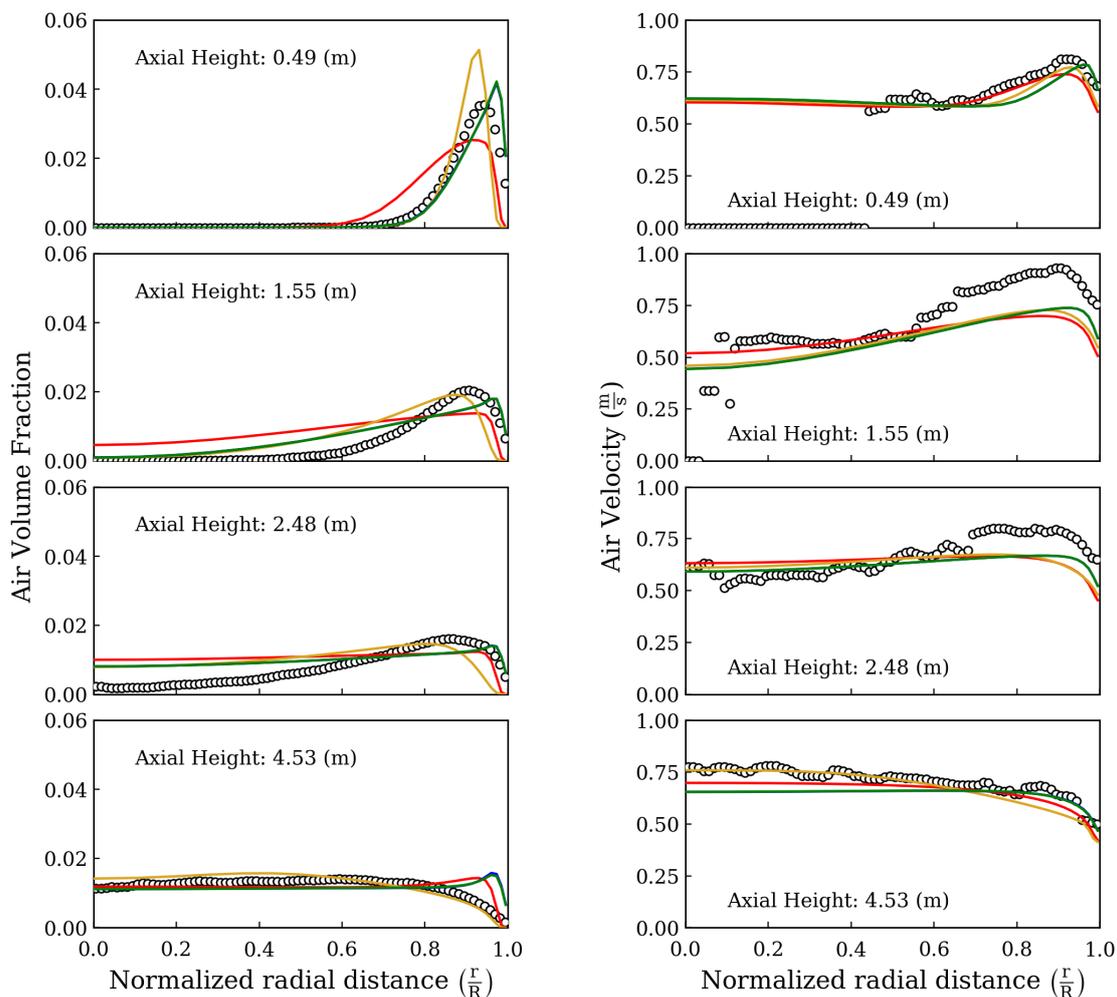
Figure 4.21: Radial profiles of the air volume fraction and velocity predicted by the tested models versus the experimental data (hollow markers) for experimental condition 028. Red curve: Model I; yellow curve: Model II ($C_L = -0.25$); blue curve: Model III; and green curve: Model IV ($C_L = 0.025$).

Experimental Condition 028

Observing the air volume fractions reported in Figure 4.21 reveals that Model I, III and IV predict a peak near the wall at the last cross-section, which is not in agreement with the measurements. However, no peak is seen in the profile at the last cross-section predicted by the Model II, which is the only model with a negative lift coefficient. Considering the entire column, it is difficult to choose one of the models that performs averagely well. While Model II may seem as a candidate, its predictions suffer from the free-of-gas zone near the wall, which is also the case for Model I, due to the wall lubrication model by Hosokawa. In contrast, this problem

is not seen in the predictions by Model III and IV, which employ Lubchenko's approach to model the wall lubrication force. However, the predictions at the last cross-section by Model III and IV are not satisfactorily, which can be associated with the positive lift coefficient. Therefore, it is interesting to perform another simulation using Model IV but with a negative lift coefficient (here -0.05) instead of the positive one. It is noteworthy that the change in the lift coefficient (including its sign) did not modify the predictions considerably in the first 2-meter portion of the column, see Figure 4.12, however it (specifically the change in the sign) may have a considerable effect in the higher sections, which are not considered to find an optimized coefficient. Figure 4.22 compares the predictions obtained by Model IV using the (positive) optimized lift coefficient (0.025) and the newly chosen negative coefficient (-0.05). While the predicted air volume fraction profiles at the lower section are almost the same, the one obtained by the negative lift coefficient show much better agreement with the experimental data at higher sections. Therefore, it confirms that the sign of the lift coefficient shows its effect at higher sections in this specific pipe flow.
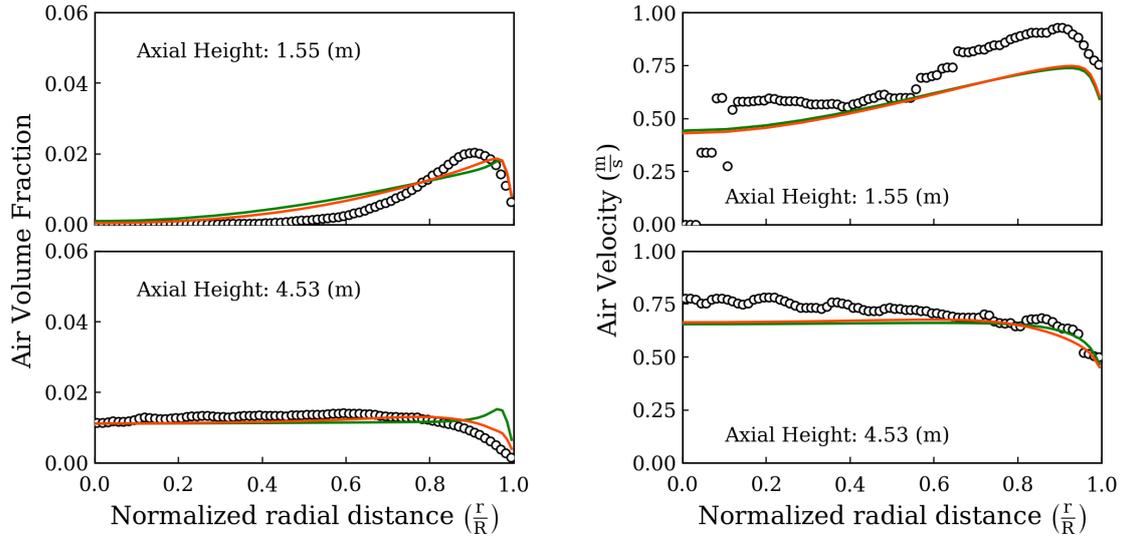

Figure 4.22: Effect of the lift coefficient sign on the predictions obtained by Model IV at high sections under experimental condition 028: green curve ($C_L = 0.025$); orange curve ($C_L = -0.05$)

79

Experimental Condition 063

Figure 4.23 shows the predicted air volume fraction and velocity profiles for experimental condition 063. Similar to experimental condition 028, the models with negative lift coefficient (here Model I and IV) predict much better at higher sections. It is worth noting that Model IV and III differ in the sign of the lift coefficient, see Figure 4.17. While their predictions at the lower sections are almost the same, they are different as the flow develops. In fact, Sugrue's model predicts positive lift coefficients for this experimental condition, leading to discrepancies at the higher sections. In other words, it does not predict the inversion of the lift coefficient, which helps in improving the results, particularly at the higher sections. The same difference, i.e. effect of the negative lift coefficient at the higher sections, can be observed by comparing the prediction by Models I and II.

Concerning Model I, the wall peak in the predicted volume fraction profiles are farther from the wall than the one demonstrated by the experimental data, as seen previously from the results obtained in the 2-meter configuration (Figure 4.13). This is associated with Hosokawa's wall lubrication model that leads to a strong force near the wall. The predicted volume fraction profiles demonstrate how this strong force pushes away virtually all the gas from the wall, which is not consistent with the experimental data. Moreover, the too underestimated negative lift coefficient by Tomiyama correlation contributes to pushing the gas phase from the wall. In contrast, the wall lubrication force modelled by Lubchenko's approach (employed in Models III and IV) allows the gas phase to exist near the wall. However, this model seems to place the peak of the air volume fraction profile at a distance equal to the radius of the bubbles from the wall, which is closer to the wall than the one of the experimental data. Among the predictions, the one obtained by Model IV shows good agreement, particularly at higher sections.
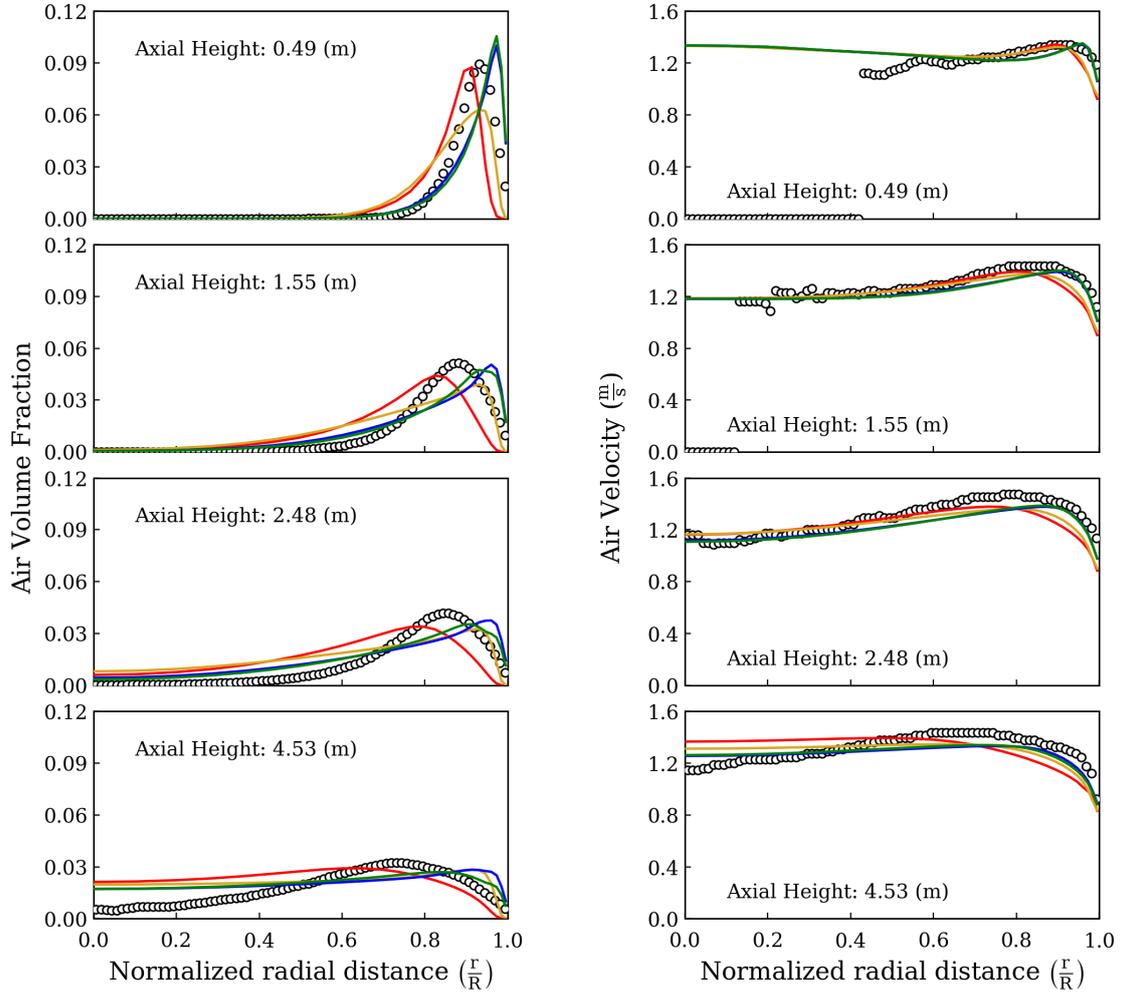
Figure 4.23: Radial profiles of the air volume fraction and air velocity predicted by the tested models versus the experimental data (hollow markers) for experimental condition 063. Red curve: Model I; yellow curve: Model II ($C_L = 0.07$); blue curve: Model III; and green curve: Model IV ($C_L = -0.05$).

Experimental Condition 072

For experimental condition 072, Model II provides the overall best agreement when considering all the sections, see Figure 4.24. However, this model employs Hosokawa's correlation, which causes a free-of-gas zone near the wall.

The comparison of predictions by Model I and II indicates that Tomiyama's model underestimates the lift coefficient. In fact, the large peak in the red profile of Figure 4.24 at the lowest section and the excessive spread of the gas toward the center of the pipe are due to the large negative lift coefficient.

Concerning Model III and IV, the discrepancies seen at the higher sections,

81

particularly the peak near the wall at the two last sections, can be associated with the positive lift coefficient. Therefore, similar to experimental condition 028, it is helpful to perform a simulation by using a negative lift coefficient (here -0.05) in Model IV. Figure 4.25 illustrates the necessity of employing negative lift coefficient to describe the migration of the bubbles towards the center of the pipe at higher sections. Moreover, a better description of the bubble migration towards the center of the pipe improves the predicted radial profile of the velocity at higher sections.
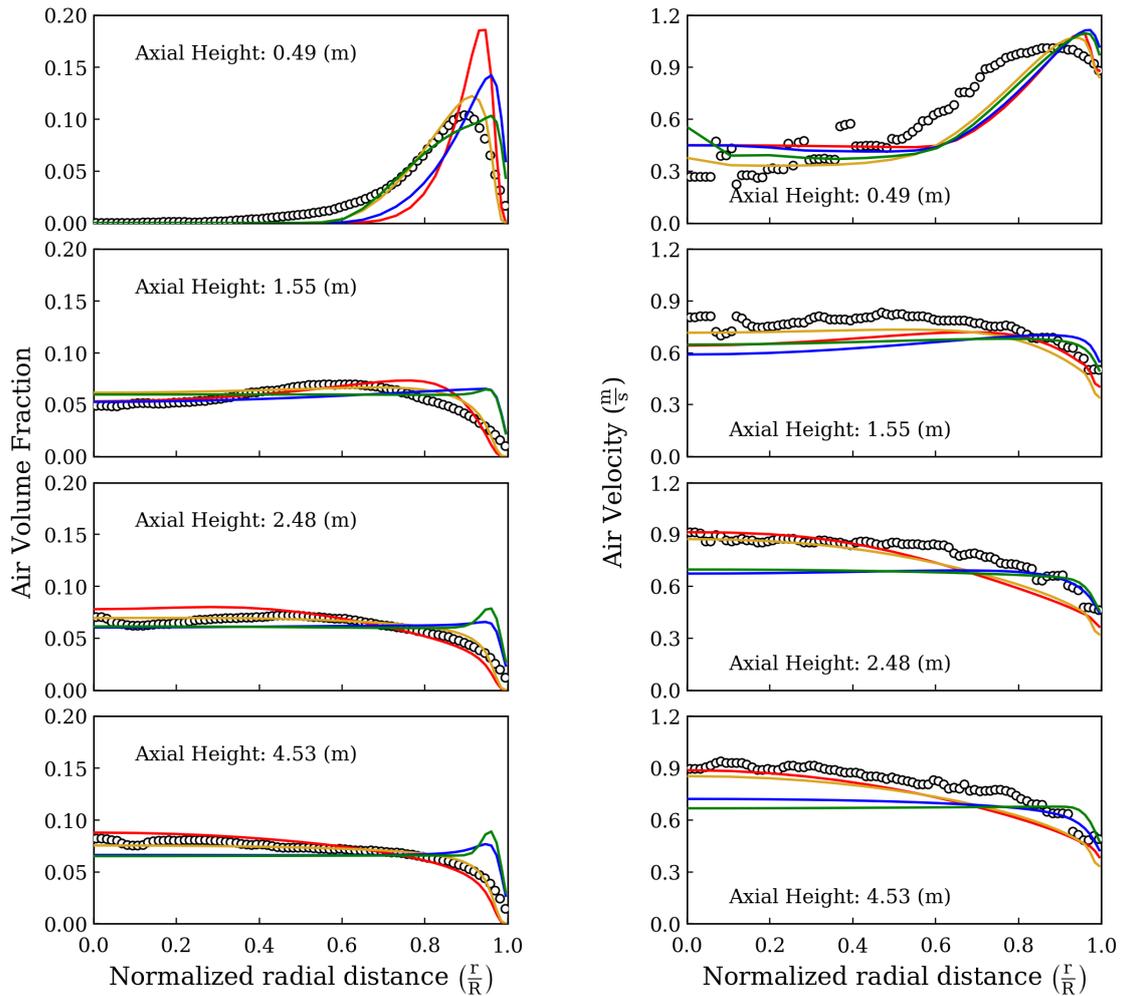

Figure 4.24: Radial profiles of the air volume fraction and velocity predicted by the tested models versus the experimental data (hollow markers) for experimental condition 072. Red curve: Model I; yellow curve: Model II ($C_L = -0.05$); blue curve: Model III; and green curve: Model IV ($C_L = 0.1$).
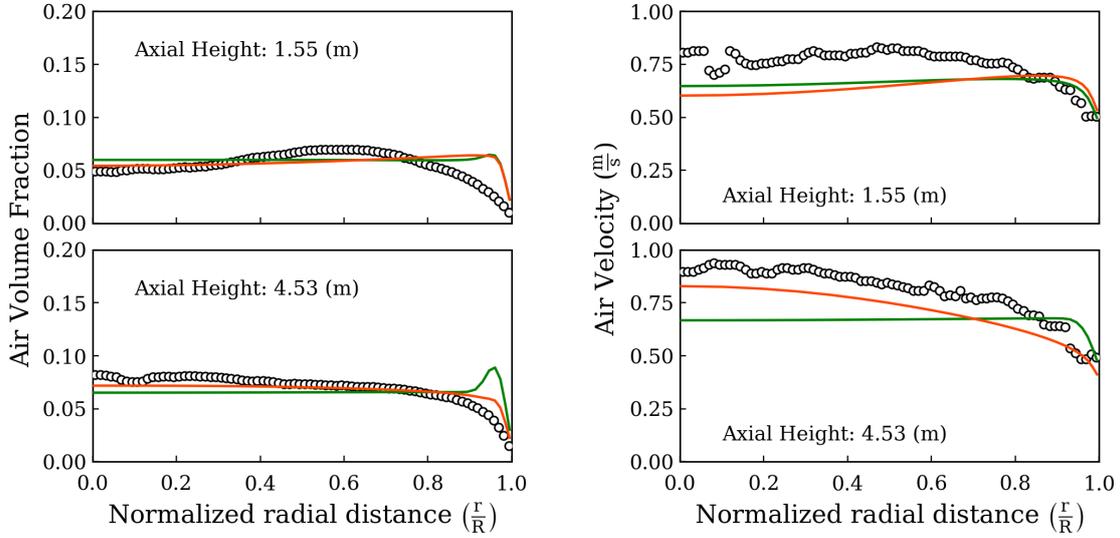
Figure 4.25: Effect of the lift coefficient sign on the predictions obtained by Model IV at high sections under experimental condition 072: green curve ($C_L = 0.025$); orange curve ($C_L = -0.05$).

4.3.3 Concluding Remarks

The simulation results revealed some valuable information that can be leveraged both for the application of the models and for the further extension of them. In the present framework, Tomiyama's correlation seems to overestimate the lift coefficient for small bubbles and underestimate the lift coefficient for large bubbles (> 5 mm). Since Tomiyama's correlation was developed based on laminar experiments ($Re < 50$), it could be postulated that the lift force is smaller for bubbles moving in turbulent flows (in this thesis $Re > 1000$) than in laminar flows, as already discussed by Shaver and Podowski [32] and Sugrue [21], but further it seems that the Eötvös number does not contain all the necessary physics to prescribe correctly the lift coefficient.

On the contrary, Sugrue's correlation leads to small positive lift coefficients for small bubbles that have noticeable effect on the volume fraction profiles only at the upper sections of the column and their effect on the profiles in the lower part of the system is insignificant. Since Sugrue's correlation was developed based on the measurements of the fully-developed outlet profiles, it is not surprising that the estimated lift coefficients are much smaller than those optimized for the lower sections. This fact highlights the importance of studying developing flows for advancing knowledge on the lift force.

Concerning the optimized lift coefficients in Models II and IV, the results of the

5-meter simulations obtained for the operating conditions with monotonic phase velocity profiles and smaller bubbles sizes, i.e. experimental conditions 008 and 042, yield acceptable predictions. However, the predictions in the 5-meter configuration obtained for the other operating conditions by employing the optimized lift coefficients are not generally satisfactory, particularly at higher sections. One reason is identified to be the positive sign of the lift coefficient, which caused discrepancies particularly at higher sections. In fact, it was shown that for larger bubble sizes ($>$ 5 mm), employing a negative lift coefficient yield more satisfactory results at both lower and higher sections. In this regard, Tomiyama's correlation predicts correctly negative lift coefficients for this range of bubble sizes, although the inversion of the lift coefficient occurs at the bubble size around 6 mm instead of 5 mm. In contrast, Sugrue's correlation may predict positive lift coefficients for this range of bubble size, giving rise to relatively larger deviation from the experimental data. This shows the limitation of Sugrue's correlation in predicting the inversion of the lift force required for the satisfactory description of the radial profiles of the air volume fraction.

Regarding the wall lubrication models, it is evident that both models can reproduce the measured gas volume fraction for the experimental cases with bubble sizes smaller than 5 mm, provided that an appropriate lift coefficient is employed. However, their predictions of the air volume fraction deviate from the experimental ones when the bubble size is larger than 5 mm. In this range, the model of Hosokawa predicts a force of such a large magnitude, see Figure B.1, that essentially creates a region with no gas near the wall, in contrast to the experimental observation. This behavior of Hosokawa's model or other similar models has been previously reported in the literature [19]. However, this exaggerated force might be avoided if a poly-disperse approach was adopted, since this approach could potentially describe the separation of small and large bubbles observed experimentally by Lucas and Tomiyama [23], i.e. small bubbles tend to stay near the wall and large bubbles move mostly in the center. In contrast, the approach by Lubchenko and co-workers produces more physical results, even though the predicted location of the peak is not in agreement with the experimental data. This approach allows the disperse phase to exist near the wall, which is crucial in various CFD simulations such as those involving heat transfer and bubble nucleation and those coupled with population balance models. Therefore, this approach is adopted for the CFD-PBM simulations in Chapter 6.

Chapter 5

Scheme for Advection of Moments[*]

As mentioned in Chapter 3, a primary cause of instabilities in the CFD-PBM simulation of multiphase flows is the realizability issue. Confining the discussion to the finite-volume method, the most common cause of the non-realizability (also known as numerical moment corruption) lies in the spatial discretization of the transport term of the moment transport equation, when high-order spatial discretization schemes are used. This problem is often related to the convective term, as in many cases the governing equations have a hyperbolic form. Desjardins et al. [64] demonstrated that the 1st-order scheme guarantees the realizability of the moments, provided the CFL (Courant-Friedrichs-Lewy) condition is respected. Despite this advantage, the 1st-order scheme results in highly diffusive solutions, leading sometimes to unacceptable predictions, hence the necessity of adopting high-order schemes. However, employing high-order finite-volume schemes for the independent transport of the moments may cause the realizability issue [61]. Therefore, the development of a realizable high-order scheme for the solution of moment transport equations is crucial. In this regard, Vikas and co-workers [62] presented the so-called realizable quasi-high-order schemes, based on the evaluation of the moment fluxes at the cell faces using the interpolated nodes and weights of the quadrature. With this method, the quadrature interpolation is performed by applying a 1st-order scheme to the quadrature nodes and a high-order scheme to the quadrature weights. This approach produces less diffusive solutions and guarantees the realizability of the transported moments, provided a criterion on the time step is respected. However, no analysis was conducted on the boundedness property of this approach, which can not be ignored since unbounded predictions are not physically allowed [66]. Kah et al. [59] formulated a 2nd-order kinetic scheme that makes use

---

of the canonical moments to transport the moments indirectly while maintaining them in the moment space. However, the application of their method to simulations with more than four moments involves difficult algebra [63]. Recently, Laurent and co-workers [63] developed a similar approach based on the reconstruction of the coefficients ζ_k (for its definition refer to [63]) instead of the canonical moments. However, their original scheme cannot be applied easily to unstructured grids and therefore they suggested a simplified version of their scheme, which involves division of the cells into three parts as proposed by Berthon [171].

This chapter introduces a new technique, called the equal-limiter scheme, to overcome the non-realizability problem when 2nd-order TVD (Total Variation Diminishing) schemes are applied to the moment transport equations. The technique is based on using an equal limiter (given by a flux-limiter function) for all the moments, and we show that it is effective to avoid non-realizable set of moments. Moreover, its application to three-dimensional unstructured grids is straightforward.

The chapter is organized as follows. First, we prove that, in a one-dimensional Riemann problem, the concept of equal-limiter emerges naturally if no source term is included in the moment transport equations. Next, the importance of using an identical limiter(given by a limiter function) for all the moments is clarified in a general case by solving the local Riemann problem at each cell face, and the role of the time step in maintaining the realizability of the moments is explained. Moreover, we discuss the application of the equal-limiter scheme to CFD codes, without any assumption on the velocity field or type of the mesh grid. In the final part, a comparison between several techniques is performed by solving moment transport equations in some one- and two-dimensional test cases.

5.1   TVD Scheme for Moment Transport Equation

5.1.1   Moment Transport Equation

Let us consider the following univariate PBE with the size of the elements of a generic disperse phase, L, as the internal coordinate:

$$\partial_t n_L + \partial_{\mathbf{x}} \cdot (\mathbf{U}_\mathrm{d} n_L) + \partial_L(\dot{L} n_L) = \mathcal{S} \,, \tag{5.1}$$

where $\mathbf{U}_\mathrm{d} \equiv \mathbf{U}_\mathrm{d}(\mathbf{x}, t)$ is the velocity of the disperse phase and $\dot{L}$ represents the continuous rate of the change in the size of elements due to the continuous processes (e.g. mass transfer driven growth). It is worth remarking that the velocity of the disperse phase appearing in Eq. (3.1) does not depend on the size of the elements.

86

The kth-order moment of n_L with respect to L is:

$$m^k(t, \mathbf{x}) = \int_0^\infty n_L(t, \mathbf{x}, L) \, L^k \, dL \,. \tag{5.2}$$

As mentioned in Chapter 3, the lower-order moments of a given NDF are associated with various integral properties of the population represented by that NDF. For instance, in this case, the 3rd-order moment with respect to L is proportional to the volume fraction of the disperse phase. The above moment definition can be used to derive the moment transport equations from Eq. (3.1), as explained in Chapter 3. For the sake of simplicity, from now on we assume a one-dimensional case where the velocity is constant (u_{d}) and the contribution of the continuous processes is negligible ($\dot{L} = 0$). The transport equation for the kth-order moment reduces to the following partial differential equation:

$$\partial_t m^k + u_{\text{d}} \partial_x m^k = \bar{\mathcal{S}}^k \,. \tag{5.3}$$

In general, the source term $\bar{\mathcal{S}}^k$ is a complex multidimensional integral that depends on the NDF itself. In this regard, the QMOM can be used to close the moment transport equations by approximating the NDF as a summation of some delta functions centered on the quadrature abscissas (L_α):

$$n_L(L) = \sum_{p=1}^N w_p \delta(L - L_p) \,. \tag{5.4}$$

The weights and abscissas are determined from the transported moments by employing an inversion algorithm (such as the PD and Chebyshev algorithms), provided the set of moments is realizable. This is usually referred to as the moment problem [140]: in particular, when the support of the NDF is $\Omega_L =]0, +\infty[$ as in this case, it is called finite Stieltjes moment problem. When the support of the NDF is different, i.e. $\Omega_L =]-\infty, +\infty[$ or $\Omega_L =]0,1[$, we refer to finite Hamburger and finite Hausdorff moment problems, respectively. These three different supports result in different constraints on the transported set of moments to ensure its realizability [139, 140]. However, the non-realizability problem is common to all these cases and poses the main challenge in practical applications of the QMOM. In the finite-volume method, this can happen particularly during the interpolation of the moments on the faces to calculate the flux of the moments at faces if high-resolution TVD schemes are employed.

5.1.2 Finite-Volume Method

As mentioned before, this chapter focuses on the realizability issue in the context of the finite-volume method. The general formulation of the finite-volume method can be found in the specialized literature [65, 172], and therefore is omitted here.

Let a single-stage explicit method be adopted to march in time and the source terms be handled using the fractional-step approach [65]. In this way, the finite-volume method transforms Eq. (5.3) into the following discretized form, written for the generic cell i of size Δx in the spatial domain:

$$m_i^{k*} = m_i^k - \frac{\Delta t}{\Delta x}(F_{i+1/2}^k - F_{i-1/2}^k)\,, \tag{5.5}$$

$$(m_i^k)^{n+1} = m_i^{k*} - \Delta t\, \bar{\mathcal{S}}_i^k\,, \tag{5.6}$$

where m_i^k, m_i^{k*} and $(m_i^k)^{n+1}$ refer to, respectively, the moment value at the current time (t_n), the intermediate value of the fractional-step approach and the moment value at the new time (t_{n+1}) after a time step of Δt. Furthermore, $F_{i-1/2}^k$ and $F_{i+1/2}^k$ denote the numerical flux along the left and right faces of the cell i respectively, each depends on the neighboring cell values at time t_n according to the selected numerical flux function. From now on, our primary focus is on Eq. (5.5), particularly the calculation of the flux of the moments at the faces. The effect of the source term will be clarified afterwards.

It is desirable to calculate the fluxes using high-resolution schemes that are formulated on the basis of slope-limiter methods. These methods use a high-order scheme where the solution is smooth enough, otherwise they switch to a low-order one to prevent non-physical oscillations in the numerical solution [65]. In this way, the solution exhibits higher order of accuracy than the 1$^{\text{st}}$-order solution, without losing the boundedness. Using the Lax-Wendroff scheme as the high-order scheme and the upwind scheme as the low-order one, we form the so-called flux-limiter methods with the following numerical flux functions [65]:

$$F_{i-1/2}^k = u_{\text{d}}^- m_i^k + u_{\text{d}}^+ m_{i-1}^k + \frac{1}{2}|u_{\text{d}}|\left(1 - \frac{|u_{\text{d}}|\Delta t}{\Delta x}\right)\phi(\theta_{i-1/2}^k)\Delta m_{i-1/2}^k\,, \tag{5.7}$$

$$F_{i+1/2}^k = u_{\text{d}}^- m_{i+1}^k + u_{\text{d}}^+ m_i^k + \frac{1}{2}|u_{\text{d}}|\left(1 - \frac{|u_{\text{d}}|\Delta t}{\Delta x}\right)\phi(\theta_{i+1/2}^k)\Delta m_{i+1/2}^k\,, \tag{5.8}$$

where

$$u_{\text{d}}^+ = \frac{1}{2}(u_{\text{d}} + |u_{\text{d}}|) \quad \text{and} \quad u_{\text{d}}^- = \frac{1}{2}(u_{\text{d}} - |u_{\text{d}}|)\,. \tag{5.9}$$

In addition, $\Delta m_{i-1/2}^k$ and $\Delta m_{i+1/2}^k$ are respectively the jumps across the left and right faces, defined following the below convention:

$$\Delta m_{i-1/2}^k = m_i^k - m_{i-1}^k\,. \tag{5.10}$$

The flux-limiter ϕ is a function of the smoothness of m^k at the face $(\theta_{i\pm1/2}^k)$. The smoothness is commonly defined as the following [65]:

$$\theta_{i-1/2}^k = \frac{\Delta m_{I-1/2}^k}{\Delta m_{i-1/2}^k} \quad \text{with} \quad I = \begin{cases} i-1 & \text{if } \bar{u} > 0 \\ i+1 & \text{if } \bar{u} < 0 \end{cases}\,. \tag{5.11}$$

A variety of flux-limiter functions are available in the literature such as minmod [173] and van Leer [174]. For instance, the minmod flux-limiter can be expressed mathematically as written below [175]:

$$\phi(\theta_{i-1/2}^k) = \max\{0, \min(\theta_{i-1/2}^k, 1)\}. \tag{5.12}$$

Substituting the numerical fluxes in Eq. (5.5) yields the following discretized equation:

$$m_i^{k*} = m_i^k - \frac{\Delta t}{\Delta x} u_\mathrm{d}^+ (m_i^k - m_{i-1}^k) - \frac{\Delta t}{\Delta x} u_\mathrm{d}^- (m_{i+1}^k - m_i^k)$$
$$- \frac{1}{2} \frac{|u_\mathrm{d}|\Delta t}{\Delta x} \left(1 - \frac{|u_\mathrm{d}|\Delta t}{\Delta x}\right) \left[\phi(\theta_{i+1/2}^k)\Delta m_{i+1/2}^k - \phi(\theta_{i-1/2}^k)\Delta m_{i-1/2}^k\right]. \tag{5.13}$$

5.2 The Concept of Equal-Limiter

The flux-limiter methods have been developed to address the issue of boundedness that occurs in the case of employing high-order schemes to solve hyperbolic problems. One would ideally desire to use these methods for the solution of the moment transport equations, particularly when the 1st-order accuracy is not sufficient to describe the behavior of the system under study. However, in general, the non-realizability problem hinders their direct practice for the solution of moment transport equations. We intend to demonstrate that this limitation can be overcome by selecting an equal limiter for all the moments.

The starting point is to show that the idea of equal-limiter emerges in the case of employing 2nd-order TVD schemes for the pure moment advection with no source term $((m_i^k)^{n+1} = m_i^{k*})$ in a Riemann problem example. We also show that in this case, the moments remain realizable. Then, the discussion continues to highlight the advantage of employing equal-limiter in a more general context, where the effect of aggregation and breakage is also taken into account.

The argument begins with rewriting Eq. (5.13) for the case $u_\mathrm{d} > 0$ without loss of generality[*]:

$$(m_i^k)^{n+1} = m_i^k - \nu_\mathrm{d}(m_i^k - m_{i-1}^k)$$
$$- \frac{1}{2}\nu_\mathrm{d}(1 - \nu_\mathrm{d})\left[\phi(\theta_{i+1/2}^k)\Delta m_{i+1/2}^k - \phi(\theta_{i-1/2}^k)\Delta m_{i-1/2}^k\right], \tag{5.14}$$

where $\nu_\mathrm{d} = u_\mathrm{d}\Delta t/\Delta x$ is the Courant number. The smoothnesses at the left and right faces are written following Eq. (5.11):

$$\theta_{i-1/2}^k = \frac{m_{i-1}^k - m_{i-2}^k}{m_i^k - m_{i-1}^k} \quad \text{and} \quad \theta_{i+1/2}^k = \frac{m_i^k - m_{i-1}^k}{m_{i+1}^k - m_i^k}. \tag{5.15}$$

---

[*]The case $u_\mathrm{d} < 0$ can be formulated similarly and leads to the same conclusions

Now let us consider a Riemann problem example with the following initial data:

$$m^k(0,x) = \mathring{m}^k = \begin{cases} \mathring{m}_l^{\,k} & \text{if } x < 0 \\ \mathring{m}_r^{\,k} & \text{if } x > 0 \end{cases}, \tag{5.16}$$

where $\mathring{m}_l^{\,k}$ and $\mathring{m}_r^{\,k}$ are the moments of the initial left and right NDFs, $\mathring{n}_{L,l}$ and $\mathring{n}_{L,r}$, and consequently constitute two realizable sets of moments. It is postulated that the numerical solution of the kth-order moment at any generic cell i and any time step t_n, including the zero time, can be expressed as:

$$m_i^k = \mathring{m}_r^{\,k} - a_i^n(\mathring{m}_r^{\,k} - \mathring{m}_l^{\,k}) \quad \text{and} \quad 0 \le a_i^n \le 1, \tag{5.17}$$

where a_i^n is a constant that changes with the cell index i and the time step but not with the moment order or value. In other words, this constant is the same for all the moments of a given cell at each time step. It is worth mentioning that the initial data (Eq. (5.16)) corresponds to $a_i^0 = 1$ for $x_i < 0$ and $a_i^0 = 0$ for $x_i > 0$. Next step is to substitute Eq. (5.17) in Eq. (5.14), which, after simplifications, yields the following:

$$
\begin{aligned}
(m_i^k)^{n+1} &= \mathring{m}_r^{\,k} - a_i^n(\mathring{m}_r^{\,k} - \mathring{m}_l^{\,k}) + \nu_{\mathrm{d}}(a_i^n - a_{i-1}^n)(\mathring{m}_r^{\,k} - \mathring{m}_l^{\,k}) \\
&\quad + \frac{1}{2}\nu_{\mathrm{d}}(1 - \nu_{\mathrm{d}})\left[\phi\left(\frac{a_i^n - a_{i-1}^n}{a_{i+1}^n - a_i^n}\right)(a_{i+1}^n - a_i^n)\right. \\
&\quad \left. - \phi\left(\frac{a_{i-1}^n - a_{i-2}^n}{a_i^n - a_{i-1}^n}\right)(a_i^n - a_{i-1}^n)\right](\mathring{m}_r^{\,k} - \mathring{m}_l^{\,k}) \\
&= \mathring{m}_r^{\,k} - a_i^{n+1}(\mathring{m}_r^{\,k} - \mathring{m}_l^{\,k}),
\end{aligned}
\tag{5.18}
$$

and a_i^{n+1} collects several coefficients that do not depend on the moment values:

$$
\begin{aligned}
a_i^{n+1} =\, & a_i^n - \nu_{\mathrm{d}}(a_i^n - a_{i-1}^n) \\
& - \frac{1}{2}\nu_{\mathrm{d}}(1 - \nu_{\mathrm{d}})\left[\phi\left(\frac{a_i^n - a_{i-1}^n}{a_{i+1}^n - a_i^n}\right)(a_{i+1}^n - a_i^n)\right. \\
& \left. - \phi\left(\frac{a_{i-1}^n - a_{i-2}^n}{a_i^n - a_{i-1}^n}\right)(a_i^n - a_{i-1}^n)\right].
\end{aligned}
\tag{5.19}
$$

Equation (5.19) has the same structure of Eq. (5.14), therefore, it appears that a_i^n is the solution of an advection equation for the variable a obtained by the 2nd-order TVD finite-volume scheme. As a consequence, it is guaranteed that a_i^{n+1} remains bounded to the values of the previous time step, i.e. between 0 and 1. Now it can be concluded that the postulated solution at time step t_n is also valid at the next time step, t_{n+1}:

$$(m_i^k)^{n+1} = \mathring{m}_r^{\,k} - a_i^{n+1}(\mathring{m}_r^{\,k} - \mathring{m}_l^{\,k}), \quad 0 \le a_i^{n+1} \le 1. \tag{5.20}$$

As mentioned before, the initial data (Eq. (5.16)) can be expressed by Eq. (5.17), therefore, the postulated solution is indeed the solution of Eq. (5.14) at any time step with the initial data defined by Eq. (5.16). Moreover, it can be proved that the solution guarantees the realizability of the moments at any time step if the initial set is realizable. To proceed with the proof, the following notation is used for representing the set of moments:

$$\mathbf{W} = \begin{bmatrix} m^0 & m^1 & ... & m^{2N-1} \end{bmatrix}^T . \tag{5.21}$$

It is worth reiterating that N is the number of quadrature nodes. The set of moments can be defined as below:

$$\mathbf{W} = \int_0^\infty n_L \mathbf{q}(L) \, dL , \tag{5.22}$$

where $\mathbf{q}(L) = [L^0 \ \ L^1 \ \ ... \ \ L^{2N-1}]^T$.
Equation (5.20) can be written for the set of moments by using the notation introduced in Eq. (5.21):

$$\mathbf{W}_i^{n+1} = \mathring{\mathbf{W}}_r - a_i^{n+1}(\mathring{\mathbf{W}}_r - \mathring{\mathbf{W}}_l) . \tag{5.23}$$

It should be emphasized that Eq. (5.23) is derived based on the fact that a_i^{n+1} is identical for all the moments. The proof follows by substituting Eq. (5.22) in Eq. (5.23) and performing some manipulations:

$$\int_0^\infty n_{L,i}^{n+1} \mathbf{q}(L) \, dL = \int_0^\infty \left[(1 - a_i^{n+1})\mathring{n}_{L,r} + a_i^{n+1}\mathring{n}_{L,l} \right] \mathbf{q}(L) \, dL \tag{5.24}$$

or

$$n_{L,i}^{n+1} = (1 - a_i^{n+1})\mathring{n}_{L,r} + a_i^{n+1}\mathring{n}_{L,l} . \tag{5.25}$$

The above equation guarantees the non-negativity of the $n_{L,i}^{n+1}$ because both $\mathring{n}_{L,r}$ and $\mathring{n}_{L,l}$ are defined to be non-negative NDFs and $0 \leq a_i^{n+1} \leq 1$. Consequently, the moment set of cell i at time step t_{n+1} is realizable, see [64].

Returning back to the equal-limiter concept, it is previously highlighted that an identical a_i^{n+1} for all the moments is essential to keep the moment set realizable in a Riemann problem example. The identical a_i^{n+1} originates, in turn, from the equal limiters calculated at the left and right faces (i.e., Eq. (5.18)):

$$\phi(\theta_{i-1/2}^k) = \phi\left(\frac{a_{i-1}^n - a_{i-2}^n}{a_i^n - a_{i-1}^n} \right) \quad \text{and} \quad \phi(\theta_{i+1/2}^k) = \phi\left(\frac{a_i^n - a_{i-1}^n}{a_{i+1}^n - a_i^n} \right) . \tag{5.26}$$

When source terms are present, the limiters are not generally identical for all the moments, because in this case, the smoothness of the moments may change differently and this may cause the non-realizability of the transported moment set. This suggests to find a technique to employ an identical limiter in the calculation of the moment fluxes at the faces.

Again Eq. (5.13) is rewritten for the case of $u_{\mathrm{d}} > 0$ (here a local Riemann problem is solved at each face of cell i):

$$m_i^{k*} = m_i^k - \nu_{\mathrm{d}}(m_i^k - m_{i-1}^k)$$
$$- \frac{1}{2}\nu_{\mathrm{d}}(1 - \nu_{\mathrm{d}})[\phi(\theta_{i+1/2}^k)\Delta m_{i+1/2}^k - \phi(\theta_{i-1/2}^k)\Delta m_{i-1/2}^k], \quad (5.27)$$

which can be rearranged by collecting the terms containing the moment of cells $i - 1$, i and $i + 1$ as follows:

$$m_i^{k*} = B_i^k m_{i-1}^k + C_i^k m_i^k - D_i^k m_{i+1}^k \quad (5.28)$$

with

$$B_i^k = \nu_{\mathrm{d}} - \frac{1}{2}\nu_{\mathrm{d}}(1 - \nu_{\mathrm{d}})\phi(\theta_{i-1/2}^k)$$
$$C_i^k = 1 - \nu_{\mathrm{d}} + \frac{1}{2}\nu_{\mathrm{d}}(1 - \nu_{\mathrm{d}})[\phi(\theta_{i+1/2}^k) + \phi(\theta_{i-1/2}^k)]$$
$$D_i^k = \frac{1}{2}\nu_{\mathrm{d}}(1 - \nu_{\mathrm{d}})\phi(\theta_{i+1/2}^k). \quad (5.29)$$

Writing Eq. (5.28) for the set of moments of order $k = 1, 2, ..., 2N - 1$ yields:

$$\begin{pmatrix} m_i^{0*} \\ m_i^{1*} \\ \vdots \\ m_i^{2N-1*} \end{pmatrix} = \underbrace{\begin{pmatrix} B_i^0 m_{i-1}^0 \\ B_i^1 m_{i-1}^1 \\ \vdots \\ B_i^{2N-1} m_{i-1}^{2N-1} \end{pmatrix}}_{\text{set i-1}} + \underbrace{\begin{pmatrix} C_i^0 m_i^0 \\ C_i^1 m_i^1 \\ \vdots \\ C_i^{2N-1} m_i^{2N-1} \end{pmatrix}}_{\text{set i}} - \underbrace{\begin{pmatrix} D_i^0 m_{i+1}^0 \\ D_i^1 m_{i+1}^1 \\ \vdots \\ D_i^{2N-1} m_{i+1}^{2N-1} \end{pmatrix}}_{\text{set i+1}}.$$
$$(5.30)$$

The three sets of moments in Eq. (5.30) can easily become non-realizable because, in general, the coefficients B_i^k as well as C_i^k and D_i^k might differ from one moment to another (belonging to the same moment set) as a consequence of unequal limiters. Marchisio and Fox [57] showed that a small change in just one moment can make a consistent set of moments non-realizable. However, if identical limiters are selected to estimate the fluxes of all the moments at the left and right faces, Eq. (5.30) can be written as follows:

$$\int_0^\infty n_{L,i}^* \mathbf{q}(L)\,dL = \int_0^\infty (B_i n_{L,i-1} + C_i n_{L,i} - D_i n_{L,i+1})\mathbf{q}(L)\,dL \quad (5.31)$$

or

$$n_{L,i}^* = B_i n_{L,i-1} + C_i n_{L,i} - D_i n_{L,i+1}, \quad (5.32)$$

where B_i as well as C_i and D_i are defined as below by choosing an equal limiter at

the left face, $\phi(\theta_{i-1/2})$, and one at the right face, $\phi(\theta_{i+1/2})$, for all the moments:

$$B_i = \nu_\mathrm{d} - \frac{1}{2}\nu_\mathrm{d}(1 - \nu_\mathrm{d})\phi(\theta_{i-1/2})$$

$$C_i = 1 - \nu_\mathrm{d} + \frac{1}{2}\nu_\mathrm{d}(1 - \nu_\mathrm{d})[\phi(\theta_{i+1/2}) + \phi(\theta_{i-1/2})]$$

$$D_i = \frac{1}{2}\nu_\mathrm{d}(1 - \nu_\mathrm{d})\phi(\theta_{i+1/2}) . \tag{5.33}$$

It should be noted that there is still no proof for the moment realizability in the case of employing equal limiters when source terms in the moment transport equation are present, because the last term in Eq. (5.32) is negative [62, 64]. However, the contribution of the negative term can be kept small enough through adjusting the time step since the coefficient D_i diminishes as the time step is reduced to zero. In other words, the non-realizability problem can be prevented by adjusting the time step, whereas it can arise easily regardless of the time step if the limiters are calculated independently. One should be careful when the moment sets lie on the boundary of the moment space. In this case, the underlying number density functions are indeed some point distributions, i.e. summation of some weighted delta functions. Therefore, if the moment sets in Eq. (5.30) are near or on the boundary of the moment space, reduction of the time step cannot resolve the realizability issue since the supports of the corresponding underlying number density functions in Eq. (5.32) may hardly match each other. A possible remedy can be adopting the 1-D adaptive quadrature technique proposed by Yuan and co-workers [148]. By this technique, the maximum number of quadrature nodes is selected in such a way that the moments required to calculate the quadrature weights and abscissas form a set that is located in the interior of the moment space.

The final point to be addressed is the choice of an equal flux-limiter at each face. In fact, the constraint on the boundedness of the solution narrows the choice of the equal flux-limiter. As mentioned before, the 2$^\mathrm{nd}$-order TVD schemes have the notable feature of preserving the solution bounded. It is extremely useful for the QMOM since the low-order moments are proportional to physical properties that are bounded in nature, such as mean size, surface area and volume fraction. Harten [176] established the sufficient criteria for a scheme to be TVD, which provide constraints on the flux-limiter functions:

$$\begin{cases} \phi(\theta) = 0 & \text{if } \theta < 0 \\ 0 \leq \phi(\theta) \leq \min(2\theta, 2) & \text{if } \theta \geq 0 \end{cases} . \tag{5.34}$$

Figure 5.1 represents these constraints graphically (shaded area) following the work of Sweby [175]. Moreover, it depicts the 2$^\mathrm{nd}$-order region proposed by Sweby [175] (hatched area) within which the flux-limiter functions lie. Two examples of such functions are shown by the solid line (minmod limiter [173]) and the dashed line (van Leer limiter [174]).
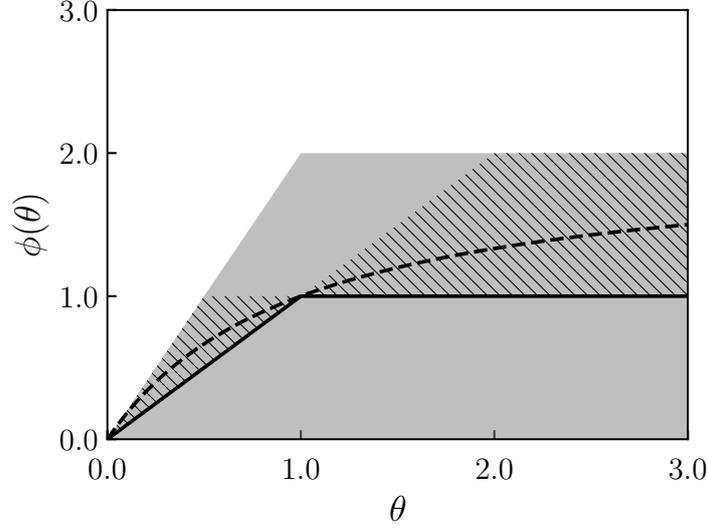
Figure 5.1: Flux-limiter functions. The shaded area specifies the TVD region and the hatched area is the 2$^{\text{nd}}$-order region by Sweby [175]. The minmod [173] and van Leer [174] limiter functions are shown by the continuous and dashed curves respectively.

The flux-limiter functions in the literature share the common feature of being non-decreasing functions of θ. Using this feature, it is simple to show that the smallest flux-limiter among all the limiters of the moments is an obvious choice that guarantees the boundedness of all the moments. The flux-limiters calculated independently by a general limiter function at a given face, e, can be represented as $\phi(\theta_e^k)$ with $k = 0,1,...,2N-1$. These limiters respect the conditions expressed in Eq. (5.34):

$$\begin{cases} \phi(\theta_e^k) = 0 & \text{if } \theta_e^k < 0 \\ 0 \leq \phi(\theta_e^k) \leq \min(2\theta_e^k,2) & \text{if } \theta_e^k \geq 0 \end{cases}. \tag{5.35}$$

Suppose that ϕ_e^{min} denotes the limiter with the minimum value:

$$\phi_e^{min} = \phi(\theta_e^m) \leq \phi(\theta_e^k) \quad \text{for} \quad k = 0,1,...,2N-1, \tag{5.36}$$

where

$$\theta_e^m \in \{\theta_e^k \mid k \in \{0,1,...,2N-1\}\}, \tag{5.37}$$

and since the flux-limiter functions are non-decreasing:

$$\theta_e^m \leq \theta_e^k \quad \text{for} \quad k = 0,1,...,2N-1. \tag{5.38}$$

In addition, the upper boundary of the TVD region shown in Eq. (5.35), $\min(2\theta_e^k,2)$, is a non-decreasing function, therefore:

$$\min(2\theta_e^m,2) \leq \min(2\theta_e^k,2) \quad \text{for} \quad k = 0,1,...,2N-1, \tag{5.39}$$

since ϕ_e^{min} respects the conditions specified in Eq. (5.35), it can be concluded that:

$$0 \le \phi_e^{min} \le \min(2\theta_e^k, 2) \quad \text{for} \quad k = 0, 1, ..., 2N - 1\,, \tag{5.40}$$

in other words, ϕ_e^{min} falls always in the TVD region specified in Figure 5.1 for all the moments. As a result, the moments remain bounded using this limiter, following the proof given by Harten [176].

It should be mentioned that, in general, the minimum limiter can fall outside the 2nd-order region of Sweby for some moments, hence resulting in solutions with accuracy of lower order. Nevertheless, the numerical results reported in the next section show remarkable improvements in comparison to the 1st-order solutions. More importantly, the results indicate a significant advantage of the proposed scheme over the realizable high-order scheme of Vikas et al. [62] since it is able to produce bounded solutions.

5.3   Application to CFD Codes

This section focuses on the application of the equal-limiter scheme to CFD codes, which is indeed our ultimate goal of introducing this scheme. For this purpose, the following three-dimensional conservative transport equation is considered for the kth-order moment:

$$\partial_t m^k + \partial_{\mathbf{x}} \cdot (\mathbf{U}_{\mathrm{d}} m^k) = 0\,. \tag{5.41}$$

The source term is not included since the focus is only on the advection of the moments. In the context of finite volume methods, Eq. (5.41) is integrated over the volume of each computational cell and then the integral of the convective term over the volume of each cell is replaced with the net flux of the kth-order moment through the faces of that cell (Gauss's theorem). Therefore, the following semi-discretized equation is obtained for a generic cell i [172]:

$$\frac{\mathrm{d}m_i^k}{\mathrm{d}t} + \frac{1}{\Delta V_i} \sum_e (\mathbf{U}_{\mathrm{d,e}} \cdot \hat{\mathbf{n}}_e) S_e m_e^k = 0\,, \tag{5.42}$$

where m_e^k and $\mathbf{U}_{\mathrm{d,e}}$ are the moment of order k and the velocity at a generic face e of cell i respectively. In addition, $\hat{\mathbf{n}}_e$ and S_e denote respectively the outward unit normal vector and the surface area of face e and ΔV_i is the volume of cell i. The transient term in Eq. (5.42) is not discretized for the reason that becomes clear later. In CFD codes, the flux of the velocity field at the cell faces, i.e. $(\mathbf{U}_{\mathrm{d,e}} \cdot \hat{\mathbf{n}}_e) S_e$, is generally known. However, the value of the moments at the faces (m_e^k) is not available and should be interpolated from the values at the centers of neighbouring cells.

It is common to interpolate the fields from cell centers to faces by employing a high-resolution TVD scheme. The idea behind these schemes is to increase the

95

accuracy and, simultaneously, preserve the monotonicity. A high-resolution TVD scheme can be thought of as a combination of a high-order scheme and a 1st-order monotone one. The high-order contribution is more important where the solution is smooth, while the 1st-order contribution prevails near the discontinuities. The implementation of high-resolution TVD schemes in CFD codes is usually on the basis of central-difference (CD) scheme, of which the anti-diffusive contribution is limited to prevent oscillations in the solution [177, 178]:

$$m_e^k = \underbrace{m_U^k}_{\text{upwind}} + \phi_e^k \underbrace{\lambda_e(m_D^k - m_U^k)}_{\text{anti-diffusive flux}}, \tag{5.43}$$

where m_U^k and m_D^k refer to the values of the moment of order k at the centers of the upwind and downwind cell neighbours of face e, respectively. The selection of the upwind and downwind cells is based on the direction of the velocity field at face e (see Figure 5.2), which is the same for all the moments. In addition, the coefficient λ_e takes on a positive constant value between 0 and 0.5, which depends on the distances between the center of face e and the centers of the two neighbouring cells. The second term on the right-hand side of Eq. (5.43) is the anti-diffusive flux, which decreases the numerical diffusion of the upwind contribution (the first term on the right-hand side of Eq. (5.43)). However, the anti-diffusive term is limited by ϕ_e^k to avoid any non-physical over- or under-shoots appearing in the results. The smoother becomes the profile of the transported moment, the larger is the value of the limiter, until it reaches the maximum imposed by the limiter function (one in the case of minmod flux-limiter). Therefore, the interpolation scheme expressed by Eq. (5.43) can change from the upwind scheme ($\phi_e^k = 0$) to the CD scheme ($\phi_e^k = 1$) as the smoothness increases. It is worth reiterating that ϕ_e^k depends on the smoothness of the transported moment of order k near face e determined by Eq. (5.11). However, in unstructured meshes, the determination of the smoothness (θ_e^k) is not generally straightforward, particularly due to the difficulty in recognising the far upwind cell for face e, e.g. cell "UU" in Figure 5.2. The reader is referred to the work by Jasak et al. [179] for more detail on the estimation of θ_e^k in arbitrarily unstructured meshes. It is noteworthy that the same method is adopted in OpenFOAM software.
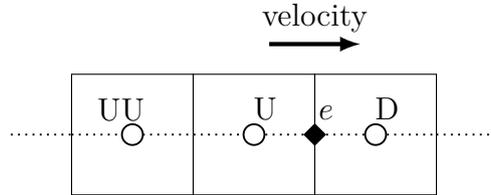

Figure 5.2: One-dimensional schematic diagram of a finite-volume cell

The value of the limiter depends on the local profile of the variable and it can be very different for the various transported variables. Unfortunately, this aspect may give rise to the non-realizability problem of the moments, when standard TVD schemes (Eq. (5.43)) are applied independently for the convection of different moments [62, 64].

The advantage of employing an identical limiter can be illustrated by rearranging Eq. (5.43) and writing it for a set of $2N-1$ moments as follows:

$$\underbrace{\begin{pmatrix} m_e^0 \\ m_e^1 \\ \vdots \\ m_e^{2N-1} \end{pmatrix}}_{\text{set e}} = \underbrace{\begin{pmatrix} (1-\lambda_e\phi_e^0)m_U^0 \\ (1-\lambda_e\phi_e^1)m_U^1 \\ \vdots \\ (1-\lambda_e\phi_e^{2N-1})m_U^{2N-1} \end{pmatrix}}_{\text{set U}} + \underbrace{\begin{pmatrix} \lambda_e\phi_e^0 m_D^0 \\ \lambda_e\phi_e^1 m_D^1 \\ \vdots \\ \lambda_e\phi_e^{2N-1}m_D^{2N-1} \end{pmatrix}}_{\text{set D}}. \tag{5.44}$$

Since the limiters for different moments, $\phi_e^0, \phi_e^1, \ldots, \phi_e^{2N-1}$ are not generally the same, the moment sets "U" and "D" can easily become non-realizable, leading to the non-realizable set of interpolated moments at face e. However, selecting an identical limiter, let it be ϕ_e^{min}, guarantees the realizability of the interpolated moment set e, as long as the moment sets "U" and "D" are realizable:

$$\underbrace{\begin{pmatrix} m_e^0 \\ m_e^1 \\ \vdots \\ m_e^{2N-1} \end{pmatrix}}_{\text{set e}} = (1-\lambda_e\phi_e^{min})\underbrace{\begin{pmatrix} m_U^0 \\ m_U^1 \\ \vdots \\ m_U^{2N-1} \end{pmatrix}}_{\text{set U}} + \lambda_e\phi_e^{min}\underbrace{\begin{pmatrix} m_D^0 \\ m_D^1 \\ \vdots \\ m_D^{2N-1} \end{pmatrix}}_{\text{set D}}. \tag{5.45}$$

It is worth reiterating that the value of limiter ϕ_e^{min} is between 0 and 2. Moreover, the moment sets "U" and "D" belong to the previous time step if an explicit method is used to advance in time, and therefore they are realizable.

It should be noted that the realizability of the interpolated moments on the faces does not ensure the realizability of the calculated moments at the new time step. To elaborate, let the transient term in Eq. (5.42) be integrated using an explicit Euler scheme [172] and then write the fully-discretized equation for the set of $2N-1$ moments:

$$\mathbf{W}_i^{n+1} = \mathbf{W}_i^n - \frac{\Delta t}{\Delta V_i}\sum_e(\mathbf{U}_{d,e}^n \cdot \hat{\mathbf{n}}_e)S_e\mathbf{W}_e^n. \tag{5.46}$$

The use of an identical limiter for all the moments guarantees that the moment set $\mathbf{W}_e^n$ be realizable, and therefore an underlying number density function ($n_{L,e}^n$) can be associated with it. This allows us to write Eq. (5.46) as the following:

$$n_{L,i}^{n+1} = n_{L,i}^n - \frac{\Delta t}{\Delta V_i}\sum_e(\mathbf{U}_{d,e}^n \cdot \hat{\mathbf{n}}_e)S_e n_{L,e}^n. \tag{5.47}$$

The summation in the above equation can be separated into two contributions of in-going and out-going fluxes:

$$
n_{L,i}^{n+1} = n_{L,i}^n - \underbrace{\frac{\Delta t}{\Delta V_i} \sum_e \min[(\mathbf{U}_{d,e}^n \cdot \hat{\mathbf{n}}_e), 0] S_e n_{L,e}^n}_{\text{in-going fluxes}} - \underbrace{\frac{\Delta t}{\Delta V_i} \sum_e \max[(\mathbf{U}_{d,e}^n \cdot \hat{\mathbf{n}}_e), 0] S_e n_{L,e}^n}_{\text{out-going fluxes}} .
$$

$$(5.48)$$

The in-going fluxes have positive sign and cannot rise the realizability issue, whereas, the outgoing fluxes have negative sign and can cause realizability issue, i.e. negativity of $n_{L,i}^{n+1}$. However, the out-going fluxes can be still decomposed into two separate upwind and downwind contributions corresponding to the upwind and downwind neighbouring cells of the corresponding faces. It is noteworthy that the upwind cell of these faces indeed coincides with cell i since the flux at these faces is out-going. Thus, the first and third terms on the right-hand side of Eq. (5.48) can be written as follows:

$$
\left(1 - (1 - \lambda_e \phi_e^{min}) \frac{\Delta t}{\Delta V_i} \sum_e \max[(\mathbf{U}_{d,e}^n \cdot \hat{\mathbf{n}}_e), 0] S_e\right) n_{L,i}^n
$$
$$
- (1 - \lambda_e \phi_e^{min}) \frac{\Delta t}{\Delta V_i} \sum_e \max[(\mathbf{U}_{d,e}^n \cdot \hat{\mathbf{n}}_e), 0] S_e n_{L,D_e}^n , \quad (5.49)
$$

where n_{L,D_e}^n denotes the (downwind) neighbouring cell separated by face e from cell i. As can be seen, the entire contribution of the cell i is positive as long as the coefficient behind $n_{L,i}^n$ is positive, leading to the following CFL-like condition:

$$
\frac{\Delta t}{\Delta V_i} \sum_e \max[(\mathbf{U}_{d,e}^n \cdot \hat{\mathbf{n}}_e), 0] S_e < 1 \qquad (5.50)
$$

Therefore, the only remaining negative contributions are due to the information (distributions) of the downwind cells (with respect to cell i) that propagates back into cell i, which is the characteristic of high-order schemes. These negative contributions can generally lead to the realizability issue, i.e. negativity of $n_{L,i}^{n+1}$. However, as discussed previously for the one-dimensional constant-velocity case, the negative contributions can be kept small (in comparison to the contribution of $n_{L,i}^n$) by controlling the time step. It is noteworthy that this technique may fail when the moment sets are near/at the boundary of the moment space, as explained before. Returning back to the time-integration of the transient term in Eq. (5.42), it should be noted that one notable advantage of the equal-limiter scheme is the possibility of using implicit time-integration for the advection of the moments. This is due to the fact that the equal-limiter scheme interpolates the moments directly, whereas, for instance, the quasi-high-order scheme is normally implemented by using explicit time-integration schemes.

Last, the proposed technique is very simple from the computational point of view and can be easily implemented in three-dimensional CFD solvers. The only

additional steps are comparing the limiter values calculated for the moments at each face and then replacing all of them with the smallest one.

5.4   Numerical Examples

This section evaluates the performance of the proposed technique for the advection of moments in two different parts. The first one is focused on comparing the predictions obtained by three schemes for the advection of the moments in a mono-dimensional constant-velocity problem. The second part evaluates the performance of the schemes by solving the moment transport equations coupled with the CFD simulation of a two-dimensional transient lid-driven cavity flow. In both parts, the results obtained by the equal-limiter scheme are compared with those obtained by the 1st-order upwind scheme and the quasi-2nd-order scheme by Vikas et al. [62]. These schemes are described in the following:

Upwind scheme. The upwind scheme assumes that the value on the face is equal to the value of the cell located at the upstream side of the face. Referring to Figure 5.2:

$$m_e^k = m_U^k\,.\tag{5.51}$$

It is commonly employed to solve the moment transport equations, since it is proved to preserve the realizability of the moment set provided the CFL condition is respected [64]. Moreover, the upwind scheme satisfies the monotonicity condition, i.e. a monotonic distribution before advection remains monotonic after advection [65]. The main drawbacks of the scheme are the 1st-order accuracy and the significant numerical diffusion appearing in the results, especially when coarse computational grids are used.

Quasi-2nd-order realizable scheme. Vikas and co-workers [62] presented an approach to develop realizable high-order schemes that are applicable to the QBMM. The central idea is to interpolate the quadrature weights and abscissas separately and then to evaluate the moment fluxes by using the interpolated weights and abscissas. They proved that the moments remain realizable when the quadrature abscissas are interpolated using the upwind scheme whereas the quadrature weights are interpolated using a high-order TVD scheme, provided the time-step (Δt) fulfills the following criterion:

$$\Delta t \leq \Delta V_i \times \frac{w_{i,p}^n}{\sum_e w_{e,p}^n \, \max(\mathbf{U}_{\mathrm{d,e}}^n \cdot \hat{\mathbf{n}}_e, 0) S_e} \qquad \forall p \in 1, 2, \ldots, N\,,\tag{5.52}$$

where $w_{i,p}^n$ and $w_{e,p}^n$ are cell and face values of the weight of the quadrature node p. The above criterion should be fulfilled in all the cells of the simulation domain.

The implementation of this scheme includes the following steps:

99

1. Calculate the quadrature abscissas and weights from the moments in each cell by applying the inversion algorithm.
2. Interpolate the quadrature abscissas on the faces using the upwind scheme.
3. Interpolate the quadrature weights on the faces by employing the high-resolution TVD scheme with *minmod* flux-limiter described in the previous section.
4. Reconstruct the moments on the faces by inserting the interpolated abscissas and weights of the quadrature into Eq. (3.23).

Last, it is noteworthy that the quasi-2nd-order scheme does not necessarily respect the boundedness criteria established by Harten [176].

5.4.1 One-Dimensional Advection with Constant-Velocity

This part employs the equal-limiter scheme for the advection of moments in spatially mono-dimensional problems with the disperse particle size as the only internal coordinate of the PBE. The first example deals with the pure advection of the moments without any source term, while the next examples include the aggregation/breakage source terms in the moment transport equations.

All the cases use a 3-node quadrature to approximate the NDF. This number of nodes requires to track the first 6 moments with respect to the particle size, $m^0, m^1, ..., m^5$. The calculation of the weights and nodes is done by using the Chebyshev algorithm. The spatial problems are defined over the spatial domain [0,1], which is discretized to cells of identical size $\Delta x = 0.01$. The fluxes at the faces are calculated by using high-resolution limited-flux methods. The limiters, in turn, are computed using the minmod function, as it was also used by Vikas et al [62]. Two ghost cells at the left side of the domain and one ghost cell at the right side are considered to cope with the three-cell stencil required by the employed high-resolution schemes. The advection velocity, u_{d}, is set to 1.0 and Δt is calculated by fixing the CFL condition equal to 0.5. The following solution procedure is used to advance in time, starting from the initial data, which is based on the explicit fractional-step method for the time integration:

1. Initialize the moments in the interior domain.

2. Apply the boundary conditions at the two left ghost cells.

3. Calculate the limiters for all the moments at each face.

4. Find the minimum limiter at each face.

5. Calculate the flux of the moments using the minimum limiter at each face.

6. Compute the intermediate values of the moments at each interior cell using the fluxes at the corresponding left and right faces after a time step equal to Δt.

7. Find the weights and the nodes of the quadrature at each interior cell using the intermediate values of the moments.

8. Calculate the source contributions at each interior cell using the corresponding quadrature approximation of the NDF.

9. Advance the intermediate values of the moments at each interior cell by one time step Δt using the calculated source terms.

10. Apply the boundary condition at the right ghost cell using zero-order extrapolation from the last interior cell of the domain.

11. Repeat steps 3 to 10 until obtaining the solution at the desired time.

Steps 8 and 9 (fractional-step approach) are obviously required only if source terms are present. In this thesis, the source terms are treated by a single-stage method as explained in steps 8 and 9. However, these steps can be modified to use a two-stage method, leading to higher accuracy for the fractional-step approach as explained by LeVeque [65]. It should be emphasized that this suggestion concerns the application of two-stage methods only for updating the intermediate moments by the source terms. Therefore, no realizability issue is generally expected in the case of using two-stage methods instead of one-stage method only to treat the source terms, provided that the intermediate moments after the advection are realizable. Furthermore, step 7 is done even in the case without source term to check the realizability of the moments.

More details on the problem settings are presented for each case separately.

Pure advection of the moments

The first example is the one-dimensional pure advection of the moments, i.e. no source term, with the following initial and boundary conditions:

$$
\begin{aligned}
\text{IC}: \quad & m^k(0, x_i) = \mathring{m}^k \qquad \text{for} \quad i = 0, 1, 2, ..., p \\
\text{BC (ghost cells)}: \quad & \left\{ \begin{array}{l} m^k(t_n, x_{-1}) = m^k(t_n, x_{-2}) = m_b^k \\ m^k(t_n, x_{p+1}) = m^k(t_n, x_p) \end{array} \right. ,
\end{aligned}
\tag{5.53}
$$

where the interior cells are numbered from 0 to p. The initial conditions $\mathring{m}^k$ and the boundary conditions m_b^k are two sets of scaled moments having the shape of different log-normal distributions, $\mathring{Y}$ and Y_b. The parameters of the distributions, i.e. the mean and the standard deviation of the corresponding normal distributions, are respectively $(\mathring{\mu}, \mathring{\sigma}) = (\ln(0.008), 0.22)$ and $(\mu_b, \sigma_b) = (\ln(0.005), 0.2)$. Furthermore, the zero-order moments are $\mathring{m}^0 = 20000$ and $m_b^0 = 800000$ respectively. It should be noted that the two log-normal distributions have different parameters to avoid their quadrature approximations having the same nodes. Otherwise, the interpolated

nodes on the faces are identical to those of the cells regardless of the employed scheme. Then, it is trivial to show that, in this special case, the quasi-2$^{\text{nd}}$-order scheme proposed by Vikas et al. [62] is essentially the same as applying the 2$^{\text{nd}}$-order scheme directly to the moments.

Figure 5.3 compares the results obtained by employing the 1$^{\text{st}}$-order scheme, quasi-2$^{\text{nd}}$-order scheme and the proposed equal-limiter scheme. Furthermore, the analytical solution is plotted in Figure 5.3 to provide a benchmark. It is pointless to report the results by the standard 2$^{\text{nd}}$-order TVD scheme since, as proved before, the corresponding results would be identical to those obtained by the equal-limiter scheme in this example. As expected, the solution given by the 1$^{\text{st}}$-order scheme is very diffusive. The quasi-2$^{\text{nd}}$-order scheme improves the accuracy of the results by applying the 2$^{\text{nd}}$-order scheme to the weights. However, applying a TVD scheme to the weights does not guarantee the boundedness of the transported moments, hence the appearance of the non-physical oscillations in the solutions. The least oscillations belong to the moment of order zero as expected, since it is simply equivalent to the sum of the weights, the variable to which the TVD scheme is applied in the quasi-2$^{\text{nd}}$-order scheme. The oscillations become more intense as the moment order increases. It should be noted that, according to our tests, the oscillations may increase or vanish depending on the characteristics of the underlying NDFs. The best predictions belong to the equal-limiter scheme, which is indeed the full 2$^{\text{nd}}$-order TVD scheme since this numerical example is the same as the pure advection Riemann problem studied in Section 5.2. Consequently, the predictions are bounded and without any oscillation.

Moment advection with source term

The next examples deal with a more practical application. The moments of a particle size distribution are introduced and advected in the domain while they are subject to local changes due to the effect of the aggregation/breakage of the particles. The initial and boundary conditions are the same as the case of pure advection (see Eq. (5.53)). In the following, two cases are presented, in which the aggregation and breakage are considered separately. Both aggregation and breakage are modelled by assuming a constant kernel. For the case of breakage, the daughter size distribution is expressed by assuming the symmetric fragmentation of the particles [112]. The reasoning behind these simplistic assumptions is the possibility of obtaining analytical solutions for the moments of the NDF.

Constant aggregation kernel. In this case, the source term in Eq. (5.6) is calculated as below [112]:

$$\bar{\mathcal{S}}_i^k = \frac{1}{2} \sum_{p=1}^{3} w_{i,p} \sum_{q=1}^{3} w_{i,q} \left(L_{i,p}^3 + L_{i,q}^3\right)^{k/3} a - \sum_{p=1}^{3} L_{i,p}^k w_{i,p} \sum_{q=1}^{3} w_{i,q}\, a\,, \qquad (5.54)$$
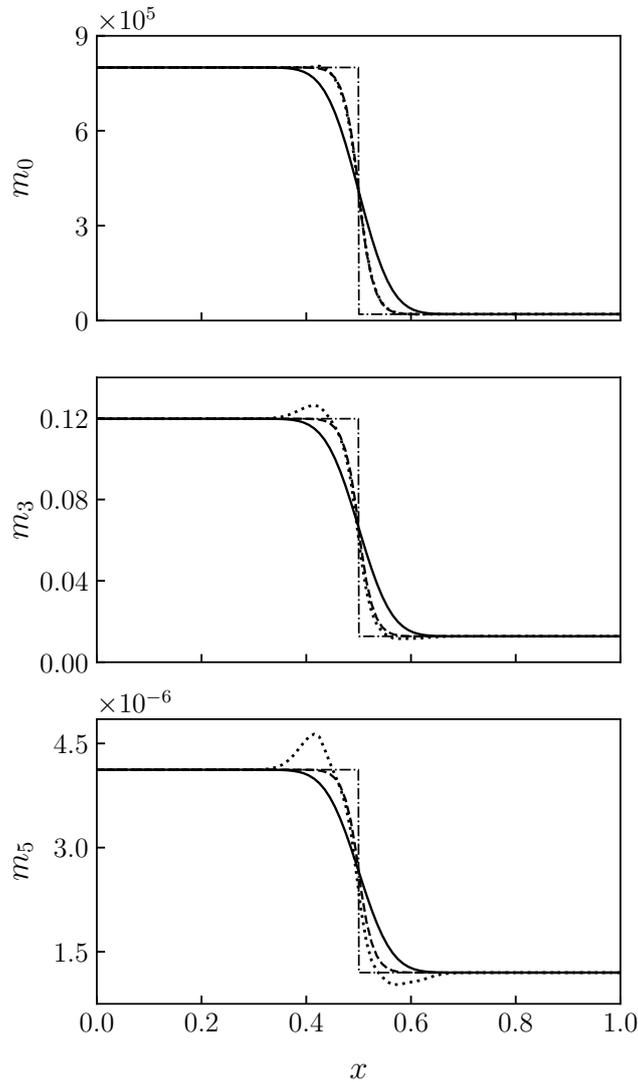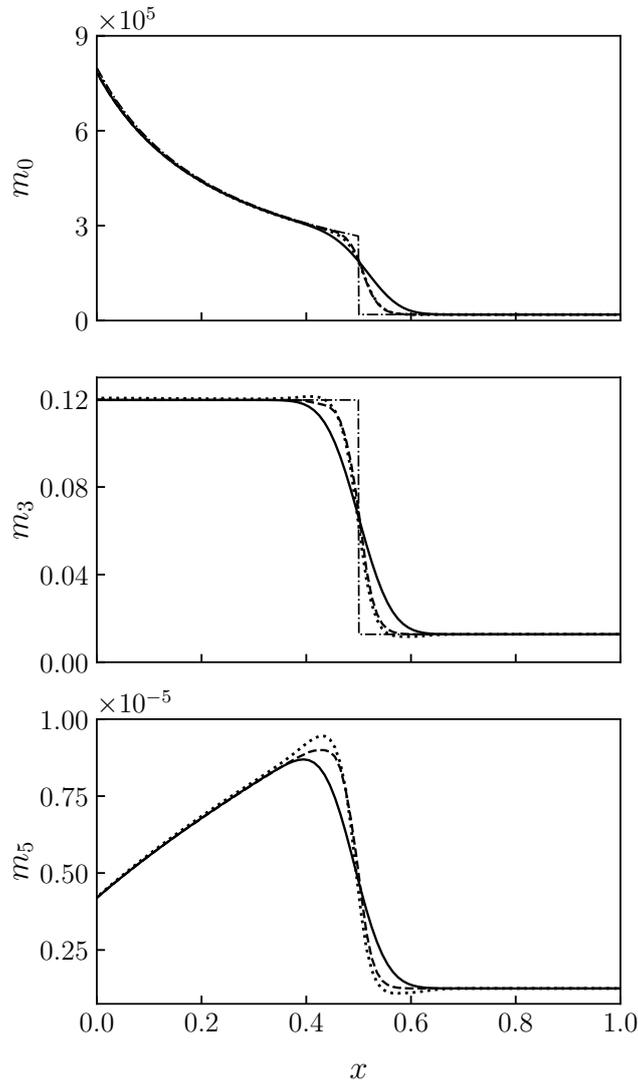
Figure 5.3: Comparison of the results obtained by employing different schemes for the case of pure advection: 1) analytical solution (dot-dashed line); 2) upwind scheme (continuous line); 3) quasi 2$^{\text{nd}}$-order scheme (dotted line); 4) equal-limiter scheme (dashed line)

where $a = 10^{-5} \ (m^3 \cdot s^{-1})$ is the aggregation kernel.

The solutions obtained by the studied schemes are shown in Figure 5.4. As it can be seen, both the quasi-2$^{\text{nd}}$-order and equal-limiter schemes improve the accuracy of the results with respect to the 1$^{\text{st}}$-order scheme. It is notable that, despite employing the minimum limiter, the equal-limiter scheme produces almost comparable results to those of the quasi-2$^{\text{nd}}$-order scheme. Moreover, the solutions of m^3 indicate that only the 1$^{\text{st}}$-order and equal-limiter schemes are bounded, as
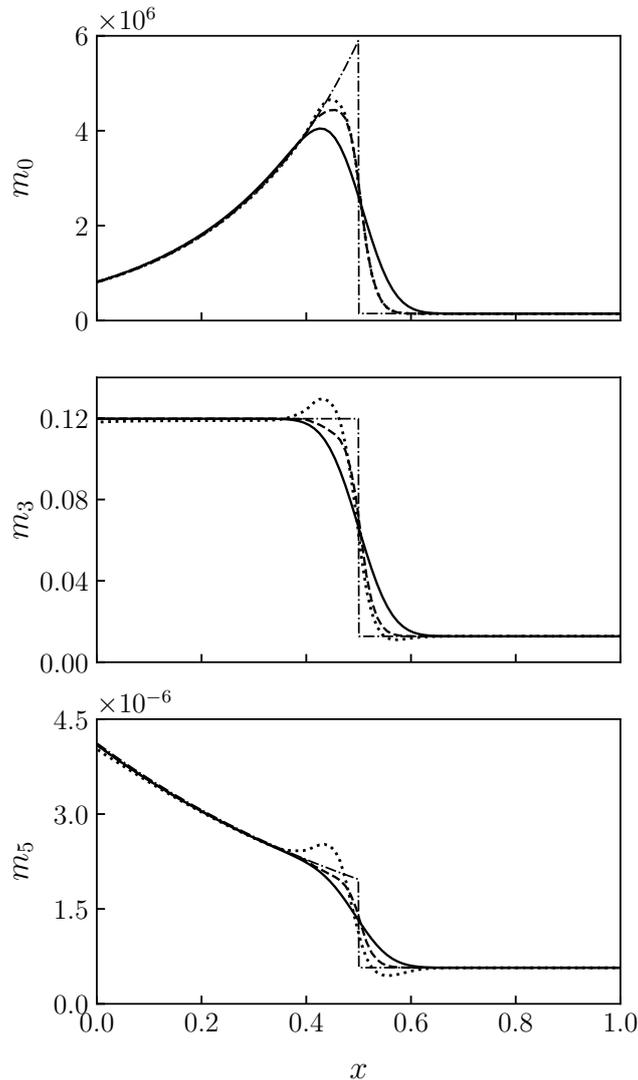
103

Figure 5.4: Comparison of the results obtained by employing different schemes for the case of constant aggregation kernel: 1) analytical solution if available (dot-dashed line); 2) upwind scheme (continuous line); 3) quasi 2nd-order scheme (dotted line); 4) equal-limiter scheme (dashed line)

expected. Instead, a slight degree of over- and under-shoot exists in the solution of the quasi-2nd-order scheme. The appearance of these spurious oscillations is certainly due to the numerics as both the aggregation and breakage of the particles have no effect on the moment of order three with respect to the particle size. Although no analytical solution is available for m^5, some degree of over- and under-shoots can be observed visually in the solution obtained by the quasi-2nd-order scheme. Again it can be seen that the amplitude of the oscillations are intensified

as the moment order increases. It is worth mentioning that employing the standard 2nd-order TVD scheme is not feasible because the moments get corrupted shortly after starting the simulation and consequently the Chebyshev algorithm fails to calculate the weights and the abscissas required for the source calculation. Even reducing the time step by a factor of 100, equivalent to an impractically small CFL value of 0.005, cannot remedy the non-realizability problem. This shows the effectiveness of the proposed equal-limiter scheme in preserving the realizability of the moments when the 2nd-order TVD schemes are employed.

Symmetric constant breakage kernel. In this case, the source term in Eq. (5.6) is calculated as below [112]:

$$\bar{\mathcal{S}}_i^k = \sum_{p=1}^{3} w_{i,p} 2^{(3-k)/3} L_{i,p}^k \, b - \sum_{p=1}^{3} w_{i,p} L_{i,p}^k \, b \,, \tag{5.55}$$

where $b = 4 \ (s^{-1})$ is the breakage kernel.

Figure 5.5 depicts the results provided by the studied schemes along with the analytical solutions. The same comments presented for the case of pure aggregation apply also to this case with the difference that here the oscillating behavior of the quasi 2nd-order scheme is more intense. This further highlights the advantage of the equal-limiter scheme whenever the boundedness of the solution is strictly required.

Figure 5.5: Comparison of the results obtained by employing different schemes for the case of symmetric constant breakage kernel: 1) analytical solution (dot-dashed line); 2) upwind scheme (continuous line); 3) quasi 2nd-order scheme (dotted line); 4) equal-limiter scheme (dashed line)

5.4.2 Pure Advection in Two-Dimensional Transient Flow

The previous part presents satisfactory results obtained by the equal-limiter scheme in some examples based on the one-dimensional constant-velocity Riemann problem. However, it is important to examine the predictions obtainable by the proposed scheme in systems with higher dimensions and realistic flow fields, e.g. non-uniform and/or transient velocity. For this purpose, a familiar two-dimensional transient flow, known as the lid-driven cavity, is selected to compare the results for

106

the pure advection of moments obtained by employing the upwind, quasi-2nd-order and equal-limiter schemes. The moments belong to a distribution that represents a population of micro-droplets transported by a carrier liquid. The micro-droplets are assumed to have negligible inertia and therefore they move with the same velocity as the carrier liquid.

The simulation domain is a square with the length (L_w) of 10 cm and it is discretized by a structured uniform Cartesian grid comprising of 10000 square cells of size 1 mm. The flow is confined by four boundaries of type wall, of which the top one moves with the velocity (U_w) of 1 m/s while the others are fixed. The kinematic viscosity of the liquid (ν_l) is set to 2.5×10^{-4} (m^2/s), which results to Reynolds number of 400 defined by $U_w L_w / \nu_l$. The liquid is assumed to be stagnant at time zero and then a transient flow develops due to the constant velocity (U_w) applied at the top wall.

The transient simulations are done by using the icoFoam solver of OpenFOAM, which solves the governing (constant-density) Navier-Stokes equations for the liquid phase numerically by using the PISO algorithm [172]. The time step is set to 0.0001 (s) to keep the maximum Courant number below 0.1. The solution of the velocity field at three time instants are shown in Figure 5.6. The solver is modified to solve simultaneously the moment transport equations. At the beginning of each time step, the moments of the micro-droplet population are advected in time by using the velocity field of the previous time step. Then, the flow field of the liquid phase is updated by using the PISO algorithm. Regarding the advection of the moments, as mentioned in Section 5.3, the implicit Euler time-integration can be used with the advection schemes that deal with the moments directly, and therefore is adopted here when the upwind and equal-limiter schemes are employed. In contrast, the quasi-2nd-order scheme is implemented with Euler explicit time-integration. The minmod limiter function is used for the interpolation of quadrature weights in the case of employing the quasi-2nd-order scheme and for the interpolation of moments in the case of employing the equal-limiter scheme.
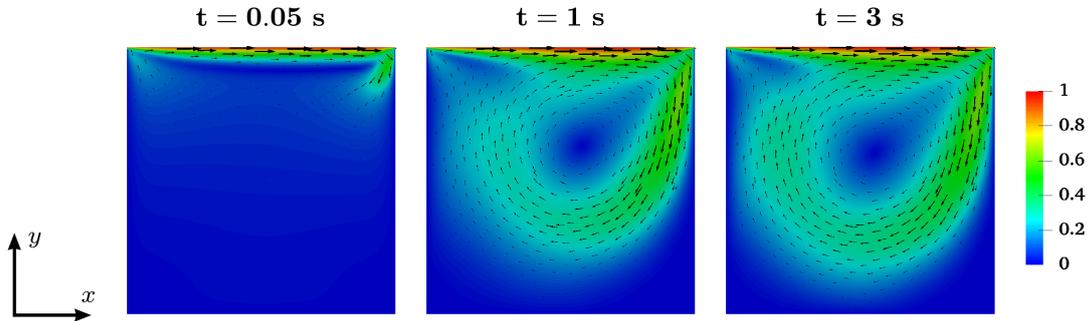

Figure 5.6: Velocity field (m/s) of the simulated two-dimensional lid-driven cavity flow at three time instants.

Two different cases corresponding to two different initial conditions for the moments are considered. The first initial condition is defined such that there is no micro-droplets in all the domain except for a square patch where a population of micro droplets with the average size of 100 μm and standard deviation of 20 μm is introduced. The population is assumed to be distributed log-normally on the size space. The initial conditions for the moments are calculated based on this log-normal distribution scaled to adjust the volume fraction of the micro-droplets equal to 0.05 (assuming the spherical shape for the micro-droplets). Figure 5.7 depicts the initial conditions for the moment of order three, along with the solutions for the same moment at $t = 3$ s obtained by employing the 1st-order upwind, quasi-2nd-order and equal-limiter schemes. As can be seen, the solution obtained by the upwind scheme suffers from a high numerical diffusion. In contrast, both the quasi-2nd-order and equal-limiter schemes yield comparable results, which have higher resolution with respect to the one obtained by the upwind scheme. It is noteworthy that the same contour plots (but of different values) are obtained for the other moments, which is expected since the shape of the distribution corresponding to the underlying NDF remains the same in this pure advection problem. As a result, the abscissas of the quadrature approximation are the same in all the cells of the domain.

As mentioned previously, the quasi-2nd-order scheme interpolates the abscissas of the quadrature with a 1st-order scheme, whereas it interpolates the weights of the quadrature with a 2nd-order scheme. Therefore, when the quadrature abscissas are the same throughout the domain, the entire resolution of the quasi-2nd-order scheme is the same as the 2nd-order scheme. The reason is that the value of abscissas on the faces are the same as those at the cell centers regardless of the employed scheme and consequently interpolating the weights with a given 2nd-order scheme onto the faces and then calculating the moments on the faces (using the same abscissas) is equivalent to interpolating the moments directly onto the faces using that 2nd-order scheme. However, this equivalency is not generally valid when the abscissas are not the same through the domain. Thus, it is worth examining the performance of the schemes in the case of co-existing two different distributions, i.e. having different quadrature abscissas, in the system at time zero. For this purpose, the same square patch (with the same population of micro-droplets) defined by the initial conditions of the previous case is considered also here. However, it is assumed that another population of micro-droplet exists outside the square patch, instead of assuming no micro-droplet existing in that zone. Let the population of micro-droplets out of the square patch be also distributed log-normally on the size space with the average size equal to 50 μm and the standard deviation of 7.5 μm. This distribution is scaled to have the volume fraction of the micro-droplets equal to 0.001. Then, the initial condition of the moments is defined based on this scaled distribution, as shown in Figures 5.8 and 5.9 for the moments of order zero and three respectively. Moreover, the predictions at $t = 3$ s are depicted by these

a)

b)

upwind   **quasi-**   **equal-limiter**
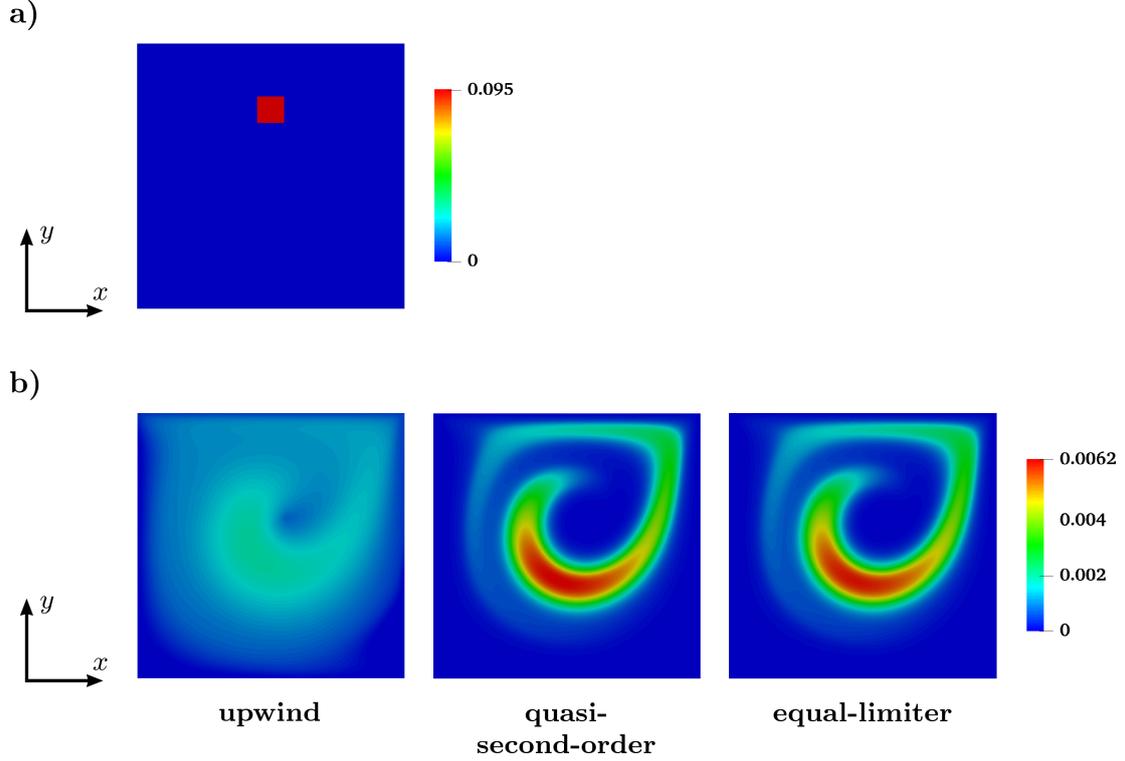   **second-order**

Figure 5.7: Comparison of the studied schemes for the advection of m_3 in the two-dimensional cavity flow. (a) The initial condition at $t = 0$; (b) the predictions obtained by employing the different schemes at $t = 3$.

figures for the mentioned moments. As it can be seen in Figure 5.8, the values of m_0 obtained by employing the quasi-2nd-order scheme do not remain bounded between the limits defined by the initial conditions. It is noteworthy that in the QBMM, the transported variables are indeed the moments and therefore in a pure advection with a solenoidal velocity field, the solution for the moments should remain bounded between the limits defined by the initial conditions. This issue concerning the quasi-2nd-order scheme can be associated with the fact that this scheme interpolates the weights and abscissas of the quadrature separately, and therefore there is no guarantee that the TVD criteria [176] are respected by this scheme. In contrast, the solution obtained by the equal-limiter scheme (when it is used with the minimum limiter) respects the boundedness property of the moments. Moreover, the applied change in the initial condition of the moments should not change the pattern of the solution contour plots, since the current initial condition with the two distributions can be changed to a problem with initial condition similar to the previous case (micro droplets existing only in a square patches) by a change of variables. However, the comparison between the results shown in Figure 5.9 with those depicted in Figure 5.7 highlights that only the equal-limiter scheme

109

reproduces the same pattern for m_3 in both cases. In addition, the pattern of the results obtained by the equal-limiter scheme for m_0 and m_3 shown in Figures 5.8 and 5.9 are the same, whereas this is not the case for the results obtained by the quasi-2nd-order scheme. This final example emphasizes the advantage of employing a scheme that interpolates the moments directly, e.g. equal-limiter scheme, instead of interpolating some variables related to the moments.
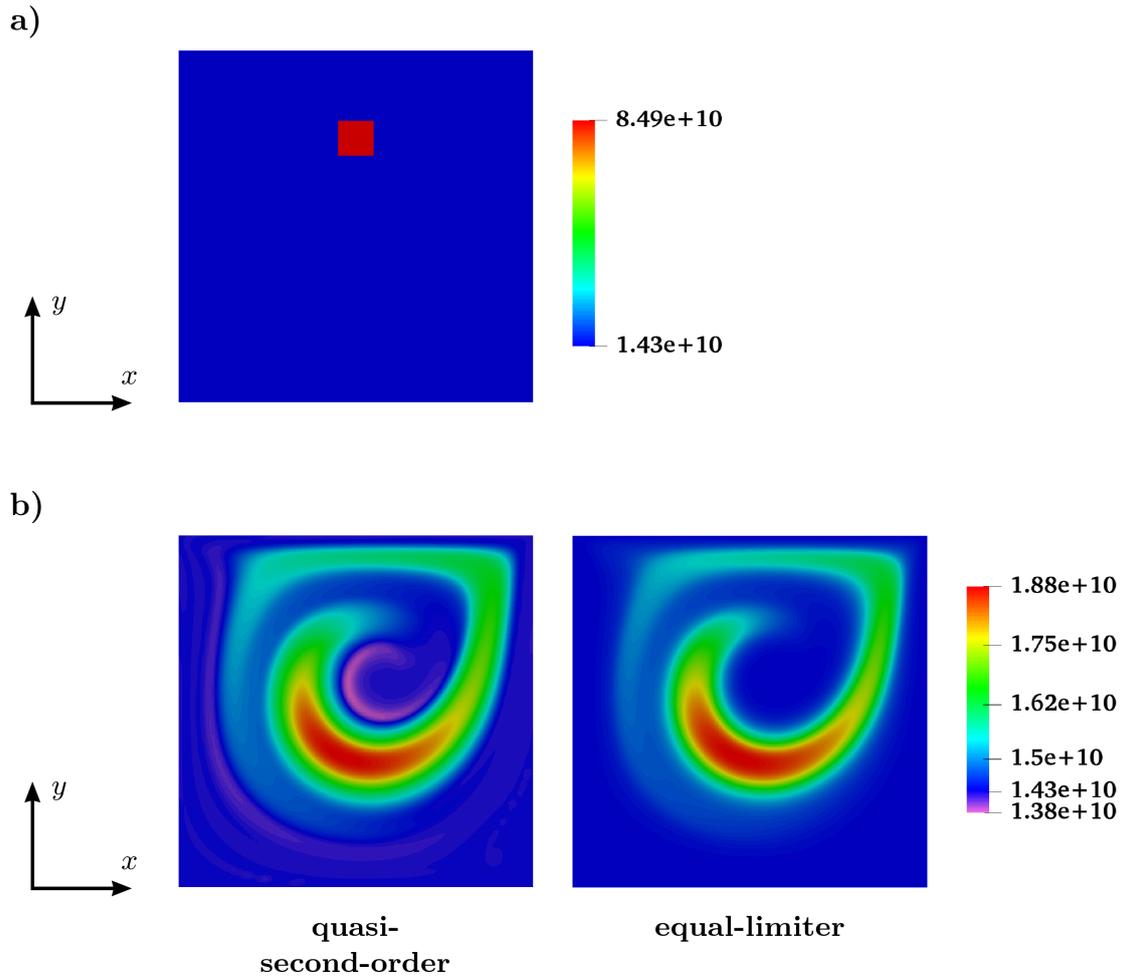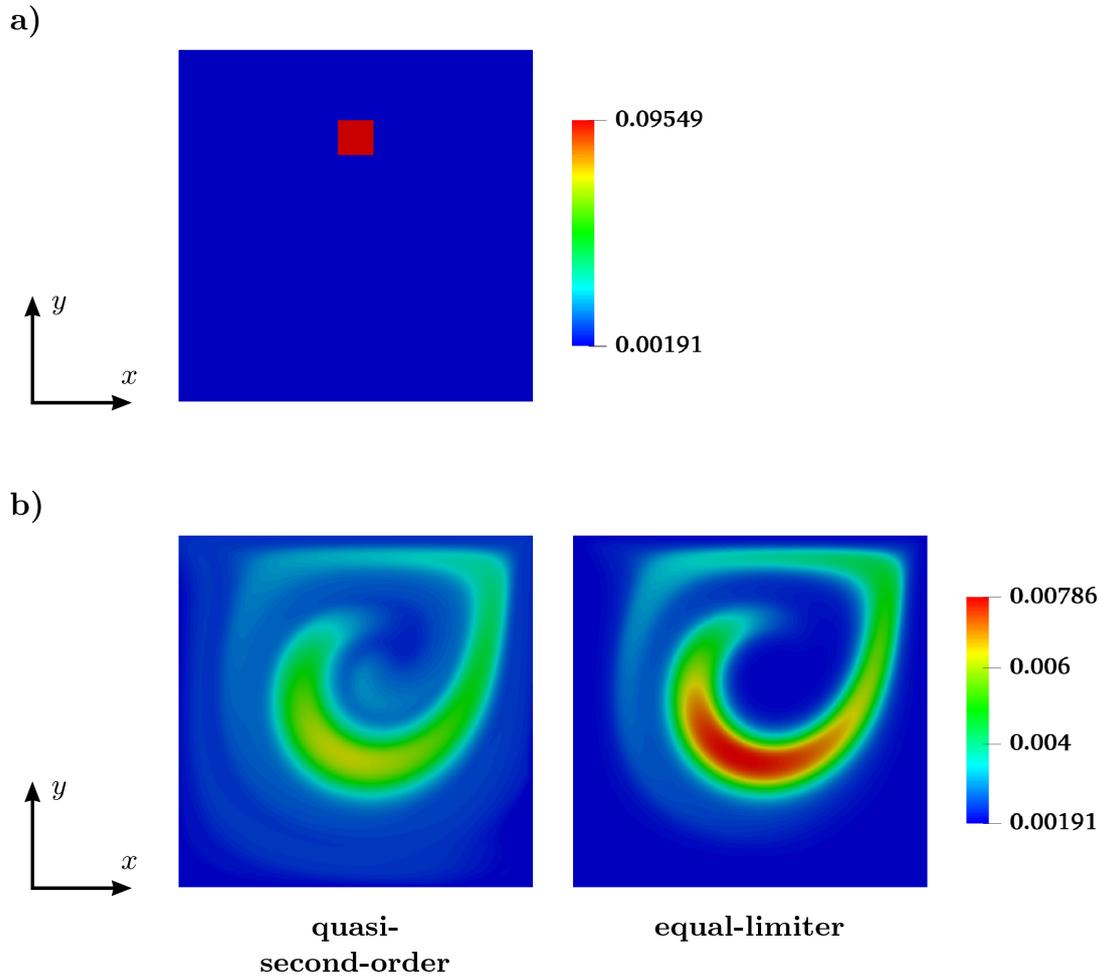
a)

b)

Figure 5.8: Comparison of the studied schemes for the advection of m_0 in the two-dimensional cavity flow in the case of existing two different distributions in the domain. (a) The initial condition at $t = 0$; (b) the predictions obtained by employing the different schemes at $t = 3$.

a)

b)

quasi-
second-order

equal-limiter

Figure 5.9: comparison of the studied schemes for the advection of m_3 in the two-dimensional cavity flow in the case of existing two different distributions in the domain. (a) The initial condition at $t = 0$; (b) the predictions obtained by employing the different schemes at $t = 3$.

In the next chapter, we apply the proposed scheme for the three-dimensional CFD-PBM simulation of the TOPFLOW facility and compare its predictions with those of the other discretization schemes.

Chapter 6

CFD-PBM Simulation of Bubbly Flows

6.1 Introduction

In the previous chapter, it is shown that the separate interpolation of weights and abscissas of the quadrature may cause non-physical oscillations in the solution of a mono-dimensional Riemann problem. To tackle this issue, a novel TVD scheme is proposed, in which the moments are directly interpolated on the cell faces, using the same flux-limiter for all the moments. It is suggested to choose the minimum limiter among the limiters calculated separately for each moment, as it guarantees the boundedness of all the moments. Eventually, the reported numerical tests on some mono- and two-dimensional problems evidences that this scheme helps in overcoming the realizability issue.

This chapter investigates the applicability of the equal-limiter scheme for the advection of moments to the CFD-PBM simulation of the TOPFLOW facility, described in Section 4.1. In this system, the streamlines for both phases are aligned dominantly in the axial direction of the pipe i.e. the axial component of the phase velocities is much larger than the radial one. However, it is the radial component of the velocities that determines the radial distribution of the phases as the flow develops in the axial direction. Therefore, the numerical diffusion must be reduced as much as possible, since it may falsely affect the predicted solution, especially in the radial and circumferential directions. Thus, it is expected that the solution of the PBE in this system requires employing high-order schemes for the convection of the moments. This chapter, first, illustrates the possible deficiency of the 1st-order upwind scheme in producing physical solutions. Next, we compare the predictions obtained by employing high-order schemes including the standard 2nd-order TVD scheme, quasi-2nd-order realizable scheme developed by Vikas and coworkers [62] and the equal-limiter scheme introduced in the previous chapter, and also discuss their cons and pros. Then, we propose a modification to the original equal-limiter

scheme to prevent this scheme from reducing virtually to the 1st-order upwind scheme.

6.2   Numerical Details

6.2.1   Solver Details

The results shown in this chapter are obtained by using a coupled TFM-PBM code, which is described in Chapter 3. In fact, the code is the built-in two-fluid solver of OpenFOAM software v5.0, which is modified to solve the PBE. The TFM predicts the turbulent flow fields, including phase volume fractions, phase velocities, pressure, turbulent kinetic energy and turbulent dissipation rate, some of which are needed by the PBM. At the same time, the PBM predicts the properties of the population of gas bubbles to be used by the TFM, here the average bubble size.

Concerning the TFM, some settings are modified with respect to those used for the fixed bubble size simulations of Chapter 4. The number of PIMPLE and PISO loops, i.e. *nOuterCorrector* and *nCorrector*, are adjusted to one and two respectively, therefore the solution algorithm can be thought of as the PISO algorithm. In addition, the PISO algorithm is configured to perform only one iteration to correct the non-orthogonal contributions. Moreover, the 2nd-order TVD *minmod* is used as the discretization scheme for the convective terms and the gradients at the cell centers are evaluated by using Gauss theorem. These modifications are made to increase the speed of the simulations. As mentioned in Chapter 4, a limiter, e.g. *cellMDLimiter*, can be applied for the estimation of gradients to prevent unbounded reconstructed face values with respect to the neighbouring cell values, particularly in the case of large gradient values. However, it causes numerical diffusion in the circumferential direction, which is not desirable. Therefore, this correction is avoided in the following simulations.

The employed interfacial forces are selected following the results shown in Chapter 4. The drag force is calculated by using Tomiyama correlation Eq. (2.13) and the turbulent dispersion by Burns' expression Eq. (2.24). The wall lubrication force is modelled following Lubchenko's approach Eq. (2.27). Finally, the lift coefficients are chosen following the results obtained previously and summarized in Table 6.1.

Table 6.1: The lift coefficients employed for the TFM-PBM simulations

Experimental condition	008	042	040	028	063	072
Mean value	0.19	0.19	0.03	-0.05	-0.05	-0.05

The coupled TFM-PBM code is specialized for a univariate PBE and therefore it adopts the QMOM as the solution method for the PBE. Moreover, it considers the

change of the gas density in the PBE formulation because the bubbles experience change in the hydrodynamic pressure as they travel upward in the TOPFLOW facility. Therefore, Eq. (3.49) is used to track the evolution of the moments. The source term, $\bar{\mathcal{S}}_k$ in Eq. (3.49), takes into account the change in the bubble size distribution (BSD) due to break-up and coalescence, which are modelled by the expressions described in Section 3.1.2.

Regarding the QMOM, this study uses a three-node quadrature, i.e. $N = 3$, following the work of Marchisio and co-workers [112], who recommended the QMOM with three nodes as a reasonable trade-off between the accuracy and computational cost. This number of nodes requires tracking the evolution of the first six moments of the NDF to calculate six unknowns consisting of three abscissas and three weights. In other words, the transport equation, Eq. (5.3), must be written for the moments of order zero to five, $[m_0 \ \ m_1 \ \ ... \ \ m_5]$. Moreover, this study employs the Chebyshev inversion algorithm [136] modified according to the adaptive algorithm suggested by Yuan and Fox [148]. The idea of the adaptive algorithm is to decrease the number of nodes of the quadrature approximation (and respectively the number of moments used for the inversion) to obtain always a realizable set of moments. For instance, if the first six moments are non-realizable but the first four moments are realizable, then the NDF will be approximated with a two-node quadrature. It may happen that only the first two moments are realizable, which is equivalent to a one-node quadrature approximation. In the worst case, no quadrature approximation can be made since one or both of the first two moments are negative. In general, it is desired to approximate the NDF with the maximum number of quadrature nodes, i.e. in this case evaluate the source terms of the moment transport equation (MTE) with three quadrature nodes, in as many computational cells as possible. This aspect is taken into account for the comparison of the discretization schemes employed here to discretize the convective term of the MTEs.

As mentioned previously, in the two-way coupling, the PBM provides the TFM with the information about the population of the bubbles. Here, this information is the Sauter mean diameter calculated from the following definition:

$$d_{32}(x,t) = 6\frac{\displaystyle\int n_L(L;x,t)\left(\frac{\pi}{6}L^3\right)dL}{\displaystyle\int n_L(L;x,t)(\pi L^2)dL} = \frac{m_3(x,t)}{m_2(x,t)}. \tag{6.1}$$

The Sauter mean diameter is used wherever the TFM requires the average bubble diameter, e.g. estimating the average drag force on the bubbles. It should be mentioned that coalescence and break-up source terms are estimated for the cells with the air volume fraction in the range of $10^{-4} - 0.3$. Below this range, the gas phase fraction is negligible and above this range, the bubbly flow assumption is hardly valid.

6.2.2 Boundary Conditions

The boundary conditions for the flow field in the TFM are similar to those mentioned in Chapter 4.

The types of the boundary conditions for the moments are the same as those used for the air volume fraction, i.e. constant values at the inlets, symmetric conditions at the symmetry planes and zero gradients at the wall and the outlet. The moment values at the inlets are obtained by imposing a log-normal distribution with the mean value shown in Table 6.2. The mean values for experimental conditions 008, 042, 040, 028 and 063 are adjusted in such a way as to have the Sauter mean diameter at the air inlet equal to the experimental averaged Sauter mean diameter at the lowest measurement section. Instead, for experimental condition 072, an extrapolation is done by using the experimental averaged Sauter mean diameter of the first four measurement sections to estimate the Sauter mean diameter at the inlet boundary and subsequently adjust the mean value of the inlet distribution. The relative standard deviation of the inlet distributions is set to 15% of the mean value. Then the distribution is scaled such that the 3$^{\text{rd}}$-order moment matches the air volume fraction at the corresponding inlet, i.e. 0.99 at the air injection surface and 10^{-6} at the water inlet. It is worth mentioning that the following relation exists between the 3$^{\text{rd}}$-order moment and the air volume fraction, α_g (assuming that the bubbles have the spherical shape):

$$\alpha_g = \frac{\pi}{6} m_3 \,. \tag{6.2}$$

Table 6.2: The mean of the log-normal distributions imposed at the air inlet

Experimental condition	008	042	040	028	063	072
Mean of the distribution (mm)	3.7	4.0	4.7	4.9	6.2	13.4

6.2.3 Schemes for Moments Convection

1$^{\text{st}}$-order upwind interpolation scheme

The upwind scheme assumes that the value on the face is equal to the value of the cell located at the upstream side of the face. It is commonly employed to solve the moment transport equations, since it is proved to preserve the realizability of the moment set provided the CFL condition is respected [64]. Moreover, the upwind scheme satisfies the monotonicity condition, i.e. a monotonic distribution before advection remains monotonic after advection [65]. The main drawbacks of the scheme are the 1$^{\text{st}}$-order accuracy and the significant numerical diffusion appearing in the results, especially when coarse computational grids are used.

Quasi-2$^{\text{nd}}$-order realizable scheme

The central idea of this scheme developed by Vikas and co-workers [62] is to interpolate the quadrature weights and abscissas separately and then to evaluate the moment fluxes by using the interpolated weights and abscissas. They proved that the moments remain realizable when the quadrature abscissas are interpolated using the upwind scheme whereas the quadrature weights are interpolated using a high-order TVD scheme, provided the time-step (Δt) fulfills the criterion expressed in Eq. (5.52). Despite the increase in the accuracy, the quasi-2$^{\text{nd}}$-order-scheme does not necessarily respect the boundedness criteria established by Harten [176], as observed in the mono- and two-dimensional examples in the previous section. Therefore, in this chapter, the results obtained by employing this scheme are examined for the boundedness issue.

It should be noted that numerical issues may arise in the cells where the bubble volume fraction is very low, close to the machine precision. Therefore, the convective term is neglected for the cells with air volume fraction below a very small threshold equal to 10^{-12}. This threshold serves to increase the robustness of the solver by avoiding the inversion of the moments when they are negligibly small.

Equal-limiter scheme

As mentioned in the previous chapter, this scheme is proposed to deal with not only the realizability issue but also the boundedness of the moments. It is argued that TVD high-order schemes should be applied directly to the moments, in order to preserve their boundedness. However, since the application of standard TVD schemes causes the realizability issue, it is suggested to interpolate all the moments by using the same value as the flux-limiter, i.e. the equal-limiter scheme. It should be noted that the realizability of the interpolated moments on the cell faces does not necessarily guarantee the realizability of the transported moments at the cell centers. However, it can help alleviating the realizability issue, as demonstrated in the previous chapter by some mono- and two-dimensional numerical examples. Additionally, the simulations described in the next section indicate that employing the equal-limiter scheme is helpful in overcoming the realizability issue also in the case of three-dimensional simulations.

Regarding the value of the equal limiter, it is shown that employing the minimum flux-limiter guarantees the boundedness of the moments. This choice of equal limiter is depicted graphically with red markers in Figure 6.1. It is evident that the minimum limiter is always inside the TVD region for all the moments, assuring the boundedness of their solutions. Moreover, the implementation of this scheme is simple. The only additional step with respect to the standard TVD schemes is the comparison of the local limiters for the different moments to find the one with the minimum value. Then, all the moments are locally interpolated by using the same minimum limiter instead of being interpolated independently.
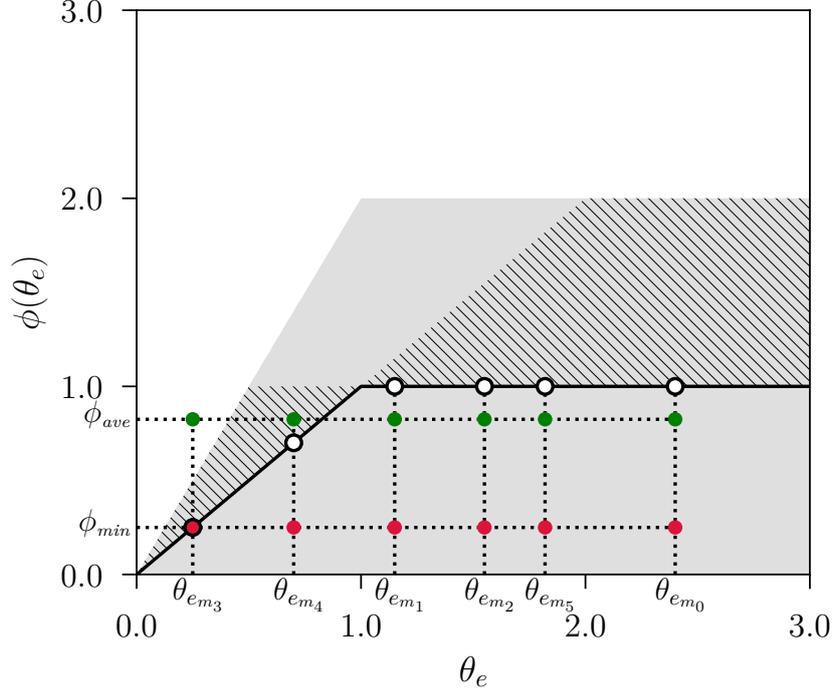
117

Figure 6.1: Schematic description of the equal-limiter scheme for the convection of, in this case, six moments. Shaded area: the TVD region [175]; hatched area: the 2nd-order region [175]; solid black line: *minmod* limiter function; hollow circle: limiter calculated based on each moment smoothness; red circle: equal-limiter using the minimum of the limiters; green circle: equal-limiter using the average of the limiters.

It should be noted that using the minimum limiter may not be always the best choice, since it may decrease the accuracy of the scheme. In the worst case, the scheme reduces to the upwind scheme if the flux-limiter of a moment is zero. Therefore, in this chapter, another approach is adopted that employs the average limiter, i.e. calculated by averaging all the limiters of the moments, when the accuracy of the minimum limiter is not satisfactory. This latter choice for the equal limiter is exemplified with green markers in Figure 6.1. It is worth mentioning that the average limiter may cause issues concerning the boundedness of the moments: in this case, however, the constraint on the boundedness-preserving property of the method is relaxed in favor of a better accuracy. For instance, in the case shown in Figure 6.1, the average limiter does not respect the TVD criteria for one of the moments, since the limiter value is located out of the TVD region, leading to a local violation of the boundedness property. Nevertheless, the effect of such a marginal violation of the TVD criteria leads to negligible effects in the simulation results, as shown in the following section.

6.3 Results

6.3.1 Part I: Convection Scheme

This part focuses mainly on the analysis and comparison of the solutions of the QMOM obtained by employing different convection schemes in the CFD-PBM simulation of the TOPFLOW facility (the 2-meter configuration). The analysis attempts to address the aspects related to the accuracy and boundedness of the solution, in addition to the moment realizability. Thus, the agreement between the predictions and the experimental data is not of primary concern, since the purpose of comparison is not the model validation but detection of any non-physical behaviour caused by the employed numerical schemes. While appreciating the physically acceptable flow pattern observed experimentally, the air volume fraction obtained by the TFM is utilized as the reference to analyze the predictions of the QMOM, in particular those for the moment of order three. There are some sound rationales lying behind this choice of the reference solution: first, the air volume fraction is the only flow field solved by the TFM that has a close connection with the PBM. In fact, the transport equations of the air volume fraction and the 3rd-order moment differ only by a constant (i.e. bubble shape factor, see Eq. (6.2)). Second, the convective term of the transport equation for the air volume fraction is discretized here by the 2nd-order TVD scheme, thus it is expected that the corresponding solution has a satisfactory order of accuracy. Last, bubble coalescence and break-up have no effect on the 3rd-order moment (both terms are zero) as well as the air volume fraction, which facilitates comparing the results from the numerical point of view.

Figures 6.2 and 6.3 depict, respectively, the contour plots and radial profiles of the air volume fraction predicted by the TFM and by the PBE solved with the QMOM for experimental condition 028. Concerning the TFM results, it can be seen that the profile of the air volume fraction, blue solid line in Figure 6.3, has features similar to those of the experimental measurements, specifically a peak close to the wall with a sharp drop towards the wall and a slow decrease towards the center of the column. Thus, despite the existing discrepancy between the predicted and the measured profiles, the TFM result can be indeed used as the reference for evaluating the predictions of the QMOM. It should be mentioned that the discrepancy between the measurements and the TFM predictions is, to a large extent, due to the modelling of the interfacial forces, as discussed in Chapter 4.
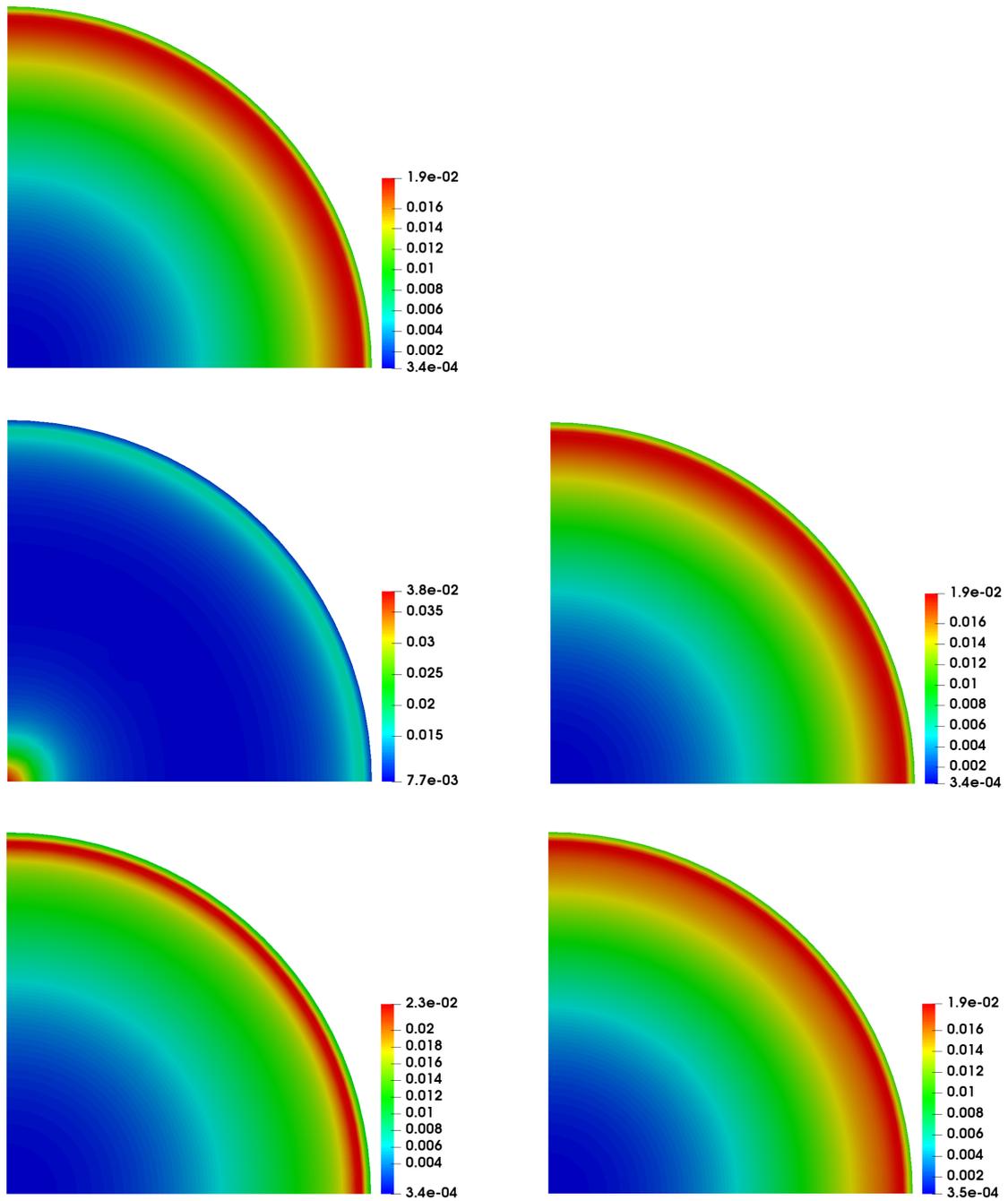
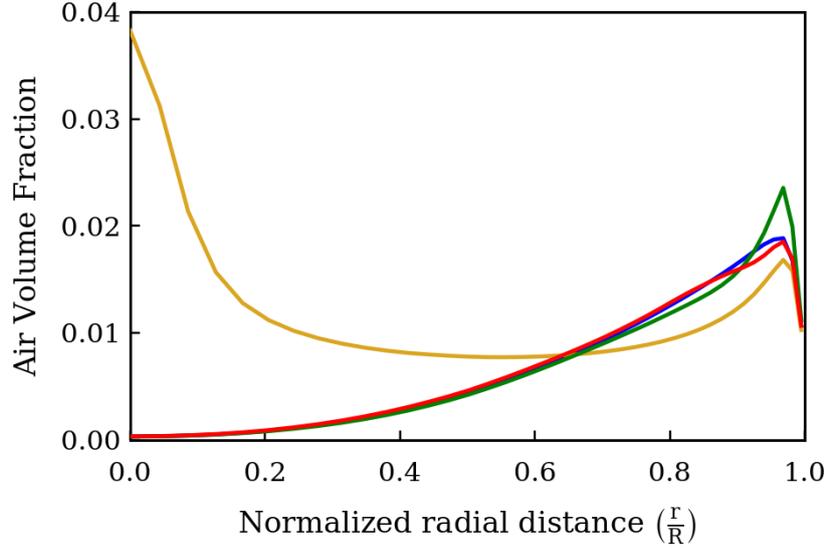**Figure 6.2:** Comparison of the contour plots of the air volume fraction for the test case A at the section 1.55 (m) above the injection point. Top left) TFM; middle left) QMOM with upwind scheme; middle right) QMOM with standard 2$^{\text{nd}}$-order *minmod* scheme; bottom left) quasi-2$^{\text{nd}}$-order scheme; and bottom right) equal-limiter scheme using minimum limiter.

120

Figure 6.3: Comparison of the predicted profiles of the air volume fraction for the test case A at the section 1.55 (m) above the injection point. Blue solid line: TFM; yellow solid line: QMOM with upwind scheme; green solid line: quasi-2$^{\text{nd}}$-order scheme; and red line: equal-limiter scheme.

Let us begin the analysis of the studied schemes by discussing the results obtained by using the 1$^{\text{st}}$-order upwind scheme. Both the contour plot (Figure 6.2) and the radial profile (yellow solid line in Figure 6.3) of the air volume fraction predicted by the QMOM show a non-physical accumulation of the air in the center of the column. It can be associated with the inherent numerical diffusion of the upwind scheme, that occurs in all the directions including the radial one. This observation justifies the necessity of employing high-order schemes in this specific system. Therefore, the standard 2$^{\text{nd}}$-order *minmod* scheme is employed. Although the prediction for the moment of order three is satisfactory (in fact, it is identical to those of the TFM since the same discretization scheme is used, see the contour plots in Figure 6.2), there exist a large number of cells (7120 out of 137088) with non-realizable sets of moments, see Figure 6.4, in which the NDF is approximated by a quadrature consisting of less than three nodes. It is worth adding that most of these cells are located in the region with a significant amount of air volume fraction, thus having an impact on the local bubble size distribution.
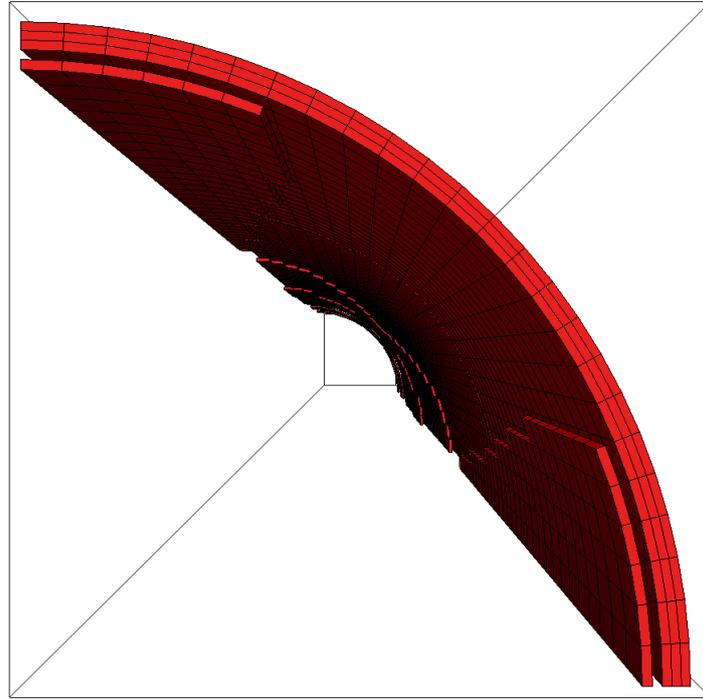
Figure 6.4: The cells with non-realizable issue appearing in the simulation of the test case A due to the standard 2$^\text{nd}$-order TVD scheme employed for the convection of the moments.

In order to avoid the non-realizability problem, the realizable quasi-2$^\text{nd}$-order scheme proposed by [62] is employed for the convection of the moments. As expected, the non-realizability problem does not arise in any computational cell during the simulation, however, the peak of the air volume fraction profile, green solid line in Figure 6.3, increases considerably in comparison to the one predicted by the TFM, blue solid line in Figure 6.3. This difference between the predictions can be also noticed by comparing the corresponding contour plots, shown in Figure 6.2. This behaviour can be associated with the fact that the realizable quasi-2$^\text{nd}$-order scheme does not respect the boundedness of the moments, as demonstrated in the previous chapter. For this reason, the equal-limiter scheme (selecting the minimum limiter) is employed to improve the predictions from the boundedness point of view. Indeed, the contour plot and the radial profile of the air volume fraction, plotted in Figures 6.2 and 6.3 respectively, show the achieved improvements in the accuracy and boundedness of the solution. Moreover, the realizability issue is not detected in the domain since the quadrature approximation has three meaningful weights in all the cells located in the region where the inversion algorithm is applied. Therefore, the equal-limiter scheme with the choice of the minimum limiter

provides the most satisfactory result than the other attempted schemes. However, as mentioned previously, the disadvantage of choosing the minimum limiter is that the scheme may reduce to the upwind scheme if the local profiles of the moments differ significantly, i.e. the shape of the NDF changes considerably along the spatial coordinates. Thus, it is necessary to assess the schemes for the operating conditions where the profiles of the moments may have large local variations, e.g. a case with stronger coalescence and break-up phenomena. For this reason, experimental condition 072 is simulated, since it has higher inlet gas velocity than experimental condition 028. Moreover, the measurements for experimental condition 072 indicate that the bubbles undergo intense break-up in the first portion of the pipe, see Figure 4.2.

The contour plots and radial profiles of the air volume fraction predicted by the TFM and by the PBE solved with the QMOM for experimental condition 072 are shown in Figures 6.5 and 6.6, respectively. It is evident from both figures that the solution obtained by the equal-limiter scheme using the minimum limiter is highly diffusive. It can be associated with the fact that the minimum limiter is either zero or close to zero for a large number of cell faces and therefore, as mentioned previously, the scheme reduces to the first-order upwind scheme. To avoid the exceedingly small values of the limiter, the minimum limiter is replaced by the average one, i.e. the average of the calculated limiters of the moments. The choice of the average limiter improves the results remarkably, as apparent from the violet solid line in Figure 6.6. Furthermore, despite using the average limiter, which does not necessarily respect the boundedness of all the moments, the predicted profile is satisfactorily comparable to the one obtained by the TFM. In contrast, the profile predicted by the quasi-2$^{\text{nd}}$-order scheme presents a second peak, in addition to the accentuated one near the wall, which is not observed in the solutions obtained by the other schemes. This highlights more the significance of the boundedness-preserving property of advection schemes. The last aspect to examine is the efficiency of the scheme in preventing the non-realizability problem. It is worth observing that the equal-limiter scheme helps to alleviate the non-realizability problem but it does not always guarantee the realizability of the moments, as explained in Chapter 5. In the conducted simulations, only the choice of the minimum limiter is able to completely prevent the realizability issue, whereas the non-realizability problem is detected in a few number of computational cells when the average limiter is employed. These cells, however, are very limited in number (32 out of 137088) and their effect on the simulation is negligible, particularly because these cells are located in regions with low gas volume fractions. Therefore, the equal-limiter scheme with the average-limiter is the best general alternative for this case, when all three aspects – accuracy, boundedness-preserving and realizability-preserving – are taken into account.
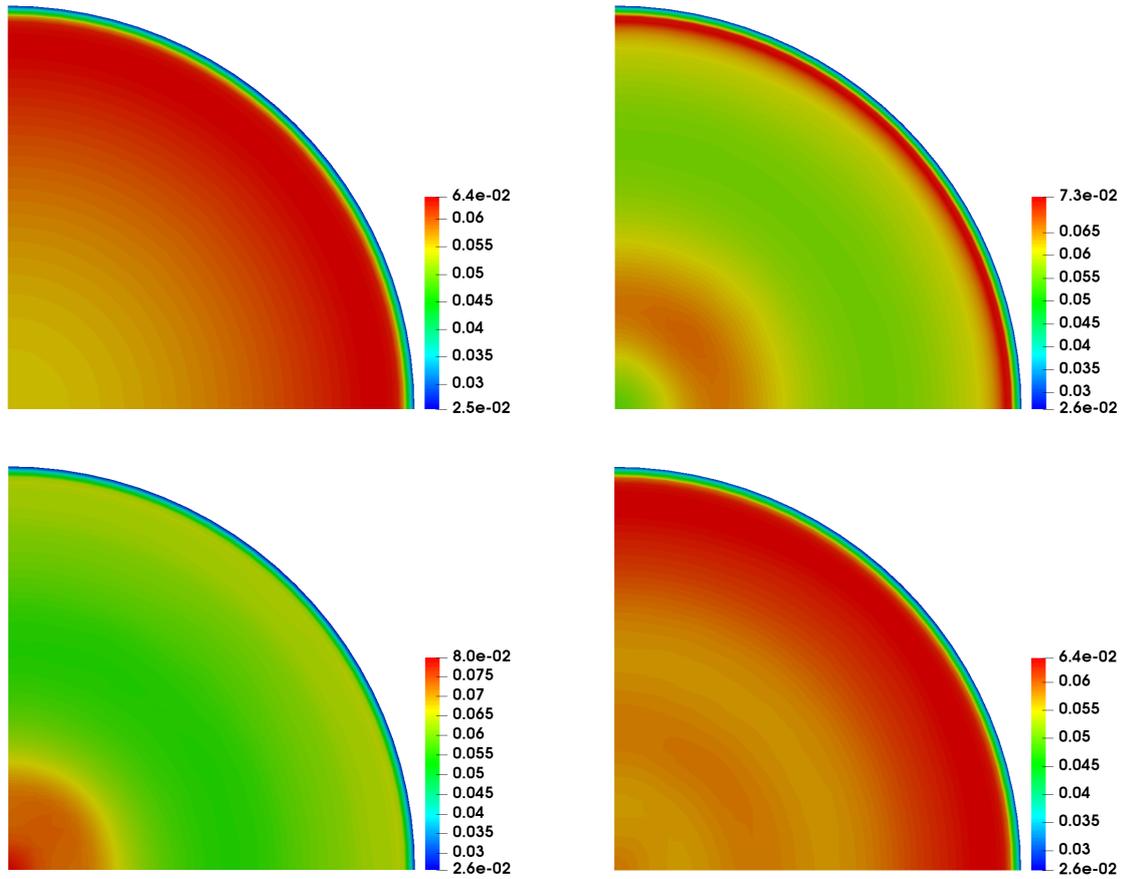
Figure 6.5: Comparison of the contour plots of the air volume fraction for the test case B at the section 1.55 (m) above the injection point. Top left) TFM; top right) QMOM with quasi-2nd-order scheme; bottom left) equal-limiter scheme using minimum limiter; and bottom right) equal-limiter scheme using average limiter.
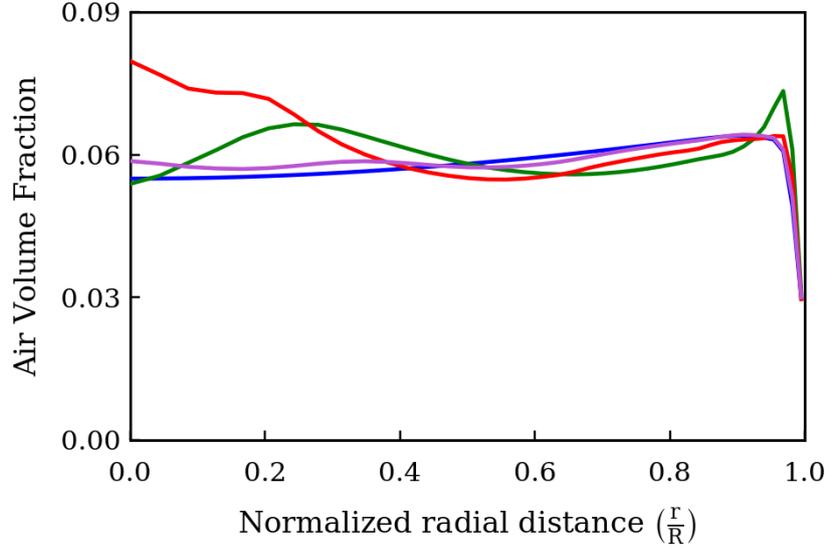
Figure 6.6: Comparison of the predicted profiles of the air volume fraction for the test case B at the section 1.55 (m) above the injection point. Blue solid line: TFM; green solid line: quasi-2$^{\text{nd}}$-order scheme; red line: equal-limiter scheme using minimum limiter; violet solid line: equal-limiter scheme using average limiter.

6.3.2 Part II: CFD-PBM Results

The results of the CFD-PBM simulation of the TOPFLOW facility (the 5-meter configuration) operating under six experimental conditions (see Table 4.2) are reported and compared with those obtained by the TFM (see Chapter 4) in Figures 6.7 to 6.18. The reported results include the radial profiles of the Sauter mean diameter (SMD), standard deviation (Std Dev) of the bubble size distribution (BSD) and air volume fraction at four sections. The figures include also the experimental data. It is noteworthy that, here, the Sauter mean diameter and standard deviation of the BSD are reported and compared to the corresponding experimental data, instead of the BSD itself. The reason is that, in the QMOM, the moments of the BSD are predicted, and the BSD is not directly available. However, these two parameters can represent partially the BSD.

Concerning the discretization scheme, the equal-limiter scheme with the average-limiter is used to discretize the convective term of the moment transport equations, following the discussion presented in Part I.
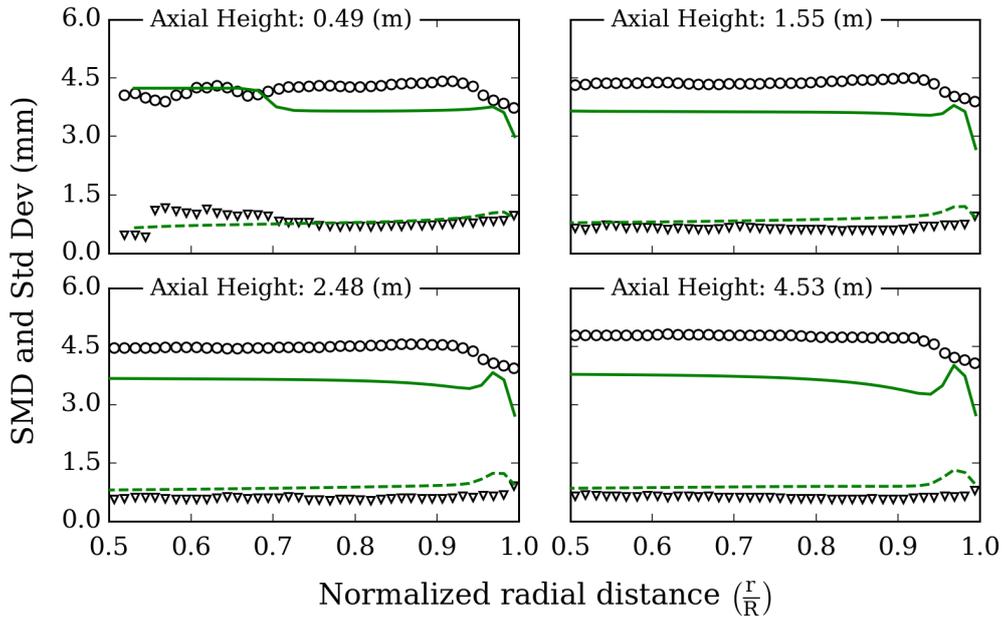
Figure 6.7: Radial profiles of the Sauter mean diameter (green solid curve) and standard deviation of BSD (green dashed curve) predicted by TFM-PBM against the measurements (hollow circles and triangles, respectively) for experimental condition 008.
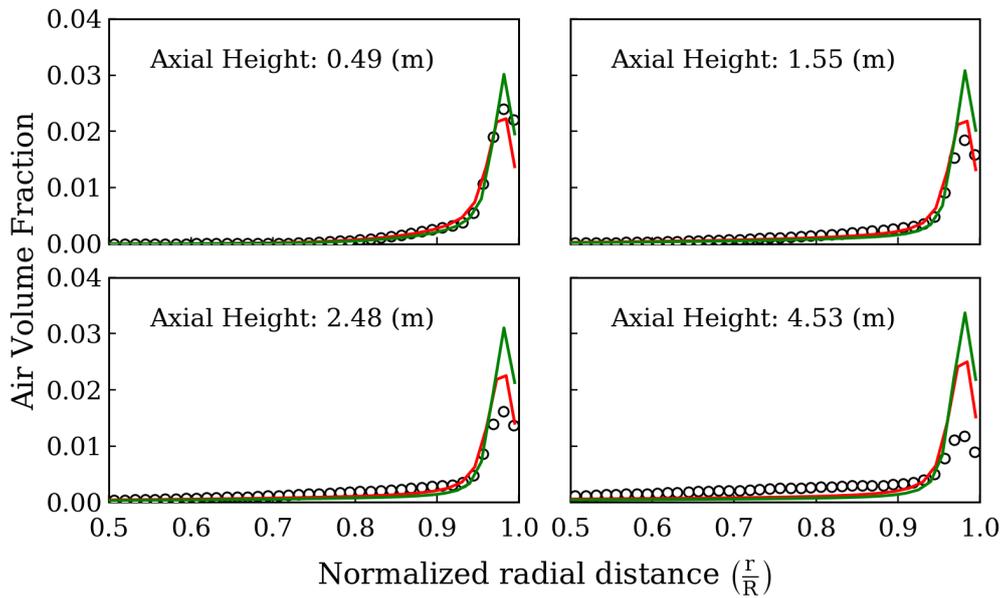
Figure 6.8: Radial profiles of the predicted air volume fraction against the measurements (hollow markers) for experimental condition 008. Red curve: by TFM; green curve: by TFM-PBM.
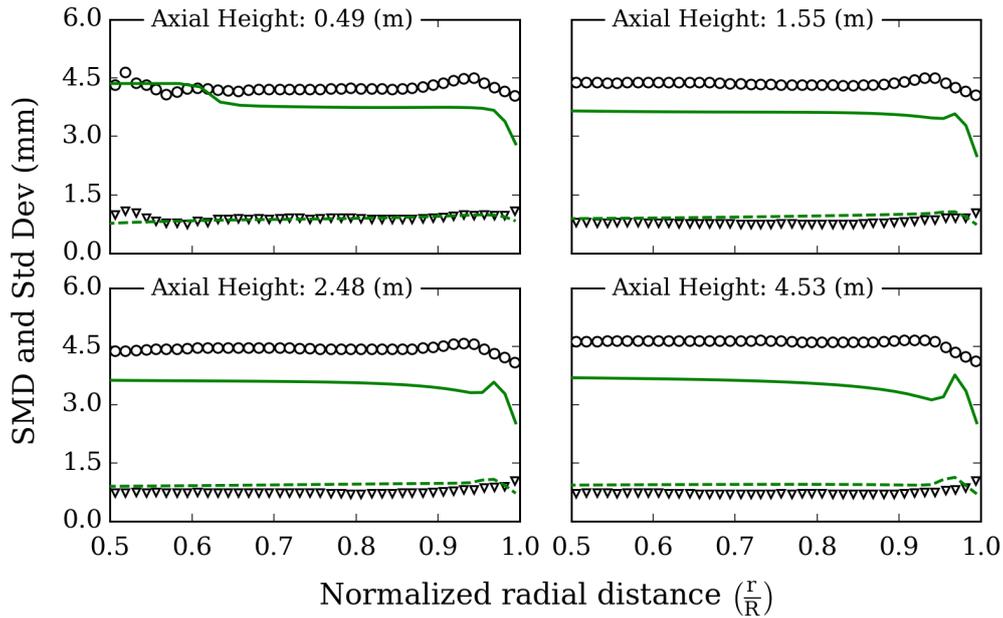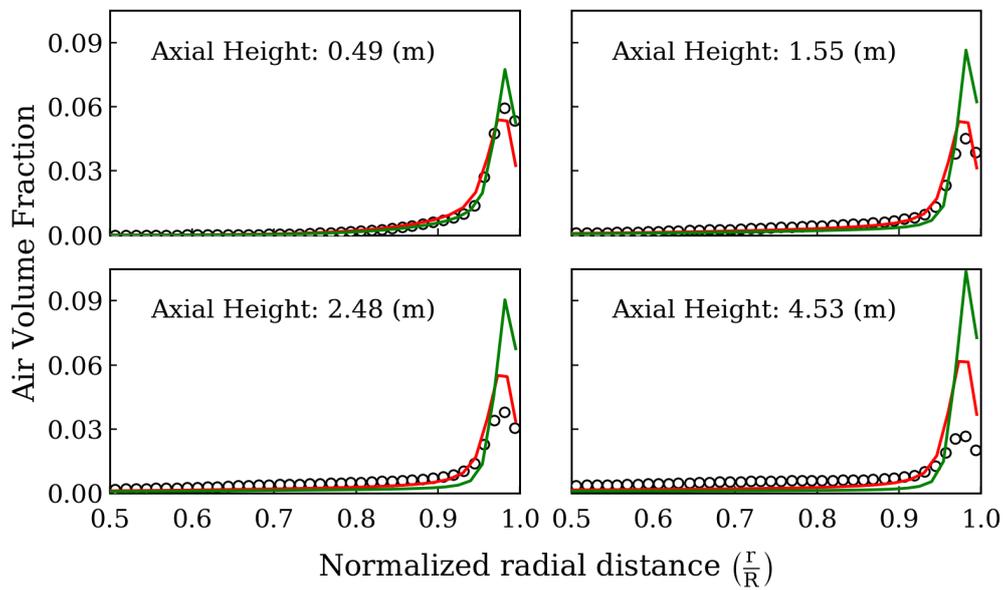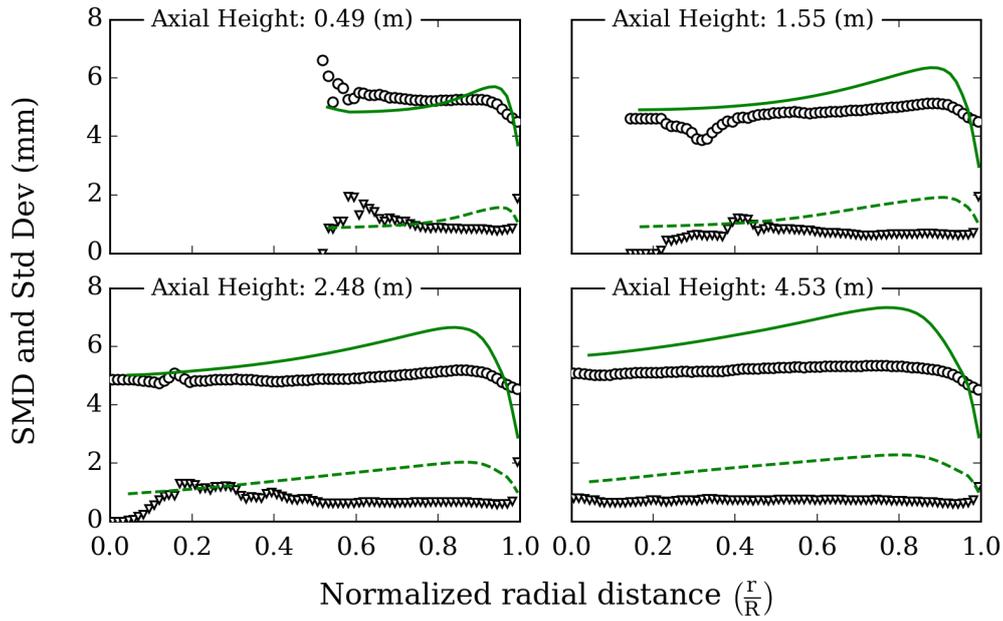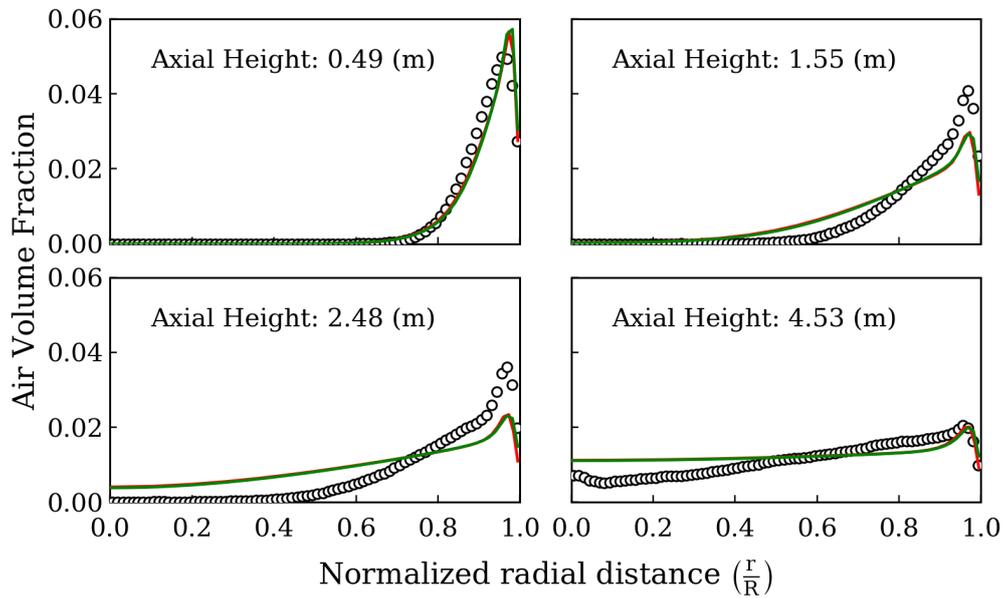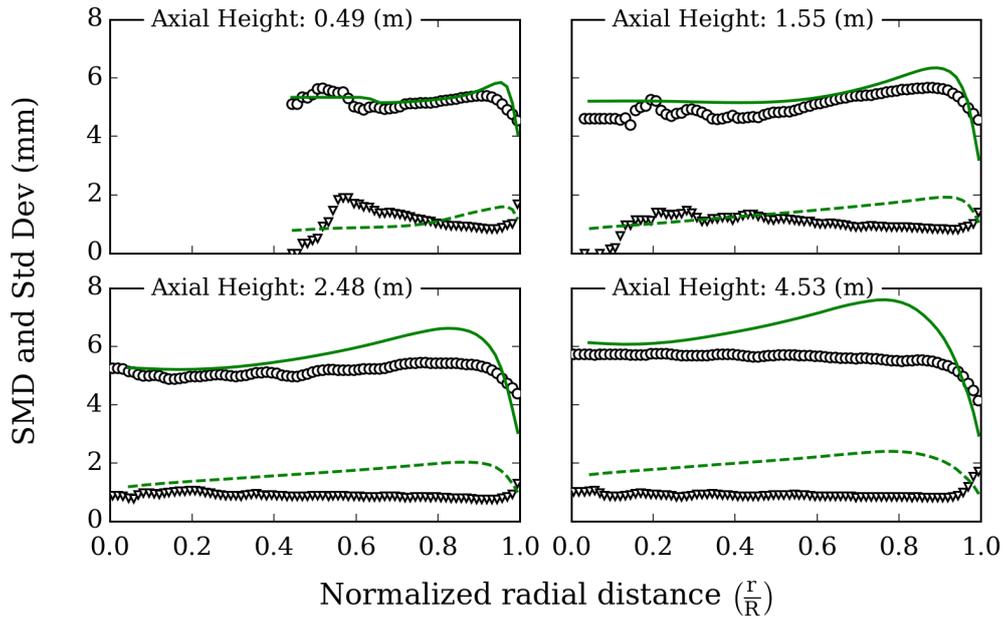
Figure 6.9: Radial profiles of the Sauter mean diameter (green solid curve) and standard deviation of BSD (green dashed curve) predicted by TFM-PBM against the measurements (hollow circles and triangles, respectively) for experimental condition 042.
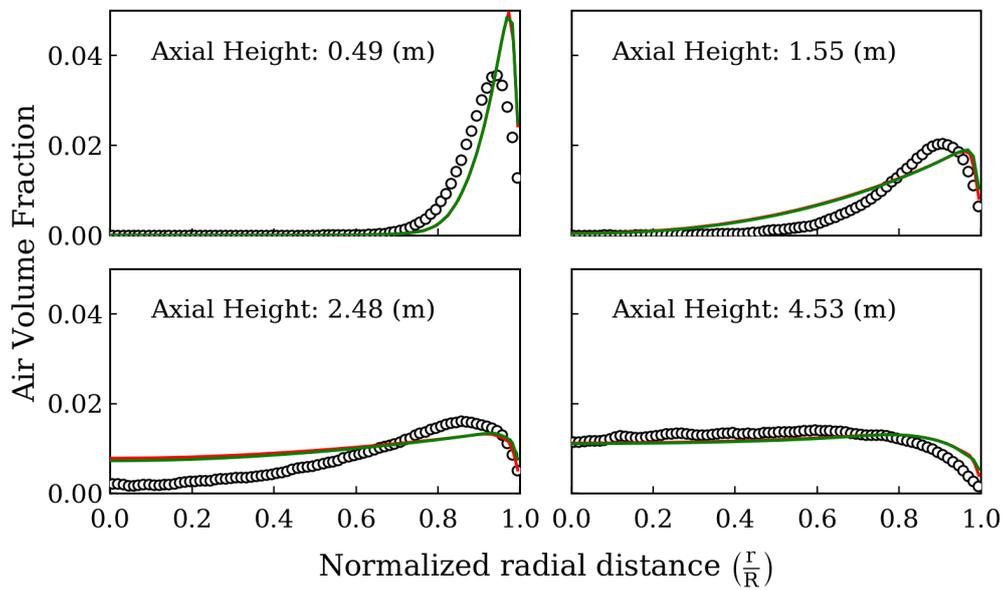

Figure 6.10: Radial profiles of the predicted air volume fraction against the measurements (hollow markers) for experimental condition 042. Red curve: by TFM; green curve: by TFM-PBM.

Figure 6.11: Radial profiles of the Sauter mean diameter (green solid curve) and standard deviation of BSD (green dashed curve) predicted by TFM-PBM against the measurements (hollow circles and triangles, respectively) for experimental condition 040.

Figure 6.12: Radial profiles of the predicted air volume fraction against the measurements (hollow markers) for experimental condition 040. Red curve: by TFM; green curve: by TFM-PBM.
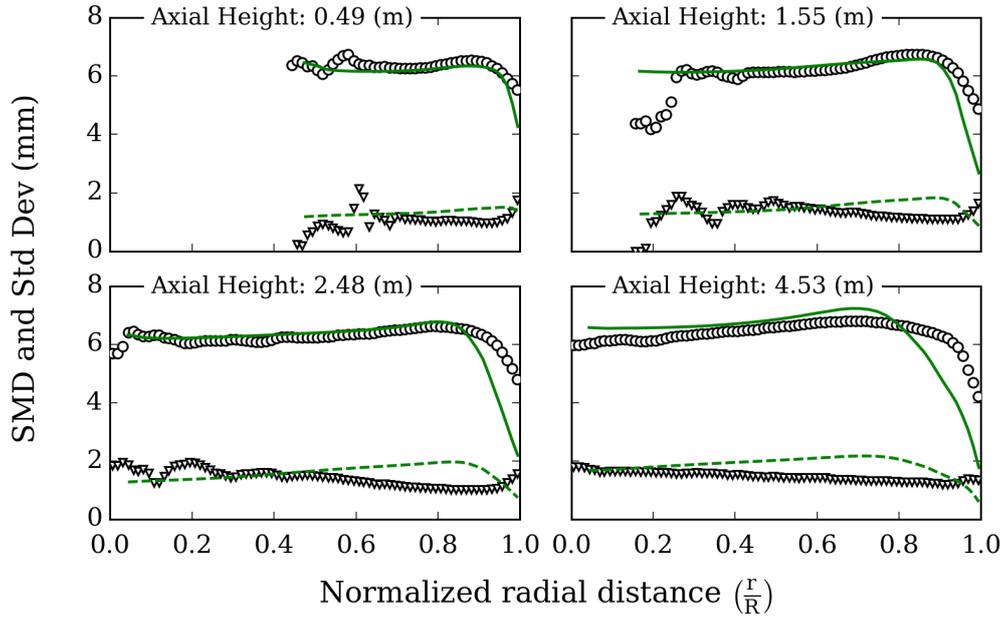
Figure 6.13: Radial profiles of the Sauter mean diameter (green solid curve) and standard deviation of BSD (green dashed curve) predicted by TFM-PBM against the measurements (hollow circles and triangles, respectively) for experimental condition 028.
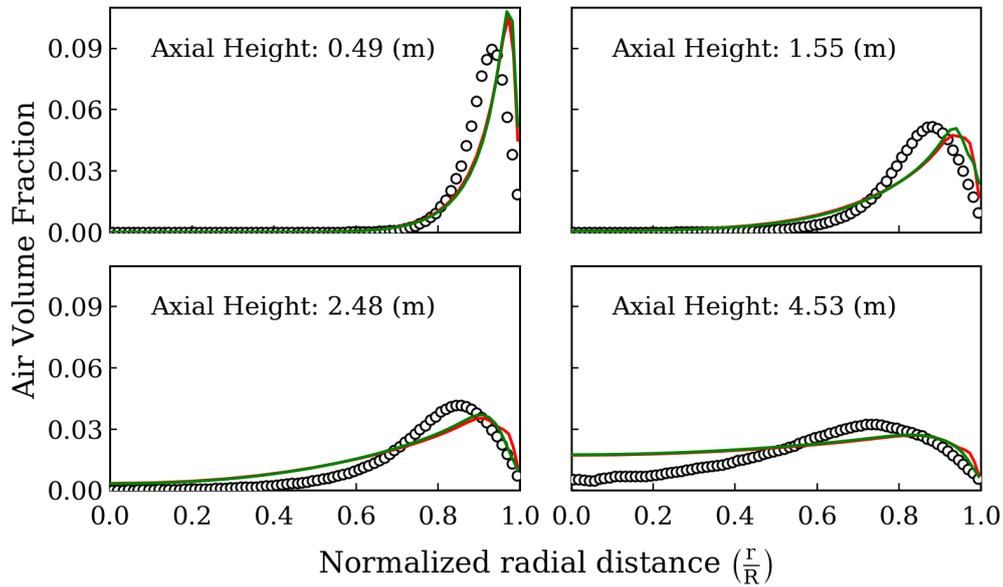

Figure 6.14: Radial profiles of the predicted air volume fraction against the measurements (hollow markers) for experimental condition 028. Red curve: by TFM; green curve: by TFM-PBM.
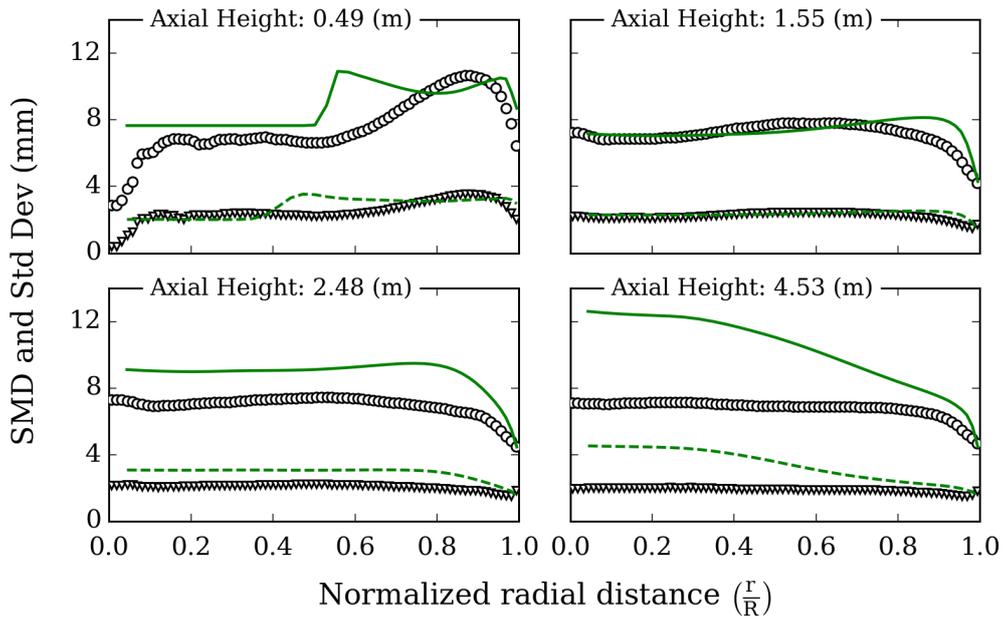
Figure 6.15: Radial profiles of the Sauter mean diameter (green solid curve) and standard deviation of BSD (green dashed curve) predicted by TFM-PBM against the measurements (hollow circles and triangles, respectively) for experimental condition 063.

Figure 6.16: Radial profiles of the predicted air volume fraction against the measurements (hollow markers) for experimental condition 063. Red curve: by TFM; green curve: by TFM-PBM.

Figure 6.17: Radial profiles of the Sauter mean diameter (green solid curve) and standard deviation of BSD (green dashed curve) predicted by TFM-PBM against the measurements (hollow circles and triangles, respectively) for experimental condition 072.
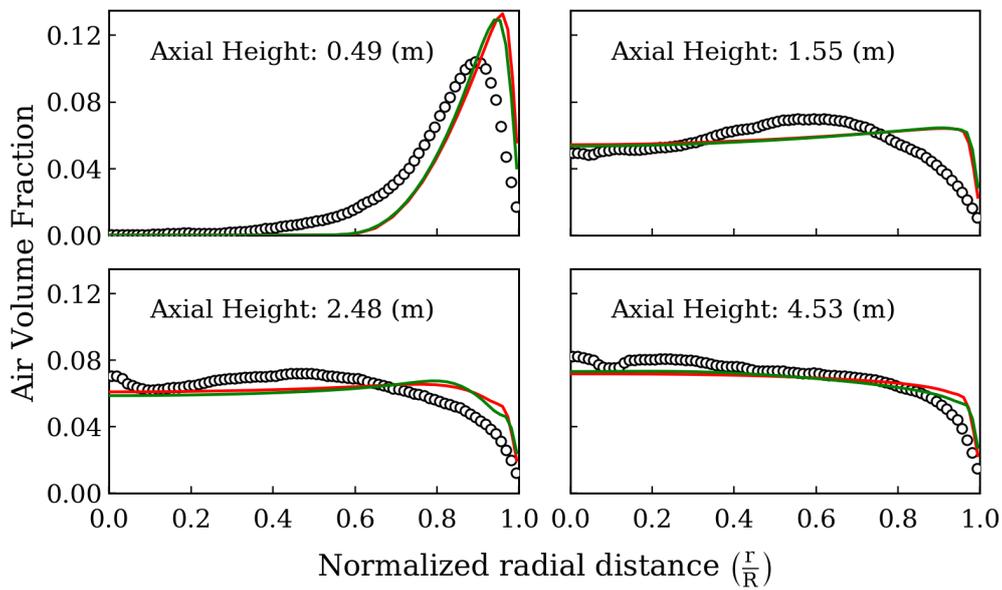

Figure 6.18: Radial profiles of the predicted air volume fraction against the measurements (hollow markers) for experimental condition 072. Red curve: by TFM; green curve: by TFM-PBM.

The first remark is about the effect of the PBM on the flow field predicted by the TFM. As it can be seen, the volume fraction profiles predicted by the TFM with and without the PBM are almost the same. It should be noted that the TFM without the PBM needs the average bubble size to be set, for example, by using the experimental data. In contrast, the PBM requires only the specification of the average bubble size at the inlet boundary, which can be estimated by empirical correlations. In the present study, one may argue that the bubble size does not change considerably in the radial and axial directions, hence allowing the estimated bubble size at the inlet to be used throughout the column. However, it is possible that the bubble size changes considerably (as in the case of experimental condition 072), and it is not known in advance.

Concerning the predictions for the radial profile of the Sauter mean diameter and and standard deviation of the BSD, it is evident that there are discrepancies between the predictions and the experimental data. For example, an observation common to the studied experimental conditions is the decrease in the predicted profile near the wall, leading to the underestimation of the bubble size near the wall in comparison to the experimental data. It is associated with the increase of the turbulent dissipation rate at the wall, predicted by the $k-\varepsilon$ model, on which the coalescence and break-up kernels depend. The underestimation of the bubble size near the wall reduces the magnitude and active zone of the wall lubrication force, which may consequently have an adverse effect on the predictions for the flow fields, e.g. experimental conditions 008 and 042. Moreover, there exist uncertainties regarding the selected kernels and also the interfacial forces, which can cause discrepancies. Nevertheless, the obtained TFM-PBM predictions present an acceptable estimation of the bubble size considering such uncertainties. The importance of the bubble size estimation can be appreciated by focusing on experimental condition 072, where the bubbles undergo intense break-up in the first portion of the pipe. The green curve with circle markers in Figure 6.19 shows the predicted Sauter mean diameter averaged over cross-sections at different axial distances from the injection points for this experimental condition. As it can be seen, the PBM predicts the decrease in the bubble size due to the break-up in the first portion of the pipe, in agreement with the experimental data. Moreover, the predicted Sauter mean diameter averaged over cross-section reaches an equilibrium state between the coalescence and break-up, which is indicated also by the experimental data. Nevertheless, there are still discrepancies between the predicted values and measured ones, particularly at higher sections, which bring to attention the existing uncertainties, e.g those concerning the turbulence modelling and employed kernels. To elaborate, let the coefficient C_γ in Eq. (3.7) be 0.28 instead of 0.88, following the work by Prince and Blanch [115]. Then, the predicted axial change of the Sauter mean diameter averaged over the pipe cross-section improves considerably, as it can be observed from the yellow curve with triangle markers in Figure 6.19. Furthermore, the predictions for the radial profile of the Sauter mean diameter

132

improve, as shown in Figure 6.20. It should be noted that this comparison does not aim to recommend any value for this coefficient, but tries to exemplify one of the mentioned uncertainties. Obviously, these uncertainties can be reduced by the availability of more comprehensive experimental data (i.e. including also the turbulence parameters) and improved models for description of involved phenomena such as coalescence and break-up.
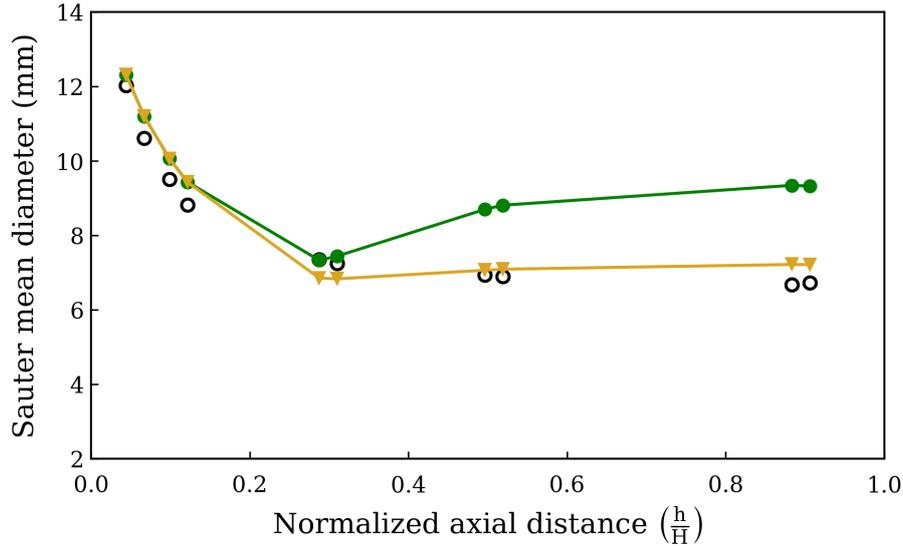

Figure 6.19: Axial change of the Sauter mean diameter averaged over pipe cross-section for experimental condition 072. Black hollow circles: experimental data; green continuous line with circle markers: predictions by setting $C_\gamma = 0.88$; yellow continuous line with triangular markers: predictions by setting $C_\gamma = 0.28$.
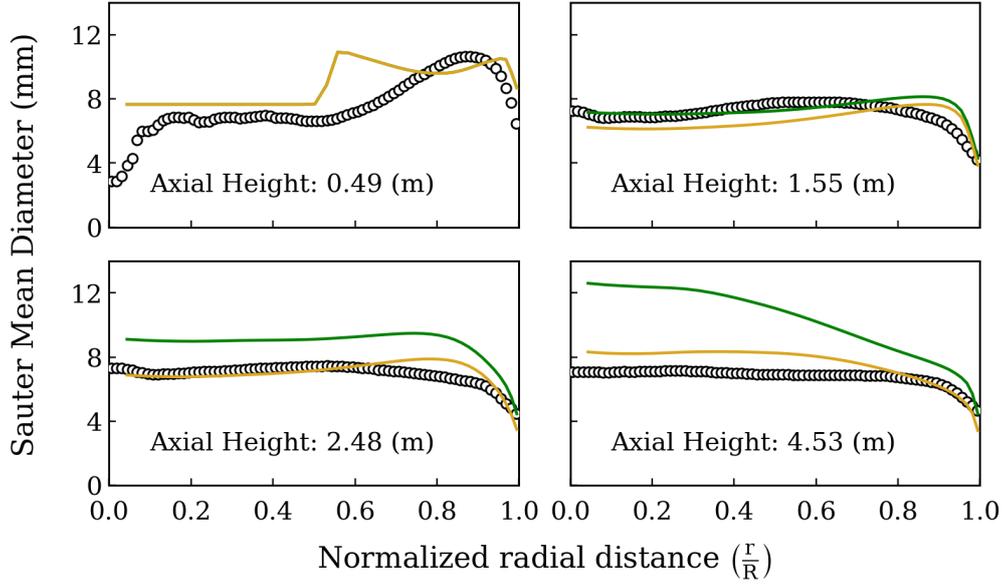
Figure 6.20: Radial profiles of the Sauter mean diameter obtained by CFD-PBM simulations for experimental condition 072. Hollow markers: experiments; green curve: $C_\gamma = 0.88$; yellow curve: $C_\gamma = 0.28$.

6.3.3 Concluding Remarks

The results of the first part reveals that the 1$^\text{st}$-order upwind scheme is too diffusive to produce a meaningful solution for the moment transport equations in the system under study. In addition, it is shown that, as expected in advance, the standard 2$^\text{nd}$-order TVD scheme leads to non-realizable moments in a large number of computational cells containing considerable amount of the disperse gas phase. This highlights the importance of employing discretization schemes that are capable of addressing the realizability issue. Additionally, the importance of boundedness-preserving property is illustrated by the predictions obtained with the quasi-2$^\text{nd}$-order scheme, as some unexpected overshoots (and also patterns) are observed in the profiles of the moment of order three for the operating conditions 028 and 072. These patterns are associated with the fact that this scheme does not generally preserve the boundedness of the solution, as highlighted in the previous chapter. In contrast, in the less-intense operating condition (028) – in other words, when there is more similarity between the profiles of the moments – the solutions for the moment of order three predicted by employing the equal-limiter scheme (using the minimum limiter) show good consistency with the TFM predictions for the air volume fraction (being considered as the "reference" solution). Moreover, it is observed that this scheme helps in preventing the non-realizability problem to a great extent. Under the intense operating condition, instead, the solution obtained by the minimum equal limiter is unsatisfactorily diffused, due to the fact that the

scheme accuracy reduces to 1st-order if the profiles of the moments differ considerably. To tackle this issue, it is suggested to use the average-limiter instead of the minimum one. As a result, the predictions for the moment of order three presents a remarkable improvement in the reduction of the numerical diffusion since they are in good agreement with the TFM predictions for the air volume fraction. Furthermore, although the average-limiter does not necessarily respect the TVD criteria for all the moments simultaneously, no strange pattern is detected in the predicted profiles. The only noticed shortcoming is that the non-realizability problem arises in a small number of cells when the average-limiter is employed in the simulation of experimental condition 072. However, the effect of the non-realizability problem in these cells is considered negligible since they are small in number and they have very low air volume fractions. Thus, the average-limiter scheme presents an acceptable compromise between the accuracy and the realizability-preserving aspects. In addition, no issue is observed in the solutions concerning the boundedness problem.

The second part of the results compares the predictions of the CFD-PBM simulation of the TOPFLOW facility (obtained by employing the equal-limiter scheme with the choice of the average limiter) with the experimental data. It is observed that the coupling of the CFD with the PBM has negligible effect on the predictions of the hydrodynamic fields in the studied system. However, the importance of the PBM should not be underestimated as it provides knowledge about the average bubble size, which is not generally known a priori. Moreover, the PBM can make differences in the hydrodynamic predictions if a multifluid approach is used, which allows bubbles of different properties (here different size) move with different velocities. Last, the predictions for the radial profiles of the Sauter mean diameter are compared with the experiments, where discrepancies are observed. These discrepancies are associated with the existing uncertainties, particularly the turbulence modelling and the employed kernels for the description of the coalescence and break-up.

Chapter 7

Conclusions

7.1 Summary

This dissertation attempted to highlight the viability of simulating bubbly gas-liquid flows by using the PBM incorporated into the CFD. In this regard, two research subjects were covered, i.e. studying the interfacial forces relevant to bubbly flows with particular focus on the lift and wall lubrication forces, and developing numerical methods to improve the stability of the two-way coupled CFD-PBM simulations. For this purpose, a considerable number of simulations were done by using the CFD and CFD-PBM, which aimed at reproducing the available experimental data measured in a developing turbulent air/water pipe flow called TOPFLOW facility.

In the first part of this thesis, the interfacial forces were studied by performing the CFD simulation of the TOPFLOW facility. First, it was shown that the turbulent dispersion force plays a key role in spreading the gas phase in the radial direction in this bubbly pipe flow. In addition, it was shown that the inclusion of the wall lubrication force improves the predictions by reproducing the near-wall-peak in the radial profile of the air volume fraction. Next, two set of models (differing in the employed correlations for the lift coefficient and wall lubrication force) were selected to perform the CFD simulations. The relations for estimating the lift coefficient include Tomiyama's correlation [22] and Sugrue's Correlation [21], while the wall lubrication force was modelled by Hosokawa's expression [26] and Lubchenko's approach [19]. Moreover, the lift coefficient was varied (instead of using the mentioned correlations) with each wall lubrication model to achieve better agreements between the predictions and the experimental data in the first 2-meter portion of the pipe.

Concerning the lift coefficient, for bubble sizes less than 5 mm, the Tomiyama correlation overestimates the lift coefficient whereas the Sugrue correlation underestimates it. For bubble sizes larger than 5 mm, the predictions with positive lift coefficients are not satisfactory at higher sections. In this regard, the Tomiyama

correlation predicts correctly negative lift coefficients for this range of bubble sizes, although the inversion of the lift coefficient occurs at the bubble size around 6 mm instead of 5 mm. However, the Sugrue correlation may predict positive lift coefficients for this range of bubble size, giving rise to relatively larger deviations from the experimental data. This shows the limitation of the Sugrue correlation in predicting the inversion of the lift force required for the satisfactory description of the radial profiles of the air volume fraction. It is notable that the optimized lift coefficients in the first 2-meter portion of the column for either wall lubrication models may be positive for the experimental cases even with the bubble sizes larger than 5 mm. Consequently, the predictions at the higher sections deviate from the experimental data for the simulations of 5-meter column. In other words, the change in the sign of the lift coefficient reveals its effect as the flow develops in the axial direction. This fact demonstrates the fundamental importance of conducting experiments on developing flows, such as TOPFLOW, in order to advance the formulation of the closure relations for the gas-liquid interfacial forces. Regarding the wall lubrication models, Lubchenko's approach was preferred to Hosokawa's correlation since it produces more physical results by allowing the gas phase to exist near the wall.

The second part of this thesis dealt with the PBM, with the primary focus on developing suitable numerical methods for the solution of the QBMM, applicable to bubbly flows. At first, a new technique called the equal-limiter scheme was proposed to overcome the non-realizability problem, which is a main source of instabilities of PBM simulations. It was shown that using an identical flux-limiter for all the moments at each face guarantees the realizability of the interpolated moments and consequently helps to preserve the realizability of the transported moments. In addition, the implementation of the scheme is simple and can be integrated into the CFD simulations easily. Although no formal proof has been given to ensure that the equal-limiter scheme preserves the realizability of the moments under general conditions, it has been shown that this feature can be achieved in the limit of small time steps (as long as the moment sets are far from the boundary of the moment space). The minimum limiter was suggested as the first choice for the identical flux-limiter, since it guarantees the boundedness of the solution (no over– or under–shoots in the solution). Moreover, the proposed scheme was evaluated and compared with the 1$^{\text{st}}$-order upwind and quasi-high-order [62] schemes in several one- and two-dimensional numerical examples. The examples indicated that the solutions obtained by the proposed scheme have higher accuracy compared to the one obtained by the 1$^{\text{st}}$-order upwind scheme and at the same time no under- or over-shoots were observed in the predictions. As our final aim, the equal-limiter scheme was employed to conduct the two-way coupled CFD-PBM simulations of the TOPFLOW facility. It was shown that the scheme helps in preventing the non-realizability problem to a great extent. Moreover, the results obtained by the equal-limiter scheme were compared with those obtained by the 1$^{\text{st}}$-order upwind

and quasi-high-order [62] schemes, considering three aspects: the accuracy, moment boundedness and moment realizability. The comparison indicated the advantages of the equal-limiter scheme over the two other employed schemes. However, it was shown that the order of accuracy of the equal-limiter scheme can reduce to essentially 1st-order with the choice of the minimum limiter. Therefore, it was suggested to use the average of limiters instead of the minimum limiter to improve the order of accuracy of the scheme. Although non-realizability issue was observed after applying this modification, however, its effect was negligibly minimal since the non-realizability was seen only in a few computational cells. Finally, the modified equal-limiter scheme was used to conduct the CFD-PBM simulations of the TOPFLOW facility. The simulation results indicated that acceptable predictions (despite the discrepancies with the experimental data) can be achieved for the Sauter mean diameter. The observed discrepancies were associated with the existing uncertainties such as those regarding the available approaches for the modelling of the turbulence, coalescence and break-up, which emphasize the need for more comprehensive experimental data and improved constitutive models.

Last, it is worth clarifying that the discussions and conclusions of this thesis are made by taking the available experimental data as the benchmark. However, as mentioned in Chapter 4, the measuring technique used to obtain this experimental data, i.e. wire-mesh sensor, has its own limitations that can introduce uncertainties in the measurements and can be identified as a source of discrepancies.

7.2   Future Work

- Further investigation of the effect of the turbulence on the lateral interfacial forces, particularly the lift force.

- Simulation of bubbly flows using a multifluid approach coupled with the PBM, in which the bubbles of different sizes located at the same position can move with different velocities. In particular, the effect of the lift force inversion on the predicted hydrodynamics can be evaluated in this way.

- Developing efficient numerical methods to overcome the realizability issue in Quadrature-Based Moment Methods considering several aspects such as the order of accuracy, oscillation-free solution, implementation in CFD codes and application to arbitrary mesh grids.

Appendix A

Supplementary Results of Mono-disperse Simulations

This appendix presents those results of the mono-disperse simulations that are not reported in Chapter 4, including the predicted radial profiles of the liquid velocity and the turbulent kinetic energy and turbulent dissipation rate of the liquid phase. The results belong to the simulations of the 5-meter configuration and they are arranged according to experimental condition.

Despite the unavailability of experimental data for the liquid velocity and turbulence parameters, some general observations can be made about their predicted radial profiles. The predicted liquid velocity profiles have a very similar pattern as the corresponding air velocity profiles in all the operating conditions. Only in the regions very close to the wall, the liquid velocity profile drops more rapidly than the air velocity profile. This observation can be associated with the no-slip boundary condition at the wall for the liquid velocity, in contrast to the slip condition for the air velocity.

Concerning the turbulence parameters, differences can be observed between the radial profiles of the turbulent kinetic energy predicted by the tested models in all the operating conditions. However, the differences mainly exist when the corresponding radial profile of the predicted air volume fraction is also different. These differences are actually expected, since the transport equations of the $k-\varepsilon$ model adapted for two-phase flows are scaled by the liquid volume fraction ($\alpha_l = 1 - \alpha_g$), which seems to have noticeable effect on the predicted turbulent kinetic energy. However, the difference between the profiles of the turbulent dissipation rate predicted by the tested models seems less significant in all the experimental conditions except in experimental condition 072.
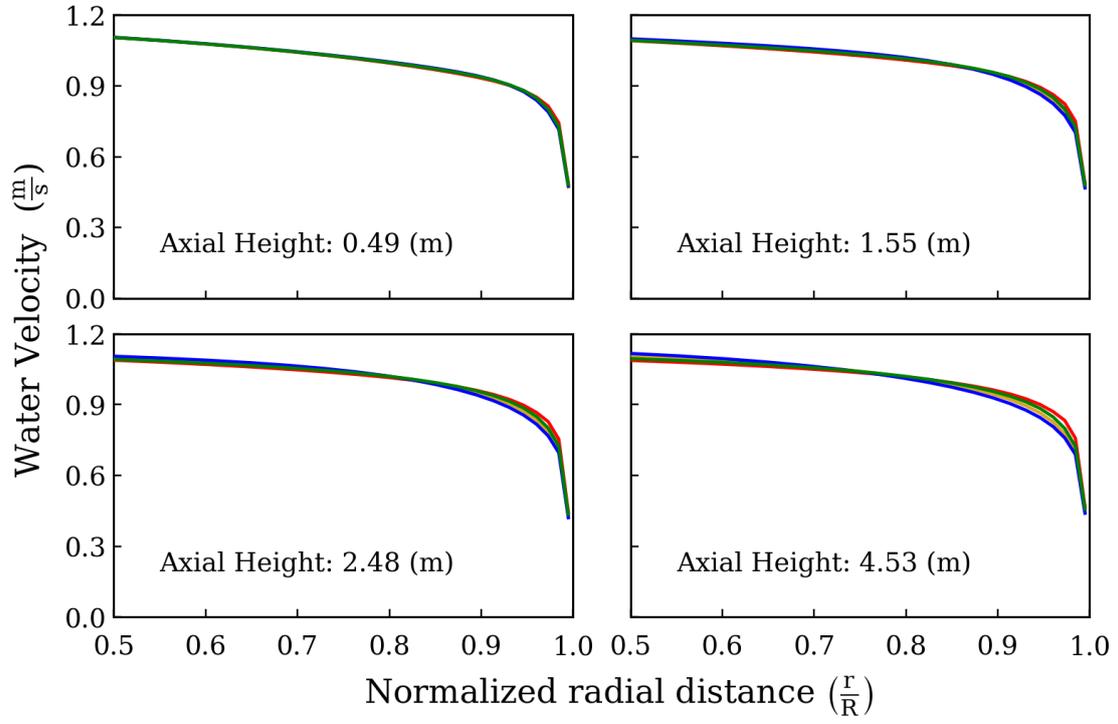
Experimental Condition 008

Figure A.1: Radial profiles of the water velocity predicted by the tested models for experimental condition 008. Red curve: Model I; yellow curve: Model II ($C_L = 0.15$); blue curve: Model III; and green curve: Model IV ($C_L = 0.19$).
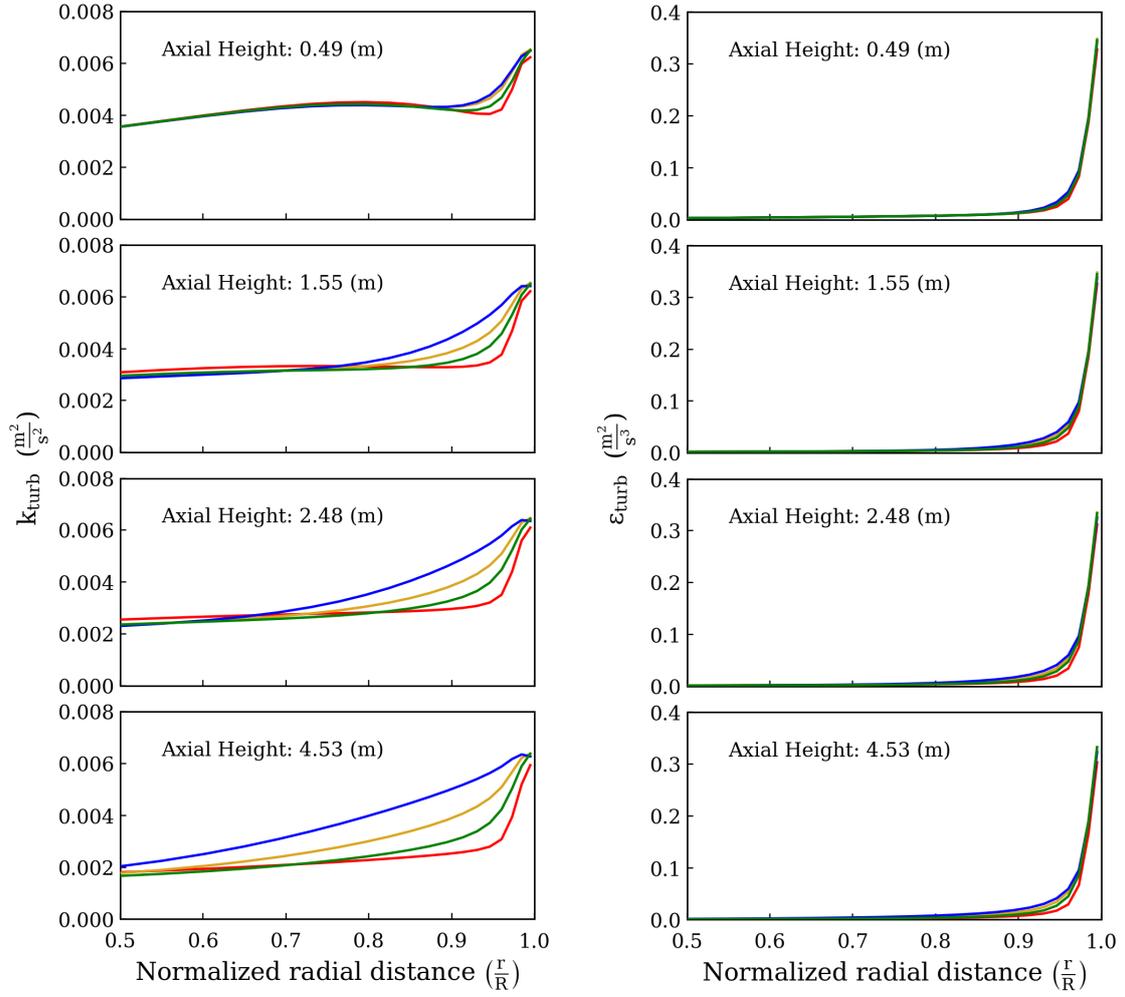
Figure A.2: Radial profiles of the water turbulent kinetic energy and water turbulent dissipation rate predicted by the tested models for experimental condition 008. Red curve: Model I; yellow curve: Model II ($C_L = 0.15$); blue curve: Model III; and green curve: Model IV ($C_L = 0.19$).
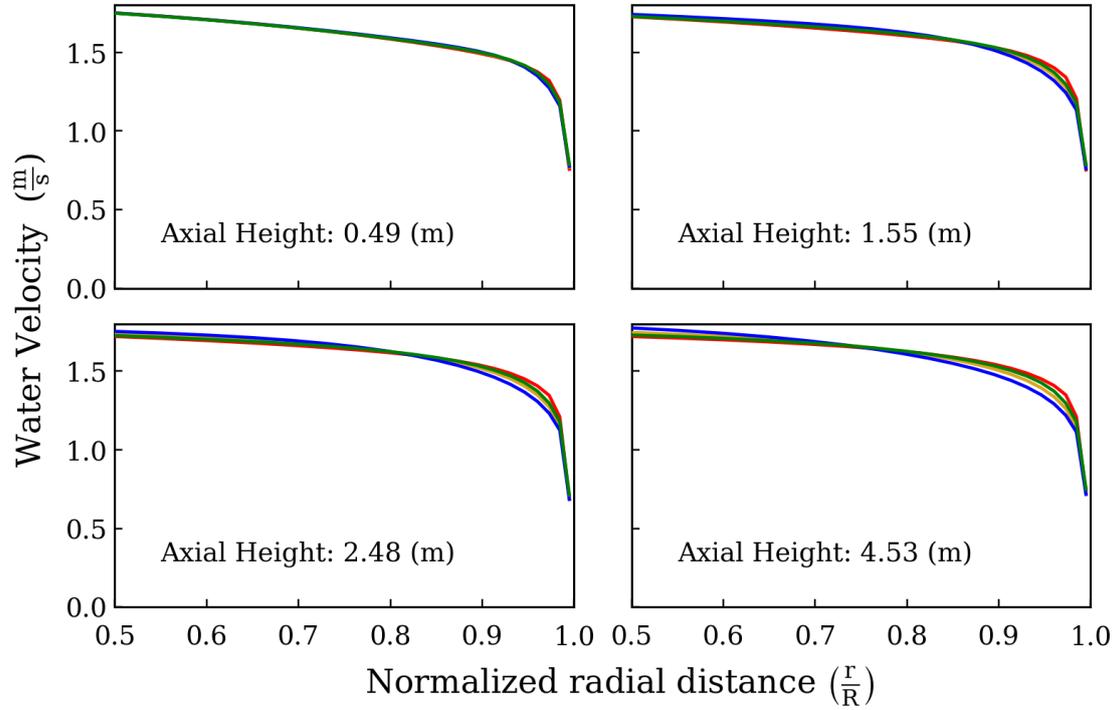
Experimental Condition 042

Figure A.3: Radial profiles of the water velocity predicted by the tested models for experimental condition 042. Red curve: Model I; yellow curve: Model II ($C_L = 0.14$); blue curve: Model III; and green curve: Model IV ($C_L = 0.19$).
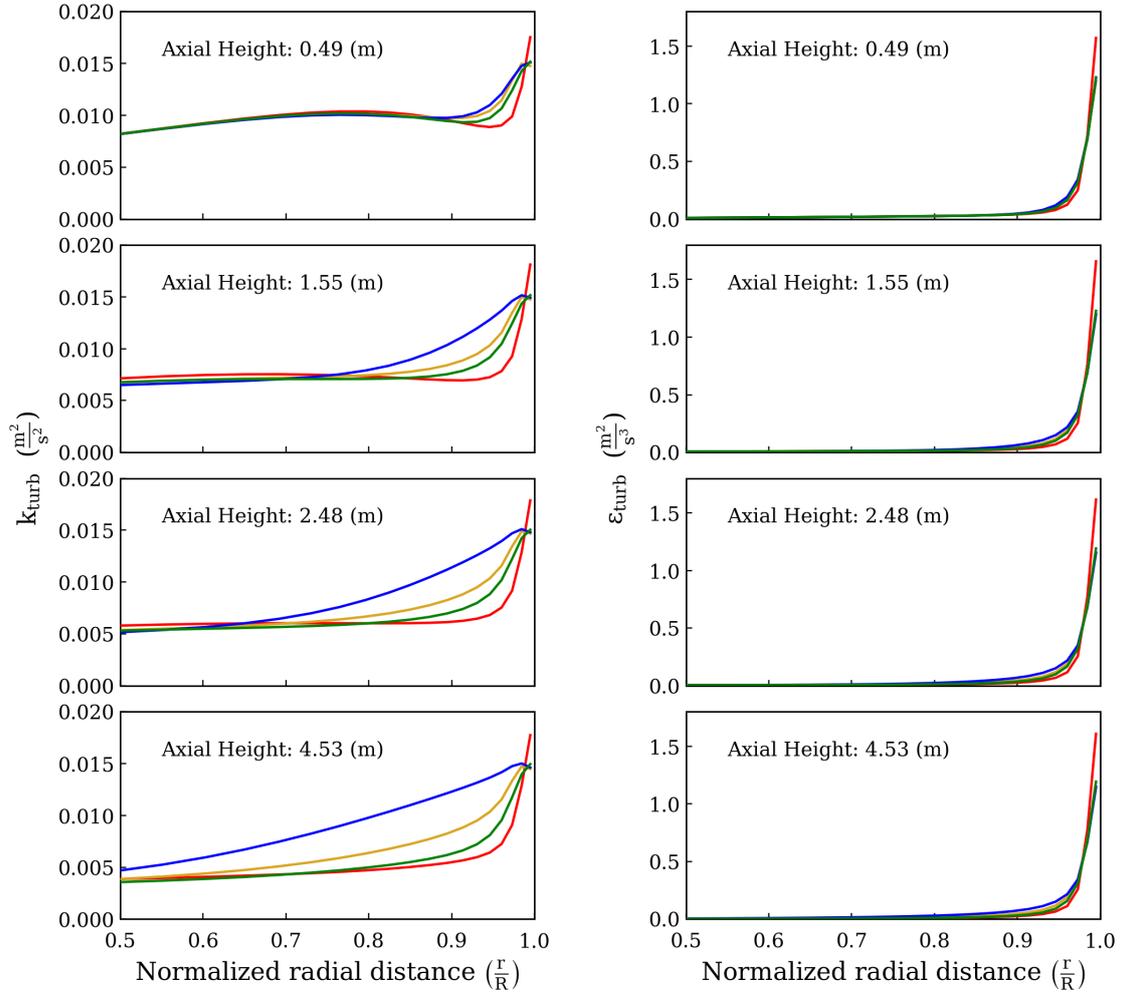
Figure A.4: Radial profiles of the water turbulent kinetic energy and water turbulent dissipation rate predicted by the tested models for experimental condition 042. Red curve: Model I; yellow curve: Model II ($C_L = 0.14$); blue curve: Model III; and green curve: Model IV ($C_L = 0.19$).
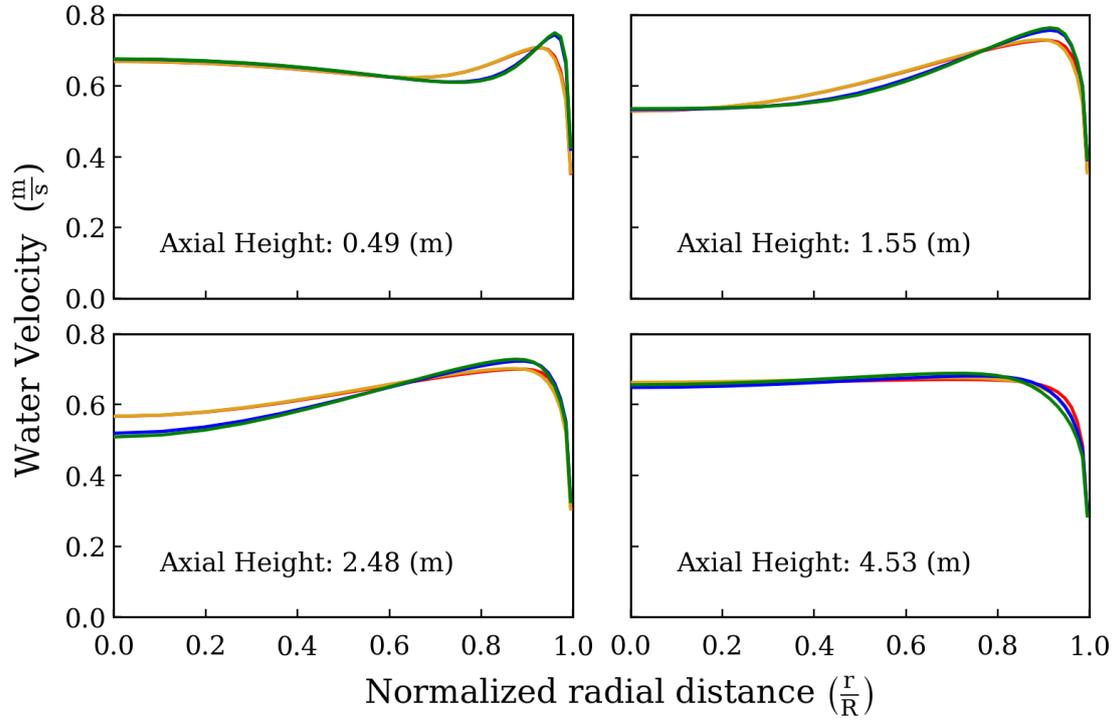
Experimental Condition 040

Figure A.5: Radial profiles of the water velocity predicted by the tested models for experimental condition 040. Red curve: Model I; yellow curve: Model II ($C_L = 0.15$); blue curve: Model III; and green curve: Model IV ($C_L = -0.015$).

Figure A.6: Radial profiles of the water turbulent kinetic energy and water turbulent dissipation rate predicted by the tested models for experimental condition 040. Red curve: Model I; yellow curve: Model II ($C_L = 0.15$); blue curve: Model III; and green curve: Model IV ($C_L = -0.015$).
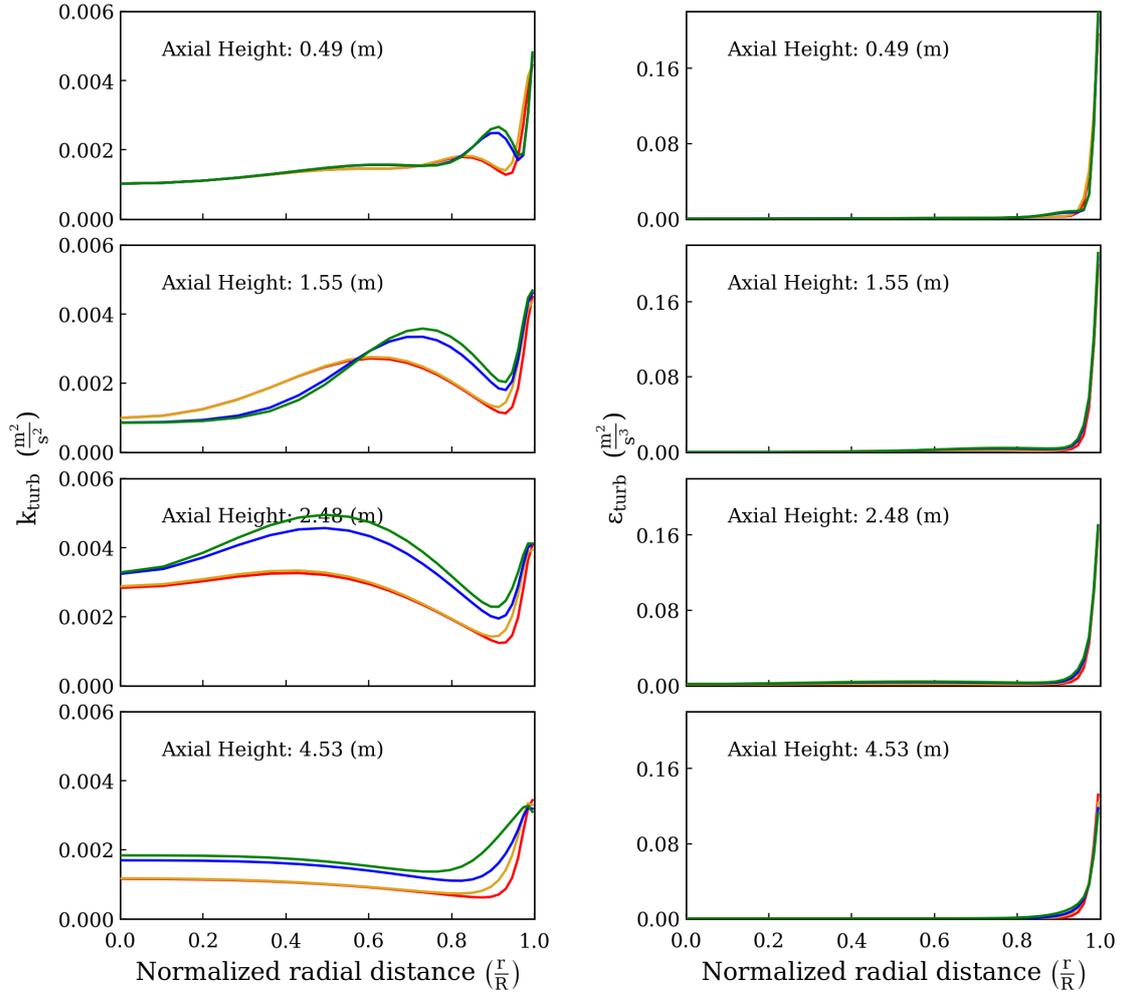
Experimental Condition 028

Figure A.7: Radial profiles of the water velocity predicted by the tested models for experimental condition 028. Red curve: Model I; yellow curve: Model II ($C_L = -0.25$); blue curve: Model III; and green curve: Model IV ($C_L = 0.025$).

Figure A.8: Radial profiles of the water turbulent kinetic energy and water turbulent dissipation rate predicted by the tested models for experimental condition 028. Red curve: Model I; yellow curve: Model II ($C_L = -0.25$); blue curve: Model III; and green curve: Model IV ($C_L = 0.025$).
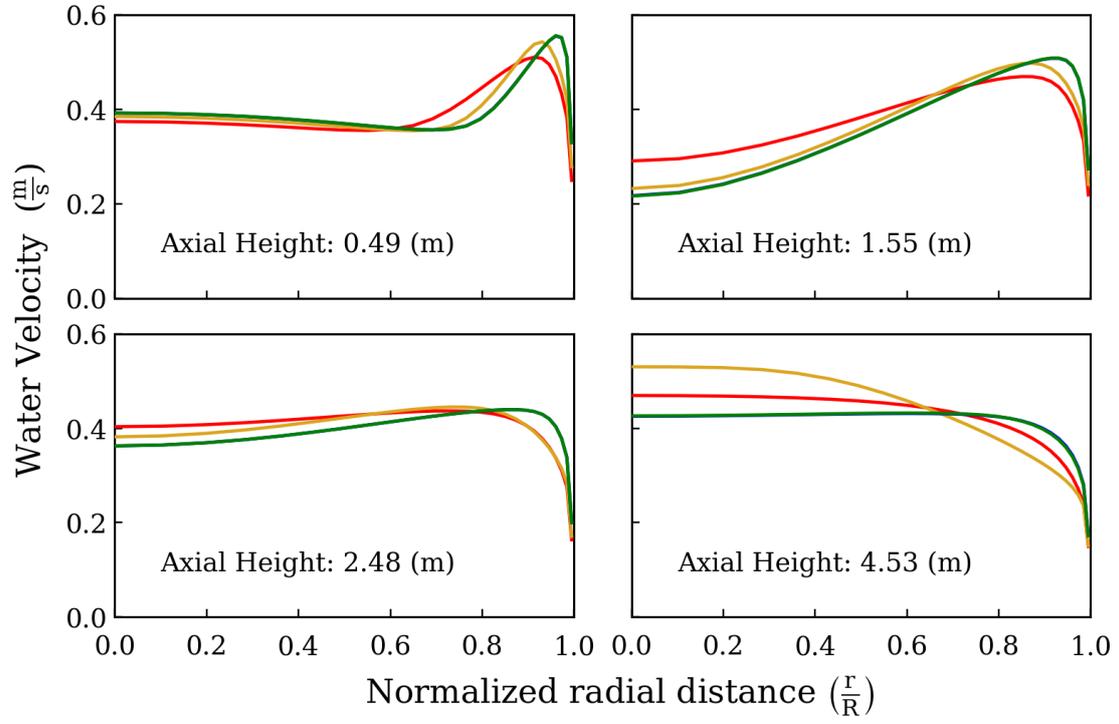
Experimental Condition 063

Figure A.9: Radial profiles of the water velocity predicted by the tested models for experimental condition 063. Red curve: Model I; yellow curve: Model II ($C_L = 0.07$); blue curve: Model III; and green curve: Model IV ($C_L = -0.05$).
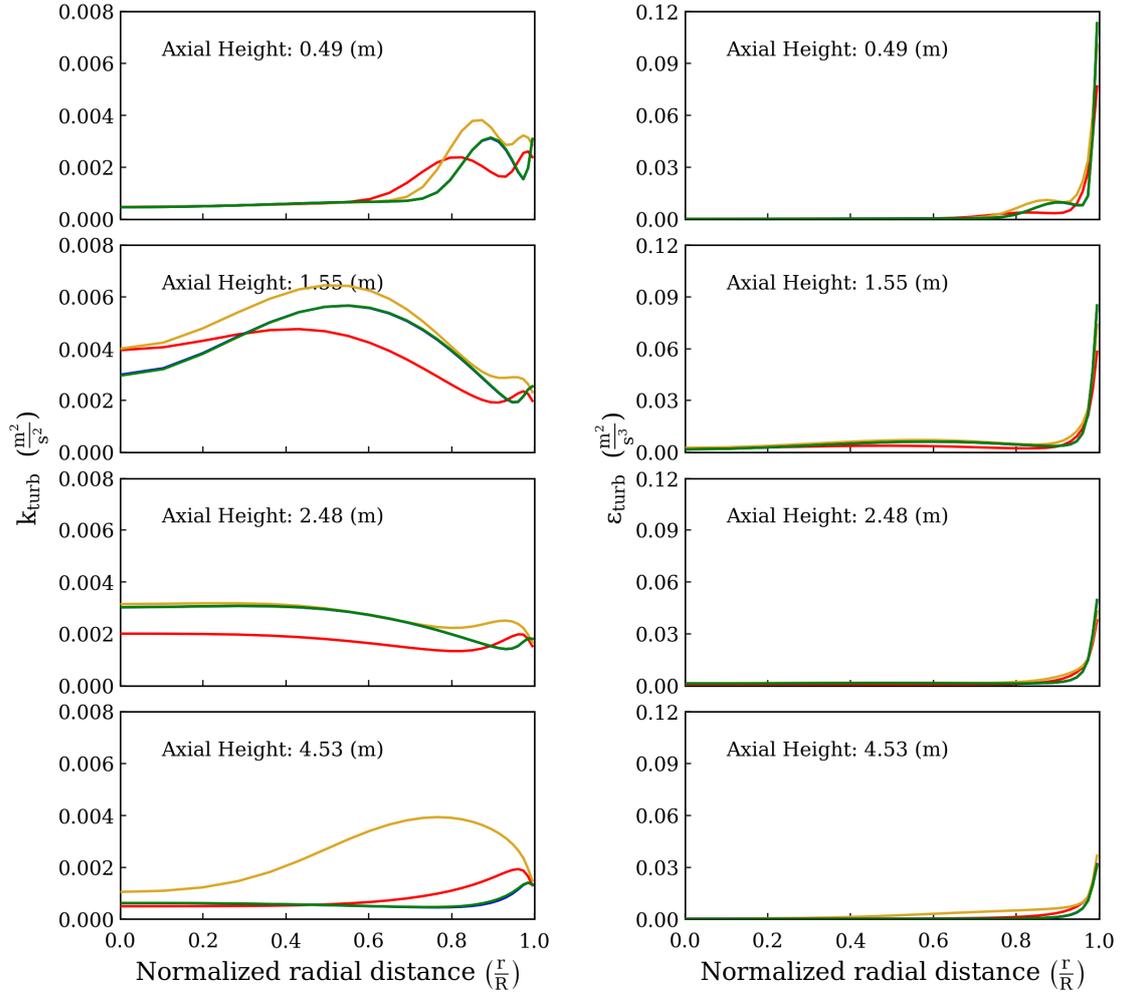
Figure A.10: Radial profiles of the water turbulent kinetic energy and water turbulent dissipation rate predicted by the tested models for experimental condition 063. Red curve: Model I; yellow curve: Model II ($C_L = 0.07$); blue curve: Model III; and green curve: Model IV ($C_L = -0.05$).
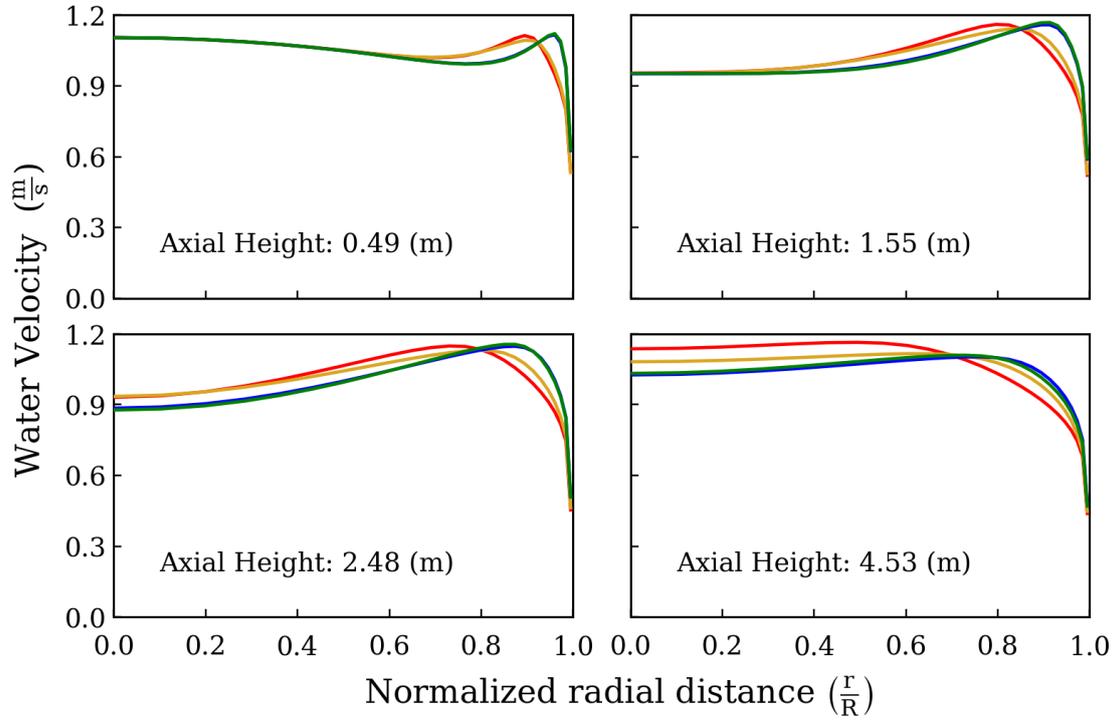
Experimental Condition 072

Figure A.11: Radial profiles of the water velocity predicted by the tested models for experimental condition 072. Red curve: Model I; yellow curve: Model II ($C_L = -0.05$); blue curve: Model III; and green curve: Model IV ($C_L = 0.1$).
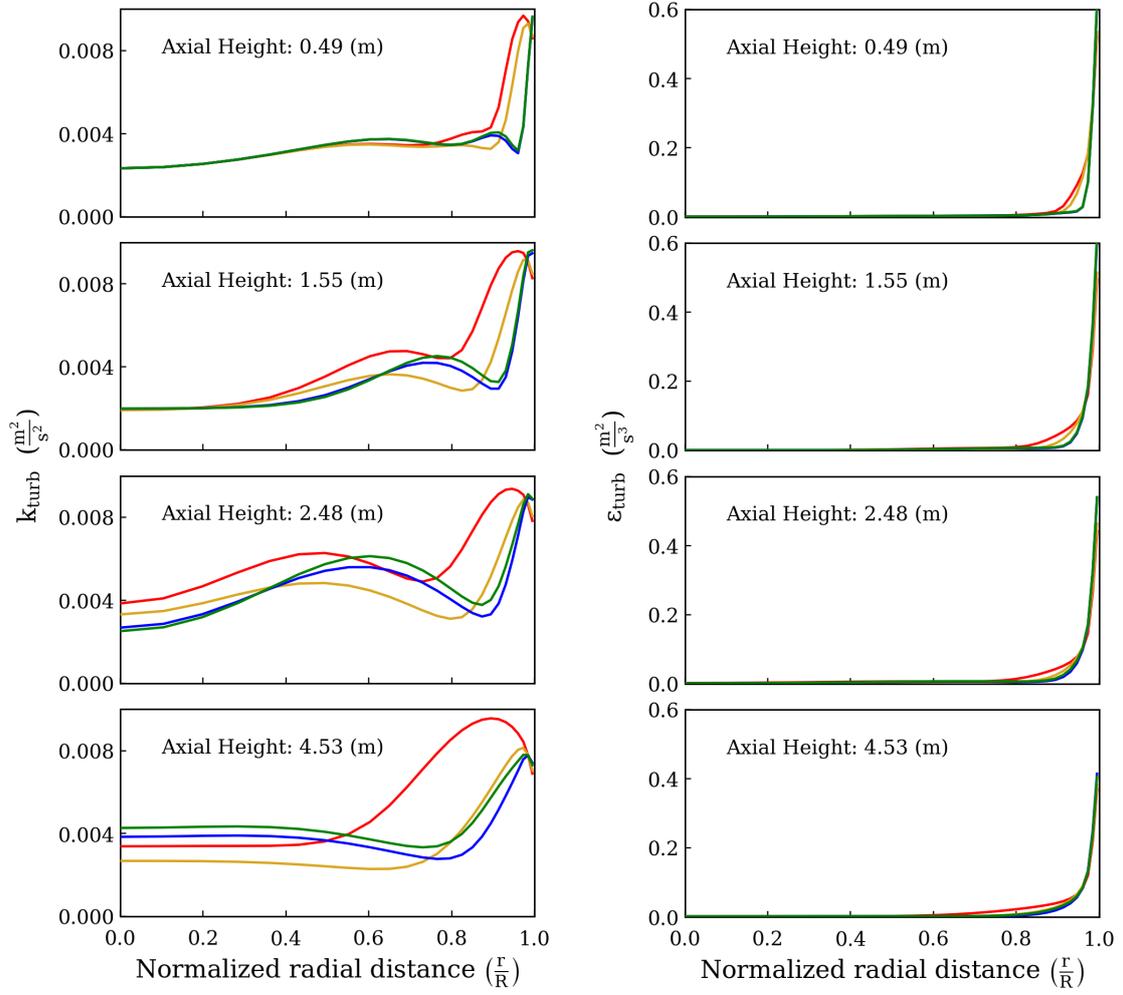
Figure A.12: Radial profiles of the water turbulent kinetic energy and water turbulent dissipation rate predicted by the tested models for experimental condition 072. Red curve: Model I; yellow curve: Model II ($C_L = -0.05$); blue curve: Model III; and green curve: Model IV ($C_L = 0.1$).

Appendix B

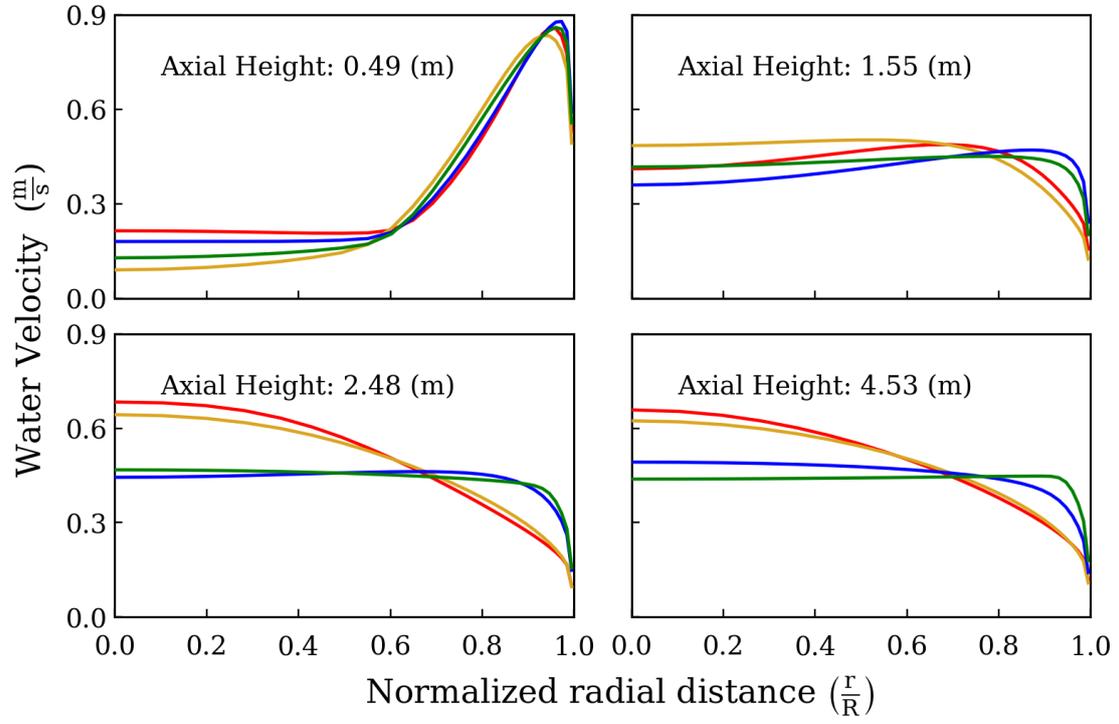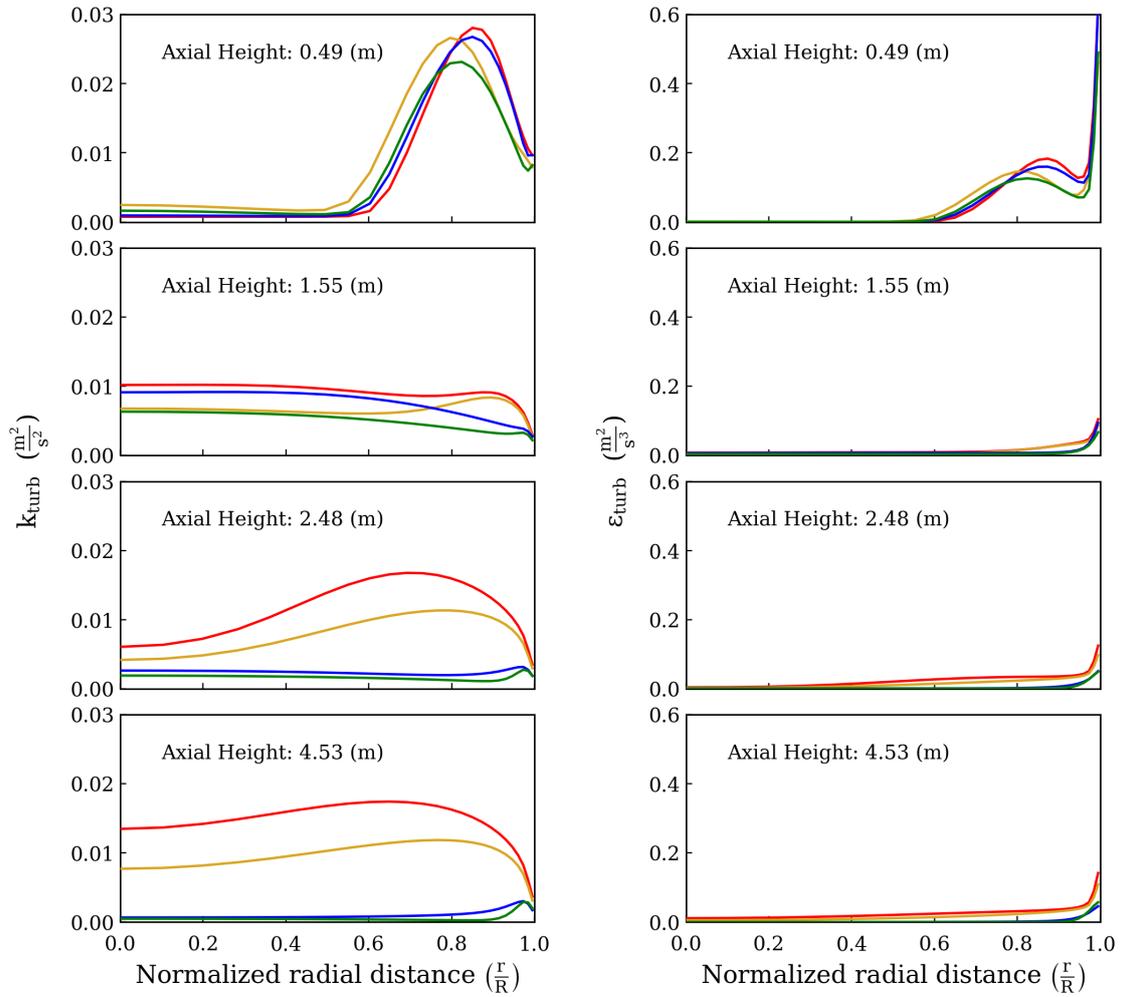# Comparison of the Wall Lubrication Models

Figure B.1 compares the wall lubrication force estimated by Hosokawa's correlation and Lubchenko's approach based on some typical values for the flow fields obtained from the simulation of two experimental conditions 008 and 063. The values used in the models are summarized in Table B.1.

It is worth mentioning that the exact behavior of the models in the simulations might be different due to the change in the local values of the flow fields near the wall, particularly the air volume fraction. Nevertheless, the comparison gives insights into the differences between the two models. It is evident that the magnitude of the wall lubrication force by Hosokawa is much higher than the one proposed by Lubchenko. Although both models depend on the value of the air volume fraction, which is usually very small near the wall, the profiles of the wall force by these models are calculated by imposing a constant small air volume fraction near the wall, i.e 0.01 for experimental condition 008 and 0.02 for experimental condition 063. Moreover, the effect of the wall lubrication force by Hosokawa propagates to distances farther than a bubble diameter from the wall. Although it can be argued that the magnitude of the force falls sharply, it remains considerable at a distance equal to the bubble diameter, particularly in experimental condition 063, which has relatively larger bubble diameter. This fact is the reason of the region without gas phase appearing close to the wall in the simulation of experimental conditions 028, 063 and 072, when Hosokawa's model is employed for the wall lubrication force.
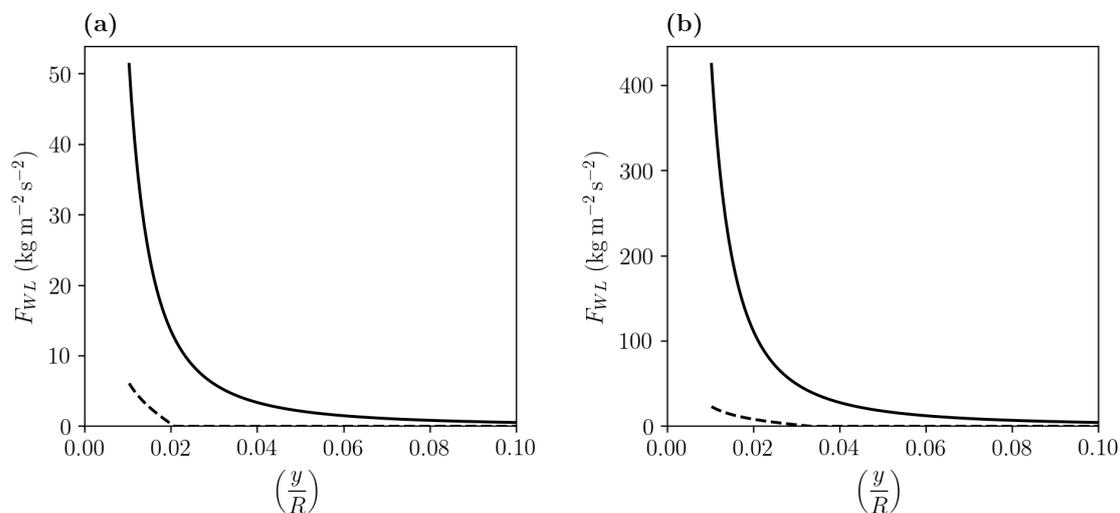
Figure B.1: Comparison of the two employed wall lubrication forces: Hosokawa's correlation (solid line) and Lubchenko's Approach (dashed line). (a) Forces evaluated by using typical values for experimental condition 008; (b) Forces evaluated by using typical values for experimental condition 063.

Table B.1: Typical values used in the comparative evaluation of the employed models for the wall lubrication force

	Operating Condition 008	Operating Condition 063
d_{b}	0.00425	0.0065
α_{g}	0.01	0.02
$\nu_{\mathrm{l}}^{\mathrm{turb}}$	0.00002	0.00003
ρ_{l}	995.7	
ρ_{g}	2.775	
μ_{l}	0.0007975	
σ	0.072	
$|\mathbf{U}_{\mathrm{r}}|$	0.23	

Appendix C

Calculation of the Experimental Sauter Mean Diameter

This appendix explains the procedure to calculate the average bubble diameters reported in Table 4.2 by using the available experimental data. In this thesis, the Sauter mean diameter is used as the average bubble diameter. As mentioned in Chapter 4, for a given experimental condition, the measurements were done by increasing the distance between the air injection point and the wire-mesh sensor. Therefore, this is equivalent to performing measurements at different axial levels from a fixed (air) injection point for that experimental condition. The measurements are related to the volume fraction (in percentage) corresponding to bubble size classes of width 0.25 mm. The data is available for the intervals in the radial direction at each measuring level. Table C.1 shows an example of the measurements at the distance of 1.55 m from the air injection point and the radial position between 0.0964 and 0.0977 m for experimental condition 028. Moreover, the integral of the radial measurements at each axial level is available.

By definition, the Sauter mean diameter is:

$$d_{32} = \frac{\sum_i n_i \, \bar{L}_i^3 \Delta L_i}{\sum_i n_i \, \bar{L}_i^2 \Delta L_i} \,, \tag{C.1}$$

where $\bar{L}_i$ is the average diameter of the bubble class i and $n_i \Delta L_i$ is the number of bubbles of class i. Eq. (C.1) can be rearranged as follows:

$$d_{32} = \frac{\sum_i k_v n_i \, \bar{L}_i^3 \Delta L_i}{\sum_i [k_v n_i \, \bar{L}_i^3 \Delta L_i]/\bar{L}_i} = \frac{\sum_i (\Delta \alpha_{\mathrm{g}})_i}{\sum_i (\Delta \alpha_{\mathrm{g}})_i/\bar{L}_i} = \frac{\sum_i (\Delta \alpha_{\mathrm{g}}/\Delta L)_i \Delta L_i}{\sum_i (\Delta \alpha_{\mathrm{g}}/\Delta L)_i \Delta L_i/\bar{L}_i} \,. \tag{C.2}$$

The values $(\Delta \alpha_{\mathrm{g}}/\Delta L)_i$ are the volume fraction of bubble class i divided by the bubble size interval defining the class i, ΔL_i. These values are available from the experimental data, for which an example is shown in Table C.1. In addition, in this thesis, the bubble size interval of class i is defined to be between L_i and L_{i-1}, meaning $\bar{L}_i = (L_i + L_{i-1})/2$.

Table C.1: An example of the available experimental data measured at the distance of 1.55 m from the air injection point and radial position between 0.0964 and 0.0977 m for experimental condition 028

class index i	L_i (mm)	$(\Delta\alpha_\mathrm{g}/\Delta L)_i$ (%/mm)
0	0.00	0.0
1	0.25	0.0
2	0.50	0.0001
3	0.75	0.0004
4	1.00	0.0003
5	1.25	0.0006
$\vdots$	$\vdots$	
35	8.75	0.0006
36	9.00	0.0036
37	9.25	0.0006
38	9.50	0.0007
39	9.75	0.0
40	10.0	0.0

Eq. (C.2) can be employed to calculate the radial profile of the Sauter mean diameter at each measurement axial level. In addition, the sectional average of the Sauter mean diameter at any axial level can be obtained by using the integral of radial measurements of that level, which is also available from the experimental data.

Finally, the average bubble diameters reported in Table 4.2 are obtained by integrating the average Sauter mean diameter calculated at the measuring axial levels from the air injection point up to the height of interest, i.e. from 0 up to 1.55 m for the nominal 2-meter column and from 0 up to 4.53 m for the nominal 5-meter column. The integration is done by using the trapezoidal rule. Since no measurement is available for the average bubble size at the air injection point, the same average value of the nearest measuring axial level is assumed at the air injection point.

Appendix D

Grid Independence Study

In the following, some details of the mesh independence study is reported, specifically those concerning the radial direction, which is more critical in this system. First, let us begin with the results of the developed single phase (water) simulations. Here, the importance of the developed single phase profiles lies in the fact that they are used as the boundary condition at the water inlet for the two-phase simulations, as explained in Section 4.2.3. Moreover, in the two-phase simulations conducted in this thesis, the turbulence is modelled by the single phase $k-\varepsilon$ model transport equations scaled by the volume fraction of the liquid phase.

When two-equation models, e.g. the $k-\varepsilon$ model, are used to simulate bounded turbulent flows, it is common to employ wall functions in regions close to walls. However, wall functions are not generally valid in the near-wall-region, and therefore, their use imposes a limitation on the minimum distance between the center of the first computational cell and the wall. The common practice is to place the first grid point (or cell center) in the logarithmic layer, i.e. the dimensionless wall distance (y^+) should be generally larger than 30 [172]. The definition of the dimensionless wall distance is

$$y^+ = \frac{\rho_l u_\tau y}{\mu_l} \,, \tag{D.1}$$

where y is the distance from the wall and $u_\tau = \sqrt{\tau_w/\rho_l}$ is the shear velocity, τ_w denotes the shear stress at the wall. At the same time, a refined mesh, particularly near the wall, is desired to capture, as much as possible, the profile in that region. However, violation of the above condition on y^+ in a significant portion of the wall boundaries can introduce errors in the predictions [172], and should be avoided. For this purpose, four grids of different level of refinement in the radial direction, particularly near the wall, are selected. Table D.1 lists some information about the radial resolution of the selected grids.

Table D.1: Radial grid resolution of the studied meshes

	Number of cells in an axial cross-section (quarter circle)	Distance between the first cell center and the wall (mm)
Grid 1	1128	≈ 0.207
Grid 2	816	≈ 0.627
Grid 3	720	≈ 0.876
Grid 4	624	≈ 1.243

Figure D.1 shows the developed profiles of the velocity, turbulent kinetic energy and turbulent dissipation rate predicted by the single phase (water) simulations with the selected radial grid resolutions for the superficial velocity of 1.611 m/s. This superficial velocity corresponds to the maximum superficial liquid velocity of the experimental (two-phase) operating conditions investigated in this thesis, see Table 4.2.

Figure D.1: Developed radial profiles of the velocity, turbulent kinetic energy and turbulent dissipation rate in the single phase (water) simulations with the grid resolutions reported in Table D.1 for the superficial velocity of 1.611 m/s. Red curve: Grid 1; green curve: Grid 2; blue curve: Grid 3; and yellow curve: Grid 4.

The comparison of the predictions in Figure D.1 suggests that the distance of the first node from the pipe wall in the four tested grids is large enough to employ standard wall functions. However, the use of wall functions is more problematic when the Reynolds number is low, as indicated also by Eq. (D.1). Therefore, it is necessary to examine the predictions by the simulations with the four grids for the superficial velocity of 0.405 m/s, which is the minimum of the superficial liquid velocities reported in Table 4.2. These predictions are depicted in Figure D.2, which imply that Grid 1 is too refined to use standard wall functions for the superficial velocity of 0.405 m/s. In particular, the prediction for the turbulent kinetic energy obtained by using Grid 1 is totally different from those obtained by using the other grids. It is worth mentioning that the same observation was made in the case of setting the superficial velocities equal to 0.641 and 1.017 m/s.
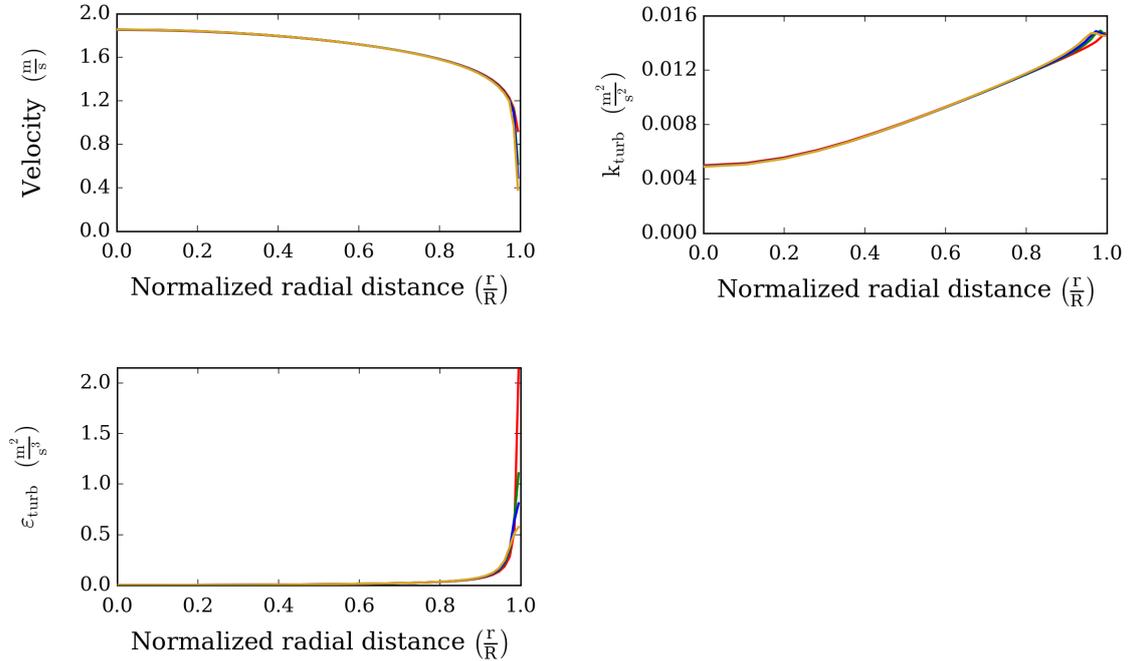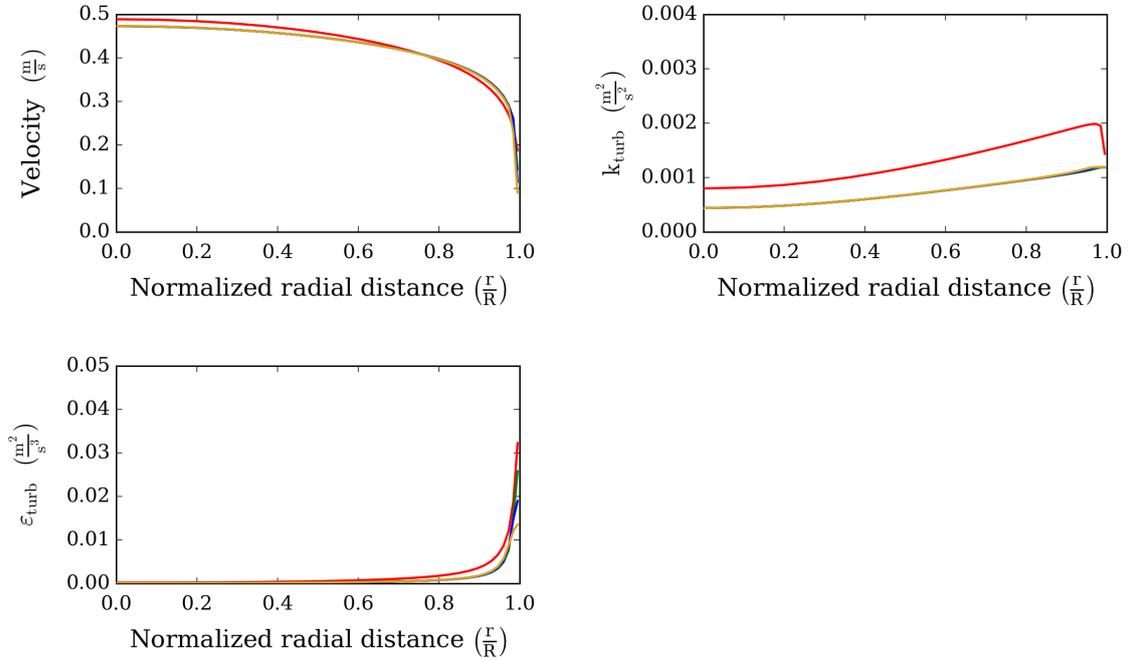

Figure D.2: Developed radial profiles of the velocity, turbulent kinetic energy and turbulent dissipation rate in the single phase (water) simulations with the grid resolutions reported in Table D.1 for the superficial velocity of 0.405 m/s. Red curve: Grid 1; green curve: Grid 2; blue curve: Grid 3; and yellow curve: Grid 4.

While Grid 2, 3 and 4 seem to be suitable for the single-phase simulations, it is not always correct when they are used to perform two-phase simulations. As mentioned previously, the grid should be fine enough, particularly near the wall, to capture the profiles of the flow fields satisfactorily. This is particularly important in the case of experimental conditions 008 and 042, where a peak is observed in the radial profiles of the air volume fraction near the wall. Therefore, the grids

reported in Table D.1 are used to simulate the nominal 2-meter column operating under experimental condition 008, for which the results are shown in Figure D.3. First, the results, particularly the radial profiles of the air volume fraction and water turbulent kinetic energy, confirm that Grid 1 is too refined for the same reason explained in the case of single phase simulations. Second, the predictions for the air volume fraction show that Grid 4 is too coarse to capture the peak near the wall and Grid 2 outperforms Grid 3 in representing the peak near the wall. Therefore, the radial resolution of Grid 2 is selected for the design of the mesh used for the two-phase simulations in this thesis.

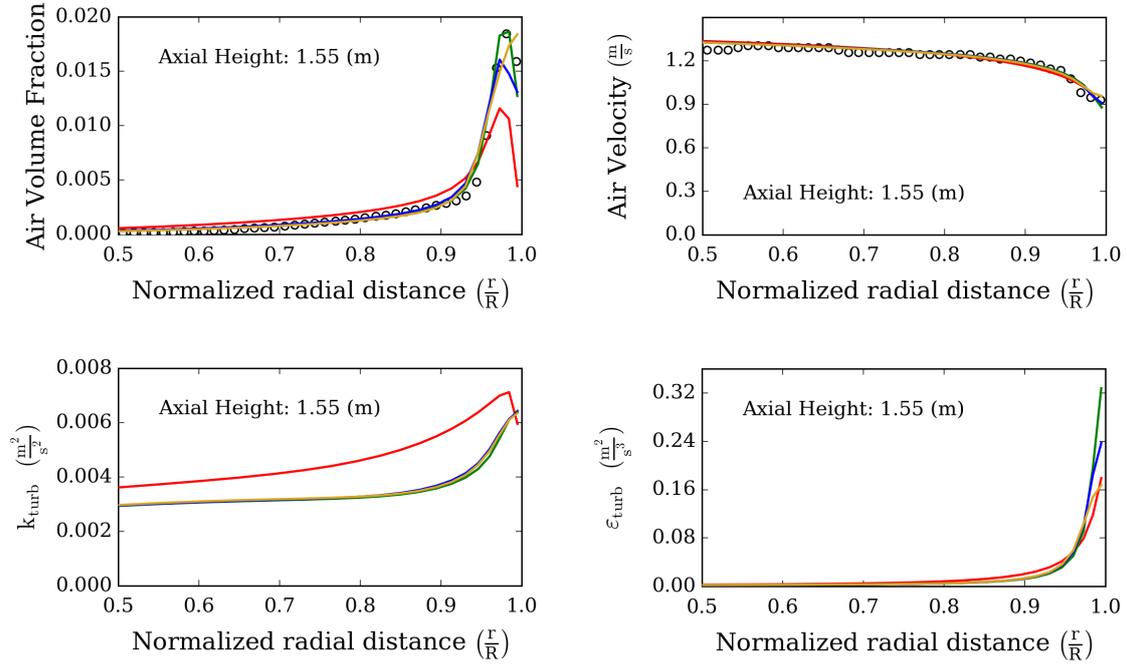**Figure D.3:** Radial profiles of the air volume fraction, air velocity, and turbulent kinetic energy and turbulent dissipation rate of water obtained by using the grid resolutions reported in Table D.1 for experimental condition 008. The employed lift coefficient is 0.15 and the wall lubrication force is modelled by Lubchenko's approach. Red curve: Grid 1; green curve: Grid 2; blue curve: Grid 3; and yellow curve: Grid 4.

List of Abbreviations

BC   Boundary Conditions

BIT   Bubble Induced Turbulence

BSD   Bubble Size Distribution

CFD   Computational Fluid Dynamics

CFL   Courant–Friedrichs–Lewy

CM   Class or Sectional Method

CQMOM   Conditional Quadrature Method of Moments

DNS   Direct Numerical Simulation

DQMOM   Direct Quadrature Method of Moments

EQMOM   Extended Quadrature Method of Moments

GPBE   Generalized Population Balance Equation

HZDR   Helmholtz-Zentrum Dresden-Rossendorf

IC   Initial Conditions

KDF   Kernel Density Function

LES   Large-Eddy Simulation

MFM   Multifluid Model

MOM   Method of Moments

MTE   Moment Transport Equation

MULES   Multidimensional Universal Limiter for Explicit Solution

NDF   Number Density Function

PBE   Population Balance Equation

PBM   Population Balance Modelling

PD   Product-Difference algorithm

PISO   Pressure-Implicit with Splitting of Operators

PTC   Particle Trajectory Crossing

QBMM Quadrature-Based Moment Method

QMOM Quadrature Method of Moments

RANS Reynolds-averaged Navier–Stokes equations

SIMPLE Semi-Implicit Method for Pressure Linked Equations

TFM   Two-Fluid Model

TVD   Total Variation Diminishing

VOF   Volume of Fluid

Bibliography

[1]   Krishna, R. et al. "Flow regime transition in bubble columns". In: *International Communications in Heat and Mass Transfer* 26.4 (1999), pp. 467–475.

[2]   Mudde, R. F. and T. Saito. "Hydrodynamical similarities between bubble column and bubbly pipe flow". In: *Journal of Fluid Mechanics* 437 (2001), pp. 203–228.

[3]   Kantarci, N. et al. "Bubble column reactors". In: *Process Biochemistry* 40.7 (2005), pp. 2263–2283.

[4]   McQuillan, K. and P. Whalley. "Flow patterns in vertical two–phase flow". In: *International Journal of Multiphase Flow* 11.2 (1985), pp. 161–175.

[5]   Liu, T. and S. Bankoff. "Structure of air-water bubbly flow in a vertical pipe–I. Liquid mean velocity and turbulence measurements". In: *International Journal of Heat and Mass Transfer* 36.4 (1993), pp. 1049–1060.

[6]   Liu, T. and S. Bankoff. "Structure of air-water bubbly flow in a vertical pipe–II. Void fraction, bubble velocity and bubble size distribution". In: *International Journal of Heat and Mass Transfer* 36.4 (1993), pp. 1061–1072.

[7]   Hibiki, T. et al. "Axial interfacial area transport of vertical bubbly flows". In: *International Journal of Heat and Mass Transfer* 44.10 (2001), pp. 1869–1888.

[8]   Krepper, E. et al. "On the modelling of bubbly flow in vertical pipes". In: *Nuclear Engineering and Design* 235.5 (2005), pp. 597–611.

[9]   Beyer, M. et al. *Air-water experiments in a vertical DN200-pipe*. Tech. rep. FZD-505. Helmholtz-Zentrum Dresden-Rossendorf, 2008.

[10] Hosokawa, S. and A. Tomiyama. "Multi–fluid simulation of turbulent bubbly pipe flows". In: *Chemical Engineering Science* 64.24 (2009), pp. 5308–5318.

[11] Pfleger, D. and S. Becker. "Modelling and simulation of the dynamic flow behaviour in a bubble column". In: *Chemical Engineering Science* 56.4 (2001), pp. 1737–1747.

[12] Khopkar, A. et al. "Gas–liquid flow generated by a Rushton turbine in stirred vessel: CARPT/CT measurements and CFD simulations". In: *Chemical Engineering Science* 60.8-9 (2005), pp. 2215–2229.

[13] Hjertager, B. H. "Multi-fluid CFD Analysis of Chemical Reactors". In: *Multiphase Reacting Flows: Modelling and Simulation. CISM International Centre for Mechanical Sciences.* Ed. by D. L. Marchisio and R. O. Fox. Vol. 492. Vienna: Springer, 2007, pp. 125–179.

[14] Tabib, M. V. et al. "CFD simulation of bubble column—an analysis of interphase forces and turbulence models". In: *Chemical Engineering Journal* 139.3 (2008), pp. 589–614.

[15] Rzehak, R. and E. Krepper. "CFD modeling of bubble-induced turbulence". In: *International Journal of Multiphase Flow* 55 (2013), pp. 138–155.

[16] Ishii, M. and T. Hibiki. *Thermo-fluid dynamics of two-phase flow.* New York: Springer, 2010.

[17] Rzehak, R. and E. Krepper. "Closure models for turbulent bubbly flows: A CFD study". In: *Nuclear Engineering and Design* 265 (2013), pp. 701–711.

[18] Politano, M. et al. "A model for turbulent polydisperse two-phase flow in vertical channels". In: *International Journal of Multiphase Flow* 29.7 (2003), pp. 1153–1182.

[19] Lubchenko, N. et al. "A more fundamental wall lubrication force from turbulent dispersion regularization for multiphase CFD applications". In: *International Journal of Multiphase Flow* 98 (2018), pp. 36–44.

[20] Rzehak, R. et al. "Comparative study of wall-force models for the simulation of bubbly flows". In: *Nuclear Engineering and Design* 253 (2012), pp. 41–49.

[21] Sugrue, R. M. "A robust momentum closure approach for multiphase computational fluid dynamics applications". PhD thesis. Massachusetts Institute of Technology, 2017.

[22] Tomiyama, A. et al. "Terminal velocity of single bubbles in surface tension force dominant regime". In: *International Journal of Multiphase Flow* 28 (2002), pp. 1497–1519.

[23] Lucas, D. and A. Tomiyama. "On the role of the lateral lift force in polydispersed bubbly flows". In: *International Journal of Multiphase Flow* 37.9 (2011), pp. 1178–1190.

[24] Ziegenhein, T. et al. "A new measuring concept to determine the lift force for distorted bubbles in low Morton number system: Results for air/water". In: *International Journal of Multiphase Flow* 108 (2018), pp. 11–24.

166

[25] Frank, T. et al. "Validation of CFD models for mono-and polydisperse air–water two-phase flows in pipes". In: *Nuclear Engineering and Design* 238.3 (2008), pp. 647–659.

[26] Hosokawa, S. et al. "Lateral migration of single bubbles due to the presence of wall". In: *ASME 2002 Joint US-European Fluids Engineering Division Conference.* American Society of Mechanical Engineers. 2002, pp. 855–860.

[27] Tomiyama, A. et al. "Effects of Eötvös number and dimensionless liquid volumetric flux on lateral motion of a bubble in a laminar duct flow". In: *Advances in Multiphase Flow.* Ed. by A. Serizawa et al. Elsevier, 1995, pp. 3–15.

[28] Antal, S. et al. "Analysis of phase distribution in fully developed laminar bubbly two-phase flow". In: *International Journal of Multiphase Flow* 17.5 (1991), pp. 635–652.

[29] Tran-Cong, S. et al. "Bubble migration in a turbulent boundary layer". In: *International Journal of Multiphase Flow* 34.8 (2008), pp. 786–807.

[30] Zaruba, A. et al. "Bubble-wall interactions in a vertical gas–liquid flow: Bouncing, sliding and bubble deformations". In: *Chemical Engineering Science* 62.6 (2007), pp. 1591–1605.

[31] Felton, K. and E. Loth. "Spherical bubble motion in a turbulent boundary layer". In: *Physics of Fluids* 13.9 (2001), pp. 2564–2577.

[32] Shaver, D. and M. Podowski. "Modeling of interfacial forces for bubbly flows in subcooled boiling conditions". In: *Trans. Am. Nucl. Soc.(Proc. ANS Winter Mtg.)* 113 (2015), p. 1368.

[33] Bakker, A. and H. Van den Akker. "A computational model for the gas-liquid flow in stirred reactors". In: *Chemical Engineering Research and Design* 72.A4 (1994), pp. 594–606.

[34] Wu, Q. et al. "One-group interfacial area transport in vertical bubbly flow". In: *International Journal of Heat and Mass Transfer* 41.8-9 (1998), pp. 1103–1112.

[35] Lane, G. et al. "Predicting gas–liquid flow in a mechanically stirred tank". In: *Applied Mathematical Modelling* 26.2 (2002), pp. 223–235.

[36] Kerdouss, F. et al. "CFD modeling of gas dispersion and bubble size in a double turbine stirred tank". In: *Chemical Engineering Science* 61.10 (2006), pp. 3313–3322.

[37] Cheung, S. C. et al. "On the numerical study of isothermal vertical bubbly flow using two population balance approaches". In: *Chemical Engineering Science* 62.17 (2007), pp. 4659–4674.

[38]   Olmos, E. et al. "Numerical simulation of multiphase flow in bubble col-umn reactors. Influence of bubble coalescence and break-up". In: *Chemical Engineering Science* 56.21-22 (2001), pp. 6359–6365.

[39]   Venneker, B. C. et al. "Population balance modeling of aerated stirred vessels based on CFD". In: *AIChE Journal* 48.4 (2002), pp. 673–685.

[40]   Chen, P. et al. "Three-dimensional simulation of bubble column flows with bubble coalescence and breakup". In: *AIChE Journal* 51.3 (2005), pp. 696–712.

[41]   Wang, T. et al. "A CFD–PBM coupled model for gas–liquid flows". In: *AIChE Journal* 52.1 (2006), pp. 125–140.

[42]   Bhole, M. et al. "CFD simulation of bubble columns incorporating pop-ulation balance modeling". In: *Chemical Engineering Science* 63.8 (2008), pp. 2267–2282.

[43]   Kerdouss, F. et al. "Two-phase mass transfer coefficient prediction in stirred vessel with a CFD model". In: *Computers & Chemical Engineering* 32.8 (2008), pp. 1943–1955.

[44]   Montante, G. et al. "Gas–liquid flow and bubble size distribution in stirred tanks". In: *Chemical Engineering Science* 63.8 (2008), pp. 2107–2118.

[45]   Krepper, E. et al. "The inhomogeneous MUSIG model for the simulation of polydispersed flows". In: *Nuclear Engineering and Design* 238.7 (2008), pp. 1690–1702.

[46]   Liao, Y. et al. "Baseline closure model for dispersed bubbly flow: Bubble coalescence and breakup". In: *Chemical Engineering Science* 122 (2015), pp. 336–349.

[47]   Sanyal, J. et al. "On the comparison between population balance models for CFD simulation of bubble columns". In: *Industrial & Engineering Chemistry Research* 44.14 (2005), pp. 5063–5072.

[48]   Gimbun, J. et al. "Modelling of mass transfer in gas–liquid stirred tanks agi-tated by Rushton turbine and CD-6 impeller: a scale-up study". In: *Chemical Engineering Research and Design* 87.4 (2009), pp. 437–451.

[49]   Petitti, M. et al. "Bubble size distribution modeling in stirred gas-liquid reactors with QMOM augmented by a new correction algorithm". In: *AIChE Journal* 56 (2010), pp. 36–53.

[50]   Buffo, A. et al. "Multidimensional population balance model for the simula-tion of turbulent gas-liquid systems in stirred tank reactors". In: *Chemical Engineering Science* 70 (2012), pp. 31–44.

[51]   Buffo, A. et al. "Multivariate Quadrature-Based Moments Methods for turbulent polydisperse gas-liquid systems". In: *International Journal of Multiphase Flow* 50 (2013), pp. 41–57.

[52]   Buffo, A. et al. "Simulation of polydisperse multiphase systems using population balances and example application to bubbly flows". In: *Chemical Engineering Research and Design* 91 (2013), pp. 1859–1875.

[53]   Petitti, M. et al. "Simulation of coalescence, break-up and mass transfer in a gas-liquid stirred tank with CQMOM". In: *Chemical Engineering Journal* 228 (2013), pp. 1182–1194.

[54]   Buffo, A. and D. L. Marchisio. "Modeling and simulation of turbulent polydisperse gas-liquid systems via the generalized population balance equation". In: *Reviews in Chemical Engineering* 30 (2014), pp. 73–126.

[55]   Buffo, A. et al. "Simulation of a reacting gas–liquid bubbly flow with CFD and PBM: Validation with experiments". In: *Applied Mathematical Modelling* 44 (2017), pp. 43–60.

[56]   Gemello, L. et al. "Population balance modelling of bubble columns under the heterogeneous flow regime". In: *Chemical Engineering Journal* 372 (2019), pp. 590–604.

[57]   Marchisio, D. L. and R. O. Fox. *Computational Models for Polydisperse Particulate and Multiphase Systems*. Cambridge Series in Chemical Engineering. Cambridge, UK: Cambridge University Press, 2013.

[58]   Marchisio, D. L. and R. O. Fox. "Solution of population balance equations using the direct quadrature method of moments". In: *Journal of Aerosol Science* 36 (2005), pp. 43–73.

[59]   Kah, D. et al. "A high order moment method simulating evaporation and advection of a polydisperse liquid spray". In: *Journal of Computational Physics* 231.2 (2012), pp. 394–422.

[60]   Yoon, C. and R. McGraw. "Representation of generally mixed multivariate aerosols by the quadrature method of moments: I. Statistical foundation". In: *Journal of Aerosol Science* 35 (2004), pp. 561–576.

[61]   Wright Jr., D. L. "Numerical advection of moments of the particle size distribution in Eulerian models". In: *Journal of Aerosol Science* 38 (2007), pp. 352–369.

[62]   Vikas, V. et al. "Realizable high-order finite-volume schemes for quadrature-based moment methods". In: *Journal of Computational Physics* 230 (2011), pp. 5328–5352.

[63] Laurent, F. and T. T. Nguyen. "Realizable second-order finite-volume schemes for the advection of moment sets of the particle size distribution". In: *Journal of Computational Physics* 337 (2017), pp. 309–338.

[64] Desjardins, O. et al. "A quadrature-based moment method for dilute fluid-particle flows". In: *Journal of Computational Physics* 227 (2008), pp. 2514–2539.

[65] LeVeque, R. J. *Finite Volume Methods for Hyperbolic Problems.* 1st ed. Cambridge University Press, 2002.

[66] Buffo, A. et al. "On the implementation of moment transport equations in OpenFOAM: Boundedness and realizability". In: *International Journal of Multiphase Flow* 85 (2016), pp. 223–235.

[67] Tryggvason, G. et al. *Direct numerical simulations of gas–liquid multiphase flows.* Cambridge University Press, 2011.

[68] Tryggvason, G. et al. "A front-tracking method for the computations of multiphase flow". In: *Journal of Computational Physics* 169.2 (2001), pp. 708–759.

[69] Hirt, C. W. and B. D. Nichols. "Volume of fluid (VOF) method for the dynamics of free boundaries". In: *Journal of Computational Physics* 39.1 (1981), pp. 201–225.

[70] Scardovelli, R. and S. Zaleski. "Direct numerical simulation of free-surface and interfacial flow". In: *Annual Review of Fluid Mechanics* 31.1 (1999), pp. 567–603.

[71] Unverdi, S. O. and G. Tryggvason. "A front-tracking method for viscous, incompressible, multi-fluid flows". In: *Journal of Computational Physics* 100.1 (1992), pp. 25–37.

[72] Osher, S. and J. A. Sethian. "Fronts propagating with curvature-dependent speed: algorithms based on Hamilton-Jacobi formulations". In: *Journal of Computational Physics* 79.1 (1988), pp. 12–49.

[73] Sethian, J. A. *Level set methods and fast marching methods: evolving interfaces in computational geometry, fluid mechanics, computer vision, and materials science.* Vol. 3. Cambridge University Press, 1999.

[74] Osher, S. and R. Fedkiw. *Level set methods and dynamic implicit surfaces.* Vol. 153. Springer Science & Business Media, 2006.

[75] Gopala, V. R. and B. G. van Wachem. "Volume of fluid methods for immiscible-fluid and free-surface flows". In: *Chemical Engineering Journal* 141.1-3 (2008), pp. 204–221.

[76] Balachandar, S. and J. K. Eaton. "Turbulent dispersed multiphase flow". In: *Annual Review of Fluid Mechanics* 42 (2010), pp. 111–133.

[77] Jakobsen, H. A. *Chemical reactor modeling*. Springer, 2014.

[78] Kitagawa, A. et al. "Two-way coupling of Eulerian–Lagrangian model for dispersed multiphase flows using filtering functions". In: *International Journal of Multiphase Flow* 27.12 (2001), pp. 2129–2153.

[79] Garg, R. et al. "Accurate numerical estimation of interphase momentum transfer in Lagrangian–Eulerian simulations of dispersed two-phase flows". In: *International Journal of Multiphase Flow* 33.12 (2007), pp. 1337–1364.

[80] Garg, R. et al. "A numerically convergent Lagrangian–Eulerian simulation method for dispersed two-phase flows". In: *International Journal of Multiphase Flow* 35.4 (2009), pp. 376–388.

[81] Subramaniam, S. "Lagrangian–Eulerian methods for multiphase flows". In: *Progress in Energy and Combustion Science* 39.2-3 (2013), pp. 215–245.

[82] Drew, D. A. "Mathematical modeling of two-phase flow". In: *Annual Review of Fluid Mechanics* 15.1 (1983), pp. 261–291.

[83] Enwald, H. et al. "Eulerian two-phase flow theory applied to fluidization". In: *International Journal of Multiphase Flow* 22 (1996), pp. 21–66.

[84] Drew, D. and S. Passman. *Theory of multicomponent fluids*. New York: Springer, 1998.

[85] Tomiyama, A. et al. "Drag coefficients of single bubbles under normal and micro gravity conditions". In: *JSME International Journal Series B Fluids and Thermal Engineering* 41.2 (1998), pp. 472–479.

[86] Žun, I. "The transverse migration of bubbles influenced by walls in vertical bubbly flow". In: *International Journal of Multiphase Flow* 6.6 (1980), pp. 583–588.

[87] Wellek, R. et al. "Shape of liquid drops moving in liquid media". In: *AIChE Journal* 12.5 (1966), pp. 854–862.

[88] Ma, T. et al. "Direct numerical simulation–based Reynolds-averaged closure for bubble-induced turbulence". In: *Physical Review Fluids* 2.3 (2017), p. 034301.

[89] Viollet, P. and O. Simonin. "Modelling dispersed two-phase flows: closure, validation and software development". In: *Applied Mechanics Reviews* 47.6 (1994), S80–S84.

[90] Sokolichin, A. and G. Eigenberger. "Applicability of the standard k–ε turbulence model to the dynamic simulation of bubble columns: Part I. Detailed numerical simulations". In: *Chemical Engineering Science* 54.13-14 (1999), pp. 2273–2284.

[91]   Borchers, O. et al. "Applicability of the standard k–ε turbulence model to the dynamic simulation of bubble columns. Part II:: Comparison of detailed experiments and flow simulations". In: *Chemical Engineering Science* 54.24 (1999), pp. 5927–5935.

[92]   Troshko, A. and Y. Hassan. "A two-equation turbulence model of turbulent bubbly flows". In: *International Journal of Multiphase Flow* 27.11 (2001), pp. 1965–2000.

[93]   Zhang, D. et al. "Numerical simulation of the dynamic flow behavior in a bubble column: A study of closures for turbulence and interface forces". In: *Chemical Engineering Science* 61 (2006), pp. 7593–7608.

[94]   Díaz, M. E. et al. "Numerical simulation of the gas–liquid flow in a laboratory scale bubble column: influence of bubble size distribution and non-drag forces". In: *Chemical Engineering Journal* 139.2 (2008), pp. 363–379.

[95]   Simonnet, M. et al. "CFD simulation of the flow field in a bubble column reactor: Importance of the drag force formulation to describe regime transitions". In: *Chemical Engineering and Processing: Process Intensification* 47.9-10 (2008), pp. 1726–1737.

[96]   Kataoka, I. and A. Serizawa. "Basic equations of turbulence in gas-liquid two-phase flow". In: *International Journal of Multiphase Flow* 15.5 (1989), pp. 843–855.

[97]   Launder, B. E. and B. Sharma. "Application of the energy-dissipation model of turbulence to the calculation of flow near a spinning disc". In: *Letters in Heat and Mass Transfer* 1.2 (1974), pp. 131–137.

[98]   Lance, M. and J. Bataille. "Turbulence in the liquid phase of a uniform bubbly air–water flow". In: *Journal of Fluid Mechanics* 222 (1991), pp. 95–118.

[99]   Shawkat, M. et al. "On the liquid turbulence energy spectra in two-phase bubbly flow in a large diameter vertical pipe". In: *International Journal of Multiphase Flow* 33.3 (2007), pp. 300–316.

[100] Theofanous, T. and J. Sullivan. "Turbulence in two-phase dispersed flows". In: *Journal of Fluid Mechanics* 116 (1982), pp. 343–362.

[101] Wang, S. et al. "3-D turbulence structure and phase distribution measurements in bubbly two-phase flows". In: *International Journal of Multiphase Flow* 13.3 (1987), pp. 327–343.

[102] Ramkrishna, D. *Population Balances: Theory and Applications to Particulate Systems in Engineering.* 1st ed. Academic Press, 2000.

[103] Laurent, F. and M. Massot. "Multi-fluid modelling of laminar polydisperse spray flames: origin, assumptions and comparison of sectional and sampling methods". In: *Combustion Theory and Modelling* 5.4 (2001), pp. 537–572.

[104] Laurent, F. et al. "Eulerian multi-fluid modeling for the numerical simulation of coalescence in polydisperse dense liquid sprays". In: *Journal of Computational Physics* 194.2 (2004), pp. 505–543.

[105] Fan, R. et al. "Application of the direct quadrature method of moments to polydisperse gas-solid fluidized beds". In: *Powder Technology* 139 (2004), pp. 7–20.

[106] Fox, R. O. et al. "Numerical simulation of spray coalescence in an Eulerian framework: direct quadrature method of moments and multi-fluid method". In: *Journal of Computational Physics* 227.6 (2008), pp. 3058–3088.

[107] De Chaisemartin, S. et al. "Eulerian models for turbulent spray combustion with polydispersity and droplet crossing". In: *Comptes Rendus Mécanique* 337.6-7 (2009), pp. 438–448.

[108] Mazzei, L. et al. "New quadrature-based moment method for the mixing of inert polydisperse fluidized powders in commercial CFD codes". In: *AIChE Journal* 58 (2012), pp. 3054–3069.

[109] Drew, D. A. "A turbulent dispersion model for particles or bubbles". In: *Journal of Engineering Mathematics* 41.2-3 (2001), pp. 259–274.

[110] Zaichik, L. et al. "An Eulerian approach for large eddy simulation of particle transport in turbulent flows". In: *Journal of Turbulence* 10 (2009), N4.

[111] Fox, R. O. "Large-eddy-simulation tools for multiphase flows". In: *Annual Review of Fluid Mechanics* 44 (2012), pp. 47–76.

[112] Marchisio, D. L. et al. "Quadrature method of moments for aggregation-breakage processes". In: *Journal of Colloid and Interface Science* 258 (2003), pp. 322–334.

[113] Coulaloglou, C. and L. Tavlarides. "Description of interaction processes in agitated liquid-liquid dispersions". In: *Chemical Engineering Science* 32.11 (1977), pp. 1289–1297.

[114] Laakkonen, M. et al. "Validation of bubble breakage, coalescence and mass transfer models for gas-liquid dispersion in agitated vessel". In: *Chemical Engineering Science* 61 (2006), pp. 218–228.

[115] Prince, M. J. and H. W. Blanch. "Bubble coalescence and break-up in air-sparged bubble columns". In: *AIChE Journal* 36.10 (1990), pp. 1485–1499.

[116] Kumar, S. and D. Ramkrishna. "On the solution of population balance equations by discretization—I. A fixed pivot technique". In: *Chemical Engineering Science* 51.8 (1996), pp. 1311–1332.

[117] Gelbard, F. et al. "Sectional representations for simulating aerosol dynamics". In: *Journal of Colloid and Interface Science* 76.2 (1980), pp. 541–556.

[118] Alopaeus, V. et al. "Solution of population balances with breakage and agglomeration by high-order moment-conserving method of classes". In: *Chemical Engineering Science* 61.20 (2006), pp. 6732–6752.

[119] Vanni, M. "Approximate Population Balance Equations for Aggregation-Breakage Processes". In: *Journal of Colloid and Interface Science* 221 (2000), pp. 143–160.

[120] Kumar, J. et al. "Improved accuracy and convergence of discretized population balance for aggregation: The cell average technique". In: *Chemical Engineering Science* 61.10 (2006), pp. 3327–3342.

[121] Kumar, S. and D. Ramkrishna. "On the solution of population balance equations by discretization—III. Nucleation, growth and aggregation of particles". In: *Chemical Engineering Science* 52.24 (1997), pp. 4659–4679.

[122] Marchal, P. et al. "Crystallization and precipitation engineering–I. An efficient method for solving population balance in crystallization with agglomeration". In: *Chemical Engineering Science* 43.1 (1988), pp. 59–67.

[123] David, R. et al. "Crystallization and precipitation engineering–IV. Kinetic model of adipic acid crystallization". In: *Chemical Engineering Science* 46.4 (1991), pp. 1129–1136.

[124] Hounslow, M. et al. "A discretized population balance for nucleation, growth, and aggregation". In: *AIChE Journal* 34.11 (1988), pp. 1821–1832.

[125] Kumar, J. et al. "The cell average technique for solving multi-dimensional aggregation population balance equations". In: *Computers & Chemical Engineering* 32 (2008), pp. 1810–1830.

[126] Buffo, A. and V. Alopaeus. "Solution of bivariate population balance equations with high-order moment-conserving method of classes". In: *Computers & Chemical Engineering* 87 (2016), pp. 111–124.

[127] Hulburt, H. M. and S. Katz. "Some problems in particle technology: A statistical mechanical formulation". In: *Chemical Engineering Science* 19 (1964), pp. 555–574.

[128] Fox, R. O. "Introduction and fundamentals of modeling approaches for polydisperse multiphase flows". In: *Multiphase Reacting Flows: Modelling and Simulation. CISM International Centre for Mechanical Sciences*. Ed. by D. L. Marchisio and R. O. Fox. Vol. 492. Vienna: Springer, 2007, pp. 1–40.

[129] Frenklach, M. "Method of moments with interpolative closure". In: *Chemical Engineering Science* 57.12 (2002), pp. 2229–2239.

174

[130] Lee, K. "Change of particle size distribution during Brownian coagulation". In: *Journal of Colloid and Interface Science* 92.2 (1983), pp. 315–325.

[131] Kruis, F. E. et al. "A simple model for the evolution of the characteristics of aggregate particles undergoing coagulation and sintering". In: *Aerosol Science and Technology* 19.4 (1993), pp. 514–526.

[132] Strumendo, M. and H. Arastoopour. "Solution of PBE by MOM in finite size domains". In: *Chemical Engineering Science* 63.10 (2008), pp. 2624–2640.

[133] McGraw, R. "Description of aerosol dynamics by the quadrature method of moments". In: *Aerosol Science and Technology* 27 (1997), pp. 255–265.

[134] Diemer, R. and J. Olson. "A moment methodology for coagulation and breakage problems: Part 2–moment models and distribution reconstruction". In: *Chemical Engineering Science* 57.12 (2002), pp. 2211–2228.

[135] Gordon, R. G. "Error bounds in equilibrium statistical mechanics". In: *Journal of Mathematical Physics* 9 (1968), pp. 655–663.

[136] Wheeler, J. C. "Modified moments and Gaussian quadratures". In: *Rocky Mountain Journal of Mathematics* 4 (1974), pp. 287–296.

[137] Massot, M. et al. "A robust moment method for evaluation of the disappearance rate of evaporating sprays". In: *SIAM Journal on Applied Mathematics* 70.8 (2010), pp. 3203–3234.

[138] Yuan, C. et al. "An extended quadrature method of moments for population balance equations". In: *Journal of Aerosol Science* 51 (2012), pp. 1–23.

[139] Pigou, M. et al. "New developments of the Extended Quadrature Method of Moments to solve Population Balance Equations". In: *Journal of Computational Physics* 365 (2018), pp. 243–268.

[140] Shohat, J. A. and J. D. Tamarkin. *The problem of moments.* New York, USA: American Mathematical Society, 1943.

[141] Shiea, M. et al. "A novel finite-volume TVD scheme to overcome non-realizability problem in quadrature-based moment methods". In: *Journal of Computational Physics* (in press).

[142] Marchisio, D. L. et al. "Role of turbulent shear rate distribution in aggregation and breakage processes". In: *AIChE Journal* 52.1 (2006), pp. 158–173.

[143] Wright Jr., D. L. et al. "Bivariate Extension of the Quadrature Method of Moments for Modeling Simultaneous Coagulation and Sintering of Particle Populations". In: *Journal of Colloid and Interface Science* 236 (2001), pp. 242–251.

[144] Yoon, C. and R. McGraw. "Representation of generally mixed multivariate aerosols by the quadrature method of moments: II. Aerosol dynamics". In: *Journal of Aerosol Science* 35 (2004), pp. 577–598.

[145] Fox, R. O. "A quadrature-based third-order moment method for dilute gas-particle flows". In: *Journal of Computational Physics* 227.12 (2008), pp. 6313–6350.

[146] Fox, R. O. "Higher-order quadrature-based moment methods for kinetic equations". In: *Journal of Computational Physics* 228 (2009), pp. 7771–7791.

[147] Cheng, J. C. and R. O. Fox. "Kinetic modeling of nanoprecipitation using CFD coupled with a population balance". In: *Industrial & Engineering Chemistry Research* 49.21 (2010), pp. 10651–10662.

[148] Yuan, C. and R. O. Fox. "Conditional quadrature method of moments for kinetic equations". In: *Journal of Computational Physics* 230 (2011), pp. 8216–8246.

[149] Press, W. H. et al. *Numerical Recipes: The Art of Scientific Computing.* 3rd ed. Cambridge University Press, 2007.

[150] Fox, R. O. "Optimal Moment Sets for Multivariate Direct Quadrature Method of Moments". In: *Industrial & Engineering Chemistry Research* 48 (2009), pp. 9686–9696.

[151] Grosch, R. et al. "Generalization and numerical investigation of QMOM". In: *AIChE Journal* 53.1 (2007), pp. 207–227.

[152] Ferry, J. and S. Balachandar. "A fast Eulerian method for disperse two-phase flow". In: *International Journal of Multiphase Flow* 27.7 (2001), pp. 1199–1226.

[153] Zucca, A. et al. "Implementation of the population balance equation in CFD codes for modelling soot formation in turbulent flames". In: *Chemical Engineering Science* 61 (2006), pp. 87–95.

[154] Bannari, R. et al. "Three-dimensional mathematical modeling of dispersed two-phase flow using class method of population balance in bubble columns". In: *Computers & Chemical Engineering* 32.12 (2008), pp. 3224–3237.

[155] Li, D. et al. "Droplet breakage and coalescence in liquid–liquid dispersions: Comparison of different kernels with EQMOM and QMOM". In: *AIChE Journal* 63.6 (2017), pp. 2293–2311.

[156] Marble, F. E. "Dynamics of dusty gases". In: *Annual Review of Fluid Mechanics* 2.1 (1970), pp. 397–446.

[157] Selma, B. et al. "Simulation of bubbly flows: Comparison between direct quadrature method of moments (DQMOM) and method of classes (CM)". In: *Chemical Engineering Science* 65.6 (2010), pp. 1925–1941.

[158] Silva, L. F. L. R. and P. L. C. Lage. "Development and implementation of a polydispersed multiphase flow model in OpenFOAM". In: *Computers & Chemical Engineering* 35 (2011), pp. 2653–2666.

[159] Icardi, M. et al. "Efficient simulation of gas–liquid pipe flows using a generalized population balance equation coupled with the algebraic slip model". In: *Applied Mathematical Modelling* 38.17-18 (2014), pp. 4277–4290.

[160] Passalacqua, A. et al. "Quadrature-Based Moment Methods for Polydisperse Gas-Solids Flows". In: *Computational Gas-Solids Flows and Reacting Systems: Theory, Methods and Practice.* Ed. by S. Pannala et al. IGI Global, 2011, pp. 221–244.

[161] Passalacqua, A. et al. "A fully coupled quadrature-based moment method for dilute to moderately dilute fluid–particle flows". In: *Chemical Engineering Science* 65.7 (2010), pp. 2267–2283.

[162] Fox, R. O. and P. Vedula. "Quadrature-Based Moment Model for Moderately Dense Polydisperse Gas- Particle Flows". In: *Industrial & Engineering Chemistry Research* 49.11 (2009), pp. 5174–5187.

[163] Spalding, D. "Numerical computation of multi-phase fluid flow and heat transfer". In: *Recent Advances in Numerical Methods in Fluids.* Ed. by C. Taylor and K. Morgan. Pineridge Press, 1980, pp. 139–167.

[164] Passalacqua, A. et al. "A second-order realizable scheme for moment advection on unstructured grids". In: *Computer Physics Communications* 248 (2020), published online.

[165] Rzehak, R. and E. Krepper. "Bubbly flows with fixed polydispersity: validation of a baseline closure model". In: *Nuclear Engineering and Design* 287 (2015), pp. 108–118.

[166] Prasser, H.-M. et al. "Bubble size measurement using wire-mesh sensors". In: *Flow measurement and Instrumentation* 12.4 (2001), pp. 299–312.

[167] Wangjiraniran, W. et al. "Intrusive effect of wire mesh tomography on gas-liquid flow measurement". In: *Journal of nuclear science and technology* 40.11 (2003), pp. 932–940.

[168] Peña, H. V. and O. Rodriguez. "Applications of wire-mesh sensors in multiphase flows". In: *Flow measurement and instrumentation* 45 (2015), pp. 255–273.

177

[169] Tompkins, C. et al. "Wire-mesh sensors: A review of methods and uncertainty in multiphase flows relative to other measurement techniques". In: *Nuclear Engineering and Design* 337 (2018), pp. 205–220.

[170] Rhie, C. and W. L. Chow. "Numerical study of the turbulent flow past an airfoil with trailing edge separation". In: *AIAA Journal* 21.11 (1983), pp. 1525–1532.

[171] Berthon, C. et al. "Stability of the MUSCL schemes for the Euler equations". In: *Communications in Mathematical Sciences* 3.2 (2005), pp. 133–157.

[172] Ferziger, J. H. and M. Peric. *Computational Methods for Fluid Dynamics.* 3rd. Berlin, Germany: Springer, 2001.

[173] Roe, P. and M. Baines. "Algorithms for advection and shock problems". In: *Numerical Methods in Fluid Mechanics.* 1982, pp. 281–290.

[174] Van Leer, B. "Towards the ultimate conservative difference scheme. II. Monotonicity and conservation combined in a second-order scheme". In: *Journal of Computational Physics* 14.4 (1974), pp. 361–370.

[175] Sweby, P. K. "High resolution schemes using flux limiters for hyperbolic conservation laws". In: *SIAM Journal on Numerical Analysis* 21.5 (1984), pp. 995–1011.

[176] Harten, A. "High resolution schemes for hyperbolic conservation laws". In: *Journal of Computational Physics* 49.3 (1983), pp. 357–393.

[177] Versteeg, H. K. and W. Malalasekera. *An introduction to computational fluid dynamics: the finite volume method.* 2nd. Pearson Education, 2007.

[178] Darwish, M. and F. Moukalled. "TVD schemes for unstructured grids". In: *International Journal of Heat and Mass Transfer* 46.4 (2003), pp. 599–611.

[179] Jasak, H. et al. "High resolution NVD differencing scheme for arbitrarily unstructured meshes". In: *International Journal for Numerical Methods in Fluids* 31.2 (1999), pp. 431–449.